Posture Dependent Vibration Resistance of Serial Robot Manipulators to Applied Oscillating Loads

by

James Hearne

A thesis
presented to the University of Waterloo
in fulfilment of the
thesis requirement for the degree of
Master of Applied Science
in
Mechanical Engineering

Waterloo, Ontario, Canada, 2009

Author's Declaration

I hereby declare that I am the sole author of this thesis. This is a true copy of the thesis, including any required final revisions, as accepted by my examiners.

James Hearne

I understand that my thesis may be made electronically available to the public.

James Hearne

Abstract

There are several advantages to replacing CNC machinery with robotic machine tools and as such robotic machining is emerging into the manufacturing and metal cutting industry. There remain several disadvantages to using robots over CNC stations primarily due to flexibility in robotic manipulators, which severely reduces accuracy when operating under high machining forces. This flexibility is dependent on configuration and thus the configuration can be optimised through posture selection to minimise deflection. In previous work little has been done to account for operating frequency and the additional complications that can arise from frequency dependent responses of robotic machine tools.

A Fanuc S-360 manipulator was used to experimentally investigate the benefits of including frequency compensation in posture selection. The robot dynamics first had to be identified and experimental modal analysis was selected due the inherent dependency on frequency characteristics. Specifically, a circle fit operation identified modal parameters and a least squares optimisation generated dynamic parameters for a spatial model. A rigid-link flexible-joint model was selected and a pseudo-joint was used to create an additional DOF to accommodate link flexibility.

Posture optimisation was performed using a gradient-descent algorithm that used several starting points to identify a global minimum. The results showed that a subset of modal data that excluded the mode shape vectors could be used to create a model to predict the manipulator vibration response. It was also found that the receptance variation of the manipulator with configuration was insufficient to verify the optimisation throughout the entire selected workspace; however the model was shown to be useful in regions containing multiple peaks where the modelled dynamics were dominant over the highly volatile measured data.

Simulations were performed on a redundant planar manipulator to overcome the lack of receptance variation found in the Fanuc manipulator. These simulations showed that there were two mechanisms driving the optimisation; overall amplitude reduction and frequency specific amplitude reduction. Using a stiffness posture measure for comparison, the results of the frequency specific reduction could be separated and were found to be particularly beneficial when operating close to resonant frequencies.

Acknowledgements

I would like to thank my supervisor Dr. William Owen for his support, knowledge, advice, patience, sense of humour, and troubleshooting skills during my studies.

I would also like to thank Dr. Kaan Erkorkmaz, Jeff Gorniak, and Yasin Hosseinkhani of the Precision Controls Lab, for the use of their modal analysis equipment, their expertise with the software, and for opening the lab door for me twice a day for a month without comment or complaint. Thank you as well to Dr. Amir Khajepour and Orang Vahid-Araghi for use of their modal analysis equipment and training on said equipment. Thank you also to Dr. Jan Huissoon for his generous loan of an industrial manipulator so that I could bash it with a hammer in the name of science.

Furthermore, I would like to thank Dr. Armaghan Salehian for her advice on modelling and modal testing, Antonio Sanchez for his help with optimisation techniques, Robin Christian and Brian Kettlewell for assorted mathematical aid, Bill Bombardier, Willem Petersen, and Matthew Millard for assorted dynamics tutoring, and Robert Wagner for his contributions with experience, joke, or wrench when either was required.

Finally, I would like to thank my friends and teammates from Grad House F.C. who carefully protected my sanity from the dangers of “working too hard,” and of course my family who somehow managed to offer meaningful support from the other side of this enormous country. It was all greatly appreciated.

Table of Contents

List of Tables

List of Figures

List of Abbreviations

DFT	Discrete Fourier Transform
DOF	Degree(s) of Freedom
FRF	Frequency Response Function
LS	Least Squares
LSFD	Least Squares Frequency Domain
MIF	Modal Indicator Function

Nomenclature

General Mathematical Notation

n	Arbitrary Integer
λ^*	Complex Conjugate of Variable λ
$\dot{x}$	First Time Derivative of x
$\ddot{x}$	Second Time Derivative of x
i	Imaginary Variable $\sqrt{-1}$
s	Laplace Variable
$\boldsymbol{I}$	Identity Matrix
$\boldsymbol{J}^T$	Transpose of Vector or Matrix $\boldsymbol{J}$
$\boldsymbol{J}^{-T}$	Inverse of the Transpose of Vector or Matrix $\boldsymbol{J}$
$\boldsymbol{J}^+$	Moore Penrose Pseudo Inverse of Matrix $\boldsymbol{J}$
$\lvert\boldsymbol{A}\rvert$	Magnitude of Vector $\boldsymbol{A}$
$\frac{\partial \alpha}{\partial q_1}$	Partial Derivative of Function α with respect to Variable q_1
$\alpha\rvert_{q=\hat{q}}$	Function α Evaluated with Variable q Equal to Value $\hat{q}$
$\frac{\partial \xi}{\partial \boldsymbol{q}}$	Partial Derivative of Function ξ with respect to Vector $\boldsymbol{q}$
$sign()$	Sign Function restricted to the domain {1, -1}

Single Link Dynamics

B_q	Joint Damping
I	Link Inertia $[kgm^2]$
J_i	i^{th} Fanuc S-360 Manipulator Joint Number
J_M	Motor Inertia $[kgm^2]$
K_q	Joint Stiffness
M	Link Mass $[kg]$
q_L	Generalised Link Coordinate
q_M	Generalised Motor Coordinate

Manipulator Dynamics

$\boldsymbol{B}_q$	Matrix of Joint Damping Values
$\boldsymbol{C}$	Christoffel Matrix
$\boldsymbol{D}$	Manipulator Inertia Matrix
$\boldsymbol{F}$	Cartesian Force Vector [N]
$\boldsymbol{J}$	Manipulator Jacobian
$\boldsymbol{J}_M$	Matrix of Motor Inertias
$\boldsymbol{K}_q$	Matrix of Joint Stiffness Values
$\boldsymbol{q}, \boldsymbol{q}_D$	Vector of Deflection Coordinates
q_i	i^{th} Joint Angle [rad]
$\boldsymbol{q}_L$	Vector of Link Coordinates
$\boldsymbol{q}_M$	Vector of Motor Coordinates
ρ	Pseudo-Joint Angle [rad]
$\boldsymbol{\tau}$	Generalised Force Vector

Single Degree of Freedom Modal Theory

$a(t)$	Measured Acceleration Signal [m/s^2]
$a(i\omega)$	Discrete Fourier Transform of $a(t)$ Expressed in the Frequency Domain [m/s^2]
$\bar{A}$	Amplitude Multiplier
$A(i\omega)$	Inertance Frequency Response Function [m/s^2N]
b	System Damping [Ns/m]
f	Axial Force Corresponding to x [N]
$F(t)$	Applied Force Signal [N]
$F(i\omega)$	Discrete Fourier Transform of $F(t)$ Expressed in the Frequency Domain [N]
k	System Stiffness [N/m]
m	System Mass [kg]
t	Time [s]
x	Linear Axis Deflection Scalar [m]
$Y(i\omega)$	Mobility Frequency Response Function [m/sN]
$\alpha(i\omega)$	Receptance Frequency Response Function [m/N]

ζ	Damping Ratio
λ	System Eigenvalue
ω	Frequency $[rad/s]$
ω_n	Natural Frequency $[rad/s]$

Multi Degree of Freedom Modal Theory

$\bar{A}^p_{u,v}$	Amplitude Multiplier for point u, excited at point v, for mode p
$A_{u,v}(i\omega)$	Inertance Curve for point u, excited at point v for all modes
$\bar{\boldsymbol{A}}^p$	Vector set of Amplitude Multipliers for mode p.
$\boldsymbol{A}(i\omega)$	Vector Set of Inertance Curves
$\boldsymbol{B}$	System Damping Values Corresponding to $\boldsymbol{x}$ $[Ns/m]$
$\boldsymbol{f}$	Vector of Axial Forces Corresponding to $\boldsymbol{x}$ $[N]$
K_R	Residual Stiffness
$\boldsymbol{K}$	System Stiffness Values Corresponding to $\boldsymbol{x}$ $[N/m]$
M_R	Residual Mass
$\boldsymbol{M}$	System Mass Values Corresponding to $\boldsymbol{x}$ $[kg]$
p	Vibration Mode
P	Number of Vibration Modes
$\boldsymbol{S}$	Augmented Mass Matrix
$\boldsymbol{T}$	Augmented Stiffness Matrix
u	Measured Degree of Freedom
v	Excited Degree of Freedom
$\boldsymbol{v}$	Concatenated Vector of Position and Velocity
$\boldsymbol{x}$	Linear Axis Deflection Vector $[m]$
$Y_{u,v}(i\omega)$	Mobility Curve for point u, excited at point v for all modes
$\boldsymbol{Y}(i\omega)$	Vector Set of Mobility Curves
$\boldsymbol{\alpha}(i\omega)$	Vector Set of Receptance Curves
β, γ	Arbitrary Scalars
ζ^p	Damping Ratio associated with mode p
λ^p	Eigenvalue associated with mode p

λ_D^p	Damped Eigenvalue Corresponding to Mode p
λ_U^p	Un-damped Eigenvalue Corresponding to Mode p
$\boldsymbol{\lambda}$	Diagonal Matrix of Eigenvalues
$\boldsymbol{\phi}$	Matrix of Eigenvectors
ϕ_u^p	Eigenvector corresponding to the receptance of the pth eigenvalue at the uth degree of freedom
$\bar{\phi}_u^p$	Eigenvector corresponding to the mobility of the pth eigenvalue at the uth degree of freedom
$\boldsymbol{\psi}$	Matrix of Mass Normalised Eigenvectors
ψ_u^p	Mass Normalised Eigenvector corresponding to the pth eigenvalue at the uth degree of freedom
ω_n^p	Natural Frequency associated with mode p

Circle Fit Method

d	Modal Circle Diameter
θ	Phasor Angle
Δ	Differential Frequency Increment

Parameterisation

B_{zi}	i^{th} Measurement Space Damping Value
$\boldsymbol{B}_z$	Measurement Space Damping Matrix
$\boldsymbol{E}$	Error Vector for Least Squares Optimisation
$\boldsymbol{F}_z$	Vector of Axial Forces Corresponding to $\boldsymbol{Z}$
I_i	Manipulator Link Inertia for Link i
K_{zi}	i^{th} Measurement Space Stiffness Value
$\boldsymbol{K}_z$	Measurement Space Stiffness Matrix
m_i	Manipulator Link Mass for Link i
$\boldsymbol{m}$	Vector of Link Mass and Inertia Values

M_{zi}	Measurement Space Mass for Body i
$\boldsymbol{M}_z$	Measurement Space Mass Matrix
$[ML]$	Inertia Mapping Matrix from the Vector of Link Mass and Inertia Values to the Manipulator Inertia Matrix
$[TR]$	Jacobian from Joint Space to Vertical Measurement Space $[TR]: \boldsymbol{q} \rightarrow \boldsymbol{Z}$
$[TS]$	Jacobian from Joint Space to Horizontal Measurement Space $[TS]: \boldsymbol{q} \rightarrow \boldsymbol{Z}_H$
Z_i	i^{th} Measurement Space Degree of Freedom
$\boldsymbol{Z}$	Vector of Measurement Space Vertical Deflections
$\boldsymbol{Z}_H$	Vector of Measurement Space Horizontal Deflections
$\boldsymbol{\delta}_H$	Horizontal Measurement Space Receptance
$\boldsymbol{\delta}_q$	Joint Space Receptance
$\boldsymbol{\delta}_z$	Vertical Measurement Space Receptance
$\boldsymbol{\lambda}_C$	Vector of Calculated Eigenvalues
$\boldsymbol{\lambda}_M$	Vector of Measured Eigenvalues
$\boldsymbol{\psi}_C$	Concatenated Vector of Measured Eigenvectors
$\boldsymbol{\psi}_M$	Concatenated Vector of Measured Eigenvectors

<u>Optimisation</u>

C_i	i^{th} Manipulator Configuration
dq	Differential Joint Angle Perturbation
dq_i	Differential i^{th} Joint Angle Perturbation
dt	Differential Time Element
$\boldsymbol{e}$	Vector of Cartesian Space Position Errors
$G(i\omega)$	Predicted Receptance with Amplitude Multipliers
$H(i\omega)$	Predicted Receptance without Amplitude Multipliers

k_{DC}	Zero Frequency Gain for Receptance of a Mechanical System
k_o	Optimisation Gain
k_v	Velocity Command Gain
$\boldsymbol{k}_o$	Vector of Optimisation Gains
$\boldsymbol{k}_p$	Vector of Error Correction Gains
K_{RB}	Rigid Body Stiffness of a Mechanical System
$\bar{q}_i$	Current Value of the i^{th} Joint q_i
$\bar{\boldsymbol{q}}$	Current Value of the Joint Vector $\boldsymbol{q}$
$\boldsymbol{u}$	Arbitrary Vector for Dynamic Parameter Projection
$\boldsymbol{V}$	Arbitrary Vector
$\boldsymbol{V}_{NULL}$	Null Space Projection of Arbitrary Vector $\boldsymbol{V}$
$\bar{\boldsymbol{\omega}}$	Current Frequency Value
$\alpha_q(i\omega)$	Predicted End-Effector Drive Point Receptance
ξ	Objective Function
ξ_K	Stiffness Measure
ξ_M	Mobility Measure
σ	Amplitude Correction Factor for Comparing $H(i\omega)$ and $G(i\omega)$
ω_{ni}	i^{th} Identified Natural Frequencies
$\acute{\boldsymbol{\omega}}$	Vector of Initial Conditions for Frequency Optimisations

Chapter 1 Introduction

1.1 Overview

While strict definitions for industrial robots and robots in general are still quite vague, they are generally considered to be machines as shown in Figure 1.1. The first industrial robot is considered to be the Unimate created by George Charles Devol in 1954 [1]. The Unimate was a reprogrammable six axis serial manipulator using hydraulic actuators and was first used in industry in 1961 for die cast handling by General Motors. Since then, the use of industrial robots has expanded to include an extremely wide variety of applications ranging from assembly [2] to neurosurgery [3] to laser welding [4] to theme park rides [5]. In manufacturing and materials handling this expanding use of industrial robots has allowed the removal of humans from hazardous working environments and has allowed the manufacturing industry to perform repetitive operations automatically, at high speeds, and with higher precision than human operators are capable of. The combination of these factors has resulted in an improvement in productivity [6]. The hazardous working environments include dusty working conditions and handling dangerous materials as well as tasks that lead to repetitive motion injury.

Figure 1.1: ABB IRB 6660 Industrial Manipulator [7]

Robotic systems have also branched out into material removal process applications, such as grinding [8], die polishing [9], routing [10], and rapid prototyping and machining systems [11]. Though initially limited to softer materials such as wax and foam with poor accuracy of the finished part [12], these systems are beginning to expand into harder materials such as aluminium and higher precision parts as the understanding of their limitations and thus the ability to compensate for the robot's limitations increases [13].

As technology advances to satisfy the desire for more accurate machining, full CNC machining centres are designed and created with precision that often surpasses the requirements for a given part. By using components of this developing technology such as higher order smooth trajectory planning [14] or adaptive control laws [15], less precise machines such as robotic machining systems can be used in place of traditional CNC machines for less demanding applications such as grinding, pre-machining, and machining of high tolerance or low precision parts.

The trend towards machining technology can be seen from the 2005 announcement of a partnership between KUKA robotics and Delcam Inc to interface CAD/CAM software and a robot controller [16] in order to facilitate implementation of industrial robots for machining applications. This is followed by ABB's IRB 6660 manipulator, which was released in 2008 [17] and marketed as a pre-machining robot. Many manufacturing companies already have robots on site for changing cutters for conventional CNC machine tools and are, therefore, familiar with robots and their capabilities. In these cases, the cost of an additional robot when switching from conventional CNC to robotic machining is removed and operator training is reduced.

The use of robots for manufacturing is still a developing field and as such there are many restrictions that need to be addressed. One of the primary concerns is the flexibility inherent in the machines themselves and the displacements caused when a machining force is applied to the end-effector. The problem addressed herein is that of vibrations in robotic machining. The dynamic properties of a robotic machining system are configuration dependent, and thus, can be adjusted through various optimisation methods to improve the vibration resistance of the system. This will enable robotic machining to improve surface finish and tolerances further and expand the range of applications for these systems.

This thesis will address the issue of vibrations resulting from robotic machining by investigating the use of posture selection for optimisation of the machining systems dynamic characteristics. The objective is to construct a desirable frequency response function that will minimise the vibration response of the system. Literature will be reviewed for robotic machining, flexibility modelling, posture selection, and control compensation.

1.2 Robotic Machining

Robotic machining began as low cost machining of soft materials as a way to implement and verify tool path generation algorithms such as the face sculpting system designed by Ko *et al.* [18]. This system extracted facial features that it could then manipulate to show facial expressions before machining them into soft material. Tangelder and Vergeest [11] attempted to use robotic systems to improve CNC based prototyping for applications not well suited to rapid prototyping machines based on curing polymer resins in layers. Whereas CNC had the advantage over alternative technologies in terms of speed, range of materials, and cost among others, robotic systems also offered larger workspaces and the potential for increased complexity of parts, which were noted as desirable traits in a prototyping system. This gave CAD users an additional prototyping tool that could support non-uniform rational B-splines (NURBs). In order to meet the dimensional requirements of their system, a serial industrial manipulator was mounted next to a turntable, which held the part as it was machined from foam stock material. Song and Chen [19] later developed a robotic machining centre comprised of a serial manipulator mounted on a track and a stationary workpiece. This gave a very large work space of $4m \times 2m \times 2m$. The complete system was able to extract surface features from a three dimensional model and generate tool paths using polyhedron and quadratic primitives as well as NURBS. The tool path planning also considered gouging and collision detection. Although developed as platforms for path planning research, these systems further demonstrated the value of robotic systems in rapid prototyping and the use of redundancy to generate large workspaces. Huang and Lin [12] created a dual robot work cell to overcome potential problems with single robot machining systems, namely that the tool may not reach all sides of the workpiece and that there may be small areas that cannot be machined since they are close to singular points. This system could be configured with a part holding robot and a machining robot or with a fixed part and two machining robots working to complete the machining tasks.

As research into robotic rapid prototyping progresses, some researchers are looking at using robotic machining systems for fabrication of final parts and metal cutting realising that the advantages of robotic systems over traditional CNC for rapid prototyping are generally preserved for final part production. Matsuoka *et al.* [20] investigated machining aluminium with a single articulated robot as opposed to a traditional CNC fluting machine. They found that at very high spindle speeds (100,000rpm) the robotic systems exhibited less vibration due to their natural frequencies being much lower than the machining speed. Conversely, the natural frequency of the CNC machine was closer to the spindle speed and resulted in more vibrations. Similarly, Coole *et al.* [21] developed a method to convert CAM data to multiple smaller robot controller language files. They were then able to directly compare the surface finish and final dimensions of plaster machined by both a robotic machining system and a 3-axis CNC machine showing that for plaster machining the robotic system performed slightly better over a range of feed speeds and cutter types. This group then went on to identify feed rate and manipulator arm extension as key contributors to surface finish and dimensions [22]. In metal cutting, researchers at the Stevens Institute of Technology in conjunction with researchers from ABB Inc. began investigations into machining and pre-machining aluminium parts [23]. They found that while the flexibility of the robotic systems was in some ways limiting, it could be compensated for to produce improved results by modelling the deflection of the cutting tool and including joint position compensation based on the measured force acting on the tool. This group also investigated the chatter mechanism in robotic machining [13] and developed stability criterion for robotic end milling. Also in metal working, Dimo *et al.* [24] investigated a stiffness posture measure optimisation to reduce vibrations in a redundant grinding robot based on minimising the displacement for a given load. This used a minimum norm deflection solution and did not consider the frequency effect of the excitation.

Robotic machining is desirable in place of traditional CNC machines for applications where the dimensional and finish tolerances of the part are less demanding. The advantages of robotic machining systems over traditional CNC machines include a larger work envelope for a given floor space, lower capital cost, and higher suitability to machine complex shapes [19]. However, these advantages come at a price. The primary disadvantage of robotic machining is the flexibility inherent in the physical machines. This flexibility results in a greater inaccuracy in the finished part due to deflections at the end-effector. The deflections caused by structural flexibility also reduce the finish of the part as they allow vibrations to propagate through the structure and create low frequency resonances that are generally less heavily damped than the equivalent high frequency resonances associated with CNC machines [25]. Due to this restriction, robotic machining systems are limited to softer materials such as foam, wood, wax, and plastic [19, 26]. Softer materials require lower machining forces and as such will cause smaller deflections and have less impact on the final dimensions of a part. These systems are effective for rapid prototyping, but not for full production where harder materials such as aluminium and steels are used. It is therefore desirable to expand robotic manufacturing to finished products and harder materials thereby reducing the cost associated with high precision CNC equipment.

1.3 Flexibility Modelling and Harmonic Drives

To compensate for the deflections and vibrations that occur in machining, the behaviour must first be modelled. Once this is achieved, corrections can be achieved through controller design or posture optimisation of redundant systems. Posture selection can also be applied to non-redundant manipulators if the end-effector location is not restricted. Robotic machining systems are primarily modelled as rigid-link flexible-joint systems as proposed by Spong [27]. The flexibility of industrial manipulators has been experimentally shown to exist primarily in the joints [23, 28-31]. The flexibility is therefore enhanced by the cantilever structure of serial robots and as such is difficult to significantly reduce. This structure potentially amplifies joint forces, which exploit any flexibility in the joints. In essence, this means that the greater the advantage in workspace when compared to CNC machines, the greater the penalty in flexibility. Although CNC machining systems also suffer from decreased accuracy with increased degrees of freedom [32], the structural nature of CNC machines decouples the axes where possible reducing these effects relative to serial robots. One of the main causes of this flexibility is the use of harmonic drives [33], which predominate in industrial manipulators. Harmonic drive gear systems are well suited to industrial manipulators since they can give very high gear ratios without the space requirements of epicyclic gearing systems and have very little backlash [34]. This allows the machines to exert larger forces and manipulate larger payloads.

Harmonic drives, shown in Figure 1.2, compose of a wave generator, a flex-spline, and a circular spline. The wave generator is a non-circular disc that rotates inside the flex-spline and causes it to deform. As the flex-spline is deformed, the teeth on the outer edge of the major axis contact the teeth on the inside edge of the circular spline. Then as the major axis rotates with the wave generator, the contacting teeth move around the circular spline. The flex-spline has fewer teeth than the circular spline and as such when the wave generator has performed a full rotation, the flex-spline has rotated slightly in the opposite direction to match the number of teeth in the circular spline. This is similar to a single planetary gear running around an annulus in a conventional epicyclic gearing system. For a high number of teeth, this gives extremely large reduction ratios. The flexibility comes from the flex-spline which is, by necessity, flexible [35]. The models range from more complex systems such as stiffening spring models with a parallel hysteresis element in [36] to the more commonly used linear spring element.

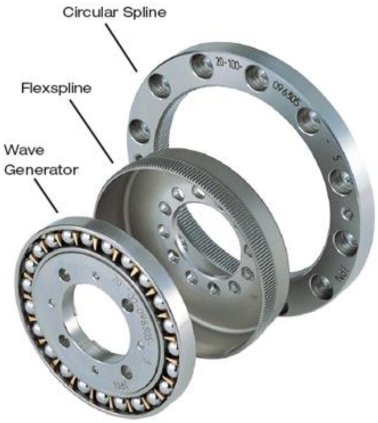

Figure 1.2: Harmonic Drive Components [37]

1.4 Redundancy and Posture Selection

Posture selection is the identification of manipulator joint angles to achieve a desired robot configuration. A simple example is position and orientation of the end-effector. In the case of an n degree of freedom (DOF) manipulator in n dimensional space, there is generally only one available configuration that meets this requirement. If the desired position is outside the dexterous workspace then there are no configurations and a minimum error configuration will likely be used. For a redundant robotic system such [19, 24], there may be multiple configurations that meet the position and orientation requirements, thus the system's redundancy can be used to satisfy other metrics to perform a set task such as optimising kinematic or dynamic properties. Often termed "task compatibility", this field of research was pioneered in 1985 by Yoshikawa with the definition of manipulability ellipsoids [38]. This was related to robotic tasks by Chiu in 1988 [39] for force or velocity dependent tasks maximising either magnitude or accuracy. It was then expanded to multiple armed systems in 1991 [40] for cooperative task completion and then to polytopes for redundant manipulators in 1997 [41] by Chiacchio *et al*. Walker [42] developed further dynamic posture measures to provide task compatibility where impacts occurred. By adjusting the manipulability, manipulating force, dynamic impact, generalised impact, or the dynamic manipulability measures, the impact response of the system could be altered. Young *et al.* [43] also proposed several posture measures as the kinematic, dynamic, and energy measures for a peg-in-hole task. The task was decomposed into stages and each section considered different optimisation parameters to generate more optimal kinematic or dynamic configurations. Owen *et al.* [44] used posture measures to prevent quasi-static deflection in robotic sculpting of a two-armed flexible-joint manipulator system. Other optimisations for redundant manipulators include kinetic energy reduction [45], obstacle avoidance [46], joint limit avoidance [47], singularity avoidance [48], and torque minimisation [49]. Kazerounian and Wang [50] developed a method to compare the local optimisation to global optimisation for joint rate optimisation using calculus of variations.

1.5 Control Methods

Active control for non-redundant industrial manipulators considering flexibility has been investigated by a myriad of authors to improve tracking errors caused by both payload/gravity deflections and vibrations. Lim *et al.* [51] used a partial state feedback controller and an observer to reduce tracking errors. The control strategy relies on measurements of both the link position and the actuator position to determine error in the observer. Spong developed several controllers using a nonlinear coordinate transformation to achieve global feedback linearization and corrective control to constrain the manipulator to an integral manifold [27] as well as developing adaptive control techniques [52] based on the adaptive sliding mode controllers designed by Slotine and Li [15] for rigid systems. In a similar upgrade of previously designed controllers, Bridges and Dawson redesigned a saturation based controller to incorporate the specific properties of harmonic drives [34]. Lozano and Brogliato developed an adaptive controller that utilised the passive properties of flexible-joint manipulators [53] and compared the tracking results of several other families of controllers [54]. They concluded that it is more practical to view a flexible manipulator as perturbation of a rigid manipulator and that there was a need for globally stable control schemes that incorporated the Coriolis matrices. A comparative study of flexible-joint controllers has also been carried out by de Queiroz *et al.* [55] with particular focus on comparing full and reduced order model based controllers. Waibel and Kazerooni developed stability conditions for a compliance controller using force feedback [56], and Salisbury developed an active control strategy for Cartesian space stiffness [57] where the joint torques were used to create a six DOF Cartesian spring at the wrist. Though effective, these control systems are all based on command compensation and measured or observed feed back and do not use the redundancy of the robot to adjust physical parameters. Specifically, the Cartesian mass, stiffness, and damping are not optimised. They would therefore benefit from a path planning algorithm that minimised deflection or vibration susceptibility allowing increased gains and tighter bounding conditions on disturbances. Combining the redundancy optimisation algorithms discussed in the previous section with the control algorithms above can potentially increase the capabilities of robotic machining to compete with CNC machining systems in a wider range of production and fabrication tasks.

Deflection compensation and vibration suppression have also been heavily investigated for flexible-link rigid-joint and flexible-link flexible-joint robots with the intention of creating lighter, faster robots to carry out pick and place tasks more accurately and to generate a better payload to weight ratio for applications such as manipulation in outer space. Wang investigated several control strategies for controlling several types of manipulators with a single flexible link including fuzzy logic [58], input shaping [59], and passive control [60]. Yue has investigated actively controlling the system to nullify end-effector vibrations [61] and residual vibrations [62] through predictions of the structural dynamics for flexible-link flexible-joint robots. The technique used requires very accurate models of the system and assume uniform bending in the links. Yue also considered the effects of using posture measures developed for rigid-link robots on flexible-link manipulators [63, 64]. Luo [65] used shear force feedback to reduce both tracking error and end-effector vibrations. Konno *et al.* investigated flexible-link controllability [66] and vibration suppression control using configuration dependant gains for pole placement [67]. Wang and Mills [68] developed a modal controller that looked at the mode shapes excited in a single link with an array for sensors and used multiple actuators to create negative interference. Zhang and Yu [69] used the redundancy to control the initial configuration and self motions of a flexible-link manipulator to reduce the end-effector tracking error. Despite the efforts in controlling vibrations in robotic systems, the majority of this work has ignored the case of external excitation in favour of controlling self excited vibrations. When dealing with machining systems however, the excitation is primarily derived from environment interactions.

1.6 Objectives

When machining, there are optimum speeds that are chosen based on the power available in the machine [70]. The spindle and feed speeds are generally dictated by the material being cut, the type of cutter, and chip thickness (which corresponds to finish). The rates can then be maximised by adjusting the tool diameter to utilise as much of the available power in the machines as is plausible and thus produce parts quickly and effectively to the standards required [71]. In a production environment, particularly for harder materials, tool life and material removal rates also need to be considered [72]. When machining softer metals such aluminium, higher speeds are normally used [72]. In high speed machining and into very high speed and even ultra high speed machining spindle speeds seldom exceed 50,000rpm and are often limited by application, such as the auto industry’s limit of 15,000rpm to reduce downtime [72]. This means that the frequency of excitation for vibration is dependent on the material and the cutting process variables and needs to be determined for each individual operation. The resistance to quasi-static machining forces can be optimised through various redundancy optimisation techniques listed earlier, however the problem of maximising stiffness has focused on the static case. As such, although vibrations have been investigated in some cases for redundant industrial systems, such as the grinding machine in [24], the techniques employed to date have all involved a maximisation of static stiffness. No consideration has yet been given to optimising posture based on the excitation frequency.

The first objective of this thesis is to develop a dynamic model of an industrial robotic manufacturing system that can be quickly parameterised and is complex enough to contain the dominant dynamics of the true mechanical system. This model will be able to predict the frequency dependent behaviour of the manipulator in a given configuration. Additional components added to the model will create unnecessary complexity that will likely amplify any errors in the experimental data whereas the identification of a simpler model will be more robust to such errors. However, if the model is oversimplified, then the model will be insufficient to capture the full dynamics of the system.

Once a model has been identified, the second objective is to identify the systems dynamic parameters (mass, stiffness, and damping characteristics) using techniques that will not require excessive machine down time or invalidate any manufacturer warrantee. As such, any disassembly of the robot is to be avoided. This will allow the optimisation algorithm to be used with existing machinery that has not been previously parameterised. When producing industrial manipulators, manufacturers seldom provide the dynamic properties of the robotic systems they produce [73]. Even with an accurate CAD model, which is also seldom available and difficult to generate without limited disassembly, it is extremely difficult to accurately predict the dynamic response of the robot to a force input. For this reason, it is essential that an accurate model can be built from measurements made without prior knowledge of the system. This model will not necessarily give physically meaningful parameters due to the assumptions and simplifications necessary to keep the complexity of the model low and to compensate for nonlinearities. The goal of the model is to accurately predict the dynamic response of the system to periodic excitation and as such the identified parameters do not need to be physically meaningful.

Finally, the main objective of this work is to design an optimisation algorithm based on the developed model that will increase the end-effectors resistance to a known applied oscillating force relative to a machining surface. This will enable the robotic system to produce parts to tighter tolerances and to machine harder materials that will exert higher forces on the tool tip. By using a redundant system, the optimisation can be superimposed on the relative tool path of the tool tip with respect to the workpiece. This can be integrated into existing systems by passing a tool trajectory in joint space rather than in Cartesian space and will not necessitate the invasive changes required to update a control law. In addition, should a control law or path planning update be desirable, the optimisation can be combined with both of these updates without losing relevance or validity. It is necessary to verify the results of the optimisation through simulation and testing.

This thesis describes the modelling and identification of a Fanuc S-360 industrial manipulator and the development of a positioning algorithm to increase resistance to machining vibrations along a known Cartesian axis at a known frequency.

1.7 Contributions and Thesis Overview

1.7.1 Contributions

The contributions of this thesis outline a configuration optimisation for industrial robotic machining systems that will allow them to cut harder materials with increased resistance to vibrations. The first contribution is the development of a method of model identification that can be applied to a range of manipulator types without requiring invasive signal measurements or manipulator disassembly. This removes manipulator down time as the experimental work can be done in a comparably short period of time and allows parameter identification without needing to understand the signal encoding of the robot being identified. The second, and most significant, contribution is an investigation into the benefits of using the frequency dependent receptance of the manipulator end effector as a posture measure to reduce vibrations. The inclusion of these effects in the optimisation is an improvement over the static load based optimisation as the effects of resonances and anti-resonances are included. The final contribution is a proposed method to extend the method investigated into multiple axes and for an enlarged configuration space. It is expected that this proposed method will increase the accuracy and effective range of the identified model used for optimisation. These developments will contribute to the continued expansion of robotic machine tools into material removal applications.

1.7.2 Thesis Overview

Chapter 2 - System Modelling and Parameterisation

Chapter 2 shows the formulation of the dynamic model used for the system and the identification process used to parameterise the model as well as the underlying theory behind the practice of modal analysis. A qualitative analysis of the system behaviour is offered to verify the assumptions used in the model followed by a detailed modal analysis parameterisation using a circle fit technique. The identified modal parameters are then used to generate a set of dynamic parameters able to reconstruct the measured frequency response of the end-effector at various configurations.

Chapter 3 - Optimisation Results and Simulations

Chapter 3 details the optimisation techniques and objective functions used for the posture and frequency selection of the Fanuc S-360 manipulator. The predicted and measured results are compared and the values of the optimisations are determined. The extension to a redundant manipulator is then explored through simulations and the mechanisms used by the optimisation are identified. The effects of including frequency response as opposed to a static stiffness optimisation are also investigated.

Chapter 4 - Summary, Conclusions, and Future Work

Chapter 4 summarises the results and observations of the previous chapters and explores the potential applications of this work to robotic machining drawing conclusions based on the value, practicality, and drawbacks of the methods used. It then elaborates on the possibilities for industrial applications and suggests directions of study for future work.

Chapter 2 System Modelling and Parameterisation

2.1 Introduction

Parameter identification of industrial robots has been carried out by various authors using a variety of approaches. For determining only stiffness characteristics, static load testing has been carried out on a joint by joint basis [28-30], and also through Cartesian space measurements [13]. These parameterisations were then used to predict static deflection and tracking errors, which in turn were used to improve system performance. However, the tracking error predictions tested were consistently conservative indicating that the effects of inertial forces need to be considered for improved performance.

Full dynamic models of robotic manipulators are often parameterized through a linearised parameter approach as pioneered in [74, 75] and greatly contributed to by M. Gautier [76-78]. There is a large body of literature proposing different schemes to develop the governing equations for these techniques as well as identifying the optimal trajectories to use and addressing the effects of measurement noise on the results. However, all these approaches have a common general approach, which is to reformulate the governing equations such that they are linear in the dynamic parameters sought and then have the system follow a given trajectory while measuring the input and output variables. These variables are usually the input torque and position response, but can also include the velocity, acceleration, and command current values depending on the parameters sought and method used. The data is then put through a linear least squares optimisation, often after heavy filtering. The governing equations used vary through the literature from dynamic equations, which can be analysed sequentially since the regressor matrix can be made upper triangular as in [79]; energy equations [76]; or power equations [78], which are all linear in the inertial parameters. The issues arising from measurement noise have been investigated by [80] among others concluding that periodic trajectories are preferable since the average value and the frequency content are known a priori.

These trajectories can be tuned to include the desired dynamics and remove any unwanted dynamic such as resonances. Depending on the type of governing equations used, a single trajectory [76] or multiple trajectories are used. Multiple trajectories are desirable when using a sequential optimisation scheme [81] or for exciting specific dynamic properties such as damping at constant speeds [82]. Multiple trajectories generally simplify the process at the expense of increased error accumulation throughout the parameters as the error in a previously identified variable is included in the current optimisation [83]. Single trajectories are also not without flaws; additional constraints were added to a single trajectory by [77] to avoid having very small singular values of the regressor matrix.

In addition to controlling the trajectories to minimize the effects of measurement noise, filters and decimation are extensively applied to the measured data since the velocity and acceleration signals are generally not available and need to be generated by differentiating the position signal [83]. Low pass filters have also been implemented at the governing equation level to remove the need for acceleration data when using the dynamic models [84] and for removing complications due to power integration when using the energy model [85].

More recently, flexible robots have also been investigated in both the time [79] and frequency [86] domains to find not only the inertial and friction parameters, but also damping and stiffness values and also by Hirzinger [87] assuming known inertial parameters. A common property of all the linearised parameter approaches is their invasive nature since many industrial robots will not export encoder or torque signals. Furthermore, more recent approaches tend to include identification of motor control system parameters, which are also unknown and are usually assumed to be constant motor gains within a reasonable bandwidth [79]. This requires measuring the supplied motor current and torque as well as the kinematic response of the system. In this thesis, the manipulator under investigation will not allow modifications to the hardware due to safety protocols in the machine software. Therefore, an invasive approach to identification is not possible and as such a linearised input-output approach is also not possible as it requires signals that are not otherwise available.

A non-invasive method to identify the full dynamics of a system is modal analysis as used in [88, 89]. The system is made to vibrate by exciting it with either an electromagnetic shaker [89] or a hammer blow [88] and a frequency response function (FRF) can be obtained by measuring the input force and output kinematics. Several FRFs can be found by moving the excitation point and measurement point and, from the relationships between the different FRFs, the mode shapes and modal parameters can be identified. From this point, a simple coordinate transformation is used to recreate the linearised system dynamics and a least squares (LS) fit is used to identify the parameters of the linearised system. Modal analysis is often performed on pure mechanical systems and structures that cannot be disassembled and measured. The behaviour is modelled as either continuous or lumped parameter depending on the characteristics of the system in the region investigated. Where possible, the number of elements in a lumped parameter is minimised for simplicity, while being sufficient to capture the dynamics observed, such is the case in [88, 89]. However, there are cases where a lumped parameter model requires a very large number of elements due to the presence of continuous vibration characteristics. In this case, an approximation can be made based on the low frequency characteristics shown using additional lumped parameter degrees of freedom [90], although to include more frequencies accurately more degrees of freedom need to be added to the model. A hybrid dynamic model can also be built as in [91] where a set of flexible finite elements are used to develop a model. It is worth noting at this point that the parameterisation for such a model is overly complex and that these models are generally used with known material parameters such that flexibility and inertia can be accurately estimated and then experimentally corrected.

Since the goal of this work is to reduce vibrations, it follows that the dynamic model should be built based on the vibration response of the structure. However, one relevant constraint of modal analysis is that it is developed for linear vibration models and thus the dynamic model of the manipulator must be linear or linearised. Manipulator dynamics are highly nonlinear due to serial rotating kinematic chains. As such the operating point for linearisation is selected as the stationary position of the manipulator and the operating point velocity is zero, thus removing the nonlinear terms and leaving the remaining terms unaffected. This assumes that the Coriolis and centrifugal acceleration terms can be neglected. Although this is a common simplification, it has been shown by Corke that it is not always valid [92] and should be avoided where possible. In this instance, the system needs to be linearised and therefore this assumption is necessary.

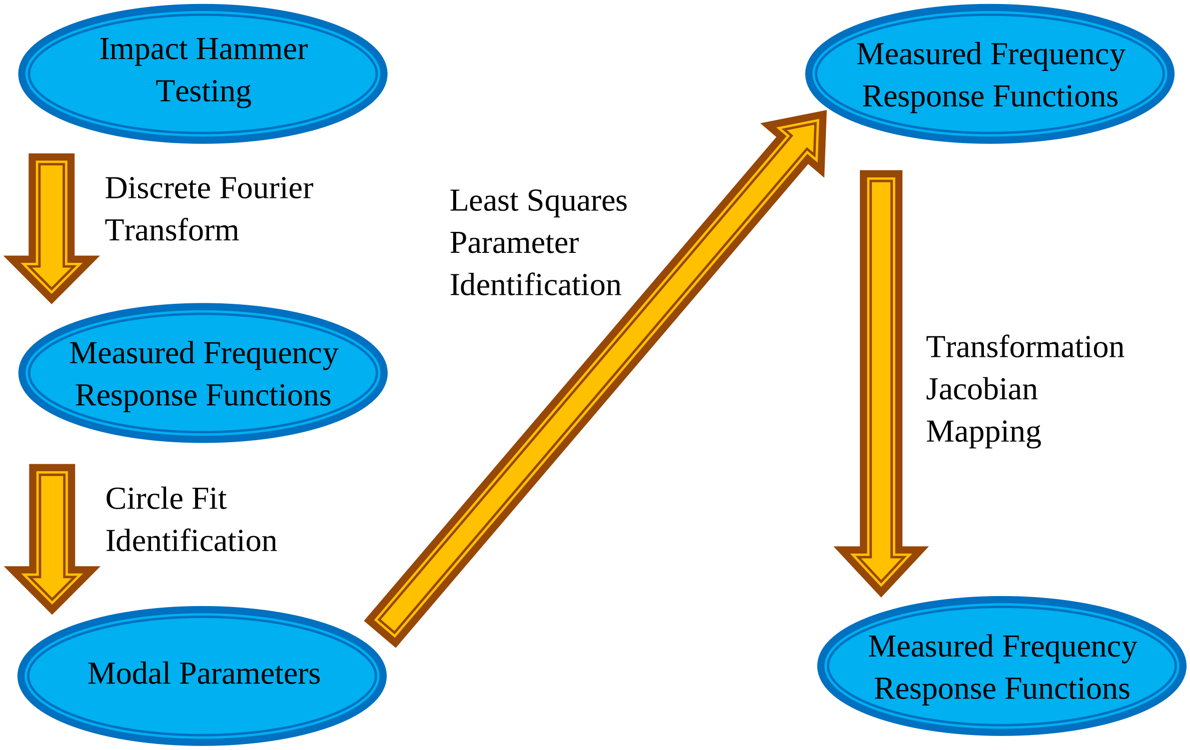

Figure 2.1: Flow Chart of Parameter Identification Procedure

Section 2.2 will outline the dynamic model used in this investigation while addressing the potential errors and complications caused by linearising a system with highly nonlinear dynamics. The effects of friction and servo flexibility will be addressed and any flexibility not initially modelled will be compensated for. Section 2.3 will briefly review the linear vibration theory relevant to this investigation and develop some of the governing equations to be used for parameter identification in following sections. Section 2.4 gives an initial qualitative evaluation of the modal response including the effects of nonlinear dynamics, rigidity assumptions, and configuration variances. Section 2.5 outlines the selected parameter identification techniques and the modal parameters identified, completing the first three steps in Figure 2.1, and Section 2.6 shows the relation of the dynamic model to the modal model and the indentified dynamic parameters, completing the remaining steps.

2.2 Dynamic Model

2.2.1 Model Formulation

The dynamic model selected is a rigid-link flexible-joint model developed by Spong [27] and verified through static load parameterisation and tracking tests by various authors [23, 26, 28-30]. The model is modified from its original form to include damping relative to the deflection rate as opposed to damping in the link velocity. The flexibility is modelled as a linear spring and viscous damper between the motor rotor and the link as shown schematically in Figure 2.2, where J_M is the motor inertia, q_M is the generalised coordinate for the motor, q_L is the generalised coordinate for the link, K_q is the joint deflection stiffness, B_q is the joint deflection damping, and M and I are the mass and inertia of the link respectively.

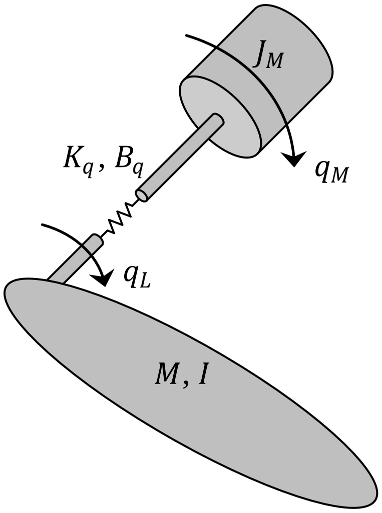

Figure 2.2: Dynamic Model of a Single Flexible Serial Manipulator Joint

The equations of motion for an n DOF manipulator are given by

$$\boldsymbol{D}\ddot{\boldsymbol{q}}_L + \dot{\boldsymbol{q}}_L^T\boldsymbol{C}\dot{\boldsymbol{q}}_L + \boldsymbol{B}_q(\dot{\boldsymbol{q}}_L - \dot{\boldsymbol{q}}_M) + \boldsymbol{K}_q(\boldsymbol{q}_L - \boldsymbol{q}_M) = \boldsymbol{J}^T\boldsymbol{F} \tag{2.1}$$

$$\boldsymbol{J}_M\ddot{\boldsymbol{q}}_M + \boldsymbol{K}_q(\boldsymbol{q}_M - \boldsymbol{q}_L) + \boldsymbol{B}_q(\dot{\boldsymbol{q}}_M - \dot{\boldsymbol{q}}_L) = \boldsymbol{\tau} \tag{2.2}$$

where $\boldsymbol{D}$ is the $n \times n$ symmetric positive definite manipulator inertia matrix, $\boldsymbol{C}$ is the $n \times n \times n$ Christoffel matrix containing the nonlinear Coriolis and centrifugal terms, $\boldsymbol{B}_q$ is the $n \times n$ diagonal positive definite matrix of damping values, $\boldsymbol{K}_q$ is the $n \times n$ diagonal positive definite matrix of joint stiffness values, $\boldsymbol{q}_L$ is a vector of link coordinates, $\boldsymbol{q}_M$ is a vector of joint coordinates, $\boldsymbol{F}$ is the Cartesian force and toque vector acting on the end-effector, $\boldsymbol{J}$ is the $n \times n$ manipulator Jacobian, $\boldsymbol{J}_M$ is the $n \times n$ diagonal matrix of rotor inertias, and $\boldsymbol{\tau}$ is the joint torque vector.

It was found through initial testing that the vibration response for the system did not change when the breaks for the system were activated or deactivated. From this, it was determined that the controller can be modelled as a rigid system and that all the flexibility is in the structure causing $\boldsymbol{q}_M$ to be zero at all times. This reduces the degrees of freedom so that Figure 2.2 becomes Figure 2.3 and the anchor symbol represents a rigid connection to the previous link.

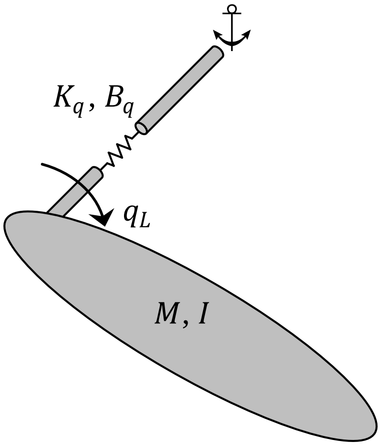

Figure 2.3: Vibration Model of a Single Flexible Serial Manipulator Joint

The equations of motion, (2.1) and (2.2), also reduce and become a single nonlinear ordinary differential equation,

$$\boldsymbol{D}\ddot{\boldsymbol{q}}_D + \dot{\boldsymbol{q}}_D^T \boldsymbol{C}\dot{\boldsymbol{q}}_D + \boldsymbol{B}_q\dot{\boldsymbol{q}}_D + \boldsymbol{K}_q\boldsymbol{q}_D = \boldsymbol{J}^T\boldsymbol{F} \tag{2.3}$$

where

$$\boldsymbol{q}_D = \boldsymbol{q}_L - \boldsymbol{q}_M \tag{2.4}$$

is the joint deflection measured as the difference between the link and joint angles and the time derivatives are equivalently defined. When linearising about an operating point with no initial velocity, the nonlinear terms are removed yielding,

$$\boldsymbol{D}\ddot{\boldsymbol{q}}_D + \boldsymbol{B}_q\dot{\boldsymbol{q}}_D + \boldsymbol{K}_q\boldsymbol{q}_D = \boldsymbol{J}^T\boldsymbol{F} \tag{2.5}$$

From this point the subscript $_D$ will be neglected.

The end-effector axes are coupled through the nonlinear dynamics of the manipulator and cannot be decoupled other than for specific configurations such as singularities. Thus, an excitation of one axis will generally cause a response on all other axes. For this investigation, only the results for a single axis will be investigated and the effects from the unexcited axes will be neglected in the analysis. The possibility to extend the single axis investigation offered in this thesis to a general case will be addressed in Chapter 4.

2.2.2 Servo Flexibility

The nature of control laws based on error feedback is that there is little or no compensation for disturbances until the disturbances have had the opportunity to displace the system. For simple control laws, such as proportional control or proportional derivative control without feed forward compensation, the mathematical response may take the same form as a mechanical system. In the case of proportional position control the characteristics are similar to that of a mechanical spring and in the case of proportional-derivative position control the characteristics resemble a spring and damper in parallel. This is often referred to as servo flexibility since the appearance of flexibility is given by the servo motor control system.

Generally, the response time for the controller can be expected to be much less than that of the manipulator as mentioned in [79], since the resonant frequencies of industrial manipulators tend to begin below 50Hz [20, 79, 88]. For the robot in question, the effects of the controller were assumed to be negligible and this was confirmed by recording the response of the system with the brakes both on and off. The resultant FRFs are shown in Figure 2.4, note that inertance is formally defined in Section 2.3.1. No significant change in the response was identified and, as such, the servo flexibility was ignored.

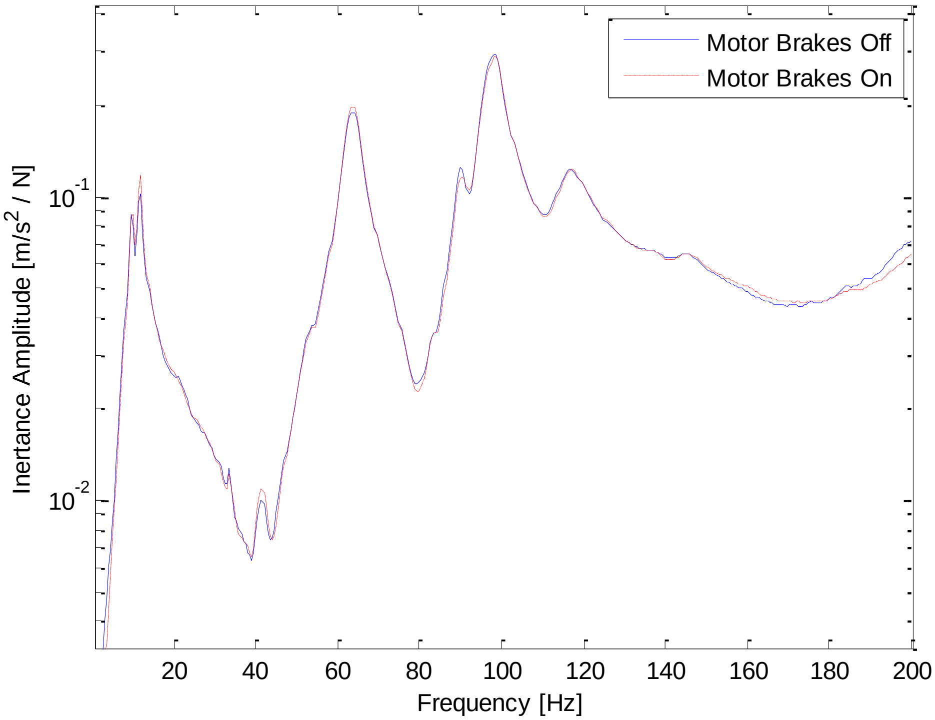

Figure 2.4: Effects of Manipulator Motors Brakes on End-Effector Frequency Response

2.2.3 Friction Model

As mentioned in the previous chapter, harmonic drive gear systems are well suited to industrial manipulators since they offer very high gear ratios without the space requirements of epicyclic systems and have very little backlash. As such they have become widely used in the industry, particularly in large payload manipulators. However, they have also been shown to be highly flexible. The manipulator under investigation here uses harmonic drives in the joints modelled and thus the dynamic model used needs to reflect the dynamics of harmonic drives where possible.

Harmonic drive systems have been shown to behave as extremely complex systems and several researchers have noted difficulty in finding an adequate model for capturing their full dynamics [93]. Taghirad and Bélanger [93] considered the primary energy loss to occur in the meshing of the flexspline and the circular spline and that there was no stiction in the system, although there was rising friction at low speeds. They also found viscous damping to be significant only at high speeds of the input shaft. This was expected to be primarily due to the much larger velocities in the input bearing. Conversely, Tuttle and Seering [94] found the input bearing viscous friction to be negligible compared to the output bearing friction even after considering the gear ratio and showed Coulomb friction to be the most significant at very low speed. Although both investigations support the dominance of constant structural damping value, Hirzinger [87] later opted to use a frequency dependent viscous damping model to parameterize a harmonic drive with a stationary rotor when developing a control system for passivity based joint control architecture.

Due to a lack of literature on the dynamics of harmonic drives with stationary inputs, the friction model was developed based on the results of the experimental FRF rather than the suspected underlying mechanics. The justification for this stems from the fact that the model is to be evaluated in the frequency domain and parameterised from an experimental FRF. Wernholt and Gunnarsson [95] recently examined the effects of dynamic nonlinearities on the experimental FRFs of serial robots with harmonic drives and made the following relevant observations.

1. For greater excitation amplitude, the effects of nonlinear hardening springs become more prevalent. While the effects are embedded all through the FRF, they can be observed as anti-resonances become more pronounced with increasing input force.

2. The main contribution of static and Coulomb friction to the FRF is to remove or greatly reduce amplitude of the resonance peaks.

The first point can be used as a restriction on the domain of the identified system. For a given excitation amplitude, the identified system may only be valid for an exciting force of that approximate amplitude. This is investigated in more detail in Section 2.4.2. Thus, for a machining system that will operate over a wide range of inputs, the identification procedure may need to be repeated for a number of excitation amplitudes and the model used for optimisation and prediction needs to be based on the expected inputs. In addition, the anti-resonances can be used as an indicator of the linearity of the springs in a given input amplitude range.

The second point can be taken as a justification for neglecting the static friction in the dynamic model and replacing the more likely case of structural damping with viscous damping. The loss of amplitude in the peaks will prevent the system from identifying physically meaningful dynamic parameters. However, the author wishes to stress at this point that a physically meaningful dynamic model is not the purpose of this identification. The goal is to define a dynamic model that can be decomposed into composite parts which can then be reassembled for new configurations and yield an accurate FRF for vibration response prediction. Given that the static friction occurs in the joints, as does viscous damping, and that its effect on the FRF is to effectively increase damping thereby reducing the resonance amplitude, it follows that a reasonable assumption is to lump the friction and true damping into the damping parameter of the linear model. Similarly, the motivation behind the structural damping model is that at higher frequencies viscous damping consumes an unrealistic amount of energy [25]. However, since the effects of static friction have been seen experimentally to be more pronounced at higher frequency, the increased energy consumption at higher frequency is more characteristic of viscous damping than of structural damping. Substituting the more likely model of structural damping and extremely complex low velocity friction with viscous friction, maintains linearity and the model is still able to account for the effects of friction.

2.2.4 Flexible Link Compensation

The manipulator under investigation is a Fanuc S-360 industrial manipulator shown in Figure 2.5 and the skeleton schematic is shown in Figure 2.6, where J_i denotes the i^{th} actual manipulator joint. One of the main assumptions in the dynamic model is that the four bar linkage in the manipulator can be modelled as the single link shown in the skeleton schematic. In the case of the four bar mechanism, the orientations of the second and third links are independent of the first joint angle, while for a serial kinematic chain they are not. For positioning and path planning purposes there is a simple transformation for the system kinematics; however the dynamic response, particularly to vibrations, cannot be transformed as easily and may restrict the region of accuracy for the model. When operating in the plane, the first, fourth and sixth actual joints can be neglected since they will see no planar forces. Thus, for the set of configurations where the end-effector remains in the plane, the schematic can be reduced to Figure 2.7, where q_i denotes the i^{th} model joint.

Figure 2.5: Fanuc S-360 Industrial Manipulator

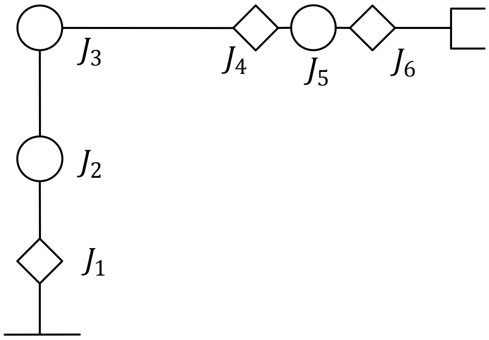

Figure 2.6: Skeleton Schematic of a Fanuc S-360 Industrial Manipulator

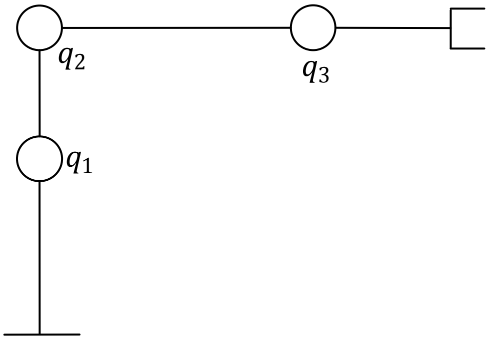

Figure 2.7: Planar Skeleton Schematic of a Fanuc S-360 Industrial Manipulator

Further examination of the physical robot identified a bolt pattern at either end of the second link as shown in Figure 2.8.

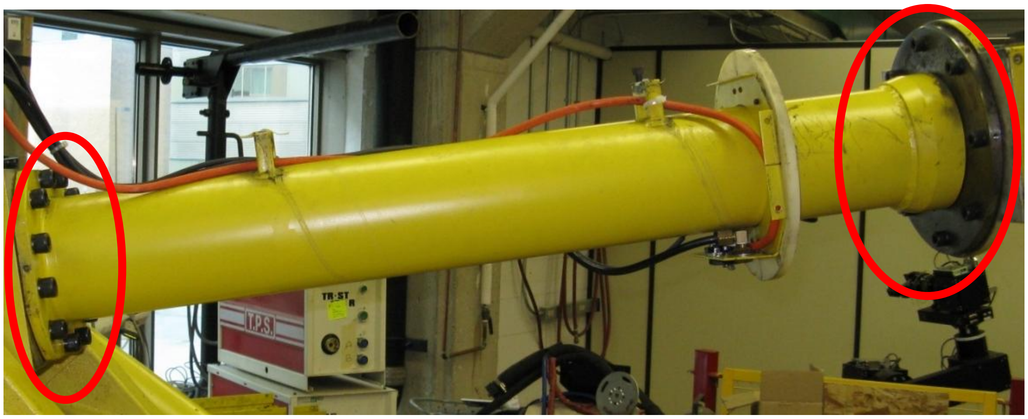

Figure 2.8: Fanuc S-360 Industrial Manipulator Second Link and Connecting Bolt Patterns (encircled)

The bolt patterns are other possible points of flexibility and should be included in the dynamic model. The inspection also identified the link itself as a possible point of flexibility due to its structure. The link is comprised of concentric drive shafts supported by a cylindrical tube. This outer tube is likely flexible due to its relative large length and small thickness. When these three additional flexibilities are incorporated into the model as rotary pseudo-joints, the model becomes as shown in Figure 2.9.

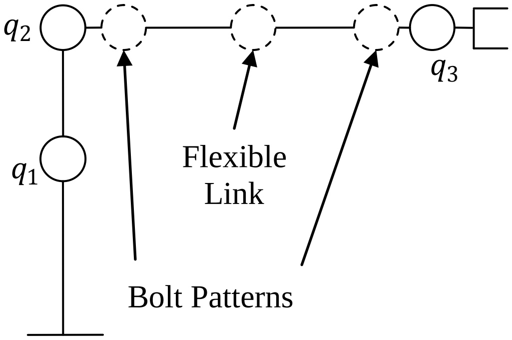

Figure 2.9: Planar Skeleton Schematic of Fanuc S-360 Industrial Manipulator including Pseudo-Joints

The dashed circles in this figure represent rotational pseudo-joints included to compensate for the expected additional flexibility. If these assumptions are false and the locations are actually rigid, then the stiffness of the pseudo-joints will be identified as very large or infinite and will be removed from the model. Similarly, if these additional pseudo-joints are insufficient to capture the dynamics of the system, either by providing an insufficient number of resonant peaks or by not offering enough degrees of freedom to capture the observed mode shape, additional pseudo-joints may be added. It is worth noting here that these pseudo-joints cannot be controlled during optimisation and are included only to increase the DOF of the dynamic model and thereby improve the accuracy of the predicted dynamics.

2.3 Modal Theory

2.3.1 Single Degree of Freedom Systems

For all dynamic systems, an FRF can be found through experimental force and response measurements. In this case, the system was excited with a hammer blow and the acceleration was measured with an accelerometer. The time domain force, $F(t)$, and acceleration, $a(t)$, signals are recorded and transformed into frequency domain using a discrete Fourier transform (DFT). The two frequency domain signals are next normalized to get an FRF. For the acceleration response to a force input, the FRF is known as inertance and denoted $A(i\omega)$, where i is the square root of -1 and ω is frequency in radians per second.

$$A(iw) = \frac{a(i\omega)}{F(i\omega)} \tag{2.6}$$

Other commonly used and useful FRFs are mobility, which is the velocity equivalent of inertance, denoted by $Y(i\omega)$, and receptance, which is the position equivalent of inertance and is denoted by $\alpha(i\omega)$.

For linear vibrating systems, the inertance can also be defined through the mechanical properties of the system. For a single DOF resonant peak with viscous damping, the inertance is given by

$$A(i\omega) = \frac{-\omega^2}{-m\omega^2 + bi\omega + k} \tag{2.7}$$

where k is the spring constant, m is the mass, and b is the damping value. This can be obtained by transforming the equations of motion of a single axis mass-spring-damper system with deflection x, velocity $\dot{x}$, acceleration $\ddot{x}$, and axial excitation force f,

$$m\ddot{x} + b\dot{x} + kx = f \tag{2.8}$$

into the Laplace domain

$$(ms^2 + bs + k)x = f \tag{2.9}$$

and then substituting $(i\omega)$ for the derivative operator.

The mobility and receptance FRFs can be determined from the inertance FRF using an equivalent substitution for the integral operator in the Laplace domain such that

$$Y(i\omega) = \frac{A(i\omega)}{i\omega} = \frac{i\omega}{-m\omega^2 + bi\omega + k} \tag{2.10}$$

and

$$\alpha(i\omega) = \frac{A(i\omega)}{(i\omega)^2} = \frac{1}{-m\omega^2 + bi\omega + k} \tag{2.11}$$

A more general way of expressing (2.7) is to substitute the physical parameters of the mechanical system $(m, b, \text{ and } k)$ with modal parameters $\bar{A}, \zeta, \text{ and } \omega_n$, representing the amplitude multiplier, damping ratio, and natural frequency of the peak so that

$$A(i\omega) = \frac{-\bar{A}\omega^2}{-\omega^2 + 2\zeta\omega_n\omega i + \omega_n^2} \tag{2.12}$$

The modal parameters for a single DOF system can be defined through the eigenvalue solution to the characteristic equation[1] of (2.7) [96].

$$\left(m\lambda + b\sqrt{\lambda} + k\right)x = 0 \tag{2.13}$$

In the un-damped case, this reduces to

$$(m\lambda + k)x = 0 \tag{2.14}$$

$$\bar{A} = \frac{1}{m} \tag{2.15}$$

$$\omega_n = \sqrt{\lambda} = \sqrt{\frac{k}{m}} \tag{2.16}$$

and the damping ratio is zero. When damping is included, the solution for the system poles, given by λ, becomes complex.

$$\zeta = \frac{b}{2\sqrt{mk}} \tag{2.17}$$

---

[1] Recall that the characteristic equation of a transfer function is its denominator. In vibrations, it is the denominator of the FRF in question and is the same for the inertance, mobility, and receptance of a system.

$$\lambda = -\zeta\omega_n \pm i\omega_n\sqrt{1-\zeta^2} \tag{2.18}$$

2.3.2 Multiple Degree of Freedom Systems

Multiple DOF resonances can be simplified through partial fraction expansion and modelled as a sum of P single DOF resonances. The full response can be expressed as a sum of independent peaks

$$A_{u,v}(i\omega) = \sum_{p=1}^{P} \frac{-\bar{A}_{u,v}^{p}\omega^2}{-\omega^2+2\zeta^p\omega_n^p\omega i+\omega_n^{p\,2}} \tag{2.19}$$

where $\bar{A}_{u,v}^{p}$ is an amplitude multiplier as before, u is the DOF where the excitation is applied, and v is the DOF measured for a response. Note that there is symmetry in the FRF such that $A_{u,v}(iw) = A_{v,u}(iw)$. Here the superscript ^{p} denotes the membership of a parameter to the specific peak p. Expressing (2.19) with mass, stiffness and damping as in (2.7) introduces the modal mass, modal stiffness, and modal damping parameters. These are different from the physical properties as they are simply another way of expressing modal information. For this reason, the modal parameters $\bar{A}$, ζ, and ω_n are generally used for modal analysis.

When investigating the FRF of a system we often wish to narrow our search to a finite number of peaks or a particular frequency range. As such the sum will be incomplete and there will be errors in the response. To account for effects of other peaks outside the domain of interest, residual terms are added to (2.19),

$$A_{u,v}(i\omega) = \frac{1}{M_R} + \sum_{p=1}^{P} \frac{-\bar{A}_{u,v}^{p}\omega^2}{-\omega^2+2\zeta^p\omega_n^p\omega i+\omega_n^{p\,2}} - \frac{\omega^2}{K_R} \tag{2.20}$$

These additional terms represent the effects of a single peak to either side of the domain of interest acting on the domain of interest as either a mass, $\frac{1}{M_R}$, or stiffness, $\frac{\omega^2}{K_R}$, characteristic at lower and higher frequencies respectively. There is an assumption that there is no additional resonance peak close to the domain of interest and that the mass or stiffness effects are therefore constant. This is generally a safe assumption when the region for investigation is chosen carefully.

The amplitude scalars $\bar{A}^{p}_{u,v}$ for the general case of viscous damping are determined by the mode shape vectors, which are found along with the natural frequencies from the characteristic eigenproblem seen for a single DOF in (2.13) [96].

$$\left(\boldsymbol{M}\lambda + \boldsymbol{B}\sqrt{\lambda} + \boldsymbol{K}\right)\boldsymbol{x} = \boldsymbol{0} \tag{2.21}$$

where $\boldsymbol{M}$, $\boldsymbol{B}$, and $\boldsymbol{K}$ are the mass, damping, and stiffness matrices corresponding to the DOF in $\boldsymbol{x}$. Unfortunately, this cannot be solved analytically since it contains twice as many unknowns as equations. There are generally n eigenvalues to be found from n equations in an eigenvalue problem, however in this case both λ and $\sqrt{\lambda}$ need to be found independently requiring $2n$ equations. As such, there are special cases to be considered. The first is the un-damped case, whereby (2.21) is reduced to

$$(\boldsymbol{M}\lambda + \boldsymbol{K})\boldsymbol{x} = 0, \tag{2.22}$$

and the second is proportional damping whereby the damping matrix is restricted to be of the form

$$\boldsymbol{B} = \beta\boldsymbol{M} + \gamma\boldsymbol{K} \tag{2.23}$$

where β and γ are arbitrary scalars. In the first case, the problem can be solved easily through row reduction methods as with general eigenvalue problems. In the second case, the eigenvalues () can be corrected and the damped eigenvalue λ^{p}_{D} can be expressed in terms of the damping ratio ζ^{p} corresponding to the vibration mode p and the un-damped eigenvalue (λ^{p}_{U}) as in (2.24, 2.25). The eigenvectors are unchanged from the un-damped case [95].

$$\zeta^{p} = \frac{\beta\lambda^{p}_{U}}{2} + \frac{\gamma}{2\lambda^{p}_{U}} \tag{2.24}$$

$$\lambda^{p}_{D} = -\zeta^{p}\lambda^{p}_{U} \pm i\lambda^{p}_{U}\sqrt{\left(1 - {\zeta^{p}}^{2}\right)} \tag{2.25}$$

In the general case, when these special properties cannot be applied, an additional identity equation can be added to the governing dynamic equations for non-proportional damping and the derivative of the DOF can be incorporated. For example, the Laplace domain dynamic equations corresponding to a linear mass-spring-damper system are given by

$$(\boldsymbol{M}s^2 + \boldsymbol{B}s + \boldsymbol{K})\boldsymbol{x} = \boldsymbol{f} \tag{2.26}$$

where $\boldsymbol{f}$ is a vector of forces acting on the axes defines by $\boldsymbol{x}$. Adding an additional identity equation, such as

$$(\boldsymbol{M}s - \boldsymbol{M}s)\boldsymbol{x} = 0 \tag{2.27}$$

and combining it with (2.26) yields

$$\left(\begin{bmatrix} \boldsymbol{B} & \boldsymbol{M} \\ \boldsymbol{M} & \boldsymbol{0} \end{bmatrix} s + \begin{bmatrix} \boldsymbol{K} & \boldsymbol{0} \\ \boldsymbol{0} & -\boldsymbol{M} \end{bmatrix}\right) \boldsymbol{v} = \begin{bmatrix} \boldsymbol{f} \\ \boldsymbol{0} \end{bmatrix} \tag{2.28}$$

where

$$\boldsymbol{v} = \begin{bmatrix} \boldsymbol{x} \\ \dot{\boldsymbol{x}} \end{bmatrix} \tag{2.29}$$

The characteristic equation yields an eigenvalue problem that can be solved as before.

The solution will now yield n conjugate pairs of eigenvalues to match the n conjugate pairs of eigenvectors of length $2n$. The receptance and mobility are then combined into a single expression of the form

$$\begin{bmatrix} \boldsymbol{\alpha}(iw) \\ \boldsymbol{Y}(iw) \end{bmatrix} = \sum_{p=1}^{2P} \frac{-\omega^2 \bar{\boldsymbol{A}}^p}{-\omega^2 + 2\zeta^p \omega_n^p \omega i + \omega_n^{p\,2}}, \tag{2.30}$$

which can be rewritten as

$$\begin{bmatrix} \boldsymbol{\alpha}(iw) \\ \boldsymbol{Y}(iw) \end{bmatrix} = \sum_{p=1}^{P} \frac{-\omega^2 \bar{\boldsymbol{A}}^p}{(i\omega - \lambda^p)} + \frac{-\omega^2 \bar{\boldsymbol{A}}^{p*}}{(i\omega - \lambda^{p*})} \tag{2.31}$$

where the superscript * denotes a complex conjugate value and $\bar{\boldsymbol{A}}^p$ is the vector of all $\bar{A}_{u,v}^p$ at frequency p.

With the eigenproblem solved, the eigenvectors can be concatenated into a mode shape matrix defining the proportional motions of each DOF for a given excitation frequency. Equation (2.32) is an example mode shape matrix for a three DOF system with proportional damping.

$$\boldsymbol{\phi} = \begin{bmatrix} \phi_1^1 & \phi_1^2 & \phi_1^3 \\ \phi_2^1 & \phi_2^2 & \phi_2^3 \\ \phi_3^1 & \phi_3^2 & \phi_3^3 \end{bmatrix} \tag{2.32}$$

The superscripts denote the eigenvalue or natural frequency associated with the entry and the subscripts denote the DOF. For the general case of viscous damping, there would be six columns indicating three pairs of complex conjugate vectors and six rows to include the derivative information as in (2.33), where $\bar{\phi}_1^1$ represents an eigenvector element corresponding to the velocity of a DOF.

$$\boldsymbol{\phi} = \begin{bmatrix} \phi_1^1 & \phi_1^{1*} & \phi_1^2 & \phi_1^{2*} & \phi_1^3 & \phi_1^{3*} \\ \phi_2^1 & \phi_2^{1*} & \phi_2^2 & \phi_2^{2*} & \phi_2^3 & \phi_2^{3*} \\ \phi_3^1 & \phi_3^{1*} & \phi_3^2 & \phi_3^{2*} & \phi_3^3 & \phi_3^{3*} \\ \bar{\phi}_1^1 & \bar{\phi}_1^{1*} & \bar{\phi}_1^2 & \bar{\phi}_1^{2*} & \bar{\phi}_1^3 & \bar{\phi}_1^{3*} \\ \bar{\phi}_2^1 & \bar{\phi}_2^{1*} & \bar{\phi}_2^2 & \bar{\phi}_2^{2*} & \bar{\phi}_2^3 & \bar{\phi}_2^{3*} \\ \bar{\phi}_3^1 & \bar{\phi}_3^{1*} & \bar{\phi}_3^2 & \bar{\phi}_3^{2*} & \bar{\phi}_3^3 & \bar{\phi}_3^{3*} \end{bmatrix} \tag{2.33}$$

Mode shapes form a basis[2] for a solution space, but since they have no fixed amplitude they are not unique. As such, when identifying mode shapes, it is necessary to know the modal masses corresponding to the mode shapes identified. Though this may sound trivial, modal parameter identification generally focuses on identification of natural frequency and damping ratios as opposed to modal mass, stiffness, and damping. Similar to the mode shapes, the damping ratio and natural frequency do not offer unique solutions for modal mass, stiffness, and damping. It is therefore often impossible to know which modal parameters correspond to which mode shape matrix elements. Restricting the values of mass or stiffness requires a priori knowledge of a given system, which is not often the case, or a measurement of steady state values either in the mass- or stiffness-dominated regions that is guaranteed not to be affected by residuals or other peaks, which is equally uncommon. For the un-damped case, there is one mode shape matrix that removes this ambiguity; this is the mass normalising mode shape matrix. In addition to being a solution to the eigenvalue problem defining the vibration response, it also has the following properties

$$\boldsymbol{\psi}^T \boldsymbol{M} \boldsymbol{\psi} = \boldsymbol{I} \tag{2.34}$$

---

[2] Basis: a set of linearly independent vectors that span a space

$$\boldsymbol{\psi}^T \boldsymbol{K} \boldsymbol{\psi} = \boldsymbol{\lambda} \tag{2.35}$$

where $\boldsymbol{I}$ is the identity matrix, $\boldsymbol{\lambda}$ is the diagonal matrix of squared natural frequencies, and $\boldsymbol{\psi}$ is the mass normalising mode shape matrix. It should be noted that all properties that are true for the general mode shape vectors $\boldsymbol{\phi}$ are also true for the mass normalised mode shape vectors $\boldsymbol{\psi}$ and that the opposite is not necessarily true.

Having made this distinction, the modal masses are all reduced to unity and are no longer relevant to the mathematics when fitting curves to identify the modal parameters experimentally. For general damping, an equivalent set of vectors are found by comparing (2.22) and (2.28) such that

$$\boldsymbol{S} = \begin{bmatrix} \boldsymbol{B} & \boldsymbol{M} \\ \boldsymbol{M} & \boldsymbol{0} \end{bmatrix} \tag{2.36}$$

$$\boldsymbol{T} = \begin{bmatrix} \boldsymbol{K} & \boldsymbol{0} \\ \boldsymbol{0} & -\boldsymbol{M} \end{bmatrix} \tag{2.37}$$

$$\boldsymbol{\psi}^T \boldsymbol{S} \boldsymbol{\psi} = \boldsymbol{I} \tag{2.38}$$

$$\boldsymbol{\psi}^T \boldsymbol{T} \boldsymbol{\psi} = \boldsymbol{\lambda} \tag{2.39}$$

where $\boldsymbol{S}$ is the augmented mass matrix and $\boldsymbol{T}$ is the augmented stiffness matrix. We can now define the amplitude multiplier as a function of the augmented mass normalising eigenvalue matrix.

$$\bar{A}^p_{u,v} = \psi^p_u \psi^p_v \tag{2.40}$$

where ψ^p_u and ψ^p_v refer to the mass normalised mode shape vector elements for frequency p at DOF u and v respectively similarly to the generic mode shapes in (2.33). In essence, the amplitude of the transfer function at a given resonance is amplified by the product of the mode shape value at the input location and the mode shape value at the output location for that frequency. This definition also holds for the general viscous damping case, where the eigenvectors are twice as long due to the occurrence of conjugate pairs. It becomes apparent at this point that if either of the mode shape values is zero or near zero, the peak will disappear from the FRF. When this occurs, the response location is said to be a ‘node’ in the mode shape.

Identification of this peak then becomes impossible and the mode shapes need to be identified from other FRFs. Furthermore, the symmetry of FRF's becomes apparent. For the FRF of the same two locations, but with the impact and measurement locations transposed, the amplitude value is the same. Also the modal parameters are unchanged and thus the FRF is the same. For the special case of u and v being the same, the system is measured directly at the excitation point. This is known as a drive point FRF.

2.4 Modal Testing

2.4.1 Measurement Technique

The idealised goal of a hammer strike is to create an input force signal resembling an impulse as closely as possible. When the DFT of a true impulse is taken it will give a constant amplitude response for all frequencies. However, an impulse is an idealised signal and is not practically achievable. Instead, the practical goal of a hammer strike is to excite the system within the frequency domain of interest with sufficiently large amplitude that a response can be accurately measured. The slight attenuation of the hammer force excitation signal over the frequency domain investigated is accounted for in the normalisation in (2.6) since a smaller input force at high frequency will result in a smaller output acceleration at the same frequency. When exciting a large heavy system, such as an industrial manipulator, a large amount of energy needs to be added to the system. The amount of energy transferred is dependent on several properties of the impact equipment. The first of these is the weight of the hammer head. A heavier hammer head is capable of transferring more energy into the structure being investigated; however, there is a cost associated with this. The heavier head will not rebound as quickly from impact as a lighter head and, if the system responds too quickly, will interfere with the vibration response of the structure as an obstacle. Thus it is necessary to use a lighter hammer head that will bounce quickly away from the impact point for a smaller structure with high frequency characteristics. Also, operator skill becomes more relevant when striking a faster structure, particularly when the higher frequency dynamics are being investigated. Developing the skill to excite the structure and quickly remove the hammer head with repeatable force is necessary in modal analysis and can require significant practice. Modal analysis software packages tend to display the measured DFT of each impact while the data is collected so that the force profile generated by the hammer can be seen and the individual hammer strikes can be accepted, rejected, or repeated as necessary. This gives the operator some feedback regarding impact repeatability and enables poor strikes to be identified and removed. In addition to the weight of the hammer head, there are practical limitations to the amount of force that can be applied to any structure or mechanism without damaging it. By controlling the coefficient of restitution in a qualitative manner, the energy and force exerted on a structure can be balanced so as to be non-damaging. This is done by adding plastic or metal tips to the hammer head during impact. A softer head allows lower peak forces for equivalent energy transfers, whereas a harder hammer tip necessitates higher peak forces. The inevitable trade-off comes from the duration of the impact and thus the DFT of the force signal. For the softer tip with lower peak force and higher impact duration, the DFT of the input signal will attenuate much earlier than that of the harder hammer tip. As such, the weight and structural integrity of the structure and the frequency range of interest determine whether modal analysis is a plausible identification procedure or not. For a heavy, fragile system, it may not be possible to excite the system with sufficient energy and low enough peak force to see the higher frequency responses without destroying the structure.

In order to transfer as much energy as possible without damaging the manipulator with high force impacts, a soft hammer tip was attached to a 3lb short handled 5802A sledge hammer from Dytran. Initial tests with a much lighter 5850B hammer were insufficient to excite the system without risking damage to the hammer. Several Dytran 3035BG accelerometers were initially distributed throughout the structure, labelled 1 through 8 in Figure 2.10, and data was recorded through MAL CutPro and LMS Test.lab as well as through National Instruments' Signal Express.

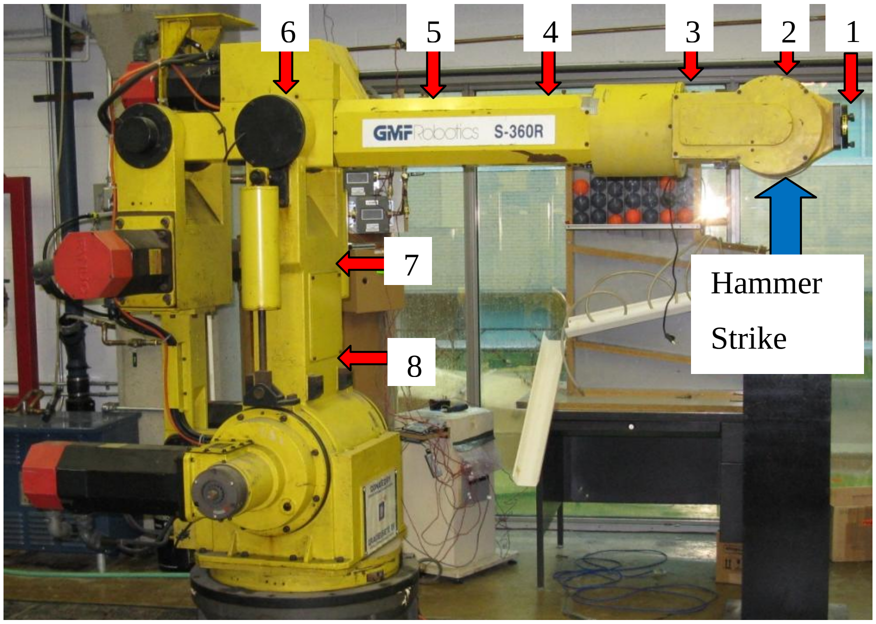

Figure 2.10: Modal Analysis Measurement Point Locations on the Fanuc S-360 Industrial Manipulator

The desired FRF is ultimately the drive point FRF at Location 1 since this is where machining forces will be exerted and also where the tool deflection occurs. However, striking at Location 1 requires a very low amplitude input to avoid overloading the accelerometer at that location. As explained above, this is undesirable since insufficient energy is transferred to the system. After an initial set of testing conducted by moving the impact hammer to various locations, it was determined that the wrist (Location 2) was not a node for any of the other input locations and, due to the symmetry of FRFs, it could be used as an impact point. This allowed larger forces to be exerted and more energy transferred to excite the low frequency dynamics without overloading the accelerometers. It has been noted in the literature that an industrial manipulators natural frequencies generally occur well below 300 Hz [20, 79, 88], so this was the region of interest. The soft hammer tip offered an acceptable force response up to approximately 400Hz and was therefore deemed suitable.

2.4.2 Nonlinear Effects

In order to gauge the effects of nonlinearities several tests were conducted with impact force, hammer weight, and hammer tip maintained. The experiment was repeated for three trials with the manipulator in a retracted configuration with the second link horizontal and the first link pointing away from the end-effector to gauge the operator repeatability. Three further trials were then conducted with a harder hammer tip. Figure 2.11 shows the end-effector response

(Location 1) for four of the experiment trials. Only one of the harder tip FRFs (Trial 4) is shown for clarity. The repeatability of the FRFs produced with the harder tip in the latter three trials is equivalent to that of the FRFs produced with the softer tip in the first three trials and as such the single FRF shown for Trial 4 is representative of all three harder tip FRFs.

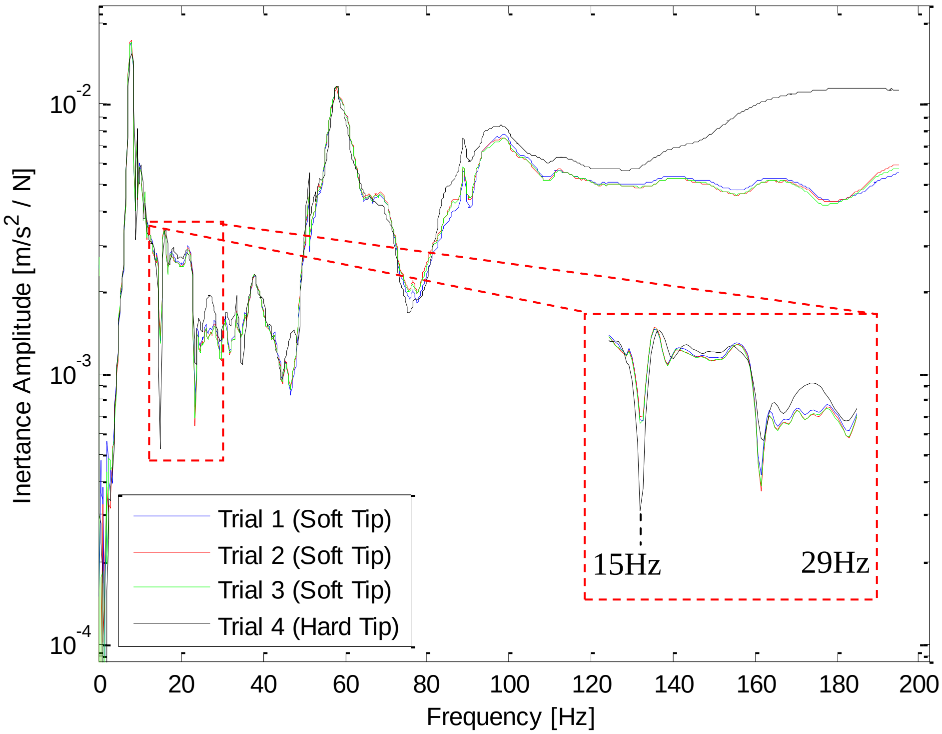

Figure 2.11: Location 1 Inertance Response for Multiple Location 2 Excitation Trials with Different Hammer Tips

The energy transferred into the system for a given excitation force is increased for a softer hammer tip due to the increased duration of the impact. Therefore the harder hammer tip was, by necessity, swung harder to excite the lower frequency dynamics. Both tips are expected to generate the same response at low frequency although the response from the softer hammer tip will attenuate earlier as frequency increases. For this reason, the low frequency discrepancies in the fourth trial are attributed to the nonlinearities in the system revealed by the changing force. The major discrepancies are the first anti-resonance at approximately 15Hz and the section of the response immediately after the second anti-resonance at approximately 23Hz as highlighted by the inset. The first anti-resonance was more pronounced in the fourth trial, which indicates the presence of hardening springs. The second anti-resonance is less pronounced indicating the presence of softening springs somewhere in the system. Given these two characteristics, it’s not surprising that following section of the FRF, until approximately 29Hz, is different for the different force levels. The dominant peaks however, are not affected to the same degree. This indicates that the spring nonlinearities have a very small effect on the eigenvalues of the vibrating system. The same correlation characteristics can be seen in most points along the system with the curves beginning to diverge in the 100-120Hz region as the expected attenuation appears. Plots for these experiments are given in 0. Although the region of interest was initially expressed as below 300Hz, there are no modal characteristics between 200 and 300Hz and so the region of interest was reduced.

2.4.3 First Link Rigidity

The initial model in Figure 2.9 makes assumptions about the locations and relevance of the various robot flexibilities. In particular, the first link is assumed rigid due to the four bar parallel mechanism and the second link is assumed to be flexible with further potential flexibility at the bolt patterns at either end of the link. The additional accelerometer readings (Locations 3, 4, 5, 7, and 8) allow data to be captured to support or deny these assumptions. If the first link is flexible, Locations 7 and 8 will not appear in phase at all the resonance frequencies. Figure 2.12, shows the phase for Locations 7 and 8 when the system is excited at Location 2.

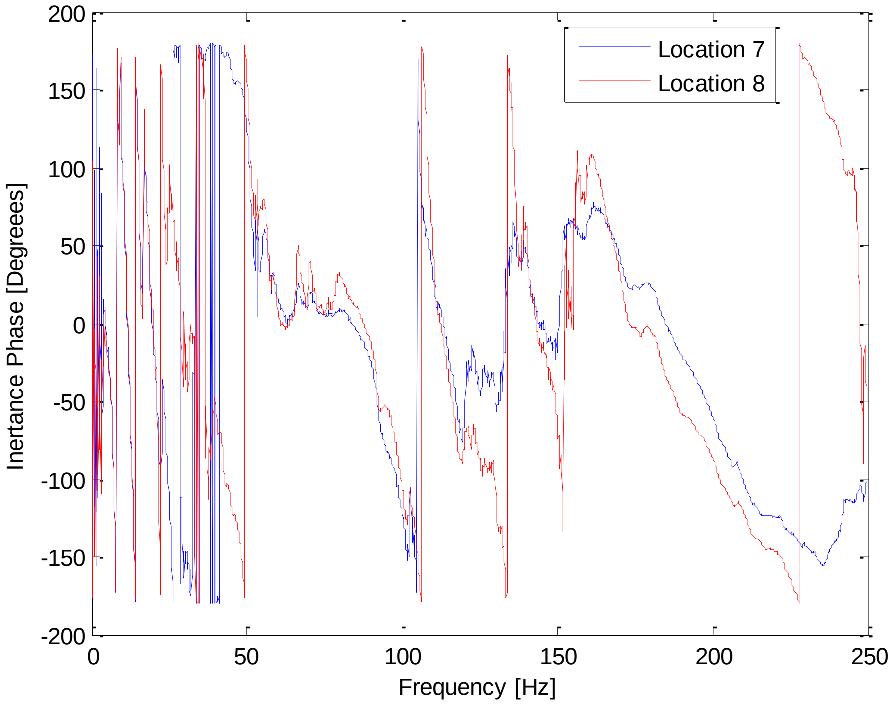

Figure 2.12: Inertance Phase Response for Locations 7 and 8 on the First Link Excited at Location 2 on the Second Link

Although the phase suffers from experimental noise, it can be clearly seen at frequencies above 50Hz in the above figure that the two points move in phase for all the mode shapes in the region of interest. The same is true for the lower frequencies, although the phase function is much more turbulent. Furthermore, there are no recognisable deflection shapes that can be obtained from peak picking that affect the deflection of Location 6. For example, the deflection at 8Hz shown in Figure 2.13 shows that Location 7 is deflecting more than Location 6, but also shows that this is not increasing the deflection at Location 6. This is due to the four bar linkage that increases the rigidity of the first link in the dynamic model. The deflection of the first link is not being carried through to the end-effector, which is the location that ultimately needs to be controlled, and so the first link can be assumed rigid. The following observations and inferences are made under the assumption that the first link is rigid.

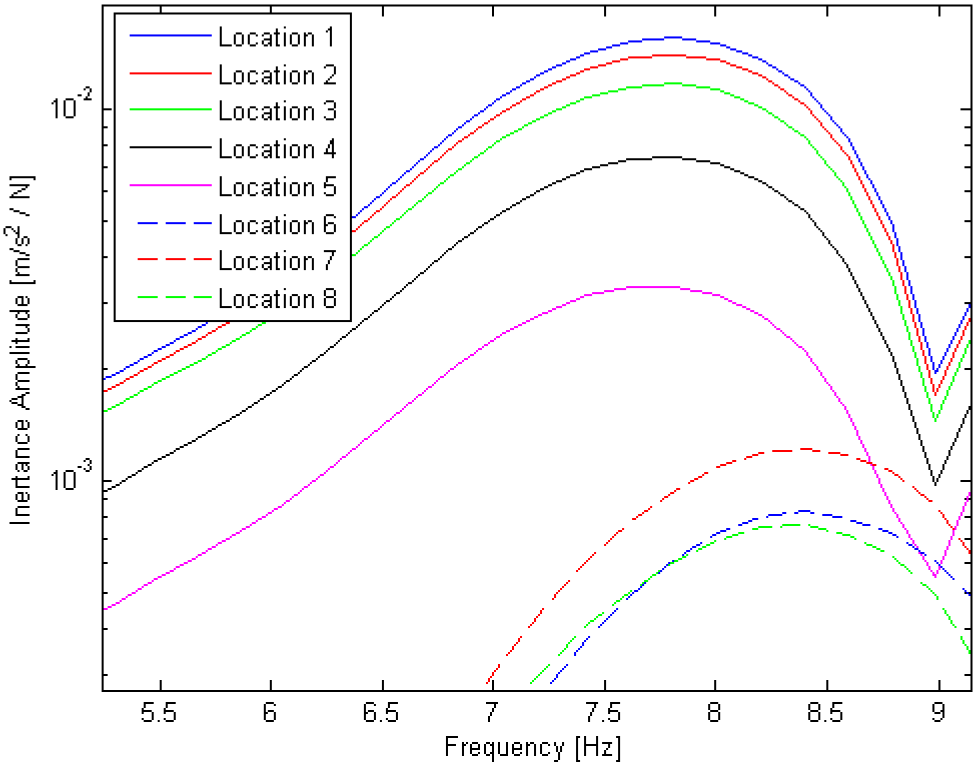

Figure 2.13: First Resonant Peak Inertance Amplitudes for Locations 1-8 Excited at Location 2

2.4.4 Second Link Flexibility

The mode shapes formed by the second link at any given frequency will not necessarily reflect the mode shape of a fixed-free beam since the end conditions of a fixed-free beam are not met due to the potentially varying mass and stiffness along the link. However, it is expected that the mode shape will contain a dominant fixed-free or fixed-fixed beam shape that can be seen. Identifying these frequencies and the shapes they form within the frequency region of interest will offer further insight into the number of DOF required to accurately model the dynamics of the vibrating system. Additional measurement locations were added along the link as shown in Figure 2.14. Locations 3, 4, and 5 were maintained as before and Locations 9, 10, 11, and 12 are introduced for this experiment.

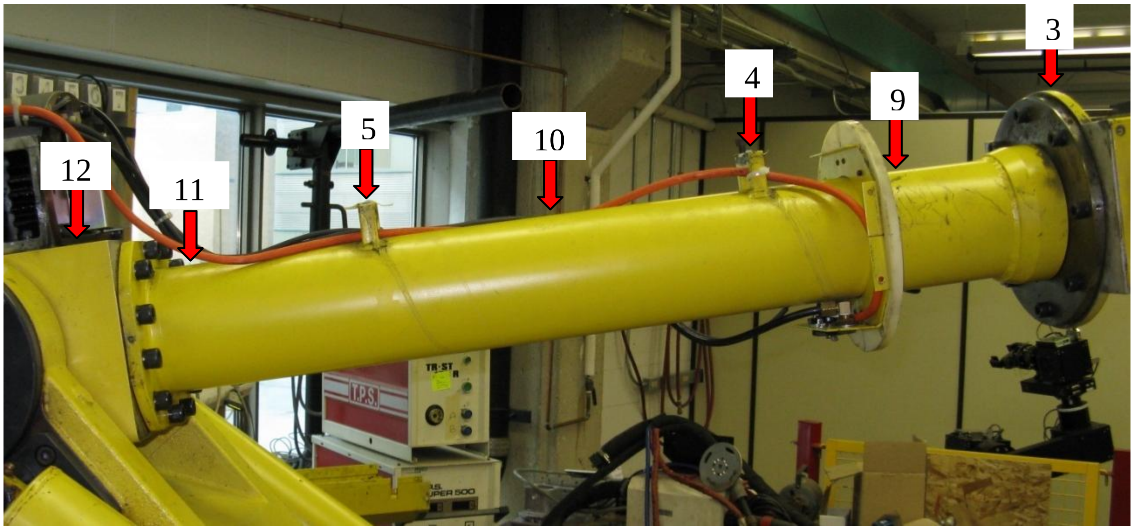

Figure 2.14: Additional Modal Analysis Measurement Point Locations for the Fanuc S-360 Industrial Manipulator for Investigating Second Link Flexibility

A first look at the FRFs for three trials can be used to further identify rigid and flexible elements in the manipulator. The experiment was conducted in an extended configuration with the first link extended toward alignment with the horizontal and the second link horizontal. The experiment was repeated for three trials to ensure that the operator and measurement error were negligible. The correlation between the trials is illustrated by the drive point FRFs in Figure 2.15 and shows repeatable results with minimal variances. The same correlation is observed for all FRFs. Plots for these experiments are given in Appendix B: .

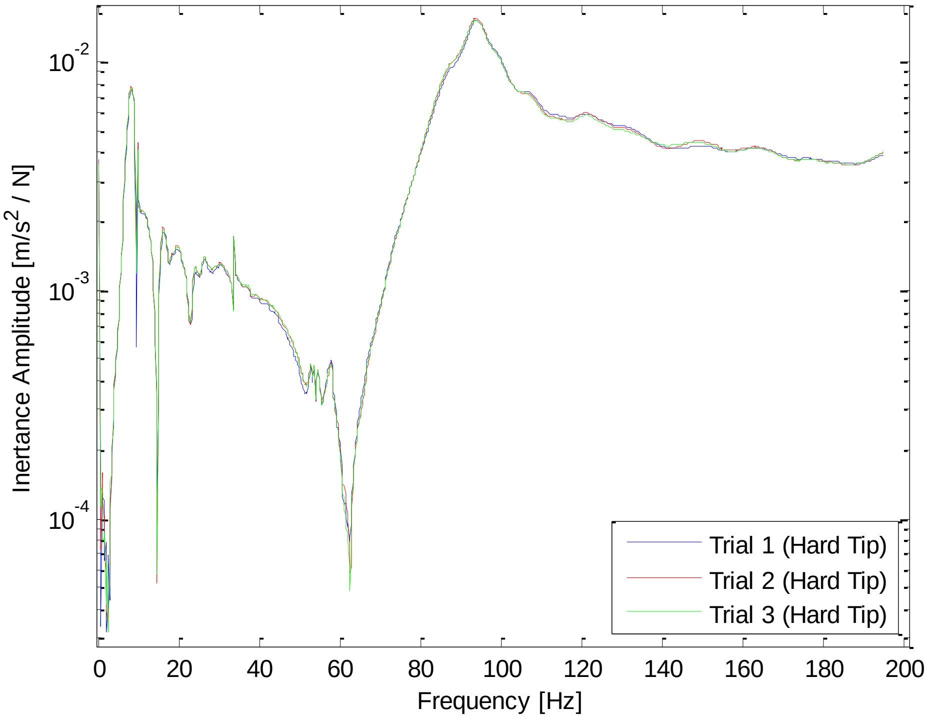

Figure 2.15: Multiple Trials of Location 3 Drive Point Inertance Amplitude

The full set of FRFs for excitation at Location 3 in the region of interest is given for the first trial in Figure 2.16. This figure shows how each of the locations is affected differently. For example the large peak around 94Hz seems to affect the locations proportionally based on distance from the shoulder joint, but following the peak the responses are very different. Location 3 appears to converge to a mass characteristic quickly as frequency increases as demonstrated by the steady amplitude value. Location 12 however, exhibits an anti-resonance characteristic before it begins to reach steady amplitude. It then takes on a stiffness characteristic as indicated by an increasing slope at approximately 160Hz. In the first case there is no indication of an upcoming resonant frequency at 180Hz, while in the latter the higher frequency peak begins to dominate the characteristics earlier at approximately 160Hz.

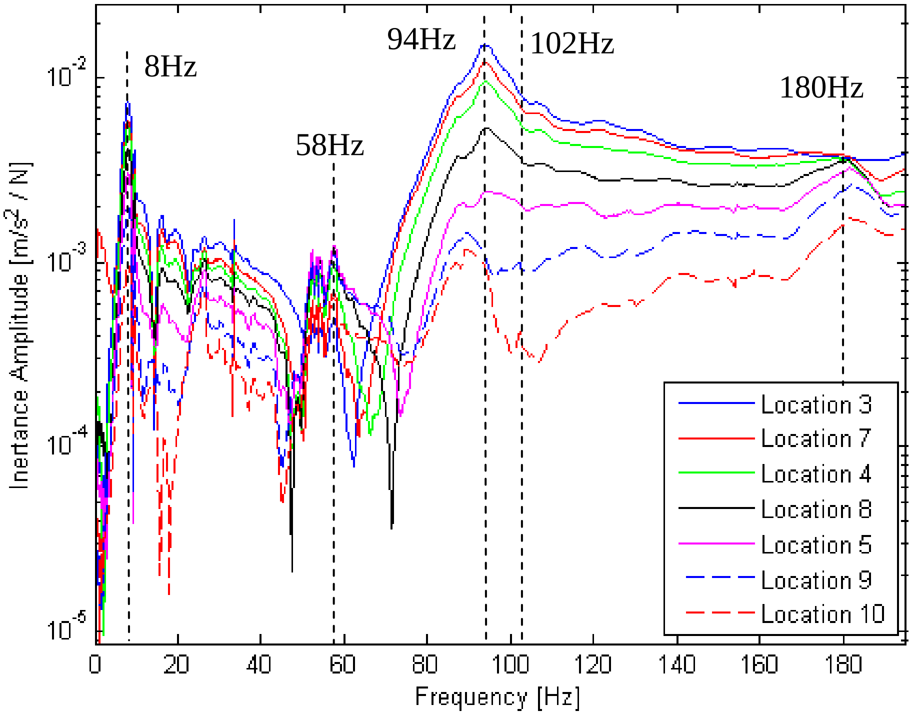

Figure 2.16: Inertance Amplitudes of Second Link Flexibility Experiment Locations Excited at Location 3

If the link has a resonant frequency in the domain of interest, we can see from Figure 2.16 that it will occur at one of 8, 58, 94, or 180 Hz. By investigating the mode shapes formed by the manipulator at these frequencies, we can gain a qualitative understanding of how the link is deforming. Figure 2.17, Figure 2.19, and Figure 2.22 show the frequency response for 8 Hz, 58 Hz, and 94 Hz respectively, at the different measurement locations along the second link for all three trials. The shapes formed by the vibrating system are found by peak picking the inertance FRF. Although the acceleration values are not accurate for deflection, the relationship between acceleration and deflection is proportional for all curves at the same frequency as shown earlier by (2.11). Therefore the proportional difference from location to location at a given frequency is the same for inertance, mobility, and receptance. A peak picking approach, whereby the FRF amplitudes at the peaks are taken as the amplitude multipliers and the phase is considered to be either 0^0 or 180^0 depending on the FRF phase, was used to approximate the amplitudes at resonance. Though considered a coarse and inaccurate approach to modal analysis, peak picking can often give a good initial insight into the nature of a vibrating system before rigorous numerical identification begins. The results from the peak picking identification are listed in Table 2.1, Table 2.2, and Table 2.3 and the deflection shapes are shown in Figure 2.18, Figure 2.20, and Figure 2.23 where the measurement locations are denoted by L1-12.

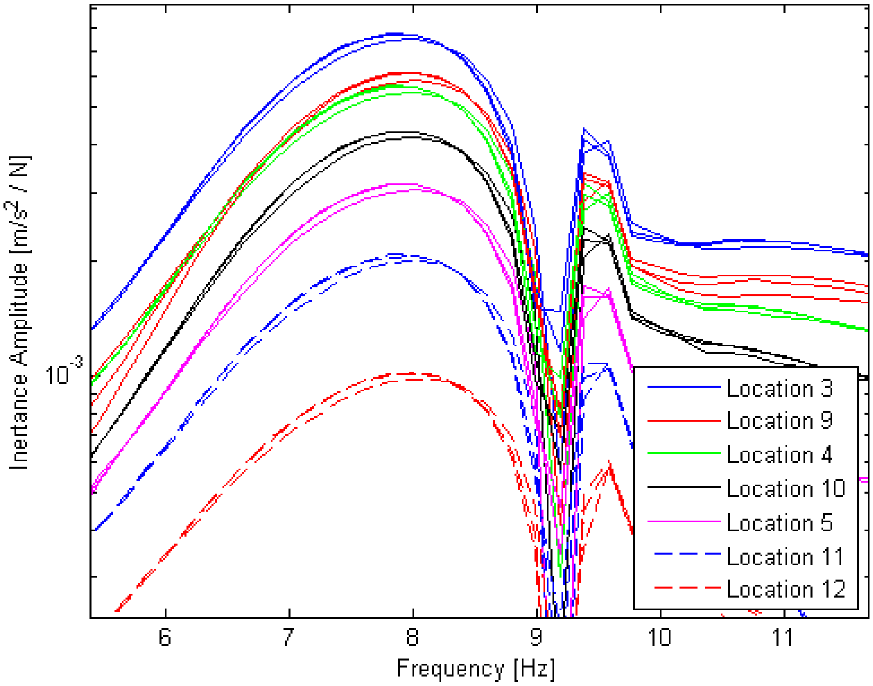

Figure 2.17: Inertance Amplitudes of the Second Link Flexibility Experiment Locations Excited at Location 3 around 8 Hz

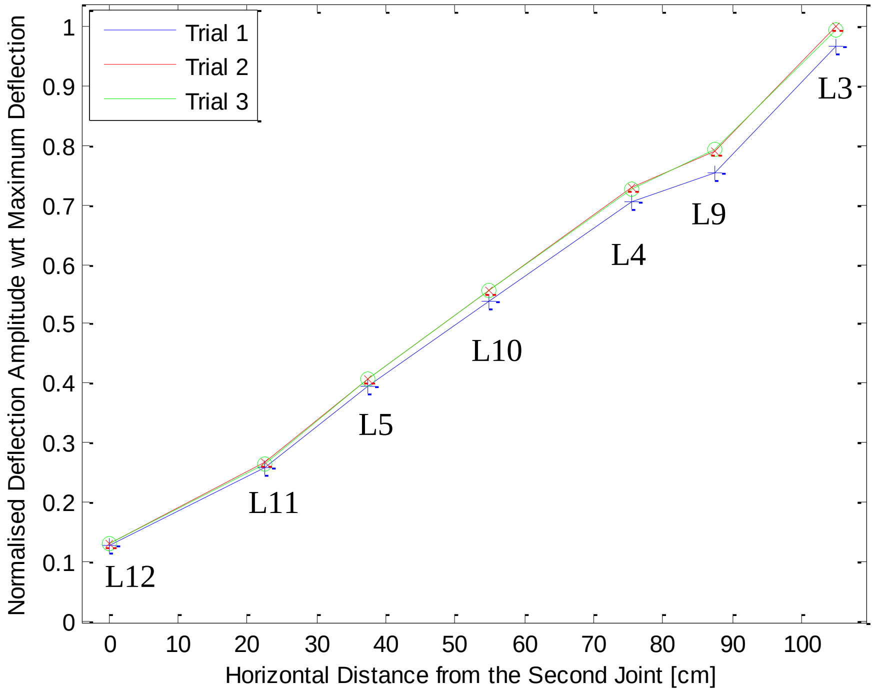

Figure 2.18: Normalised Deformation Shape of the Second Link Excited at Location 3 at 8 Hz

From Figure 2.18 it can be seen that the 8Hz resonant peak is dominated by the deflection in the second joint. This low frequency can be manually excited and the mode shape from the data can be observed visually. As such there is little to be learned from this peak regarding the flexibility of the link except that it is significantly stiffer than the second joint.

Table 2.1: Inertance Peak Values of Second Link Flexibility Experiment Locations Excited at Location 3 at 8Hz

Location	Frequency [Hz]	Amplitude – Trial 1 $[(m\ /\ s\text{^}2\ )/N]$	Amplitude – Trial 2 $[(m\ /\ s\text{^}2\ )/N]$	Amplitude – Trial 3 $[(m\ /\ s\text{^}2\ )/N]$
3	8	7.49×10^{-3}	7.76×10^{-3}	7.70×10^{-3}
7	8	5.85×10^{-3}	6.13×10^{-3}	6.16×10^{-3}
4	8	5.47×10^{-3}	5.67×10^{-3}	5.64×10^{-3}
8	8	4.17×10^{-3}	4.32×10^{-3}	4.32×10^{-3}
5	8	3.06×10^{-3}	3.16×10^{-3}	3.15×10^{-3}
9	8	1.99×10^{-3}	2.07×10^{-3}	2.05×10^{-3}
10	8	9.86×10^{-4}	1.02×10^{-3}	1.02×10^{-3}

In Figure 2.20, the 58 Hz peak shows a deformation in the link corresponding to the first resonance shape of a fixed-fixed cantilever beam. Although the beam would ideally be a fixed-free cantilever, the mass of the manipulator wrist is sufficient to appear immovable at this frequency. The mode shape is not exactly that of a fixed-fixed beam as can be seen in the non-zero deflection of Locations 3 and 12 indicating that there are other dynamics affecting this mode shape. Frequency harmonics occur at approximate integer multiples of the fundamental frequency, where the first mode shape appears. Therefore, a second fixed-fixed beam mode shape can be expected at approximately 116 Hz corresponding to the second natural frequency. Referring back to Figure 2.16, there is a minor phenomenon occurring at approximately 102Hz, which is most easily seen for the Location 10 response and is the only peak in the expected region around 116Hz that could represent the second mode shape. Figure 2.11 shows that the end-effector (Location 1) does not exhibit a peak at 102Hz that is significant compared to the 94Hz peak. Similarly, the inertance for Location 2 also fails to show a significant response at this frequency. This peak was therefore neglected from the model since it doesn't affect the end-effector. A similar characteristic occurs at the 180 Hz peak identified earlier and again the effect on the end-effector is negligible, thus the higher order dynamics of the second link can be ignored.

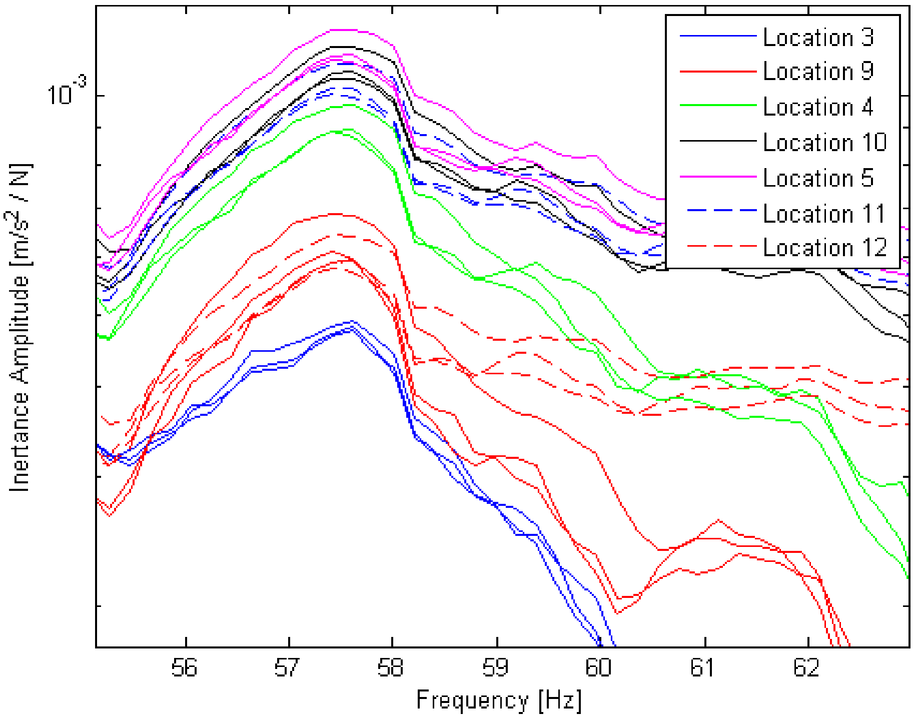

Figure 2.19: Inertance Amplitudes of the Second Link Flexibility Experiment Locations Excited at Location 3 around 58 Hz

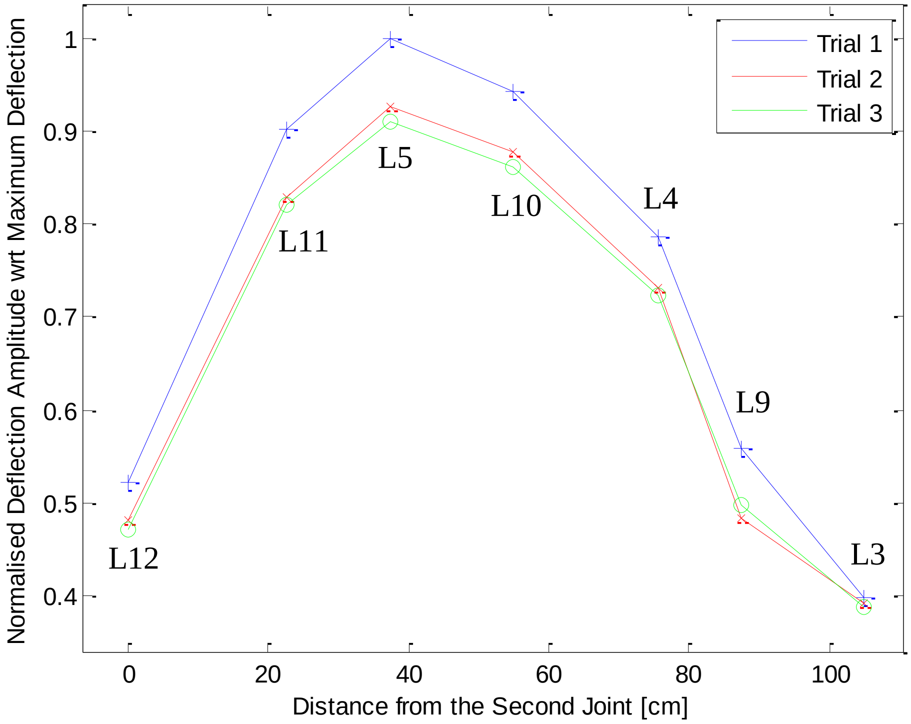

Figure 2.20: Normalised Deformation Shape of the Second Link Excited at Location 3 at 58 Hz

Table 2.2: Inertance Peak Values of Second Link Flexibility Experiment Locations Excited at Location 3 at 58Hz

Location	Frequency [Hz]	Amplitude – Trial 1 $[(m / s^2)/N]$	Amplitude – Trial 2 $[(m / s^2)/N]$	Amplitude – Trial 3 $[(m / s^2)/N]$
3	58	4.90×10^{-4}	4.83×10^{-4}	4.78×10^{-4}
7	58	6.88×10^{-4}	5.95×10^{-4}	6.12×10^{-4}
4	58	9.66×10^{-4}	8.99×10^{-4}	8.90×10^{-4}
8	58	1.16×10^{-3}	1.08×10^{-3}	1.06×10^{-3}
5	58	1.23×10^{-3}	1.14×10^{-3}	1.12×10^{-3}
9	58	1.11×10^{-3}	1.02×10^{-3}	1.01×10^{-3}
10	58	6.43×10^{-4}	5.92×10^{-4}	5.79×10^{-4}

In order for the beam flexibility to be relevant to the model, the deflection of the beam needs to be significant when compared to the deflection of the joints. At the 58 Hz peak, the deflection of Locations 1-6 measured by peak picking gives the mode shape in Figure 2.21 for the full manipulator structure.

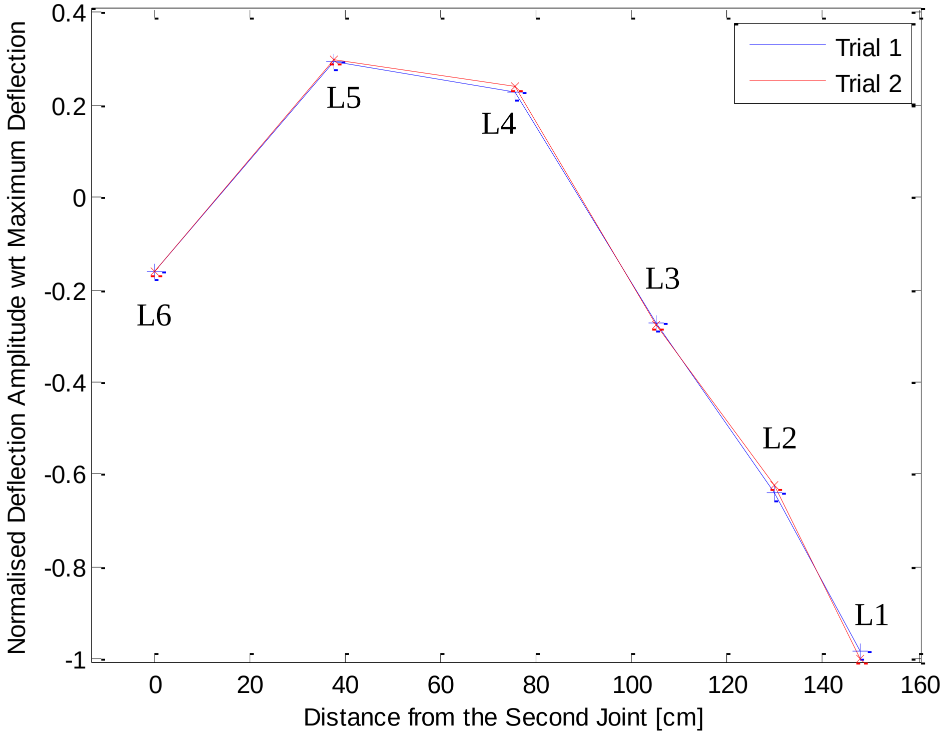

Figure 2.21: Normalised Deflection Shape of Locations 1-6 Excited Location 2 at 58Hz

It can be seen from Figure 2.21 that the beam deflection is significant to the overall mode shape from the significant increase in deflection from Location 6 to Location 5 and the following decrease from Location 5 to Location 3. All these locations are on the second link and so any rigid body effects would cause a proportional increase or decrease along the link. Furthermore, the change in phase from Location 5 to Location 3 would not be possible if the link was rigid since only the lever arm from the joints would be changing and this would not affect the phase of the response. In this overall mode shape, the beam deflection is significant and necessary to change the sign of the deflection angle from positive at Location 6 to negative at Location 3 and, as such, cannot be neglected. A single pseudo-joint is sufficient to compensate for the link flexibility at this frequency since the flexibilities at Locations 4 and 5 can be combined.

The amplitude response in Figure 2.22 shows several peaks clustered together and a change in dominance with location. Each of the clustered peaks offers a very similar mode shape and so the peak at 94 Hz was selected to represent the region as it dominates the majority of locations. The mode shape can be approximated using the joints and pseudo-joint already identified and so no further pseudo-joints are necessary.

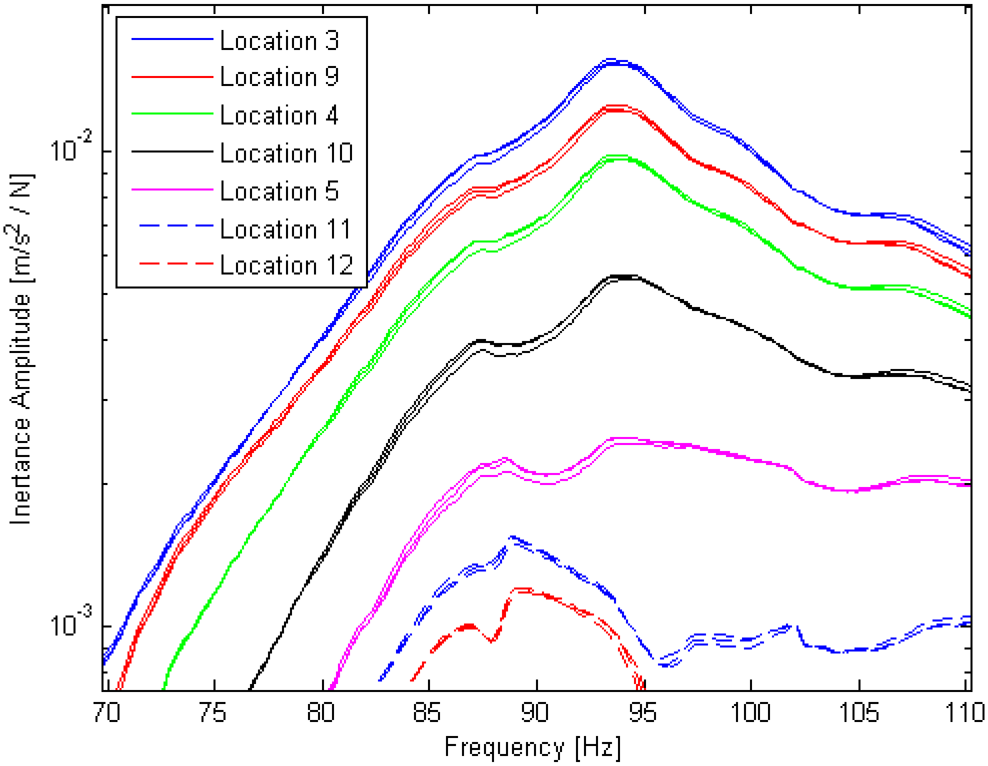

Figure 2.22: Frequency Response of the Second Link Flexibility Experiment Locations Excited at Location 3 at 94 Hz

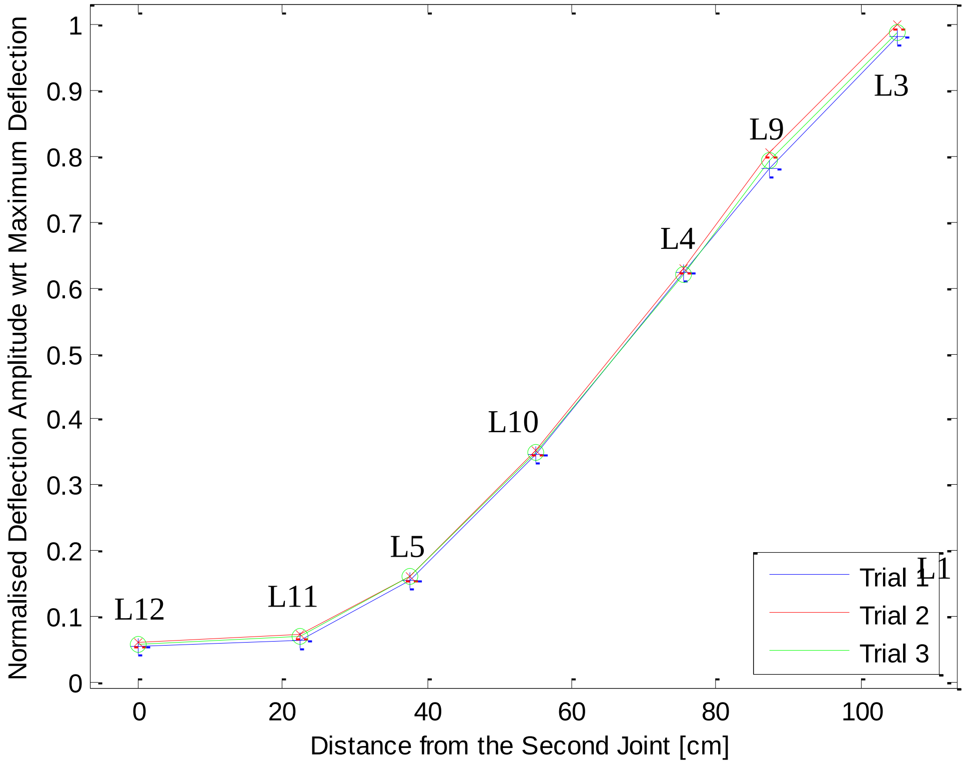

Figure 2.23: Normalised Deformation Shape of the Second Link Excited at Location 3 at 94 Hz

Table 2.3: Inertance Peak Values of Second Link Flexibility Experiment Locations Excited at Location 3 at 94Hz

Location	Frequency [Hz]	Amplitude – Trial 1 $[(m / s^\wedge 2)/N]$	Amplitude – Trial 2 $[(m / s^\wedge 2)/N]$	Amplitude – Trial 3 $[(m / s^\wedge 2)/N]$
3	94	1.52×10^{-2}	1.55×10^{-2}	1.53×10^{-2}
7	94	1.21×10^{-2}	1.25×10^{-2}	1.23×10^{-2}
4	94	9.66×10^{-3}	9.77×10^{-3}	9.62×10^{-3}
8	94	5.37×10^{-3}	5.48×10^{-3}	5.42×10^{-3}
5	94	2.43×10^{-3}	2.49×10^{-3}	2.49×10^{-3}
9	94	9.80×10^{-4}	1.12×10^{-3}	1.11×10^{-3}
10	94	8.40×10^{-4}	9.50×10^{-4}	9.10×10^{-4}

2.4.5 Variance with Configuration

Manipulator dynamics are not only nonlinear for a given position; they are also nonlinear in joint space. Thus, the linearised dynamics are still joint dependent and will be different for all configurations. Taking the limits of the manipulator reach shows the effects of configuration on both the frequencies of interest and the mode shapes at those frequencies. Figure 2.24 shows the end-effector response (Location 1) excited at Location 2 in fully extended and fully retracted configurations.

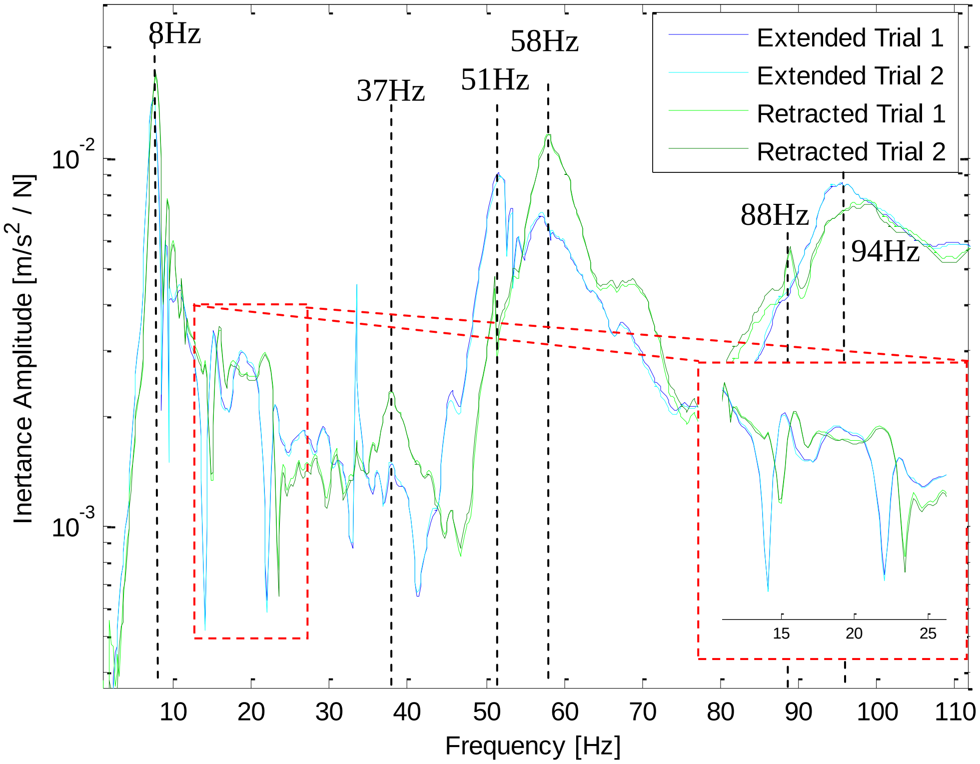

Figure 2.24: Effects of Configuration on Location 1 Inertance Amplitude Excited at Location 2

When the manipulator is retracted, it appears that the entire FRF is shifted almost uniformly. This is most easily seen by taking the two anti-resonances in the inset as reference points. In both cases, the anti-resonances occur between two and three hertz higher when the manipulator arm is retracted.

The amplitudes of the resonant peaks can be seen as configuration dependent, particularly when looking at the relative amplitudes of the 51 and 58 Hz peaks. In the extended configuration both peaks are of comparable amplitude, while in the retracted configuration the 51Hz peak is much less significant than the 58Hz peak. Though the 8 Hz peak has not been significantly affected, supporting the observation earlier that it is dominated by the second joint flexibility, the 94 Hz peak is noticeably reduced and shifted to a slightly higher frequency. The variance in amplitude of the 51, 58, and 94 Hz peaks as the first joint angle changes shows that the first joint flexibility is relevant to the manipulator deformation. By adjusting the first link angle, the moment arm about the first joint changes affecting the amplitude and placement of these higher frequency resonances.

A very lightly damped peak occurs at 33Hz and the amplitude substantially increases in the retracted configuration. The peak is so narrow that an accurate reconstruction is not realistically attainable. Furthermore, the peak does not appear to affect the region around it and as such the response will only be affected in the immediate locality of the peak. For these reasons the peak is neglected from the parameterisation. A similar peak occurs at 88Hz and is again much more pronounced in the retracted configuration. As with the 33Hz peak, the effect of the 88Hz peak on the overall curve is minimal and the likelihood of an accurate fit is very low. Therefore this peak is also neglected from the parameterisation.

2.4.6 Further Observations

Figure 2.25 outlines a curiosity in the first link response. Though the first link was found to be rigid by investigating the phase of the response at various frequencies and the mode shapes formed, a curious property occurs at 51Hz whereby the amplitudes of Locations 7 and 8 are equal and in phase. The accelerometers are not placed at symmetric locations along the length of the link and so this does not match any expected mode shape that would correspond to a fixed-fixed beam mode shape, which would be expected for a beam that isn't behaving as a fixed-free beam. This characteristic cannot be immediately explained, although the author speculates that due to the variations in the link, specifically a hole that that been cut in the link, that the mode shapes of the beam are deformed and that the shape is a deformed fixed-fixed beam shape.

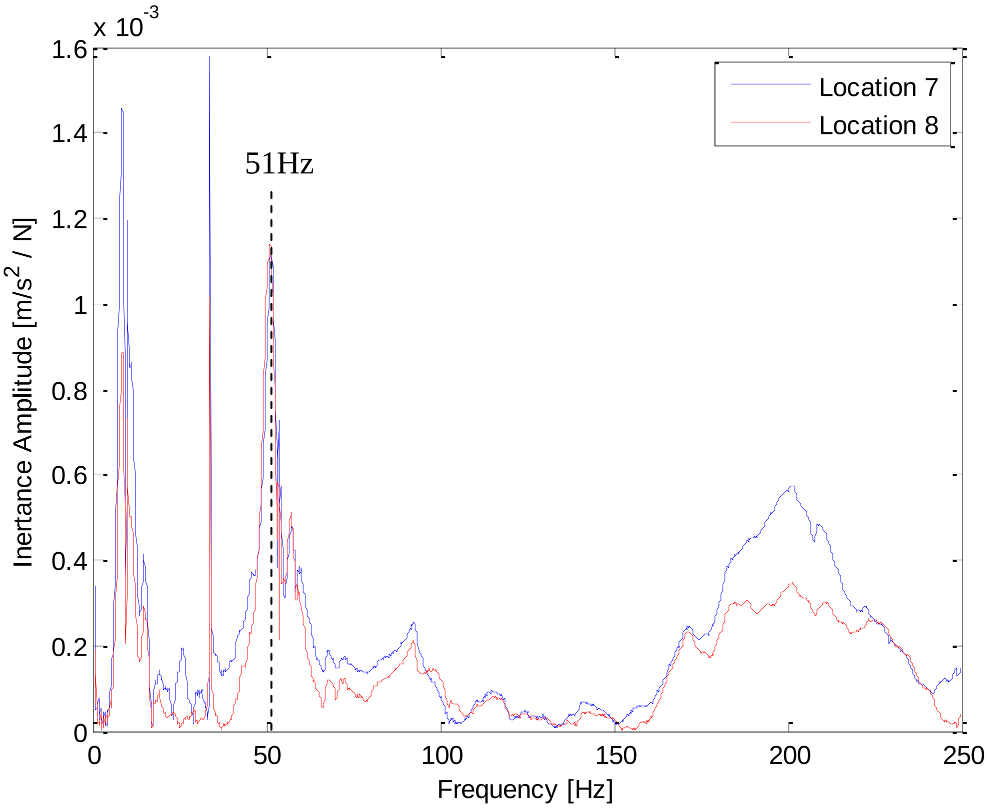

Figure 2.25: Inertance Amplitudes of Locations 7 and 8 Excited at Location 2

Additionally, a torsional mode was discovered about the second link axis at approximately 76Hz. At this frequency, one of the shoulder connections vibrates significantly more than the other as shown in Figure 2.26. There is no significant corresponding peak at this frequency in any of the other locations and thus it doesn’t contribute to the end-effector vibrations. This torsional resonance was omitted from the results by ignoring the 76Hz peak and using the response of the left shoulder, which is less affected.

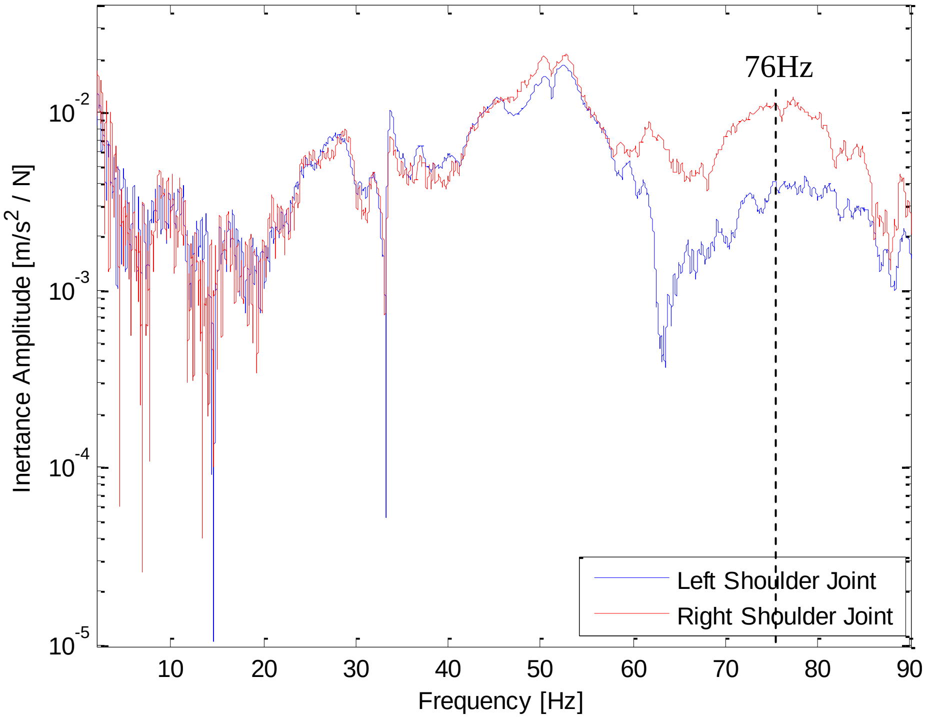

Figure 2.26: Inertance Amplitude for Location 6 measured on the Left and Right Shoulders Excited at Location 2

Referring back to Figure 2.13 the frequencies at which the first peak appears show a distinct shift across the second joint. Locations 1-5 give a resonant frequency at around 7.7Hz, while Locations 6-8 show a resonance at approximately 8.4Hz. Furthermore this behaviour was not seen for the measured FRFs in extended configurations; this is unexpected and difficult to explain.

2.5 Modal Parameter Identification

2.5.1 Modal Analysis Method

There are a number of curve fitting techniques that can be used for identifying single or multiple peak FRFs. For single peaks, there are no residual effects from higher order dynamics or neighbouring peaks and as such the FRF is fully controlled by a single set of modal parameters. For multiple peaks, a common assumption is that very near the peak of interest the behaviour is dominated by that peak alone. As such, single peak methods and extended single peak methods such as the peak-picking method can be used for few well spaced peaks.

While often good enough for initial identification, peak picking is an overly simplified approach that neglects the phase information captured in the FRF other than to define a data point as in or out of phase. For an un-damped system this is accurate since the phase will be of this nature, however for a damped system the phase will be more complex in nature. Another approach that uses the same assumption of peak independence is the circle fit method [25]. In this method, the Nyquist plot of the FRF is considered around the peak and the effects of neighbouring peaks can be removed without being identified. The shape of the FRF is considered rather than the exact amplitude and phase thereby removing phase and amplitude offsets and allowing residual terms to be identified for a given peak. More robust fits require fitting the entire curve to (2.20). While not very efficient computationally, this also has the effect of removing the user, and therefore the users judgement, from the operations. Depending on the complexity of the system, this can be time saving or problematic.

$$A_{u,v}(i\omega) = \frac{1}{M_R} + \sum_{p=1}^{P} \frac{-\bar{A}_{u,v}^{p}\omega^2}{-\omega^2 + 2\zeta^p \omega_n^p \omega i + {\omega_n^p}^2} - \frac{\omega^2}{K_R} \tag{2.20}$$

Modal identification can also be carried out in the time domain. One way to do this is through the complex exponential method. This method requires an Inverse Fourier Transform (IFT) to be taken of the theoretical model given in (2.20). It is much more difficult to gain an intuitive understanding of the system when viewed in the time domain, and as such the user is again removed from the identification process. Furthermore, additional modes are generally required to absorb the imperfections of the technique. These modes then need to be identified and removed from the final results. The Ibrahim time domain method [96] extends the previous method from a single FRF analysis to a complete analysis of the system in a single step thus further removing the user and increasing the number of additional modes. It is worth noting however that time domain systems are much simpler to implement for viscously damped systems due to complications that arise for the general case of structural damping.

LMS Test.Lab [97] was initially used to identify the natural frequencies and damping ratios from a modal indicator function (MIF) and mode shapes from a least squares frequency domain (LSFD) optimisation that fitted all FRFs to (2.20) simultaneously. However, the frequencies and damping ratios were inconsistently identified for multiple test trials when the test trials showed highly repeatable behaviour. In addition, the fitted curves were not consistent and did not accurately reflect the mode shapes. Similarly, MAL CutPro was unable to produce consistent or reasonable values of modal mass, stiffness, or damping values, often producing negative mass and damping ratios, and assumed an amplitude scalar of unity for all peaks. The failure of these software products indicated that the data was not optimal for linear identification and as such operator input was necessary at several steps throughout the identification procedure. A frequency domain circle fit approach was chosen to allow user input to compensate for the errors and approximations in the identification process. These were unavoidable to prevent the poor results produced by the software packages. The peaks identified through hammer testing were not initially assumed to be well spaced and so the circle fit algorithm was only applicable to certain well spaced peaks. For these peaks, a circle fit method was used to identify natural frequency, damping ratio, and amplitude multipliers. The remaining peaks were identified in groups such that cumulative effects such as anti-resonances were not falsely attributed to a single mode. This identification initially used a LS fit to (2.20) for each peak separately from the rest of the FRF and the other FRFs in the set. It was later determined that the circle fit algorithm was robust enough to peak spacing that it could be used over a small region for the closely spaced peaks provided there was sufficient amplitude at that peak.

2.5.2 Data Pre-Processing Filtering

The DFT for each FRF was performed using the fft() function in MATLAB [98]. Due to the noise in the DFT results, it was necessary to filter the mobility FRF with a band-pass filter before attempting to analyse it with a circle fit technique. The data was filtered differently for each peak at each location with the lightest filtering tending to be on the lowest peaks. The filtering was different for each peak to minimise the amount of data manipulation before analysis in all cases. Figure 2.27 and Figure 2.28 show the Nyquist plot and amplitude response of a section of the end-effector (Location 1) drive point FRF before and after filtering. These are typical of the filtering effects at all locations.

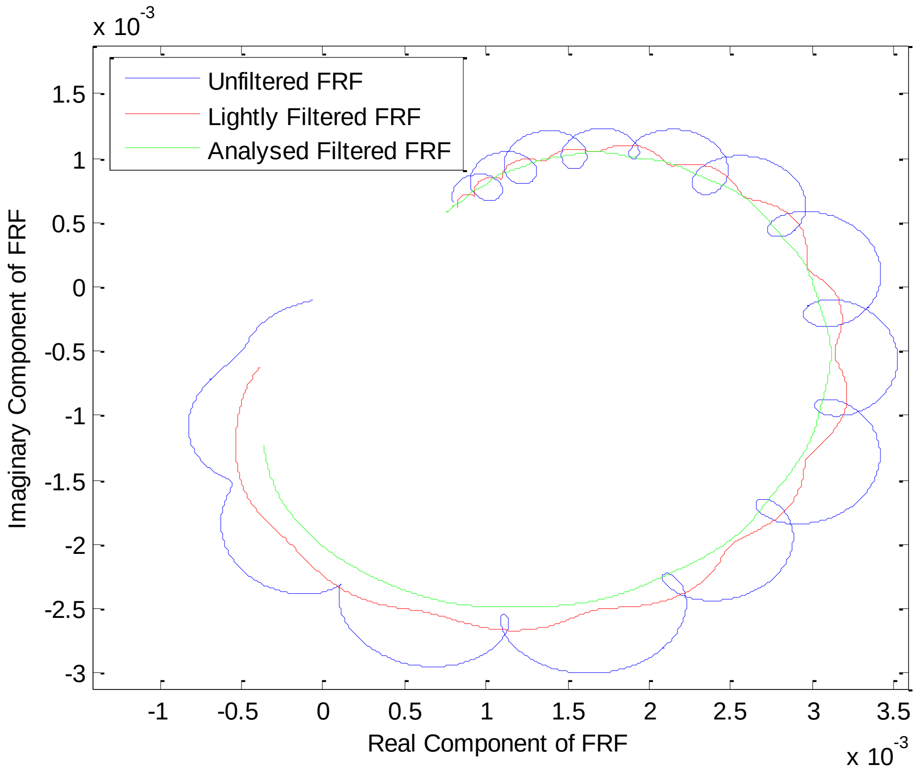

Figure 2.27: Results of Mobility Filtering in Nyquist Domain

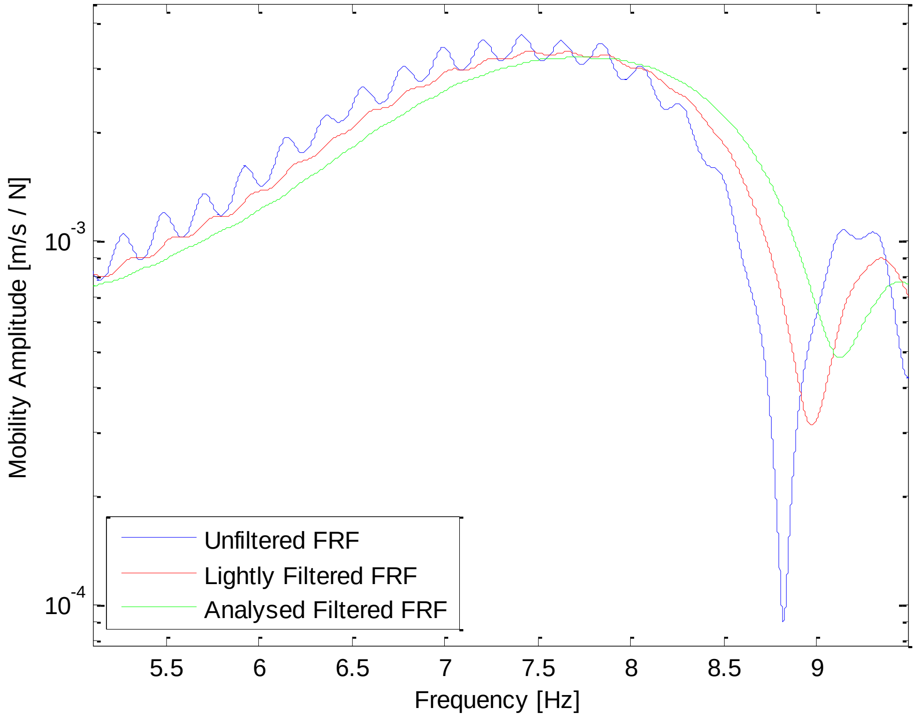

Figure 2.28: Results of Mobility Filtering on Amplitude

2.5.3 Circle Fit Algorithm

Viscously damped systems have mobility FRFs that produce a circle in the imaginary plane in the vicinity of a resonant peak [96]. This can be used to identify whether the selected range of data is within the region dominated by a given peak. Once this is confirmed, the traverse rate, defined as $\frac{d\theta}{d\omega^2}$, can be determined from a symmetric difference quotient

$$\frac{d\theta}{d\omega^2} = \frac{\theta(\omega+\Delta)-\theta(\omega-\Delta)}{2((\omega+\Delta)^2-(\omega-\Delta)^2)} \tag{2.41}$$

where Δ is a small change in frequency and θ is the angle from the centre of the circle to the data point anticlockwise from the real axis. The maximum traverse rate occurs at ω_n[25] and evaluating the traverse rate at this frequency yields

$$\frac{d\theta}{d\omega^2}\Big|_{\omega=\omega_n} = \frac{1}{2\zeta\omega_n^2} \tag{2.42}$$

From here the natural frequency and damping ratio of the peak can be identified by finding the maximum traverse rate frequency and then solving (2.42) for ζ. From the diameter of the circle given by

$$d = \frac{|\bar{A}^p_{u,v}|}{2\zeta\omega_n}, \tag{2.43}$$

the magnitude of the amplitude multiplier can be found by solving (2.43) for $|\bar{A}^p_{u,v}|$. The angle of the amplitude multiplier is given by θ and so the complete value can be found from

$$\bar{A}^p_{u,v} = |\bar{A}^p_{u,v}|(\cos(\theta) + \sin(\theta)\,i) \tag{2.44}$$

2.5.4 Comparison of Circle Fit to Least Squares Fit

When compared to the reconstructed peaks identified through the LS fit to (2.20), the circle fit results were more consistent for mode shapes and system poles and therefore the circle fit parameters were used in the dynamic model parameterisation. However, there was still a lack of consistency for the circle fit method at several peaks; specifically, the resonant frequencies were inconsistent across the second joint as seen in Figure 2.13. To compensate for this systematic error, when the identified frequency did not match the majority of identified frequencies for that peak, the identified frequency was replaced with the average frequency found from other FRFs and used for the circle fit identification. The selected average frequency was chosen from the other circle fit results or the LS fit results depending on which were perceived as more accurate. The damping ratio and amplitude multiplier were then identified based on the new natural frequency. In the few cases where the damping was also inaccurately identified, the damping ratio was also replaced in the circle fit method by more accurately identified data, again from either other circle fit results or LS results, and only the amplitude multiplier was calculated for that peak in that FRF. The same approach was taken for the LS fit when it failed to produce reasonable values if confidence in the circle fit data was low and verification was deemed necessary.

Despite forcing certain parameters to match previously identified values that are known with more confidence, the reconstructed peaks often appeared to be too wide since the reconstruction failed to capture the anti-resonance behaviour either before or after the peak. When the anti-resonances occurred close to the peak of interest, the amplitude dropped off quickly on the side closest to the anti-resonance. In these cases, a second peak was added to the LS fit to compensate and also to verify the parameters found from the circle fit. Initially, residual terms were used for this, but it was quickly determined that the sensitivity of the algorithm to the residual terms was too low and the optimisation returned the initial conditions more often than not. The additional peaks compensated for the lack of residuals and also exhibited a better sensitivity to the input variables. The LS fit to (2.20) was therefore adjusted to neglect the residual terms and became a fit to (2.19) for all parameter identification including the single peak fit outlined in the above paragraph. Figure 2.29 and Figure 2.30 show the results for the circle fit identification of one peak and the results of using a LS fit to (2.19) with the amplitudes adjusted so that the maximum amplitudes are equal and the curves are superimposed. The identified values for each type of fit are given in Table 2.4.

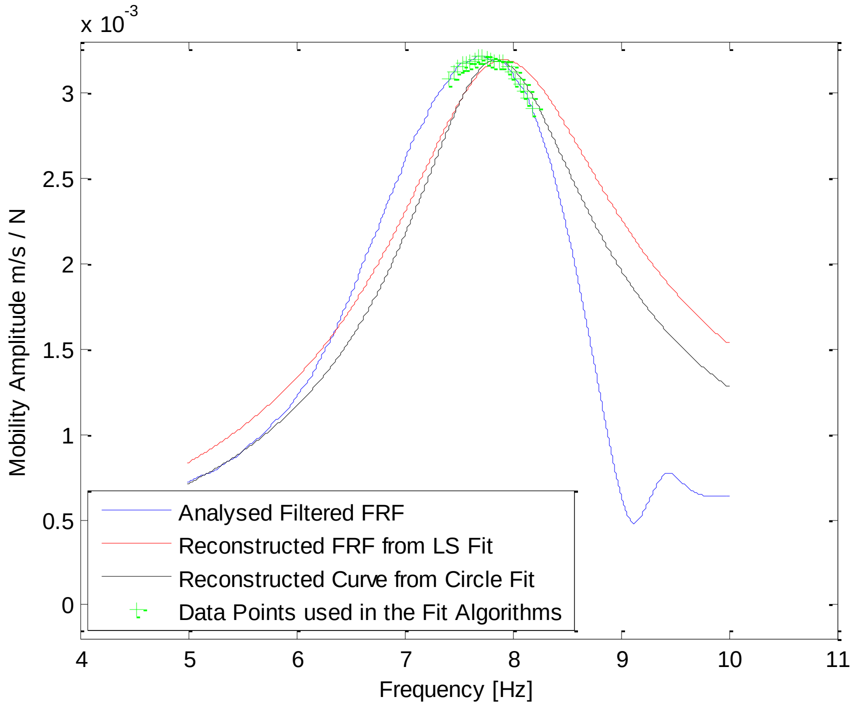

Figure 2.29: Location 1 Drive Point Mobility Amplitude Reconstructions for Modal Parameter Identification with LS and Circle Fit Methods

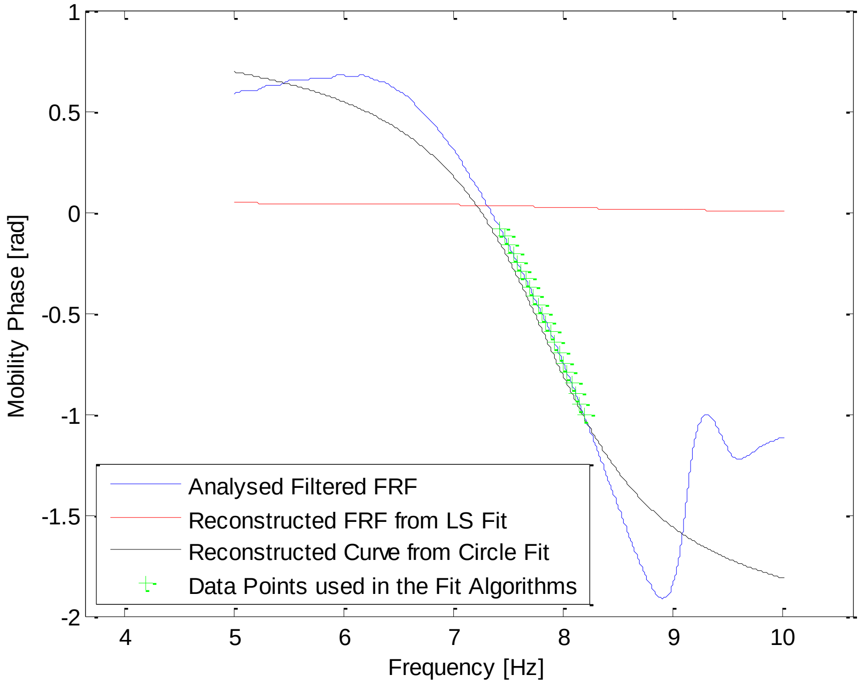

Figure 2.30: Location 1 Drive Point Mobility Phase Reconstructions for Modal Parameter Identification with LS and Circle Fit Methods

Table 2.4: Identified Modal Parameters for Location 1 Drive Point Mobility using a Circle Fit Method and a LS Method at 8Hz

Parameter	Circle Fit	LS Fit
Damping Ratio [-]	0.11	0.13
Natural Frequency [Hz]	7.86	7.92
Amplitude Multiplier [-]	0.034-0.026i	0.328+2.52i
Amplitude Correction	1.26	62.06

The results show a further advantage of the circle fit technique as opposed to a general LS approach other than the repeatability of the results. In this case, and in many other cases, the LS fit to (2.19) was unable to accurately capture the phase data. The results from the circle fit were used for the dynamic model parameterisation and the identified values for the configurations used in the identification are tabulated in Appendix C: .

2.6 Dynamic Parameter Identification

2.6.1 Inertial Parameters

The manipulator dynamic model is generated based on the Denavit-Hartenberg convention and does not assume that inertia is a known function of mass. The assumption that the parallel mechanism can be modelled as a single link requires the additional mass and inertia to be accounted for by the first and second links for different vibration shapes. This will not appear as a simple addition to mass that can be included in geometric inertia calculations and thus there needs to be a correction variable to account for this difference. For example, when the first mode is dominant the response is dominated by the deflection in the second joint and the parallel mechanism will deform adding some of its weight to the apparent weight of the second link. However, it will contribute to the apparent inertia of the second link as a point mass at a given radius on the second link and not as a distributed mass along the length of the second link. In addition, the locations and masses of the motors are not considered in the model and so the additional masses and inertias they contribute will again appear as point masses. Furthermore, the masses for each link were assumed to be in the centre of that link and any error in this assumption is partially compensated for in independent link inertia parameters.

2.6.2 Selected Degrees of Freedom

The dominant resonant peaks in the region of interest occur at approximately 8, 38, 51, 58, and 94 Hz. Identification of the 38Hz peak was not possible since the peak is not present in sufficient configurations and thus the mode shapes cannot be identified for the corresponding FRFs. This leaves four dominant peaks to be identified at 8, 51, 58, and 94Hz requiring four degrees of freedom in the spatial model. At the bolt pattern (Location 3) the 51 and 58Hz peaks could not be accurately parameterised in the fully extended configuration and as such that degree of freedom was removed. Similarly, the reconstruction of Location 4, while acceptable, was inferior to that of Location 5 and so Location 5 was selected to represent the flexibility in the second link. The final model now includes the three joints and a single pseudo-joint to represent the second link flexibility. For clarity, the joint variables will be referred to as q_1, q_2, and q_3, and the angle of the pseudo-joint will be referred to as ρ.

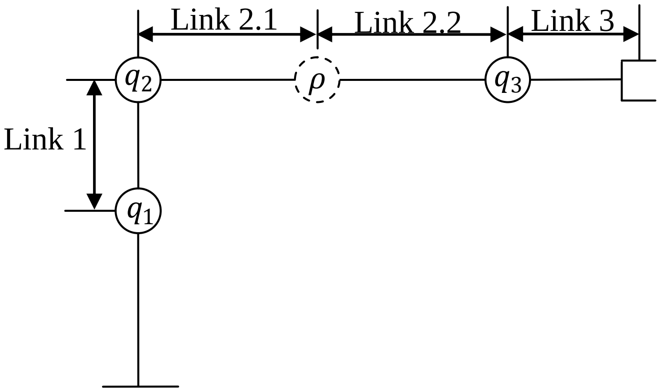

Figure 2.31: Final Planar Skeleton Schematic of a Fanuc S-360 Industrial Manipulator including Pseudo-Joints

2.6.3 Model Updating

In the field of finite element analysis, experimental model updating is used to improve the accuracy of models which would otherwise not be accurate enough to provide a useful simulation or prediction of a systems behaviour [99, 100]. The corrections made to the model are often thought of as fine tuning, although it is not uncommon for additional degrees of freedom to be added to a model at this stage. As a developed field of engineering, there are several approaches and algorithms that use modal data for updating physical parameters of a mechanical system. Mottershead and Friswell [99] identified three common forms of model error

1. Model Structure Errors
2. Model Parameters Errors
3. Model Order Errors

The first of these refers to simplifications such as linearization. In the current model, a linear system is required for parameterisation and so the linearization is necessary and cannot be removed. In addition, the nonlinear spring elements identified in Section 2.4.2 show that even if the ideal dynamics were fully modelled there would still be un-modelled nonlinearities in the system. The third type of error refers to the number of degrees of freedom in a model. The DOF in the selected model is purposefully kept low to match the number of dominant peaks in the frequency response and the apparent DOF of the system. Thus, of the three types of errors, structural and order errors are deemed necessary and only parameters errors are to be reduced.

In the techniques reviewed by [99, 100], the mathematics driving the model updating techniques rely on the linearity of the system, specifically the orthogonality property given earlier in (2.37). Rearranging (2.37) and solving for the augmented mass matrix yields

$$\boldsymbol{S} = \boldsymbol{\phi}^{-T}\boldsymbol{I}\boldsymbol{\phi}^{\boldsymbol{-1}} \tag{2.45}$$

The elements of $\boldsymbol{S}$ are all physical parameters corresponding to mass and damping values, which must be real, and must also match the form of (2.36)

$$\boldsymbol{S} = \begin{bmatrix} \boldsymbol{B} & \boldsymbol{M} \\ \boldsymbol{M} & \boldsymbol{0} \end{bmatrix} \tag{2.36}$$

However, when testing the identified mode shapes, (2.45) did not yield real values nor did it produce an $n \times n$ zero matrix in the lower right entries. It is clear at this point that the mathematical techniques for model updating in the literature are designed to generate an accurate model in terms of all three error types defined by [99] and so an unwillingness to correct the model in terms of one type of error will hamper any techniques ability to reduce other types of error. An alternate and more general approach is therefore needed to identify the dynamic parameters from the modal parameters developed in the following section.

2.6.4 Dynamic Parameter Identification

The experimental data is recorded for each of the measurement locations in the vertical direction corresponding to the 4DOF linear system in Figure 2.32.

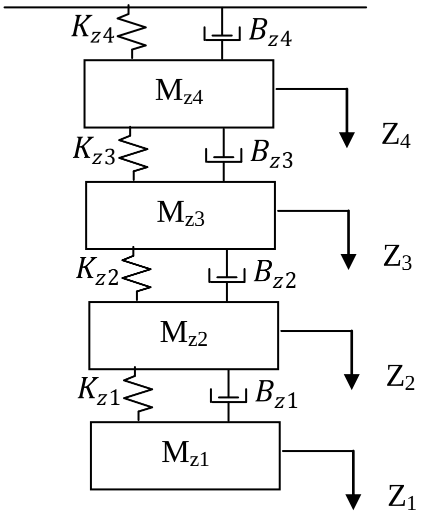

Figure 2.32: Measurement Space Dynamic Model for the 4DOF Manipulator Model

The measurement space is therefore a set of vertical axes at each of these locations and we can define the vector ***Z*** as the deflection along each of these axes.

$$\boldsymbol{Z} = \begin{bmatrix} Z_1 \\ Z_2 \\ Z_3 \\ Z_4 \end{bmatrix} \tag{2.46}$$

In order to identify the manipulators physical parameters, the vibration model must be transformed from the measurement space into joint space. The configuration dependent transformation Jacobian [TR] is the matrix that satisfies

$$\dot{\boldsymbol{Z}} = [TR] \begin{bmatrix} \dot{q}_1 \\ \dot{q}_2 \\ \dot{\rho} \\ \dot{q}_3 \end{bmatrix} \tag{2.47}$$

where $\dot{\boldsymbol{Z}}$ is a vector of measured deflection rates at the different measurement locations. The relationship [TR] can be identified from the dimensions given by Figure 2.33.

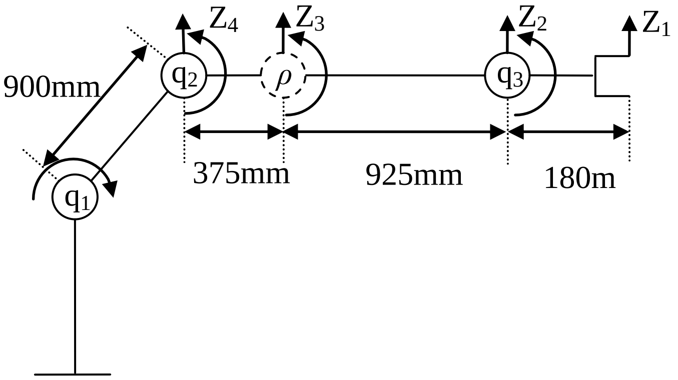

Figure 2.33: 4DOF Manipulator Joint and Measurement Space Axes

The measurement space mass ($\boldsymbol{M}_z$), stiffness ($\boldsymbol{K}_z$), and damping ($\boldsymbol{B}_z$) matrices can be approximated as functions of the manipulator joint space inertia ($\boldsymbol{D}$), stiffness ($\boldsymbol{K}_q$), and damping ($\boldsymbol{B}_q$) parameters defined in Section 2.2.1 and the transformation Jacobian [88].

$$\boldsymbol{M}_Z = [TR]^{-T}\boldsymbol{D}[TR]^{-1} \tag{2.48}$$

$$\boldsymbol{K}_Z = [TR]^{-T}\boldsymbol{K}_q[TR]^{-1} \tag{2.49}$$

$$\boldsymbol{B}_Z = [TR]^{-T}\boldsymbol{B}_q[TR]^{-1} \tag{2.50}$$

Now the eigenvalue problem in (2.28) can be solved using the transformed dynamic model and a LS optimisation can be used to fit the parameters. The approach taken did not rely on the linearity of the dynamics in the parameters. Instead the inertia matrix was reassembled from the mass and inertia values of each link using a configuration dependent inertia mapping matrix [ML]. For the vector of masses and inertias arranged as

$$\boldsymbol{m} = \begin{bmatrix} m_1 \\ I_1 \\ m_2 \\ I_2 \\ \vdots \\ m_n \\ I_n \end{bmatrix}, \tag{2.51}$$

the inertia mapping matrix is defined as the matrix that satisfies

$$\begin{bmatrix} \boldsymbol{D}(1,1) \\ \boldsymbol{D}(1,2) \\ \vdots \\ \boldsymbol{D}(2,1) \\ \vdots \\ \boldsymbol{D}(n,n) \end{bmatrix} = [ML]\boldsymbol{m} \tag{2.52}$$

The optimisation was performed using data from several different configurations to ensure that the determined parameters produced an accurate measurement space FRF for different configurations in the workspace. The error was defined as

$$\boldsymbol{E} = \begin{bmatrix} \boldsymbol{\lambda}_M - \boldsymbol{\lambda}_C \\ \boldsymbol{\psi}_M - \boldsymbol{\psi}_C \end{bmatrix} \tag{2.53}$$

where $\boldsymbol{\lambda}_M$ denotes a column vector of the eigenvalues identified with the circle fit, $\boldsymbol{\lambda}_C$ denotes a column vector of the eigenvalues of the fitted dynamic model, $\boldsymbol{\psi}_M$ denotes the column vector of concatenated mode shape column vectors identified by the circle fit, and $\boldsymbol{\psi}_C$ denotes the same vector for the fitted dynamic model. It was found that, as with the residual terms of (2.20), the sensitivity of the mode shape vectors was insufficient for the optimisation to fit them accurately. The optimisation was frequently affected to the point that the initial conditions were returned. Removing the eigenvectors from the error such that

$$\boldsymbol{E} = \boldsymbol{\lambda}_M - \boldsymbol{\lambda}_C \tag{2.54}$$

produces much better results for the overall fit and also for the eigenvalues.

The algorithm for the identification of the dynamic parameters can be summarised as:

1. Assemble the joint space mass ($\boldsymbol{D}$), damping ($\boldsymbol{B}_q$), and stiffness ($\boldsymbol{K}_q$) matrices from the initial conditions of each joint stiffness and damping value and each link mass and inertia using $[ML]$ and (2.52) and rearranging to generate $\boldsymbol{D}$.

2. Use the transformations in (2.48), (2.49), and (2.50) to determine the measurement space dynamic parameters $\boldsymbol{M}_z$, $\boldsymbol{B}_Z$, and $\boldsymbol{K}_z$.

3. Generate the measurement space dynamic model given by substituting $\boldsymbol{M}_z$, $\boldsymbol{B}_Z$, $\boldsymbol{K}_z$, $\boldsymbol{Z}$, $\dot{\boldsymbol{Z}}$, and $\boldsymbol{F}_z$ into (2.28), where $\boldsymbol{F}_z$ is a vector of forces acting on each of the measurement space axes.

$$\left(\begin{bmatrix} \boldsymbol{B}_z & \boldsymbol{M}_z \\ \boldsymbol{M}_z & \boldsymbol{0} \end{bmatrix} s + \begin{bmatrix} \boldsymbol{K}_z & \boldsymbol{0} \\ \boldsymbol{0} & -\boldsymbol{M}_z \end{bmatrix}\right) \begin{bmatrix} \boldsymbol{Z} \\ \dot{\boldsymbol{Z}} \end{bmatrix} = \begin{bmatrix} \boldsymbol{F}_z \\ \boldsymbol{0} \end{bmatrix} \tag{2.55}$$

4. Find the solution to the eigenvalue problem given by the characteristic equation of measurement space dynamic model (2.55).

5. Evaluate the squared error using the error value defined by (2.53) or (2.54).

6. Adjust the joint and link parameters based on the change in error and repeat until convergence to a minimum error value.

When fitting to multiple manipulator configurations simultaneously, steps 1-4 are repeated for all configurations and the error vectors generated in step 5 are simply concatenated for step 6.

Figure 2.34 shows the results of identifying the dynamic parameters with and without including the eigenvectors, thus showing the benefits of using (2.54) in place of (2.53).

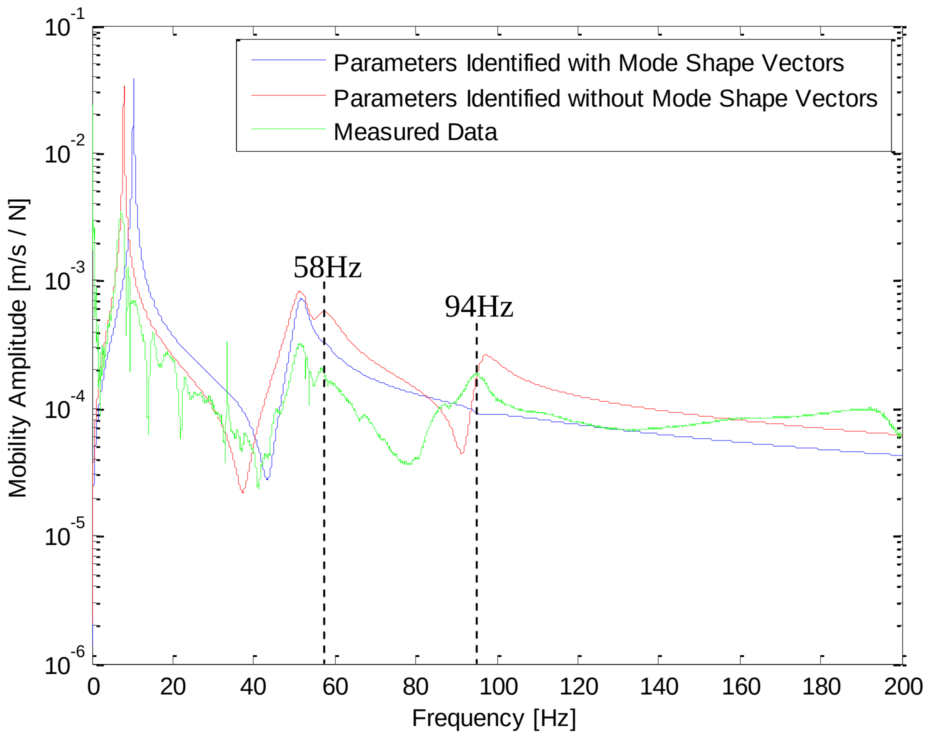

Figure 2.34: Reconstructed Mobility Amplitudes for Location 1 Excited at Location 2 using Parameters Identified by the Circle Fit Method with and without including Eigenvectors in the Parameterisation

Both reconstructed FRFs in Figure 2.34 are defined by

$$A_{u,v}(i\omega) = \sum_{p=1}^{P} \frac{-\bar{A}_{u,v}^{p}\omega^{2}}{-\omega^{2}+2\zeta^{p}\omega_{n}^{p}\omega i+\omega_{n}^{p\,2}} \tag{2.19}$$

where the modal parameters are all defined as described in Section 2.3.2 using the transformations in (2.48), (2.49), and (2.50). The amplitude of the curves has been adjusted in this figure so that the curves are superimposed in the region shown. Looking at the regions around 58 and 94Hz, the resonant peaks are missing from the reconstructed FRF that included the eigenvectors for parameterisation. This is due to the increased error in the model eigenvalues that causes the calculated peaks to be much more damped than their identified counterparts. As such it is desirable to ignore the eigenvalues in the parameterisation and focus instead on reducing the eigenvalue error by minimising the error given by (2.54) rather than by (2.53).

Although the fit was much better with the eigenvectors neglected from the parameterisation algorithm, the calculated eigenvectors, whatever they may be, are still necessary to generate the amplitude multipliers for an accurate for reconstruction of the Mobility FRFs. Figure 2.35 shows the effects of including and neglecting the amplitude multipliers on the FRF reconstruction using the dynamic parameters identified using (2.54). In the case where the calculated eigenvectors are neglected, the amplitude multipliers ($\bar{A}^{p}_{u,v}$) in (2.19) are reduced to unity.

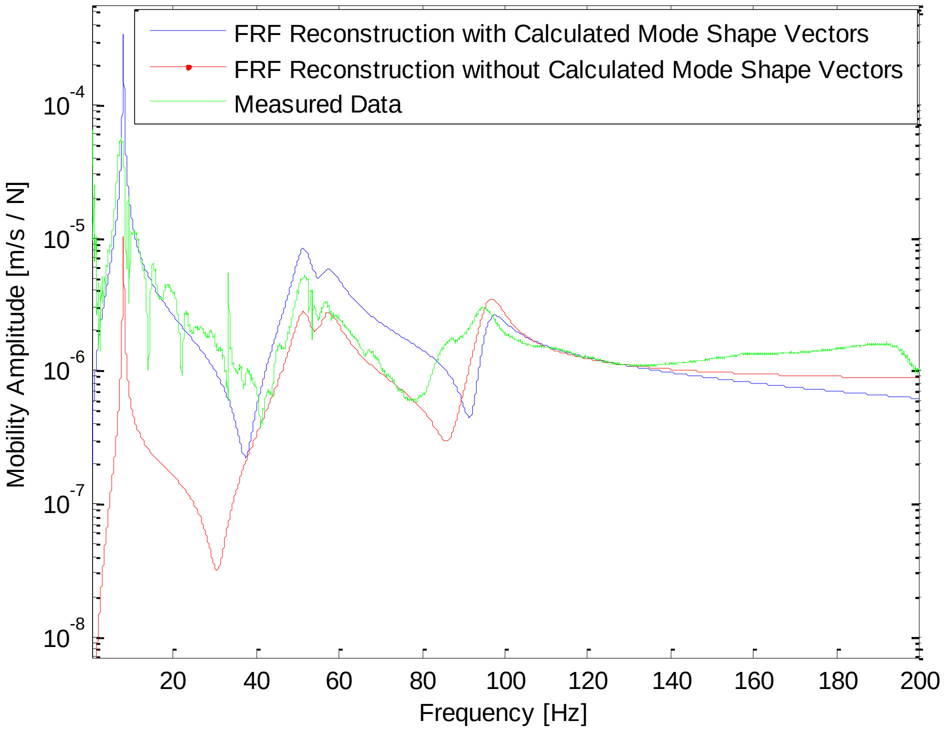

Figure 2.35: Reconstructed Mobility Amplitudes at Location 1 Excited at Location 2 using Parameters Identified by the Circle Fit Method without including Measured Eigenvectors and Reconstructed with and without Calculated Eigenvectors

Although the general shape of the curve is preserved, when the amplitude multipliers are neglected, the amplitude of the 8Hz peak is drastically reduced. With the amplitude multipliers included, the amplitude of the first peak is corrected. Therefore, although the identified eigenvectors are not used in the identification, it is necessary for the amplitude multipliers from the identified parameters to be included in the reconstruction of the Mobility FRFs to reproduce the amplitude of the first peak accurately.

Seven configurations were measured with high frequency resolution in order to provide large amounts of data for identification and to be robust to filtering. The location of the inertia, stiffness, and damping elements is such that changing the second joint angle with respect the first joint angle is equivalent to simply changing the base frame since for practical reasons the vibrations can only be measured normal to the second link. Similarly, changing the configuration of the third joint was undesirable as the response of the end-effector could only be measured normal to the third link. Changing the orientation therefore changed the nature of the signal being measured and was undesirable. The configurations measured and used for identification are shown in Table 2.5 and the definitions of the joint angles are given by Figure 2.36. Figure 2.37 and Figure 2.38 show the extended and retracted configurations respectively.

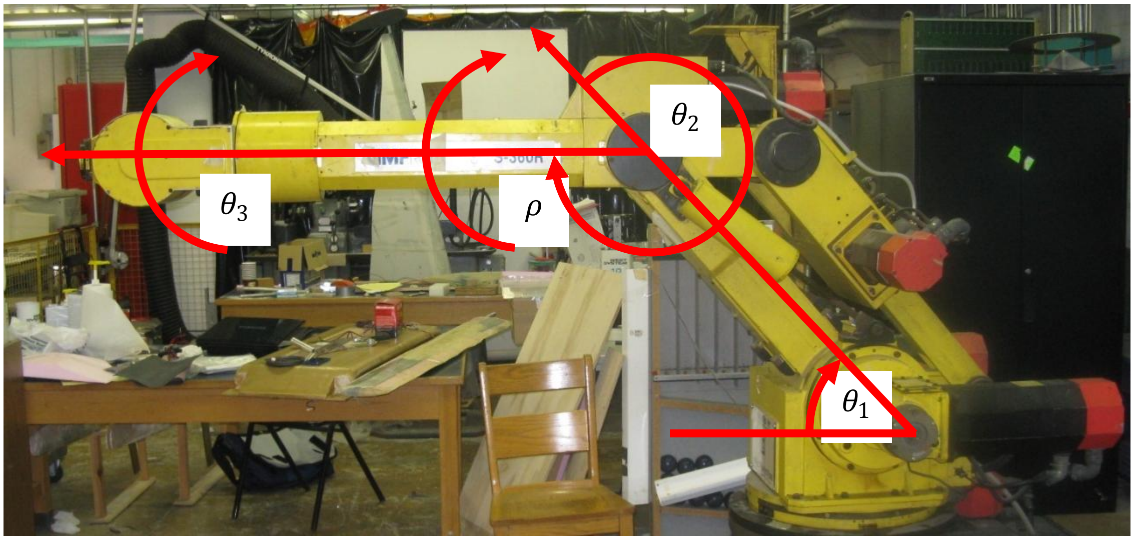

Figure 2.36: Manipulator Extended Configuration for Modal Analysis and Joint Angle Definitions

Table 2.5: Manipulator Configurations used for Experimental Parameter Identification and Verification

Configuration	First Joint Angle	Second Joint Angle	Pseudo-Joint Angle	Third Joint Angle
1	50^0	-50^0	0^0	0^0
2	70^0	-70^0	0^0	0^0
3	80^0	-80^0	0^0	0^0
4	90^0	-90^0	0^0	0^0
5	100^0	-100^0	0^0	0^0
6	110^0	-110^0	0^0	0^0
7	123^0	-123^0	0^0	0^0

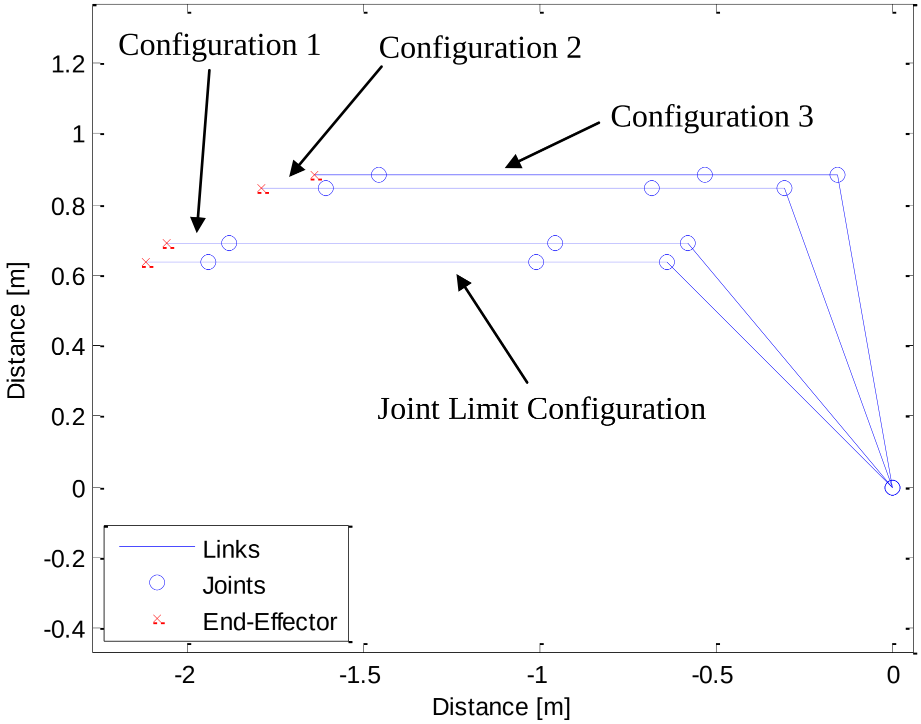

Figure 2.37: Skeleton Schematic of Extended Manipulator and Joint Limit Configurations

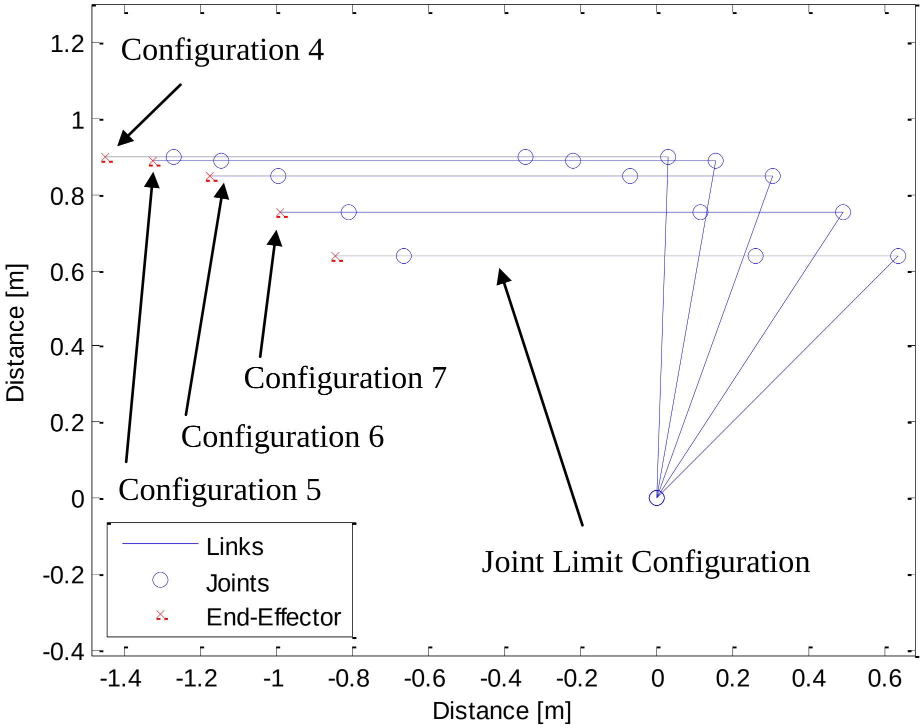

Figure 2.38: Skeleton Schematic of Retracted Manipulator and Joint Limit Configurations

Configurations 1 and 7, representing the largest and smallest first joint values, were fitted individually to find the dynamic parameters corresponding to each configuration and then fitted together to get a model that would span the configuration space. The identified parameters are given in Table 2.6, Table 2.7, and Table 2.8. The boundary and initial conditions used for the fit are given in Appendix D: .

Table 2.6: Identified Dynamic Parameters using the Modal Parameters Identified from the Location 1 Mobility Excited at Location 2 in Configuration 1

Link / Joint	Link Mass [kg]	Link Inertia [kgm^2]	Joint Stiffness [N/rad]	Joint Damping [Ns/rad]
1 /1	1.00	1.00	4.79×10^5	200.00
2.1 /2	1.00	20.33	8.88×10^5	200.00
2.2 /Pseudo	45.74	2.70	6.24×10^5	200.00
3 /3	1.00	1.60	3.94×10^5	17.79

Table 2.7: Identified Dynamic Parameters using the Modal Parameters Identified from the Location 1 Mobility Excited at Location 2 in Configuration 7

Link / Joint	Link Mass [kg]	Link Inertia [kgm^2]	Joint Stiffness [N/rad]	Joint Damping [Ns/rad]
1 /1	1.11	1.18	1.98×10^5	200.00
2.1 /2	1.19	3.49	6.03×10^5	200.00
2.2 /Pseudo	1.60	42.92	7.08×10^5	97.40
3 /3	2.23	4.70	5.56×10^5	124.21

Table 2.8: Identified Dynamic Parameters using the Modal Parameters Identified from the Location 1 Mobility Excited at Location 2 in both Configurations 1 and 7

Link / Joint	Link Mass [kg]	Link Inertia [kgm^2]	Joint Stiffness [N/rad]	Joint Damping [Ns/rad]
1 /1	1.48	1.59	5.03×10^5	1.00
2.1 /2	1.00	3. 84	2.63×10^4	104.07
2.2 /Pseudo	1.00	2.12	3.57×10^5	149.42
3 /3	1.00	2.10	3.36×10^5	1.00

The identified values for Table 2.6 and Table 2.7 do not show a strong correlation, indicating that these configurations will not share a common set of physical parameters and that the parameters in Table 2.8 will not provide an accurate fit to either configuration. However, when the eigenvectors are not restricted, as in this case, the solution found to satisfy the eigenvalue optimisation is not unique and finding a solution that meets the requirements of both configurations is possible. Figure 2.39 and Figure 2.40 show the reconstructed end-effector (Location 1) FRFs for Configurations 1 and 7 scaled to match the amplitudes of the measured FRFs at 126Hz with and without the amplitude multipliers included in the reconstruction. This frequency was selected since the effects of the resonant peaks are sufficiently reduced and the FRF sensitivity to frequency is much lower than in the earlier regions. The predictions and measured responses of the remaining configurations are given by Figure 2.41, Figure 2.42, Figure 2.43, Figure 2.44, and Figure 2.45. All reconstructions and predictions use the parameters found from both configurations combined given in Table 2.8.

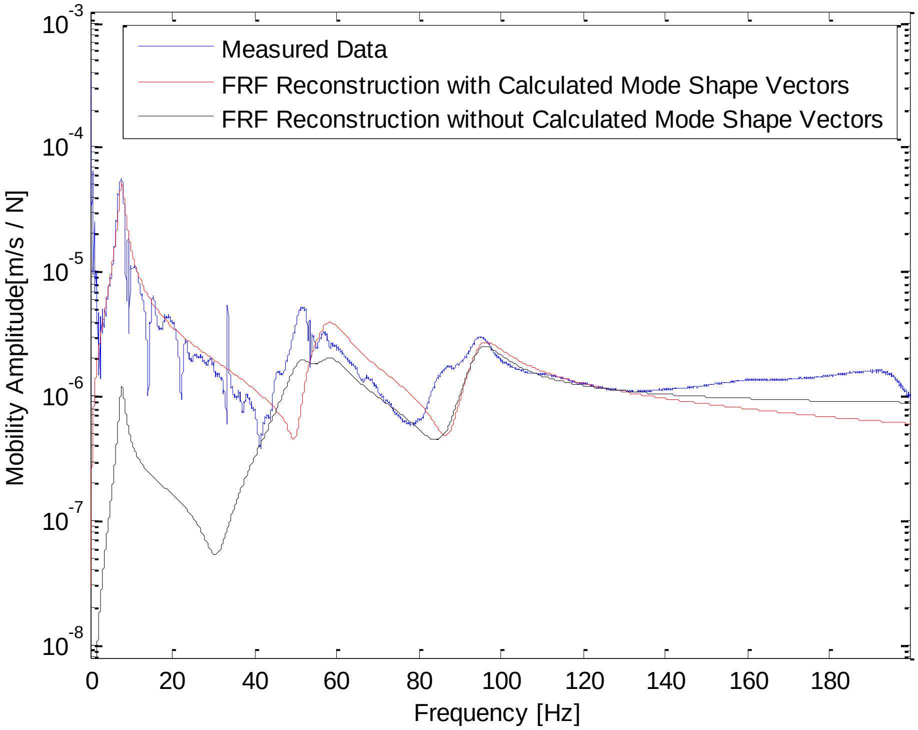

Figure 2.39: Mobility Amplitude for Location 1 Excited at Location 2 in Configuration 1 using a Parameterised Dynamic Model Reconstructed with and without Calculated Mode Shape Vectors

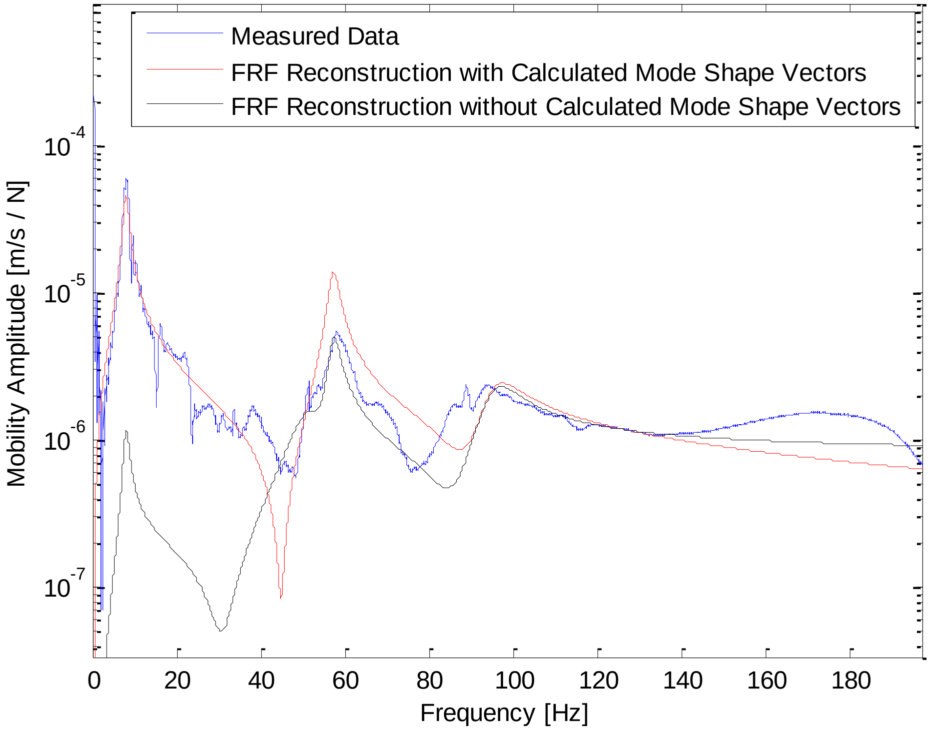

Figure 2.40: Mobility Amplitude for Location 1 Excited at Location 2 in Configuration 7 using a Parameterised Dynamic Model Reconstructed with and without Calculated Mode Shape Vectors

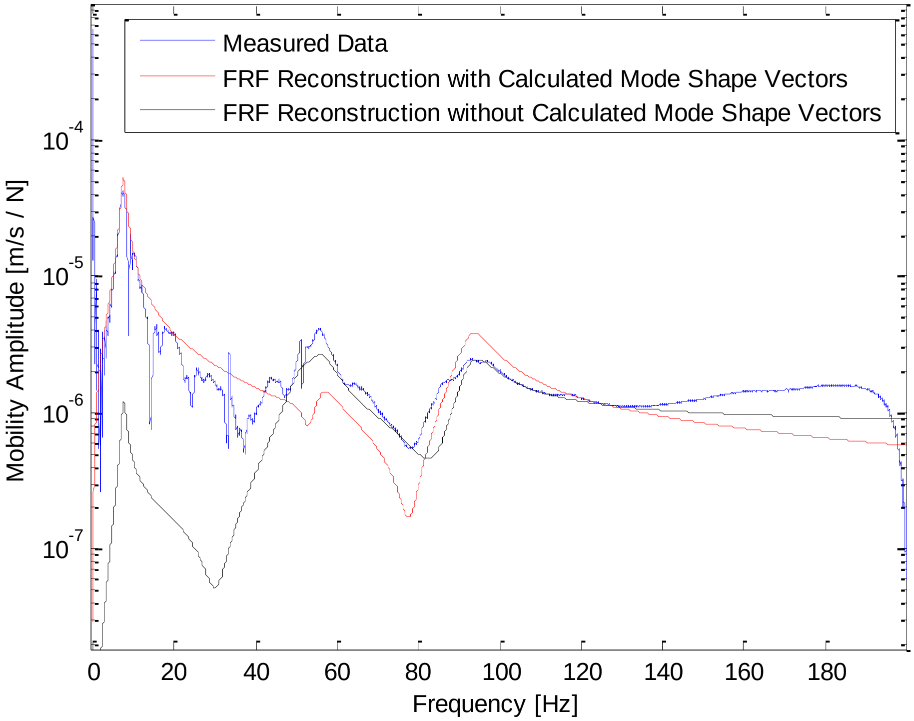

Figure 2.41: Mobility Amplitude for Location 1 Excited at Location 2 in Configuration 2 using a Parameterised Dynamic Model Predicted with and without Calculated Mode Shape Vectors

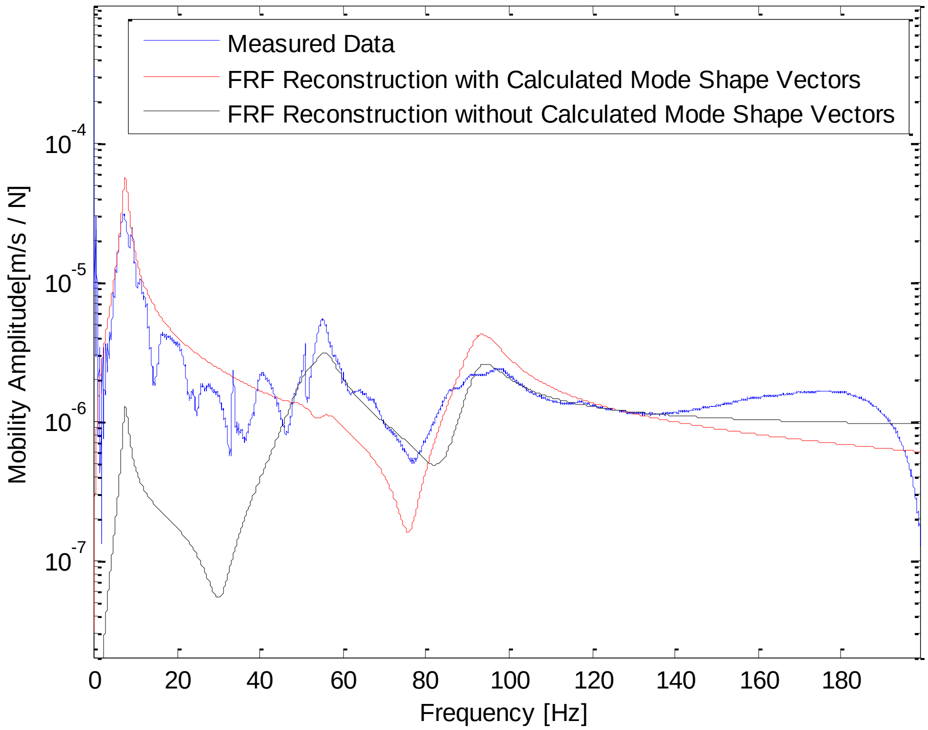

Figure 2.42: Mobility Amplitude for Location 1 Excited at Location 2 in Configuration 3 using a Parameterised Dynamic Model Predicted with and without Calculated Mode Shape Vectors

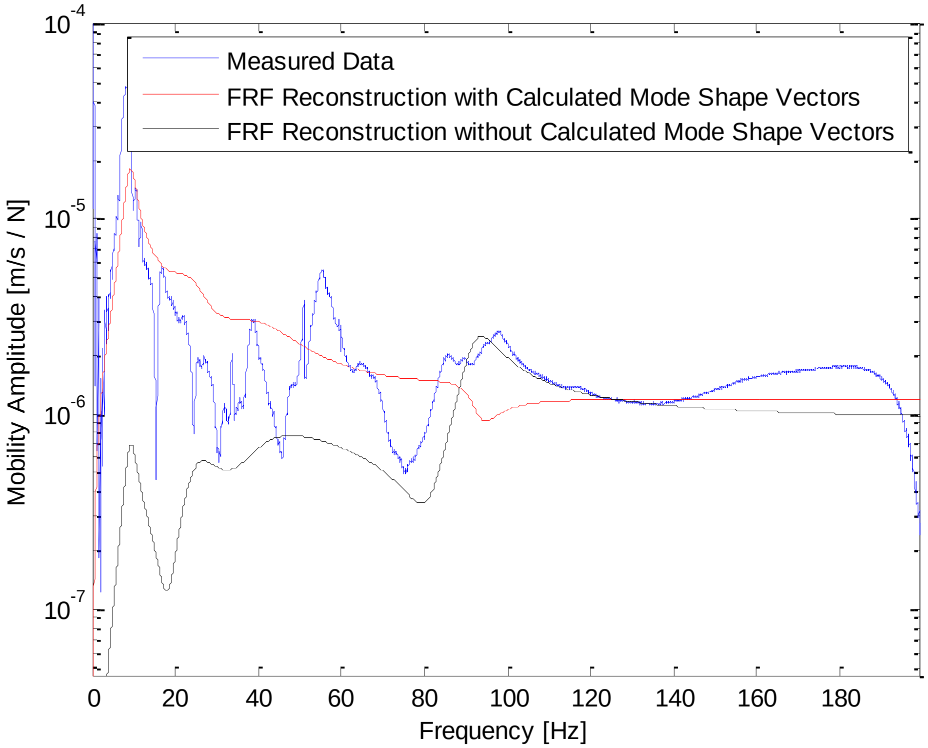

Figure 2.43: Mobility Amplitude for Location 1 Excited at Location 2 in Configuration 4 using a Parameterised Dynamic Model Predicted with and without Calculated Mode Shape Vectors

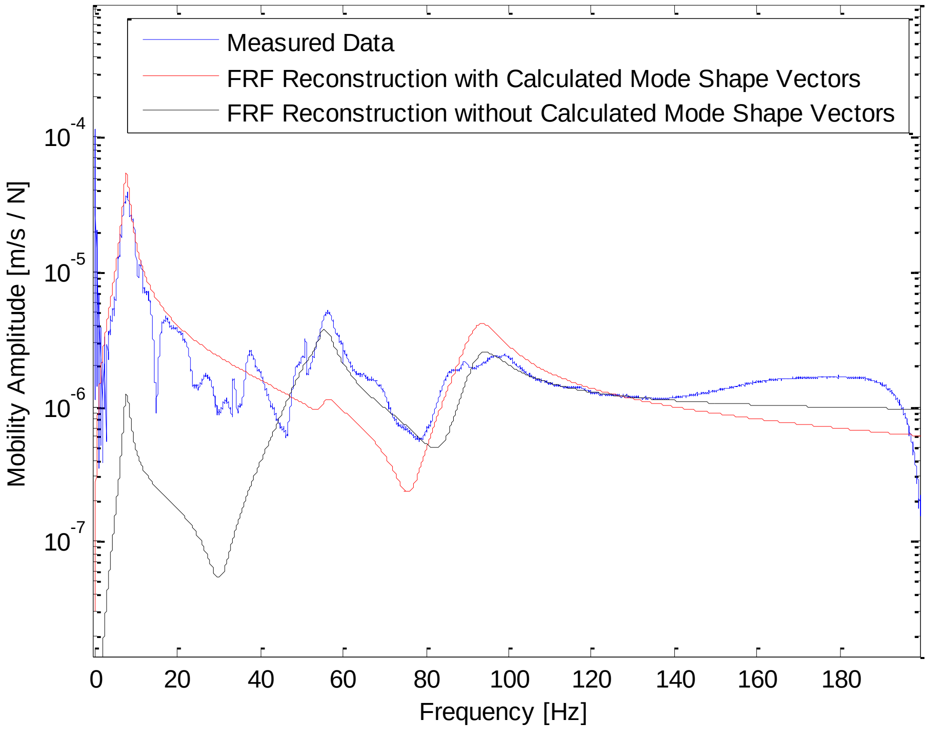

Figure 2.44: Mobility Amplitude for Location 1 Excited at Location 2 in Configuration 5 using a Parameterised Dynamic Model Predicted with and without Calculated Mode Shape Vectors

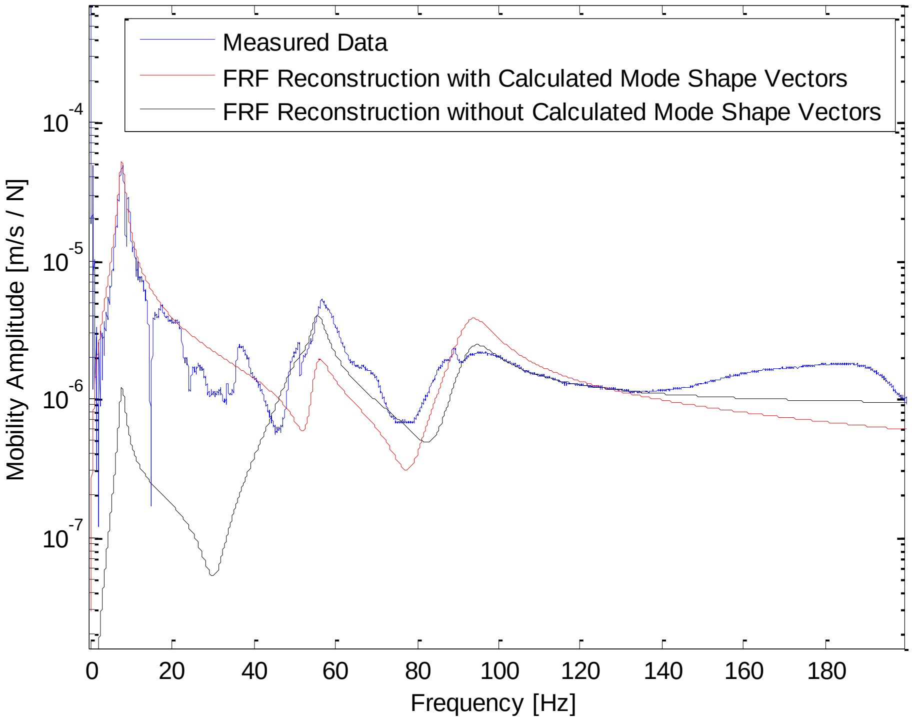

Figure 2.45: Mobility Amplitude for Location 1 Excited at Location 2 in Configuration 6 using a Parameterised Dynamic Model Predicted with and without Calculated Mode Shape Vectors

The amplitude multipliers necessary to accurately reproduce the first peak can be seen to have an adverse effect on the 51 and 58Hz peaks in all configurations. A piecewise model is therefore necessary to reconstruct the required amplitude of the first peak without negatively impacting the shape of the higher frequency peaks. For each configuration, excluding Configuration 4, the curves intersect at or close to the local minimum at approximately 46Hz. This is therefore an ideal place to concatenate the two models for any configuration since frequency domain identification for any configuration will identify an artificial local minimum at or very close to an actual local minimum. The identified parameters give accurate predictions for the measured data when considering a piecewise model that uses the amplitude multipliers for the region around the first peak and neglects them for the remainder of the FRF. The exception to this is configuration 4, which performs poorly in both cases. The cause of this is the loss of rank in the transformation Jacobian caused by the first link being aligned with the measurement axes. The resulting numerical error is sufficient to render the model ineffective in this region. Furthermore, the near-singular condition of the transformation Jacobian prevents this configuration from being parameterised individually. When optimising, a linear interpolation of amplitude will be necessary in this region in order to generate a more accurate reconstruction of the model.

In an attempt to generate a more accurate model of the system, Configurations 2 and 6 were added to the parameterisation. The parameters identified with all four configurations are given in Table 2.9.

Table 2.9: Identified Dynamic Parameters using the Modal Parameters Identified from the Location 1 Mobility Excited at Location 2 in Configurations 1, 2 ,6, and 7

Link/Joint	Link Mass [kg]	Link Inertia [kgm^2]	Joint Stiffness [N/rad]	Joint Damping [Ns/rad]
1 /1	1.19	2.00	5.59×10^5	1.00
2.1 /2	1.00	3.12	0.20×10^5	94.03
2.2 / Pseudo	1.00	1.16	1.99×10^5	107.58
3 /3	1.37	1.37	2.02×10^5	1.00

Comparing Table 2.9 to Table 2.8, there appears to be a strong correlation in the parameter trends and values, thus the reconstructions and predictions are likely to be very similar. Figure 2.46 shows the FRF prediction for Location 1 in Configuration 3, which was not used in either of the parameterisations, for both sets of identified parameters reconstructed with amplitude multipliers included and reduced to unity.

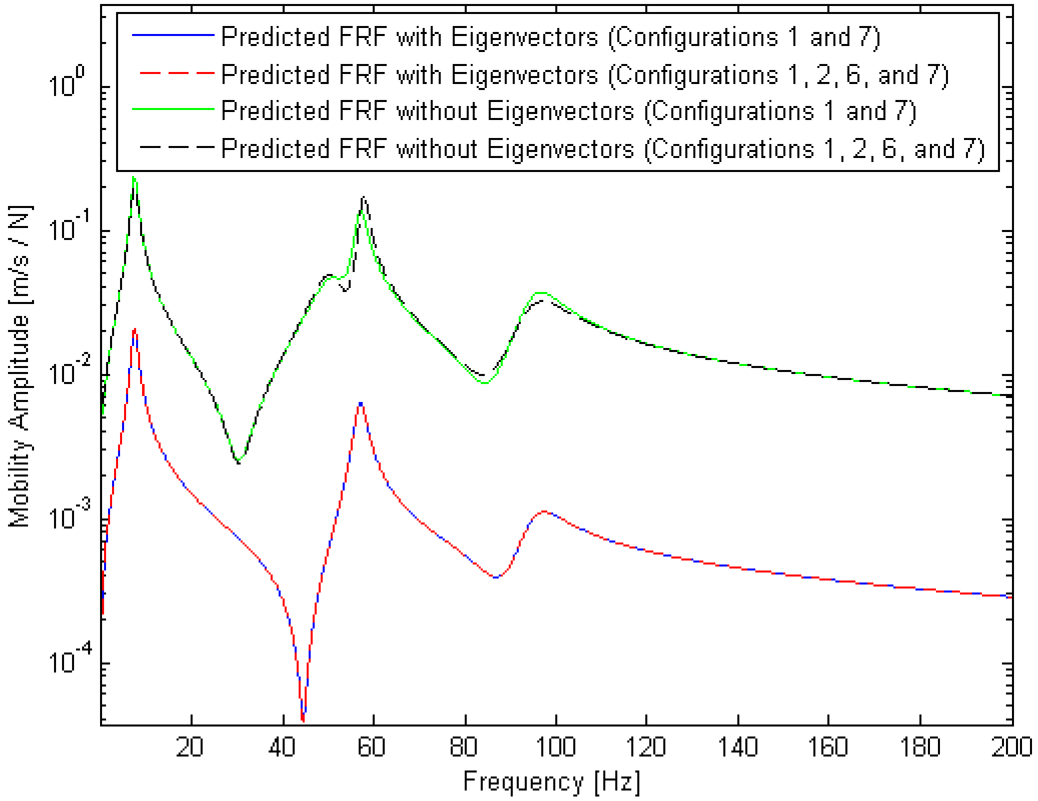

Figure 2.46: Mobility Amplitude for Location 1 Excited at Location 2 in Configuration 3 using a Dynamic Model Parameterised in both 2 and 4 Configurations Predicted with and without Calculated Mode Shape Vectors

It can be seen that the change in the FRF prediction is minimal when using the parameters identified using additional points. This is taken as further verification that the dynamic parameters in Table 2.8, while not physically meaningful, will provide an accurate prediction of the system response when entered into the linearised model given by (2.5) and transformed into the measurement model coordinate frame.

$$\boldsymbol{D}\ddot{\boldsymbol{q}}_D + \boldsymbol{B}_q\dot{\boldsymbol{q}}_D + \boldsymbol{K}_q\boldsymbol{q}_D = \boldsymbol{J}^T\boldsymbol{F} \tag{2.5}$$

2.7 Summary

In the preceding chapter a dynamic model has been developed based on the trends and characteristics found in the literature for modelling the dynamics of industrial manipulators. The model assumes flexible joints and rigid links since the majority of flexibility in industrial manipulators has been shown to be caused by the harmonic drives in the joints. The deflection characteristics of harmonic drives have been found to be extremely complex by a number of authors. However, there is little agreement on how these characteristics should be modelled. Linear springs were therefore selected to allow the linearization of the model and the model was linearised about a zero velocity operating point, which removed the nonlinear dynamic terms entirely and left the remaining terms unaffected. The linearization was necessary to allow for parameterisation by modal analysis since other potentially viable identification techniques could not be implemented. For simplicity, and to maintain the linearity of the model, viscous friction was deemed sufficient to capture the dynamics of the system.

Another potential error in the model is the rigid link assumption. In order to compensate for potential flexibility in the links, the linearised model was expanded through the addition of a pseudo-joint so that any flexibility in the links could be approximated while maintaining the rigid-link flexible-joint assumption and a low DOF model. Following the development of the model, a qualitative evaluation of the data was made to determine the effects of nonlinear dynamics and components, identify the link flexibilities, and gain an intuitive understanding of the systems dependence on configuration. The effects of nonlinear stiffness elements could be seen from the change in the response with different force input amplitudes. The changes in the anti-resonance amplitudes at low frequencies indicated the presence of both hardening and softening springs. The flexibility of the links was investigated for the first two links using an approximated peak picking method. It was determined that the first link could be assumed rigid due to the parallel mechanism of the physical robot despite the obvious deformation occurring along the length of the beam. The second link flexibility could not be neglected due to its significant contribution to the overall manipulator mode shape. However, only a single frequency was found to be affected by these characteristics and the deformation shape was a simple bending deflection. Therefore the flexibility was modelled by a single pseudo-joint on the link.

With the qualitative investigation completed, the manipulator was again struck with an impact hammer in several configurations and the modal parameters were identified using a circle fit technique. A least squares parameterisation was then used to identify the dynamic parameters of the manipulator by matching the eigenvalues of the measurement space system with the identified modal parameters. The identification was repeated with data from additional configurations and showed correlation in both the absolute and relative values. Further verification was seen by using the identified parameters to reconstruct the FRFs used in the identification and to predict those not used. The reconstructed and predicted FRFs were found to be accurate over different frequency ranges depending on the inclusion or exclusion of the amplitude multipliers in the generated FRF. It was therefore determined that a piecewise model could be used with a boundary located so that the artificial minimum created by switching model sections would coincide with an actual local minimum in the frequency domain.

Chapter 3 Optimisation Results and Simulations

3.1 Introduction

There are several optimisation strategies for finding solutions to nonlinear multi-input problems [101, 102]. The simplest solution is to use hill-climbing methods. These are methods that look at minimising an objective function by following the gradient to a minimum. Examples of this are the Cauchy method of steepest descent, the downhill simplex method, and Powell's direction set method [102]. The simplest of these, the Cauchy method, is also the one which requires the most information. In this case the gradient function needs to be known for the method to be implemented. Tuning of hill-climbing optimisations is done with a gain to determine the rate of traverse along the gradient. In order to descend to a minimum, this gain must be negative. Increasing the gain amplitude and therefore the step size too much may cause the solution to skip over one minimum and approach another if the solution space has a relatively steep gradient. This can be avoided by adjusting the optimisation gain based on the step size or the iteration number, or by limiting the step size to a value considered to be safe. There are several drawbacks to hill-climbing techniques. Firstly, the results for a multi-modal system are dependent on the initial conditions since there is no way for the solution to recognise or escape from a local minimum when correctly implemented with the appropriate gains and without additional guidance from a higher level optimisation algorithm. When dealing with tightly spaced local minima, it is difficult to find initial values to correctly identify a global minimum without prior knowledge of the system even when using a higher level guiding algorithm such as genetic algorithms or simulated annealing is used. These are known as directed random searches since they randomly search the workspace for solutions, but also incorporate a form of memory and volatility control to narrow the available solution space as they progress. The problem of identifying only local minima is further amplified when using an unguided random search algorithm, such as simply using multiple arbitrary starting solutions, since there is no guarantee that any of the initial conditions will eventually lead to the global minimum. Secondly, for a discontinuous function, the gradient is only piecewise defined requiring the optimisation to be repeated for all sections and then compared to identify the global optimisation. This again does not guarantee a global solution unless each section of the function is convex[3]. Thus, for a global optimisation, hill-climbing methods, while quick and easy to implement, will not necessarily find the best solution.

Although there are powerful optimisation tools available for finding solutions to optimisation problems, such as genetic algorithms, simulated annealing, and neural networks, they require substantial effort to implement and time to execute. The problem of posture optimisation for the Fanuc S-360 manipulator has only a single DOF when restricted to move in a single axis, as was the case in the parameter identification. Thus global search algorithms are excessive and unlikely to improve the results. The likelihood of multiple extrema is high, but the number of local extrema will also likely be very low so the global minimum can be found from a gradient-descent hill-climbing method using an undirected random search as a higher level algorithm. The random search algorithm is simply to repeat the gradient-descent at several points in the workspace in order to identify a small set of local minima which can be quickly compared to find a global minimum.

3.2 Configuration Optimisation

3.2.1 Configuration Optimisation Procedure

When excited at a known frequency, the configuration of an industrial manipulator can be optimised such that the receptance is minimised at the end-effector. This corresponds to Location 1 for the measurement space points on the manipulator. A gradient-descent algorithm was developed in the subset of the workspace defined by maintaining horizontal second and third links and keeping the first joint within the physical joint limits. Restricting the movements of the manipulator this way produced configurations that fell within the expected accurate range of the parameterised model.

The optimisation uses the symmetric difference quotient

$$\frac{\partial \alpha_q(i\omega)}{\partial q_1} = \frac{\alpha_q(i\omega)\big|_{\substack{q_1=\bar{q}_1+dq \\ q_2=\bar{q}_2-dq}} - \alpha_q(i\omega)\big|_{\substack{q_1=\bar{q}_1-dq \\ q_2=\bar{q}_2+dq}}}{2dq} \tag{3.2}$$

where $\bar{q}_1$ and $\bar{q}_2$ are the current first and second joint angles, dq is a small change in q_1 and q_2, and $\alpha_q(i\omega)$ is the predicted Location 1 drive point receptance. The second link is held

---

[3] A function is said to convex if it contains only a single extremum that is a minimum

horizontal by adjusting q_2 such that it changes an equal amount to q_1 in the opposite direction. Therefore the derivative is found by considering the effects of the second joint rotation as well as the first joint rotation. The third joint does not need to be adjusted to maintain the horizontal condition and so it is maintained at zero throughout the optimisation. The Location 1 receptance is used as the objective function and is approximated by the absolute value of

$$\alpha_q(i\omega) = \sum_{p=1}^{4} \frac{\bar{A}_{1,1}^{p}}{(i\omega - \lambda_p)} + \frac{\bar{A}_{1,1}^{p*}}{(i\omega - \lambda_p^{*})} \tag{3.3}$$

This uses only a subset of the eigenvectors corresponding to the receptance of the end-effector (Location 1) at each frequency, with the eigenvectors and eigenvalues calculated as outlined in Section 2.3.2 in Chapter 2. When the excitation frequency is above 46Hz, the amplitude multiplier is reduced to unity for improved model performance as determined in Section 2.6.4. The configuration is updated using the derivative of the objective function to generate a velocity command and position update scheme

$$\dot{\boldsymbol{q}} = k_v \begin{bmatrix} \frac{\partial \alpha_q(i\omega)}{\partial q_1} \\ \frac{-\partial \alpha_q(i\omega)}{\partial q_1} \\ 0 \end{bmatrix} \tag{3.4}$$

$$\boldsymbol{q} = \bar{\boldsymbol{q}} + \dot{\boldsymbol{q}}dt \tag{3.5}$$

where $\bar{\boldsymbol{q}}$ is the vector of current joint angles, $\dot{\boldsymbol{q}}$ is the vector of joint velocities, k_v is a velocity gain, and dt is a time increment.

3.2.2 Configuration Optimisation Results

A joint angle sweep of the first joint was performed on the objective function at an operating frequency of 8Hz. As was noted in Section 2.6.4, a piecewise model is needed to capture the amplitude of the peaks relative to each other with the lower frequency section of the model using the calculated mode shape vectors and the higher frequency section neglecting them. At 8Hz the calculated mode shape vectors are included in the model. The range of the first joint is from 45 to 135 degrees corresponding to fully extended and fully retracted respectively. It was found that the function had a single minimum at this frequency as shown in Figure 3.1 where Configurations 1-7 are labelled as C_{1-7}.

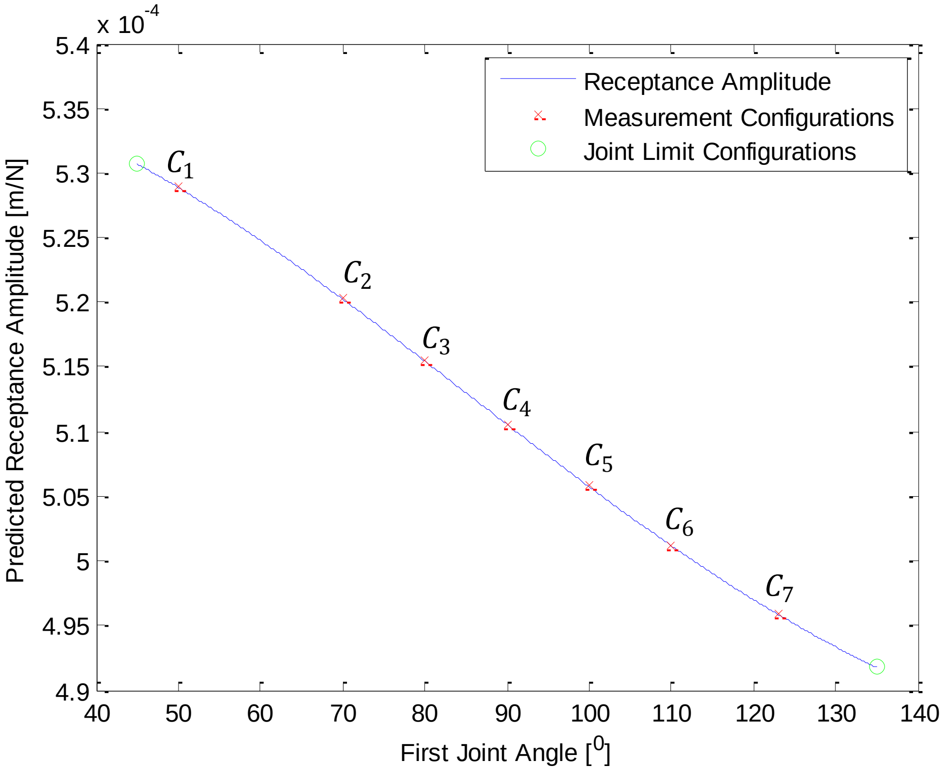

Figure 3.1: Location 1 Drive Point Receptance Amplitude Prediction as a Function of First Joint Angle at 8Hz

The optimisation was then performed beginning at each of the configurations used for identification and verification of the dynamic model in the previous chapter listed in Table 2.5. Table 3.1 shows the results for the optimisation at the first resonant peak verifying the gradient-descent optimisation.

Table 3.1: Configuration Optimisation Results for Location 1 Drive Point Receptance at 8Hz at Various Initial Conditions

Configuration	q_1 Start Point [^{0}]	q_1 End Point [^{0}]
1	123	135
2	110	135
3	100	135
-	92[4]	135
-	88	135
5	80	135
6	70	135
7	50	135

---

[4] The model cannot be evaluated at 90^0 since the transformation Jacobian [TR] is singular at that configuration and therefore an interpolation between 88^0 and 92^0 is used when generating a single objective function value in that range

From Figure 3.1 it can be seen that the manipulator is retracting as far as possible at the first resonance and meeting the maximum joint limit at 135^0. This resonance was previously identified as being heavily dominated by the deflection in the second joint, which is a property of the joint and therefore not configuration dependent. However, there is also a contribution from the first joint deflection that can be minimised through configuration optimisation. When fully extended, the entire mechanism deforms in the same direction and therefore the amplitude of the first link is added to that of the second link. In the retracted configuration, the rotation of the first link reduces the overall deflection by rotating the second link. The results can therefore be said to match the expected dynamics of a manipulator of the form used in the model. However, when compared to the experimental results in Table 3.2 it can be seen that the prediction results using the identified model are not accurate and that the trend cannot be verified. The experimental values were determined by integrating the measured inertance in the frequency domain as in (2.11) in Section 2.3.1.

Table 3.2: Predicted and Measured Location 1 Drive Point Receptance at 8Hz at Various Configurations

Configuration	q_1 [^{0}]	Prediction [m/N]	Measurements [m/N]
-	45	5.31×10^{-4}	-
1	50	5.29×10^{-4}	7.03×10^{-6}
2	70	5.20×10^{-4}	8.59×10^{-6}
3	80	5.16×10^{-4}	5.99×10^{-6}
4	90	5.11×10^{-4}	1.33×10^{-5}
5	100	5.06×10^{-4}	1.04×10^{-5}
6	110	5.01×10^{-4}	1.204×10^{-5}
7	123	4.96×10^{-4}	1.62×10^{-5}
-	135	4.92×10^{-4}	-

The majority of this error comes from the slight differences in the resonant frequencies between the configurations. This has a large impact on the measured data for the 8Hz peak since the peak is lightly damped and the amplitude is very sensitive to frequency in the immediate region. The small shifts in the frequency were not captured by the circle fit parameterisation, but can be seen from the peak frequency discrepancy between Configurations 1 and 6 in Figure 3.2. These configurations were selected as they display the characteristic occurring at this frequency.

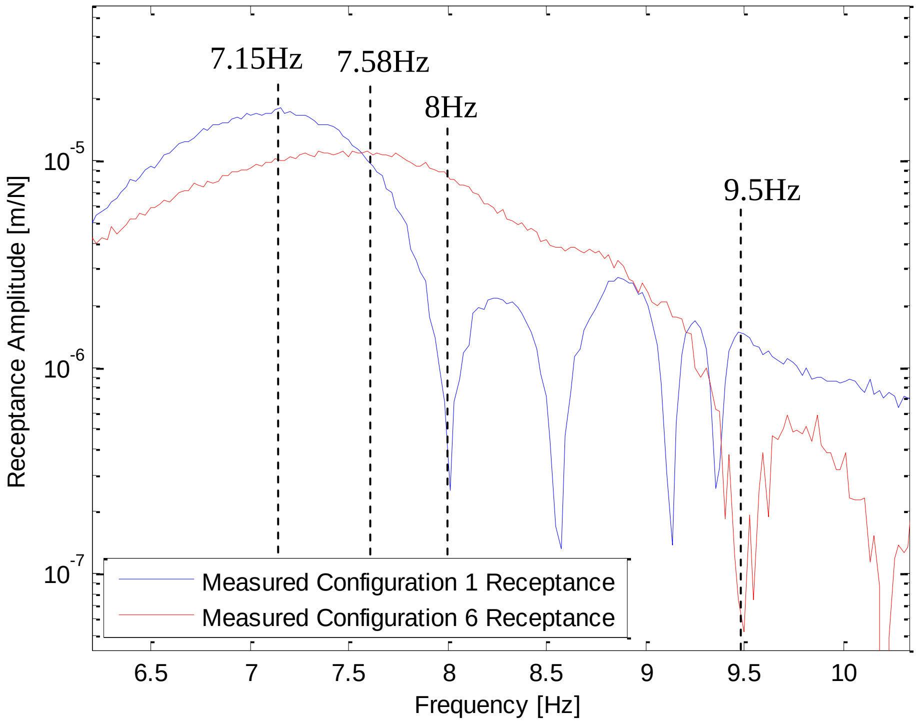

Figure 3.2: Measured Location 1 Drive Point Receptance Amplitude for Configurations 1 and 6 around 8Hz

It can be seen from Figure 3.2 that at 7.58Hz the amplitude of the Configuration 1 FRF is sufficiently reduced to suggest that the peak value is less than that of the Configuration 6 FRF. However, when each is observed at its own local maximum, the Configuration 1 FRF is clearly of greater amplitude. In addition, at 8Hz an un-modelled anti-resonance is further reducing the amplitude of the Configuration 1 FRF making the numerical response much lower than the model will predict. The opposite phenomenon occurs at 9.5Hz, where the Configuration 6 FRF shows a noisy anti-resonance characteristic that will not be captured by the prediction and the Configuration 1 FRF shows a slight resonance.

The frequency inconsistency is further compounded by varying damping ratios and the presence of smaller anti-resonances that cause the FRFs to become highly volatile. Investigating the frequency up to 46Hz, at which point the effects of the following peaks begin to show on the FRFs of some configurations, shows a response that is still dominated by the 8Hz peak and is therefore still predicted with the amplitude multipliers included. The sensitivity of the FRF to frequency is now much lower due to the distance from the resonant peak and therefore the relevance of signal volatility is greatly increased. Verification of optimisation in this frequency range encounters a similar problem to that of the 8Hz optimisation in that the separation between the curves is insufficient to produce a clear optimal configuration due to the smaller resonances and anti-resonances in the measured data. This can best be seen from the measured and predicted mobility for Configurations 1 and 5 in the range of the first peak as shown by Figure 3.3.

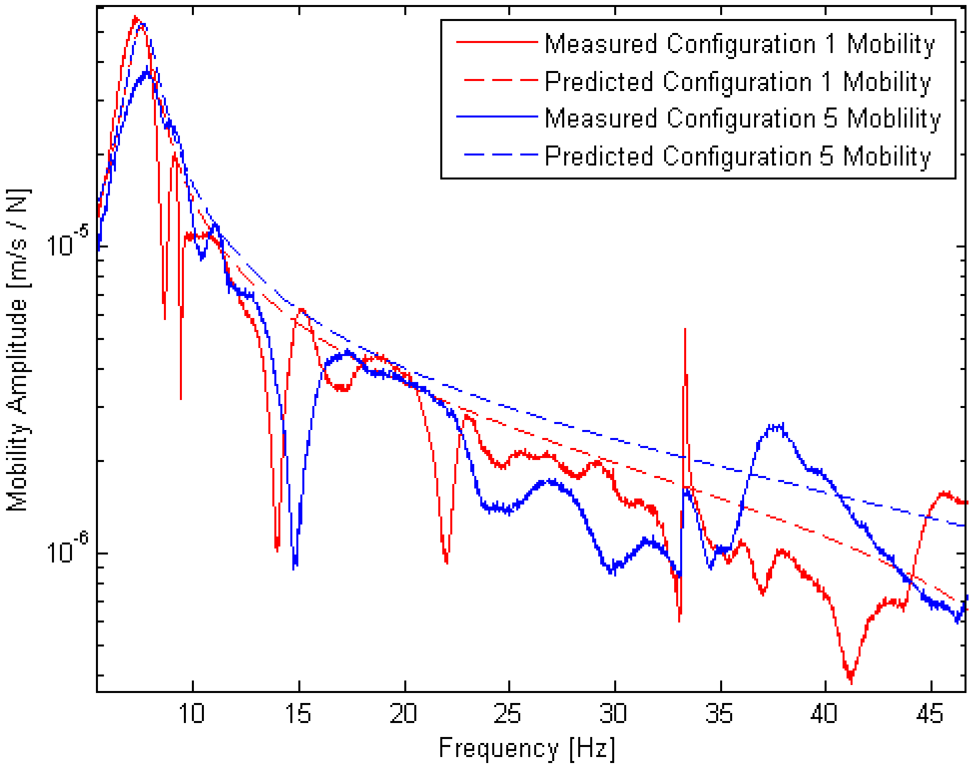

Figure 3.3: Volatility of Measured Location 1 Drive Point Receptance Amplitude for Configurations 1 and 5 up to 45Hz

The measured data shows that a direct comparison over the frequency range of the amplitude multiplier model is not plausible due to the volatility of the frequency response in this region. The model is not detailed enough to capture the full dynamics of the manipulator and so when the amplitudes are very similar, these additional dynamics become dominant for configuration selection. A configuration optimisation based on a low DOF dynamic model in this region is therefore unfeasible given the volatility of the response and modelling such turbulent behaviour present a formidable task. Thus, any accurate prediction in this region will be based on measured data rather than a linearised and transformed dynamic model.

At higher frequency, the shape of the FRF becomes more relevant. Looking at the 50-60Hz region, the amplitude is more strongly dependent on configuration and less volatile at the peaks. The configuration optimisations for 53 and 58Hz are shown in Figure 3.4 and Figure 3.6, and the measured receptance curves are shown in Figure 3.5 and Figure 3.7.

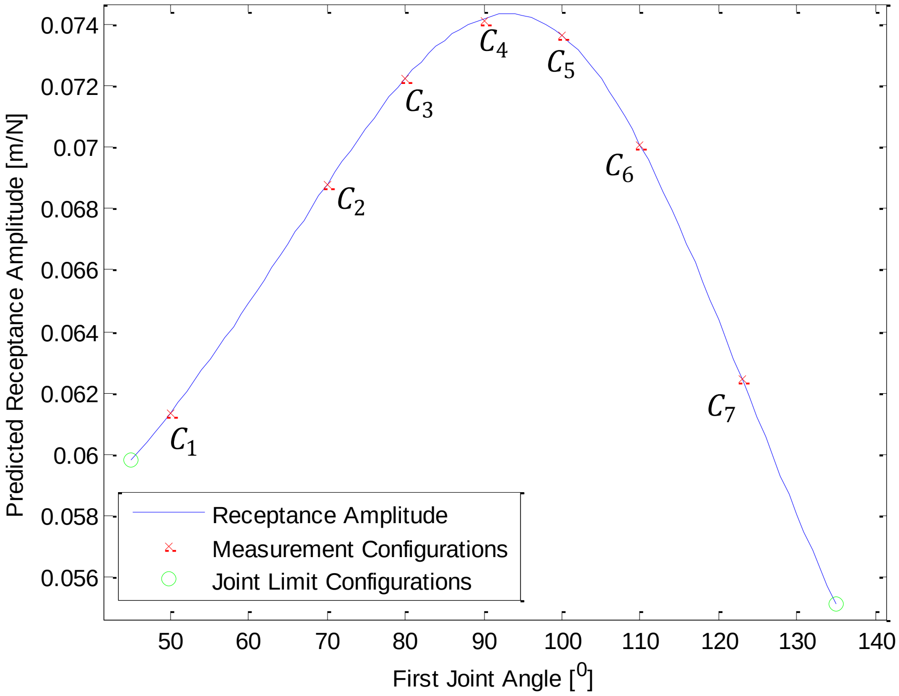

Figure 3.4: Location 1 Drive Point Receptance Amplitude Prediction as a Function of First Joint Angle at 53Hz

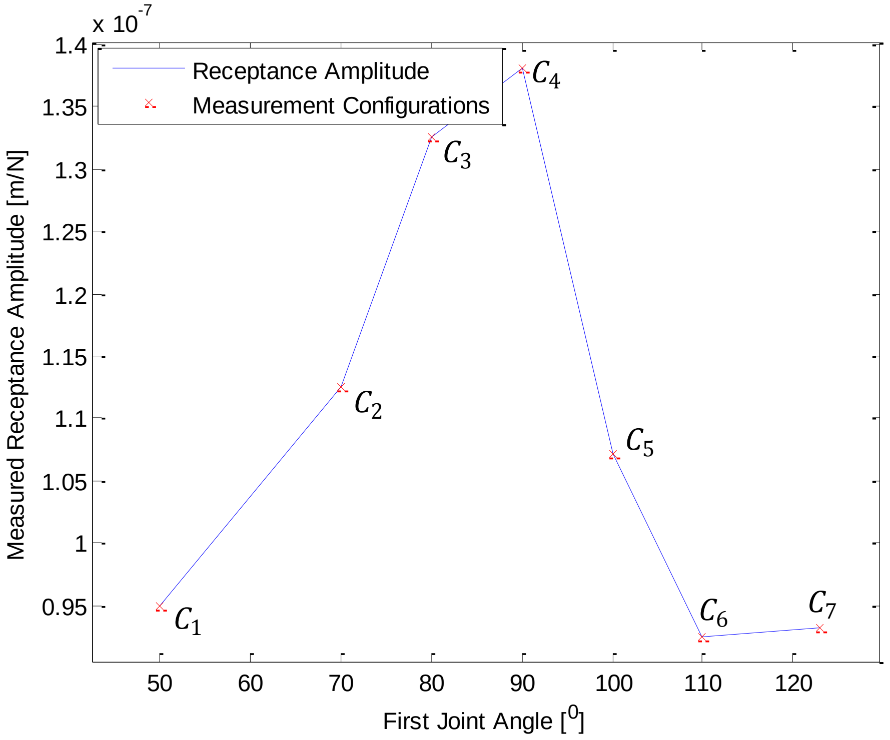

Figure 3.5: Location 1 Drive Point Receptance Amplitude Measurements at Various First Joint Angle Values at 53Hz

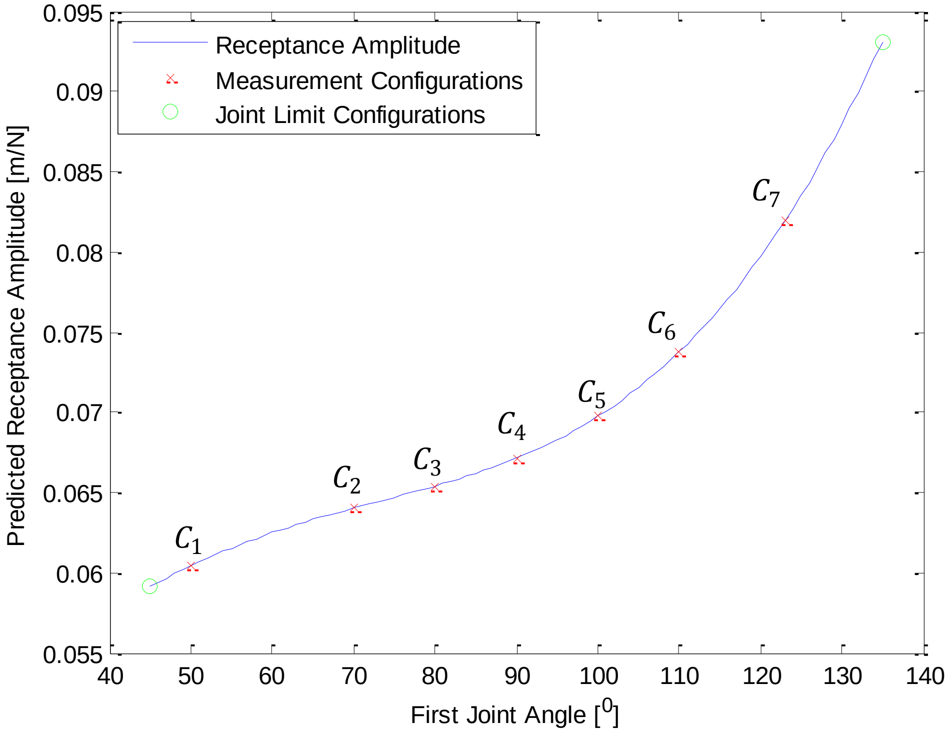

Figure 3.6: Location 1 Drive Point Receptance Amplitude Prediction as a Function of First Joint Angle at 58Hz

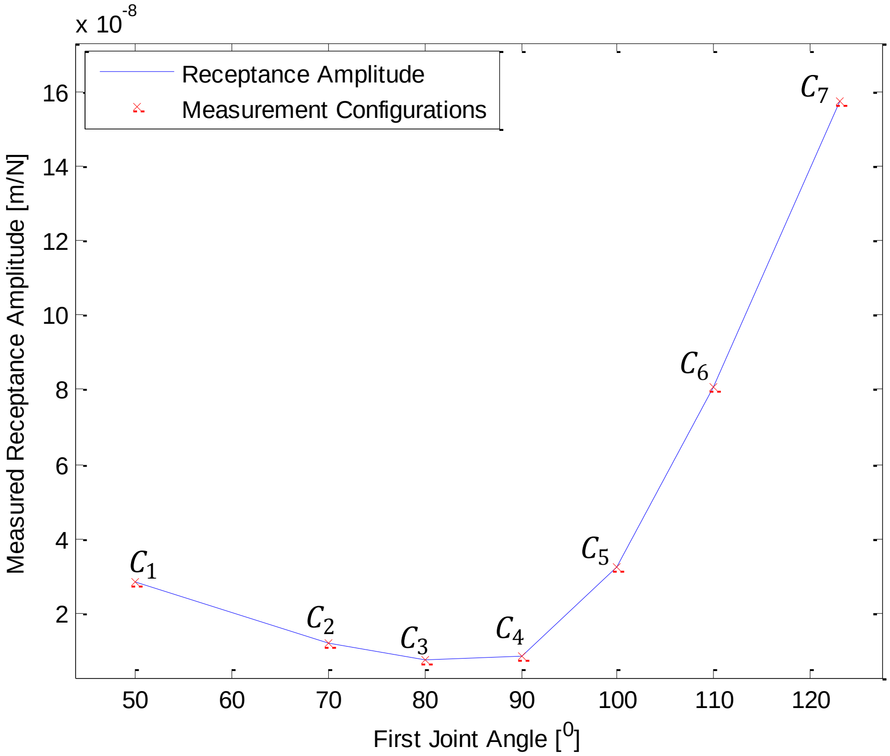

Figure 3.7: Location 1 Drive Point Receptance Amplitude Measurements at Various First Joint Angle Values at 58Hz

The predictions perform much better in this frequency range than previously, although the amplitudes are several orders of magnitude higher for the predicted receptance curves. This is expected given that the true amplitude data is contained in the true eigenvectors, which could not be identified experimentally. Disregarding the numerical values, the trends are very similar. At 53Hz, Figure 3.4 shows that the optimisation will try to avoid the upright configuration (Configuration 4) and attempts to move away from this configuration toward either one of the joint limits. This is supported by the experimental data in Figure 3.5, with the exception of the most retracted configuration (Configuration 7) which shows a slight increase in receptance. At 58Hz, Figure 3.6 shows that the predicted receptance optimises to the fully extended configuration as a global minimum. The FRF shows a minimum gradient at around 85^0, but there is no local minimum present. The measurements in Figure 3.7 show a similar trend with the exception that the minimum gradient becomes a shallow local minimum. Although the prediction does not accurately identify the local minimum at approximately 85Hz it successfully identifies the retracted configuration as significantly more responsive than the majority of the curve. The predicted and measured receptance values are given in Table 3.3.

Table 3.3: Predicted and Measured Location 1 Drive Point Receptance Amplitude Values at 53 and 58Hz at Various Configurations

Configuration	q_1 [^{0}]	53Hz Prediction [m/N]	53Hz Measurements [m/N]	58Hz Prediction [m/N]	58Hz Measurements [m/N]
-	45	5.98×10^{-2}	-	5.92×10^{-2}	-
1	50	6.14×10^{-2}	9.49×10^{-8}	6.04×10^{-2}	2.84×10^{-8}
2	70	6.88×10^{-2}	1.13×10^{-7}	6.40×10^{-2}	1.20×10^{-8}
3	80	7.22×10^{-2}	1.33×10^{-7}	6.54×10^{-2}	7.43×10^{-9}
4	90	7.41×10^{-2}	1.38×10^{-7}	6.71×10^{-2}	8.37×10^{-9}
5	100	7.36×10^{-2}	1.07×10^{-7}	6.98×10^{-2}	3.24×10^{-8}
6	110	7.01×10^{-2}	9.25×10^{-8}	7.38×10^{-2}	8.06×10^{-8}
7	123	6.25×10^{-2}	9.32×10^{-8}	8.19×10^{-2}	1.57×10^{-7}
-	135	5.52×10^{-2}	-	9.31×10^{-2}	-

It is desirable to extend the model outside of the identification range toward and into machining frequencies, which begin at around 18,000rpm (300Hz) for softer metals such as aluminium [71]. High speed fluting performed by Matsuoka *et al.* [20] used a spindle speed of 100,000rpm, which corresponds to approximately 1700Hz. It should be noted here that the spindle speeds of machine tools do not directly convert to excitation frequency and need to be multiplied by the number of teeth on the cutting tool. For a four tooth cutting tool with spindle speed of 300Hz, the excitation frequency of the cutting forces would therefore be 1200Hz. Table 3.4 shows the predicted receptance values for higher frequency operation.

Table 3.4: Predicted Location 1 Drive Point Receptance Amplitude at Higher Frequencies at Various Configurations

Configuration	q_1 [^{0}]	500Hz Prediction [m/N]	1000Hz Prediction [m/N]	1500Hz Prediction [m/N]
-	45	2.29×10^{-3}	1.28×10^{-3}	8.50×10^{-4}
1	50	2.29×10^{-3}	1.28×10^{-3}	8.50×10^{-4}
2	70	2.28×10^{-3}	1.28×10^{-3}	8.50×10^{-4}
3	80	2.28×10^{-3}	1.28×10^{-3}	8.50×10^{-4}
4	90	2.28×10^{-3}	1.28×10^{-3}	8.50×10^{-4}
5	100	2.28×10^{-3}	1.28×10^{-3}	8.50×10^{-4}
6	110	2.28×10^{-3}	1.28×10^{-3}	8.50×10^{-4}
7	123	2.28×10^{-3}	1.28×10^{-3}	8.50×10^{-4}
-	135	2.29×10^{-3}	1.28×10^{-3}	8.50×10^{-4}

The receptance predictions converge to a single value for all configurations at each frequency suggesting that the effects of configuration are insignificant to the model at higher frequencies. As expected for a grounded dynamic system, a decreasing trend in receptance with increasing frequency can be also seen from the predicted receptance values in the table. This corresponds to a constant mass characteristic in the receptance FRF. Table 3.5 shows the receptance values recorded at each of three trials for Configurations 1, 2, 5, and 7.

Table 3.5: Measured Location 1 Drive Point Receptance Amplitude at High Frequency for Multiple Trials at Various Configurations

Configuration	$q_1[^0]$	Trial	500Hz Measurement [m/N]	1000Hz Measurement[5] [m/N]	1500Hz Measurement [m/N]
1	50	1	2.87×10^{-12}	2.58×10^{-13}	4.57×10^{-12}
1	50	2	2.38×10^{-12}	5.67×10^{-13}	3.28×10^{-12}
1	50	3	3.27×10^{-12}	5.89×10^{-13}	2.56×10^{-12}
2	70	1	2.52×10^{-12}	8.95×10^{-13}	4.03×10^{-12}
2	70	2	2.11×10^{-12}	1.15×10^{-12}	4.02×10^{-12}
2	70	3	2.17×10^{-12}	1.39×10^{-12}	3.39×10^{-12}
5	100	1	2.97×10^{-12}	5.86×10^{-13}	3.22×10^{-12}
5	100	2	2.74×10^{-12}	6.54×10^{-13}	3.75×10^{-12}
5	100	3	2.71×10^{-12}	4.40×10^{-13}	3.42×10^{-12}
7	123	1	2.28×10^{-12}	8.72×10^{-13}	2.32×10^{-12}
7	123	2	2.66×10^{-12}	1.46×10^{-13}	3.39×10^{-12}
7	123	3	2.69×10^{-12}	5.54×10^{-13}	1.93×10^{-12}
	Mean		2.61×10^{-12}	6.75×10^{-13}	3.32×10^{-12}

The necessity for multiple trials becomes clear from the variation in the measured receptance values for different trials in the same configuration shown in the table. At higher frequency the repeatability of the data decreases and the data cannot be used for verification of the selected configurations; however, it can be used to verify of refute trends identified by the receptance prediction. The receptance values in Table 3.5 show that the trend of decreasing receptance with frequency identified from the model data in Table 3.4 is inaccurate when compared to the measured response. Excluding the third trial at Configuration 1, all FRF measurement trials increased in amplitude from 500 to 1500Hz and are significantly lower at 1000Hz than at both 500 and 1500Hz.

Though the predicted frequency trend has been shown false, the configuration optimisation at higher frequency can be neither confirmed nor refuted. The measurements for receptance at these frequencies cannot be accurately measured due to variance in the measured response. Whereas the repeatability of the measurements was extremely high for the mid-range frequency responses as shown in Figure 3.8 and also the low frequency responses as seen in

---

[5] An anti-resonance is present at 1000Hz reducing the receptance amplitude relative to the surrounding frequencies

Appendix B, the repeatability at higher frequency was insufficient when compared to the small difference between the responses at the different configurations as shown in Figure 3.9.

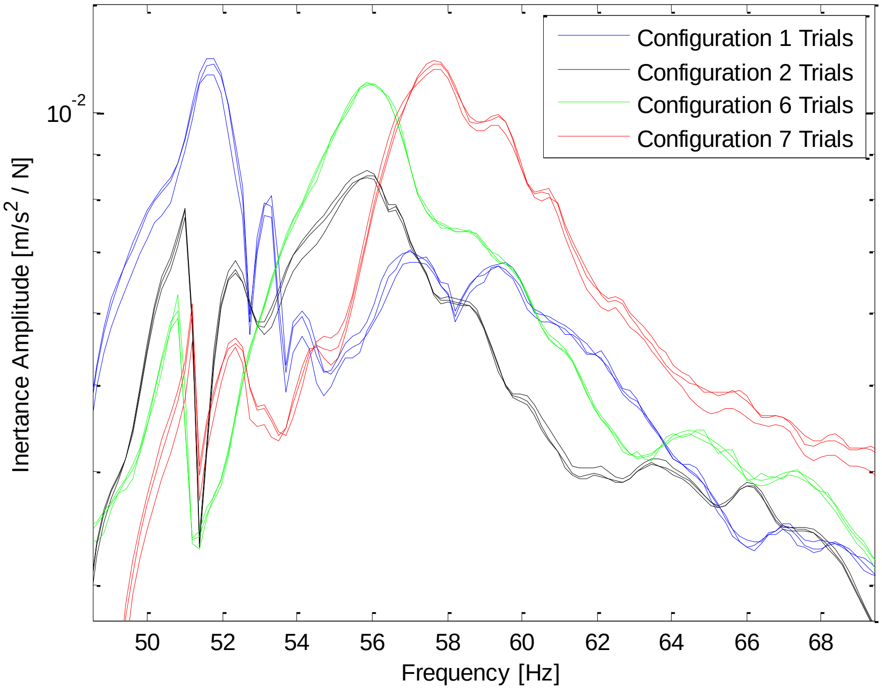

Figure 3.8: Location 1 Drive Point Inertance Amplitude Repeatability at Various Configurations in the 50-70Hz Range

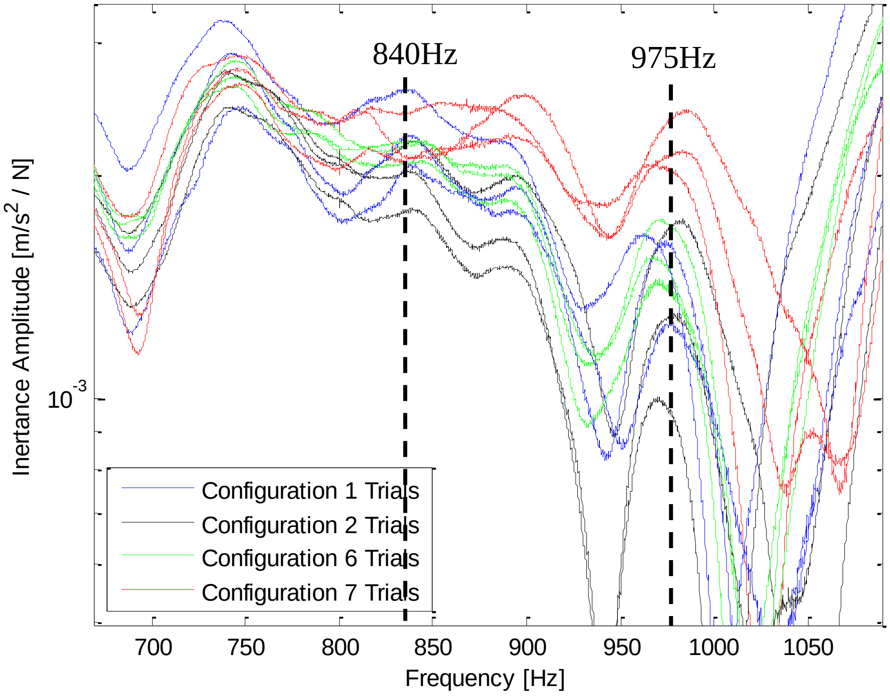

Figure 3.9: Location 1 Drive Point Inertance Amplitude Repeatability at Various Configurations in the 700-1050Hz Range

The different configurations show greatly reduced repeatability at higher frequencies preventing the selection of a preferable or optimal operating configuration. For example, investigating the Configuration 1 FRFs in Figure 3.9, a large variance can be seen, particularly at around 840Hz. When comparing this variance within a single configuration to the variance across configurations at this frequency it can be seen that these are comparable in amplitude and that it is therefore impossible to identify which configurations are preferable. Similarly, at 975Hz, even though the variance of Configuration 7 becomes less relevant as the amplitudes of the other configurations are substantially reduced, the variances of the other FRFs including Configuration 5 are now too large for configuration dependent amplitudes to be separated. For practical purposes, it can be said that the receptance convergence is accurate at higher frequency since there is no distinguishable pattern. However, this is not to say that the model can be used in this range since it fails to accurately predict the receptance as shown by comparing the order of magnitude for the values in Table 3.4 and Table 3.5.

A bode plot of measured receptance magnitude in Figure 3.10 shows that the amplitude does not continue to decrease with frequency as would be expected for a linear system. Instead, as is often the case with mechanical systems, the system response becomes erratic at frequencies much higher than the dominant dynamic resonances.

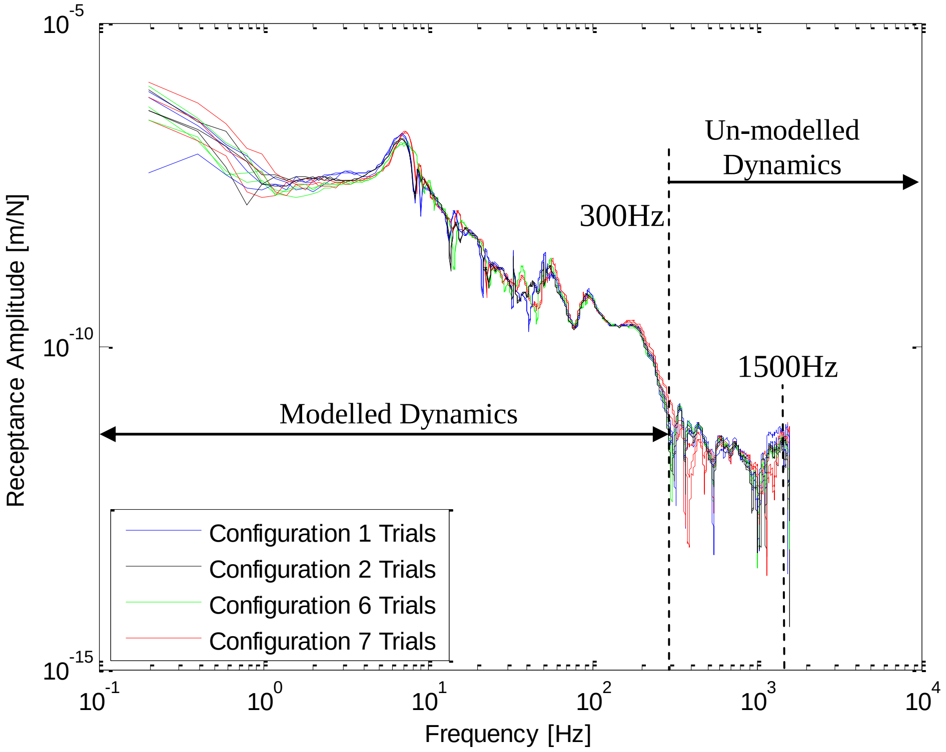

Figure 3.10: Logarithmic Manipulator Receptance Amplitude Plots for Multiple Trials in Various Configurations

It becomes clear that a configuration optimisation is only useful within the 0-200Hz range for which the model was developed. In the case of highly volatile data, the model is only useful when the modelled dynamics are dominant over the un-modelled dynamics. This was seen by comparing the results in the 0-45Hz region with those of the 50-60Hz region. When the modelled dynamics were smooth and non-volatile in the 0-45Hz range, the predictions were poor and failed to capture the main differences between the true manipulator FRFs. However, in the higher 50-60Hz range the effects of the two resonant peaks had a large overall effect on the manipulator dynamics and the receptance trends were successfully modelled at 53 and 58Hz.

3.3 Frequency Optimisation

3.3.1 Frequency Optimisation Procedure

Given a known configuration, the operating frequency can be optimised to reduce vibrations in the end-effector. A gradient-descent algorithm was developed using a symmetric difference quotient similar to the configuration optimisation.

$$\frac{\partial \alpha_q(i\omega)}{\partial \omega} = \frac{\alpha_q(i\omega)|_{\omega=\varpi+\Delta} - \alpha_q(i\omega)|_{\omega=\varpi-\Delta}}{2\Delta} \tag{3.6}$$

where ϖ is the current frequency, Δ is a small change in ω, and $\alpha(i\omega)$ is the predicted Location 1 receptance used as the objective function and approximated by the absolute value of (3.3) as with the configuration optimisation. The operating frequency is updated equivalently to the joint angle

$$\omega = \varpi + (k_o) sign\left(\frac{\partial \alpha_q(i\omega)}{\partial \omega}\right) \tag{3.7}$$

where k_o is a single gain to control the step size of the optimisation. The sign function was introduced to counter the low receptance derivative and thus very low objective function derivative values in certain regions of the predicted FRFs. This way the step size can be controlled and the optimisation can be discouraged from leaving the vicinity of a local minimum.

Unlike the configuration optimisation where little was initially known about the objective function characteristics, several local minima are expected for a frequency optimisation with one occurring before the first resonance, between each set of neighbouring peaks, and following the final resonance. The maximum number of resonance is known through the degrees of freedom and so the initial conditions for the optimisation (initial frequencies) can be automatically selected to ensure that all these minima are identified. The initial frequencies are selected as a function of the resonant frequencies at the configuration on interest

$$\boldsymbol{\omega}' = \left\{\frac{\omega_{n1}}{2}, \frac{\omega_{n1}+\omega_{n2}}{2}, \frac{\omega_{n2}+\omega_{n3}}{2}, \frac{\omega_{n3}+\omega_{n4}}{2}, 1.2\omega_{n4}\right\} \tag{3.8}$$

As mentioned briefly for the configuration optimisation, the model is piecewise and the switch between the two pieces occurs at 46Hz. In the frequency optimisation, the gradient decent will likely need to switch from one piece of the model to another and so, to account for differing amplitudes in the two sections of the piecewise models, the amplitude correction factor (σ) is introduced as

$$\sigma = \frac{H(i\omega)|_{\omega=2\pi(46)}}{G(i\omega)|_{\omega=2\pi(46)}} \tag{3.9}$$

where $G(i\omega)$ and $H(i\omega)$ denote the predicted receptance with and without the amplitude multipliers respectively. The receptance prediction before 46Hz is then modified as

$$\alpha_q(i\omega)|_{\omega<2\pi(46)} = \sigma H(i\omega) \tag{3.10}$$

3.3.2 Frequency Optimisation Results

A frequency sweep was performed on the objective function defined in Section 3.3.1in each of the 7 configurations. The results for Configurations 1, 2, and 7 are shown in Figure 3.11 with the model switch point at 46Hz marked. The effects of the configuration on the relative peak amplitudes can be seen easily in the inset and only three configurations are shown for clarity. Table 3.6 shows the frequency optimisation results for each of the three configurations.

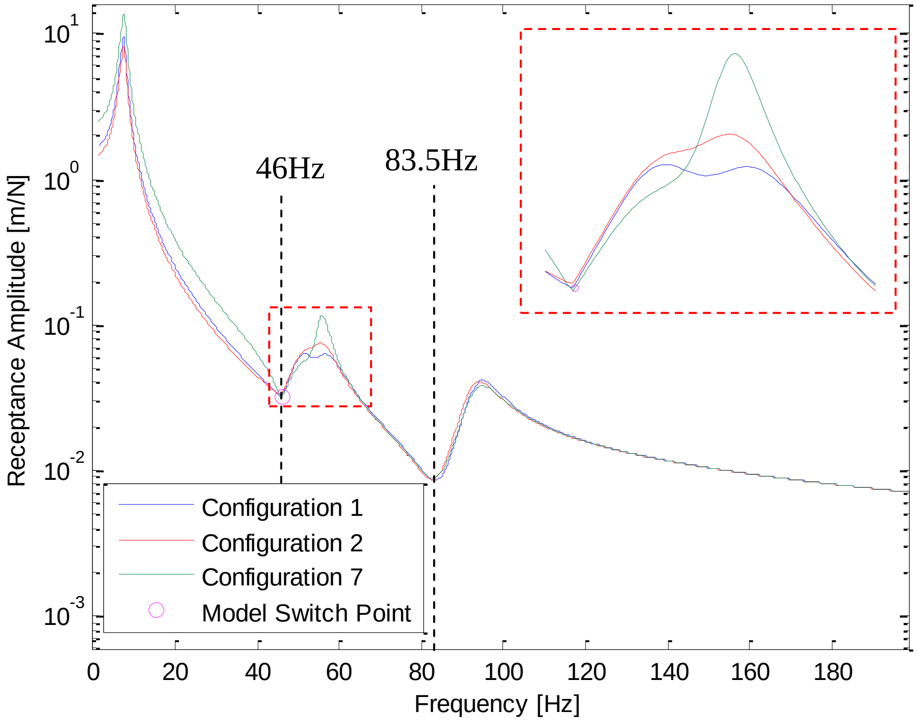

Figure 3.11: Location 1 Drive Point Receptance Amplitude Predictions for Various Configurations using a Piecewise Modal Model

Table 3.6: Location 1 Operating Frequency Optimisation Results for Various Configurations with Various Initial Conditions

Configuration	q_1	$\acute{\omega} = 4\text{Hz}$	$\acute{\omega} = 30\text{Hz}$	$\acute{\omega} = 54\text{Hz}$	$\acute{\omega} = 76\text{Hz}$	$\acute{\omega} = 113\text{Hz}$
1	50	0Hz	46Hz	54Hz	83.5Hz	Increases Unbounded
2	70	0Hz	46Hz	46Hz	83.5Hz	Increases Unbounded
3	80	0Hz	46Hz	46Hz	83.5Hz	Increases Unbounded
	88	0Hz	46Hz	46Hz	83.5Hz	Increases Unbounded
	92	0Hz	46Hz	46Hz	83.5Hz	Increases Unbounded
5	100	0Hz	46Hz	46Hz	83.5Hz	Increases Unbounded
6	110	0Hz	46Hz	46Hz	83.5Hz	Increases Unbounded
7	123	0Hz	46Hz	46Hz	83.5Hz	Increases Unbounded

From Figure 3.11and the results in Table 3.6, the operating point is selected as either 83.5Hz or the maximum practical spindle speed of the tool since the receptance at 83.5Hz clearly gives a lower receptance value than the other local minima. In general, it appears desirable to operate at the highest available frequency. Since the spindle speed when machining is multiplied by the number of teeth on the cutter, it appears that a cutting tool with more teeth is desirable to increase the excitation frequency artificially and take advantage of the decreased receptance at higher frequency.

The measured data doesn’t support the exact frequencies selected by the optimisations due to the volatility of the signals with respect to frequency as explored in the previous section. However, a more general verification can be done of the frequency optimisation. The measured responses all show a local minimum at extremely low frequency. This frequency is typically around 1Hz and below this the repeatability of the measured data quickly degrades. This supports the optimisation to zero of the first initial frequency $\acute{\omega}(1) = \frac{\omega_{n1}}{2}$. For the second initial frequency, the results are also intuitively accurate. As discussed in the previous chapter, the 46Hz model section switching frequency was selected to produce a modelled local minimum at a measured local minimum. Thus, when optimising between peaks in this vicinity, 46Hz gives an optimal or near-optimal frequency for machining. The next initial frequency is only relevant for Configuration 1. The optimal measured value in this range is 54.30Hz, although a gradient-descent from this region would likely have found another local minimum in the measured data due to the signal noise. The model successfully captured the dominant dynamics and produced an optimal frequency of 54.28Hz. In the remaining configurations, there is no peak seen for 51Hz and the algorithm accurately identifies the 46Hz minimum as the optimal frequency. The next minimum was identified at 83.5Hz by the optimisation, whereas the measured data places the minimum at approximately 77Hz. This discrepancy comes from neglecting the eigenvectors of the system in the model. The anti-resonance in the model can be adjusted through the phase of the amplitude multiplier, however these were not accurately determined as was shown in the previous chapter and as such their inclusion into the model will not improve the accuracy of the results. Finally, the optimisation identified infinite frequency as the desired machining point when operating at a frequency above all the modelled peaks. This is an accurate optimisation up to 300Hz as shown in Figure 3.10. After this point, the increase in frequency up to 1600Hz offers no advantage in response amplitude. The un-modelled high frequency dynamics become dominant and the nature of the measurements becomes highly volatile with no general trends to be observed. This makes a frequency optimisation ineffective in this region.

When operating in a given configuration, there appears to be a limiting frequency after which the response is no longer controlled by the governing dynamics of the machinery. This phenomenon is also seen in machine tools as shown in Figure 3.12.

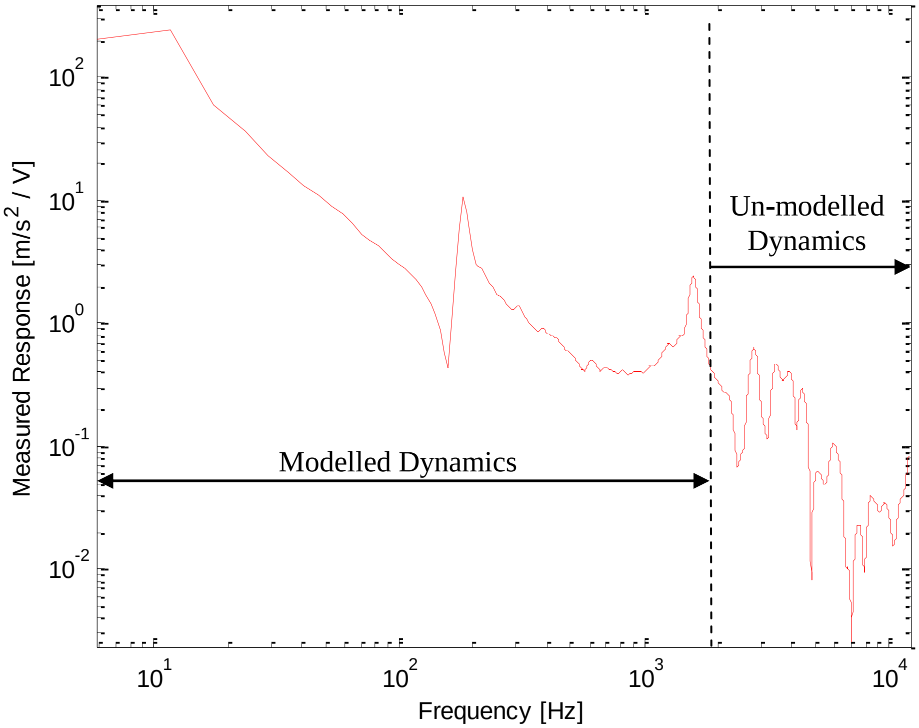

Figure 3.12: Open Loop Transfer Function for a High Precision Machine Tool Axis [103]

After reaching the frequency of constant returns, there appears to be little or no benefit in increasing the operating frequency for reducing vibrations. This frequency of constant returns, once identified, can be used as a lower bound for machining frequencies in a given configuration. In essence if the machining frequency is maintained above this frequency, the receptance of the end-effector is at a minimum and below this frequency the model needs to be used to avoid machining at resonant or other high receptance frequencies. It is worth noting that for the high precision machine tool the frequency at which the dynamics are no longer dominant is much higher than for the manipulator under investigation here. The CNC tool rigid body characteristics lose dominance at approximately 3000Hz compared to the 300Hz identified for the manipulator. This is due to the higher stiffness and natural frequencies typically found in the more rigid machine tools.

3.4 Redundant Manipulator Optimisation

3.4.1 Modelling and Optimisation of a Redundant Manipulator

One of the issues facing the optimisation of the Fanuc S-360 manipulator is the lack of variance in the response with configuration. Ideally, the optimisations carried out on the manipulator would be used for a redundant system, thus offering a highly versatile system with large variances in the dynamic properties with configuration. Such a system was not available for experimental testing; however simulations were carried out with the configuration optimisation algorithm used for the Fanuc manipulator and a dynamic model was developed for the six link manipulator shown in Figure 3.13 using the same procedure and assumptions as for the Fanuc manipulator.

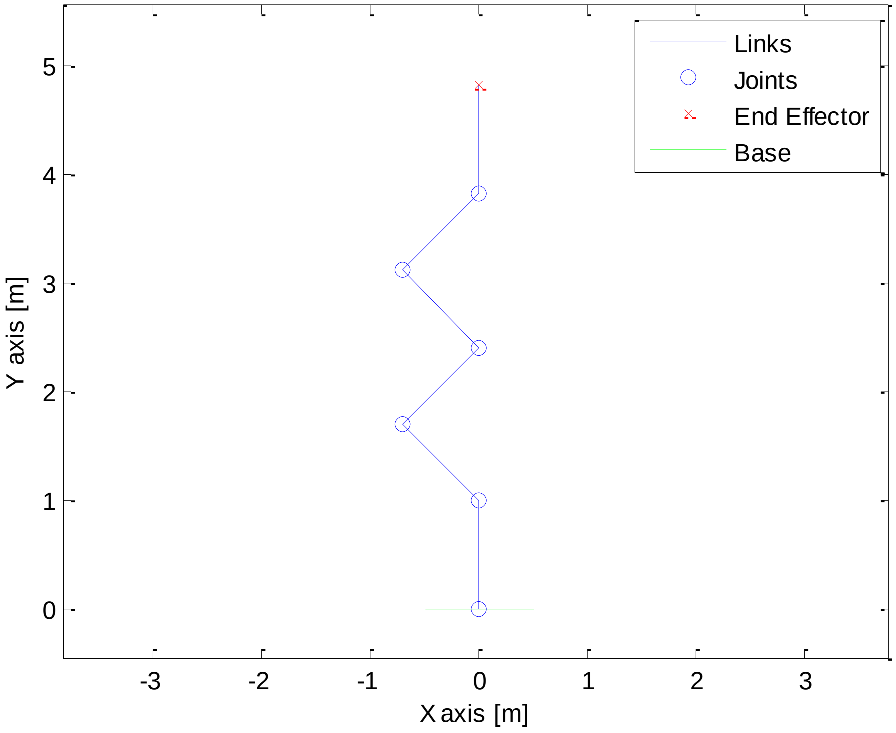

Figure 3.13: Skeleton Schematic of the Planar Six Link Manipulator

The dynamic parameters for the simulated manipulator are given in Table 3.7.

Table 3.7: Planar Six Link Manipulator Dynamic Parameters

Link / Joint	Mass [kg]	Inertia [kgm^2]	Stiffness [Nm/rad]	Damping [Nms/rad]
1	10.00	0.83	3000.00	500.00
2	10.00	0.83	2000.00	500.00
3	10.00	0.83	1500.00	500.00
4	10.00	0.83	1500.00	500.00
5	10.00	0.83	1000.00	500.00
6	10.00	0.83	1000.00	500.00

In the case of a planar manipulator the full kinematic Jacobian is rank deficient and so the $6 \times n$ Jacobian is reduced to a $3 \times n$ Jacobian representing the planar axes and orientation. The out of plane axis and remaining rotations are removed. For a planar manipulator with $n > 3$ the Jacobian is redundant and said to be short since it has more columns than rows and is no longer invertible. In this case, the Moore-Penrose pseudo inverse ($\boldsymbol{J}^{+}$) [104] is the unique solution that satisfies

$$\boldsymbol{J}\boldsymbol{J}^{+} = \boldsymbol{I} \tag{3.11}$$

and is calculated as

$$\boldsymbol{J}^{+} = \boldsymbol{J}^{T}(\boldsymbol{J}\boldsymbol{J}^{T})^{-1} \tag{3.12}$$

where $\boldsymbol{I}$ is the $n \times n$ identity matrix and thus $\boldsymbol{J}^{+}$ can be used in place of $\boldsymbol{J}^{-1}$ for several situations.

The projection of an arbitrary vector onto the null space of the manipulator is identified using the pseudo inverse [105].

$$\boldsymbol{V}_{Null} = (\boldsymbol{I} - \boldsymbol{J}^{+}\boldsymbol{J})\boldsymbol{V} \tag{3.13}$$

where $\boldsymbol{V}$ is an arbitrary vector and $\boldsymbol{V}_{Null}$ is the vector projection in the null space. Using this projection on the objective function derivative allows the formation of a gradient-descent optimisation in the velocity command.

$$\dot{\boldsymbol{q}}(t) = \boldsymbol{k}_{o}(\boldsymbol{I} - \boldsymbol{J}^{+}\boldsymbol{J})\frac{\partial\xi}{\partial\boldsymbol{q}} + \boldsymbol{k}_{p}\boldsymbol{J}^{+}\boldsymbol{e} \tag{3.14}$$

where $\boldsymbol{k}_{o}$ is a vector of gains for the optimisations of the various joints, ξ is the objective function, $\boldsymbol{k}_{p}$ is a vector of joint error gains, and $\boldsymbol{e}$ is a vector of Cartesian space position errors. The addition of Cartesian space errors allows a main task to be performed by the manipulator such as a machining or pre-machining operation with accurate tracking. In this case, the end-effector will simply be held stationary in a desired location. As before, to minimise an objective function, $\boldsymbol{k}_{o}$ must be negative. In the implementation of the optimisation the joint error gains were increased by a factor of ten for the last one hundred iterations in order to correct for the position errors caused by the optimisation. This was necessary as the starting configurations often produced large motions that were not fully contained in the null space.

3.4.2 Receptance Optimisation Results

An initial optimisation was done without error correction or null space projection using the equivalent of (3.2) for each joint. These resultant values were concatenated as the objective function derivative vector, $\frac{\partial\xi}{\partial\boldsymbol{q}}$, as in (3.15). The modal multipliers were included for all frequencies since they are known exactly.

$$\dot{\boldsymbol{q}} = \boldsymbol{k}_{o}\frac{\partial\xi}{\partial\boldsymbol{q}} \tag{3.15}$$

This was carried out to give an intuitive understanding of the optimal configuration for the redundant manipulator. Three starting locations were chosen at (-3.5, 1), (-2, 2), and (0, 1.5) in an attempt to recognise local and global minima. The natural frequencies of the manipulator typically fell between 0.5 and 30Hz at each of the starting locations and so the initial optimisations were carried out at 0 and 100Hz using each of the starting location joint coordinate as initial conditions for the optimisation. This was done to gain an intuitive understanding of the manipulator optimisation mechanism. The applied force axis is vertical and defined as acting at the end-effector by using the end-effector drive point receptance as the objective function. This is again a parallel to the configuration optimisation performed on the industrial manipulator. The manipulator generally converged to a singularity similar to that shown in Figure 3.14 such that there was a loss or severe reduction of manipulability along the applied force axis. This trend was observed for both frequencies at all end-effector locations.

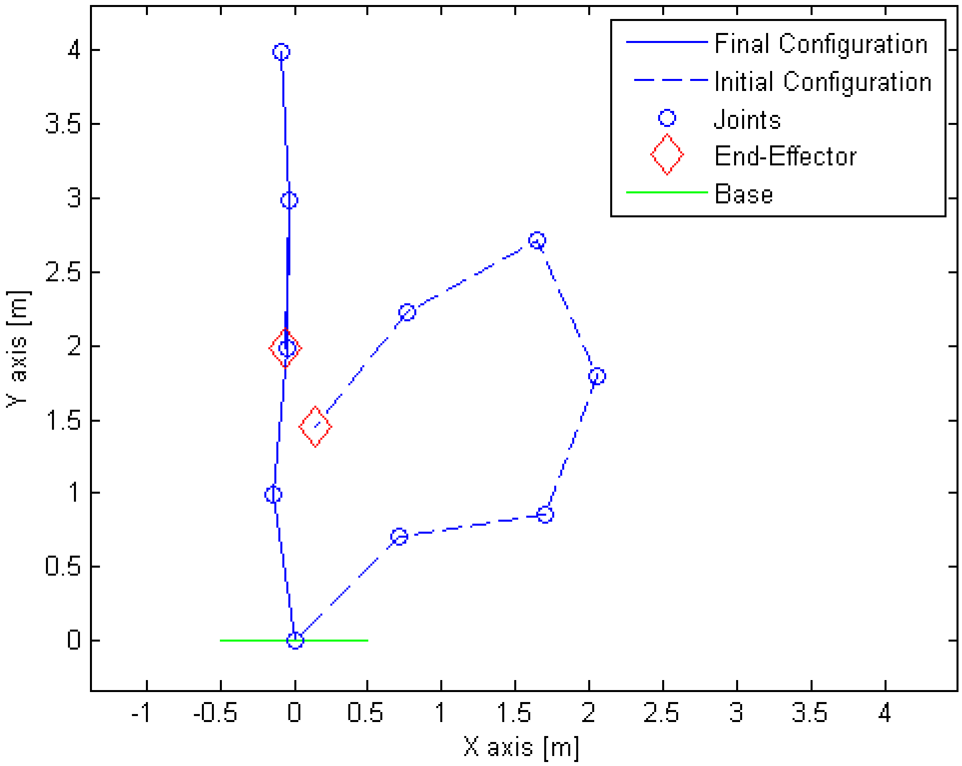

Figure 3.14: End-Effector Drive Point Receptance Optimised Configuration of the Simulated Manipulator at 0Hz Initially Positioned at Location (0, 1.5)

In the cases where the manipulator did not converge toward a singularity, it approached an aligned configuration and was limited by the optimisation gains, which were in turn limited by the initial values of the objective function derivatives. Increasing these gains too much, caused some joints to oscillate about the optimal value without converging, while reducing these gains too much caused the solution traverse to slow significantly and the manipulator never arrived at the optimum configuration. The greatest improvement in the receptance value was found at 100Hz starting from position (0, 1.5) and ending in approximately the same configuration as the 0Hz optimisation. Table 3.8 shows the joint angles, natural frequencies, and receptance amplitudes before and after the optimisation. The full set of optimisation results is given in Appendix E: .

Table 3.8: Initial and Final Natural Frequencies and Receptance Values for End-Effector Drive Point Receptance Optimisation at 100Hz Starting at Location (0, 1.5)

Initial Joint Values [rad]	Initial Natural Frequencies[6] [Hz]	Final Joint Values [rad]	Final Natural Frequencies [Hz]
1: 0.7854	10.9518	1: 1.4707	40.2364
2: -0.6283	9.3648	2: 0.0458	11.0669
3: 1.0472	5.1605	3: 0.0168	7.8127
4: 0.7854	4.4986	4: 0.0312	6.4884
5: 1.6535	3.3036	5: 3.1111	5.5875
6: 0.3927	1.6958	6: 0.0295	4.4489
	1.1914		2.4299
			1.2463
Initial Receptance Amplitude [m/N]	1.286×10^{-7}	Final Receptance Amplitude [m/N]	2.926×10^{-10}

The range of natural frequencies of the system is being increased with manipulator alignment and the receptance amplitude near the singularity is significantly decreased. This trend indicates that a pole placement algorithm could be used for the unrestricted case investigated here where the end-effector is free to move in the workspace. This pole placement algorithm would maximise the deviation between the maximum and minimum natural frequencies, which would correspond to a vertical singularity similar to the one shown in Figure 3.14. Possible implementation of this algorithm would be a LS maximisation of the ratio of the largest eigenvalue to the smallest eigenvalue.

Once the unrestricted optimal configuration was identified, the end-effector position error was reintroduced and the optimisation was relegated back to the manipulator null space. This meant that, although the links could realign to improve the receptance at the operating frequency, the

---

[6] Repeated Frequency Values are Omitted

end-effector could not move. The same three end-effector locations were selected as before. These were selected since they are of varying distance from the manipulator base, while still offering sufficient kinematic redundancy to make the optimisation significant. In addition, these configurations avoided postures with high condition numbers early in the optimisation by avoiding aligning any two neighbouring links and prevented any links from being initially aligned with the excitation axis. The initial configurations are shown in Figure 3.15.

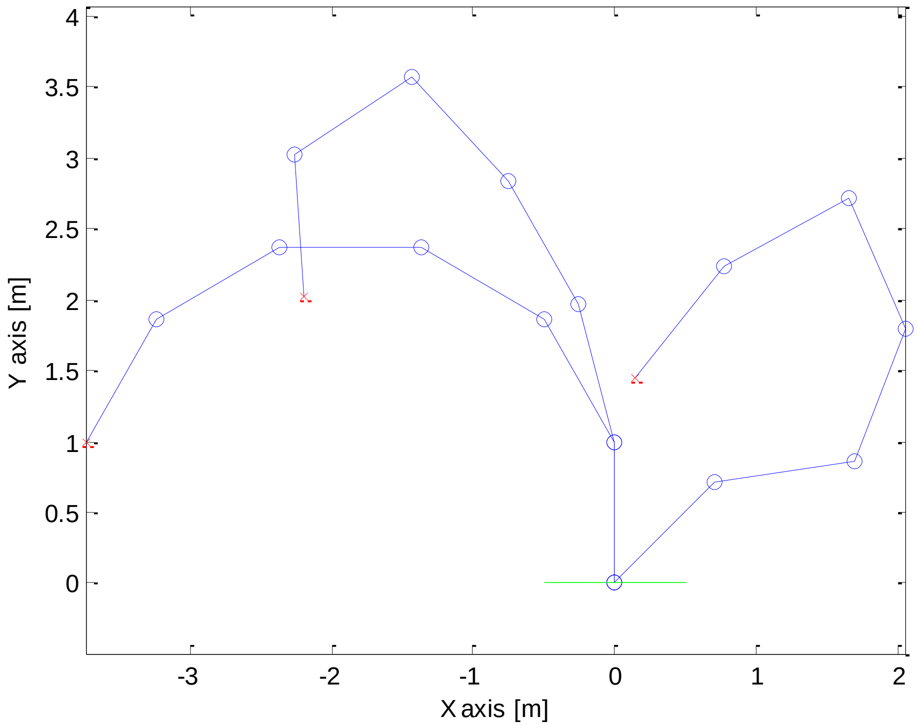

Figure 3.15: The Three Initial Configurations for the Simulated Manipulator End-Effector Drive Point Receptance Optimisation

The optimisation was carried out for 1, 5, and 20Hz based on the natural frequencies observed in the initial unrestricted optimisation. A general observation is that at all frequencies and in all machining positions the manipulator moved to a configuration more aligned with the vertical axis. This is most predominant in the results for the 5Hz optimisation at (-2, 2) shown in Figure 3.16. The full set of plots is given in Appendix G: .

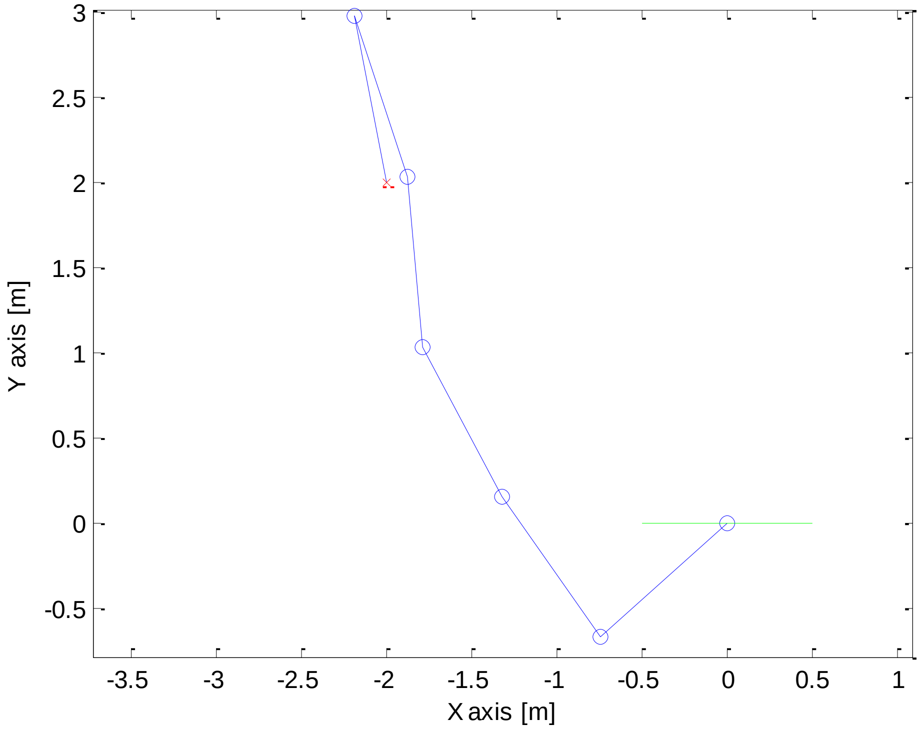

Figure 3.16: End-Effector Drive Point Receptance Optimised Configuration of the Simulated Manipulator 5Hz at Location (-2, 2)

Table 3.9 shows the results of the 5Hz optimisation at (-2, 2). It can be seen that the largest natural frequency was increased substantially from 9.9 to 48Hz while the smallest was slightly reduced from 0.81 to 0.75Hz. This combination increases the condition number of the eigenvalue problem, as before, as the manipulator moves toward a singular configuration. In addition, the three natural frequencies closest to the operating frequency have been changed from 5.8, 4.8, and 4.6Hz to 7.0, 5.8, and 4.2Hz. The resonances associated with each of these frequencies are moving away from the 5Hz operating point.

Table 3.9: Initial and Final Natural Frequencies and Receptance Values for End-Effector Drive Point Receptance Optimisation at 5Hz at Location (-2, 2)

Initial Joint Values [rad]	Initial Natural Frequencies [Hz]	Final Joint Values [rad]	Final Natural Frequencies [Hz]
1: 1.5708	9.8557	1: 3.8681	48.0462
2: 0.2618	5.7912	2: -1.6855	6.9557
3: 0.2618	4.7526	3: -0.1226	5.7486
4: 0.2094	4.6377	4: -0.4073	4.2074
5: 1.4280	3.0509	5: 0.2442	3.4311
6: 1.0472	1.4478	6: 3.0108	2.5526
	0.8135		0.7496
Initial Receptance Amplitude [m/N]	2.948×10^{-5}	Final Receptance Amplitude [m/N]	1.127×10^{-5}

In addition to shifting the resonant peaks, the amplitude of the peaks is also reduced. Figure 3.17 shows the FRF for the manipulator before and after optimisation.

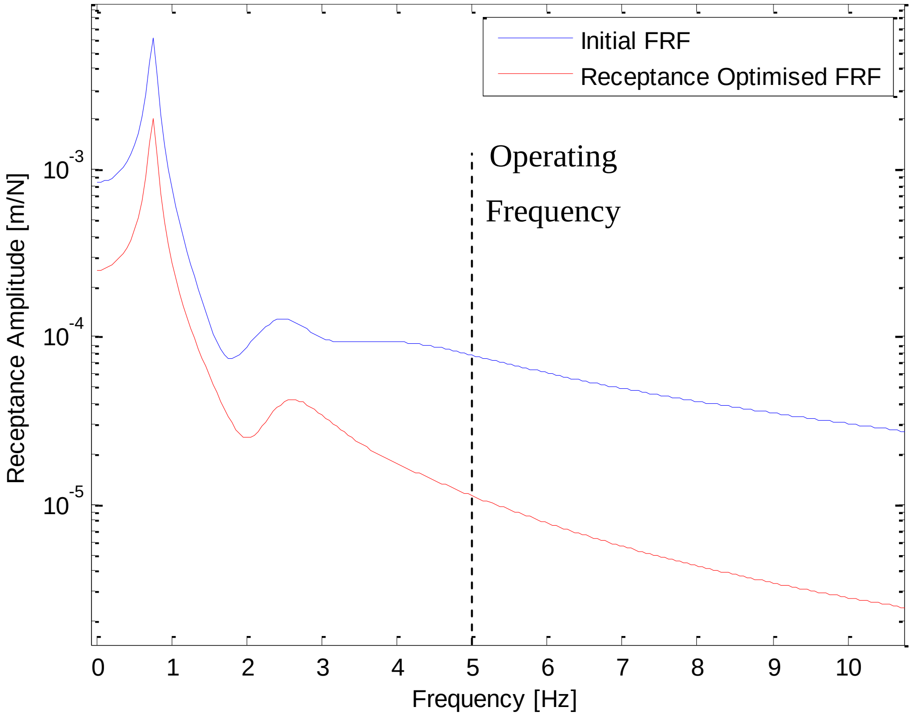

Figure 3.17: Simulated Manipulator End-Effector Drive Point Receptance Optimisation Results at 5Hz at Location (-2, 2)

It can be seen that the amplitude of the peaks close to the operating point have been reduced significantly and that the overall amplitude is also reduced by decreasing the DC receptance. The DC gain of a mechanical structure is controlled by the rigid body stiffness for a grounded system; that is, a system with one fixed end condition. The DC gain for such systems is given by

$$k_{DC} = \frac{1}{K_{RB}} \tag{3.16}$$

where K_{RB} is the rigid body stiffness and k_{DC} is the zero frequency gain. From this observation, the mechanisms of the optimisation can be stated as

1. Pole Placement: The poles are being adjusted in order to reduce resonance and increase anti-resonances in the region around the operating point.
2. DC Gain Control: The DC gain is being reduced where possible corresponding to a maximisation of rigid body stiffness.

The receptance function can be seen to operate with the two different mechanisms, however it is difficult to exactly measure or compare the effects of each since they are occurring together since the purpose of this research is to include the effects of frequency on the posture selection optimisation, it is desirable to identify the relevance of the pole placement component compared to the DC gain control component.

3.4.3 Stiffness Optimisation Results

For a single arbitrary response axis defined by the vector $\boldsymbol{u}$, an objective function, known as the stiffness measure, can be built to describe the Cartesian rigid body stiffness along that axis [44].

$$\xi_K = \boldsymbol{u}^T \boldsymbol{J}^{+T} \boldsymbol{K}_q \boldsymbol{J}^{+} \boldsymbol{u} \tag{3.17}$$

Given that the joint axis stiffness matrix is diagonal, as is the case for the dynamic model used in this work, this measure is effectively a weighted inverse of the mobility performance measure identified by Yoshikawa [38] using the joint stiffness as a weighting on each DOF.

$$\xi_M = \boldsymbol{u}^T \boldsymbol{J} \boldsymbol{J}^T \boldsymbol{u} \tag{3.18}$$

Intuitively, minimising the mobility performance measure will lead the manipulator to a singularity on the projection axis. By extension, maximising the inverse will also lead the manipulator to a singularity on this axis. Using the joint stiffness values as a weighting function will therefore also eventually lead the manipulator to a singularity along the projection axis. This general concept has been used for several configuration optimisations as outlined in Section 1.4. We are now in a position to separate the frequency effects of the simulated results from the stiffness effects of the simulated results by optimising the six link manipulator according to (3.17) and comparing the results to those obtained previously. This will highlight the effects of the pole placement in the receptance optimisation. The results of the stiffness optimisation are shown with the receptance optimisation and initial curve in Figure 3.18.

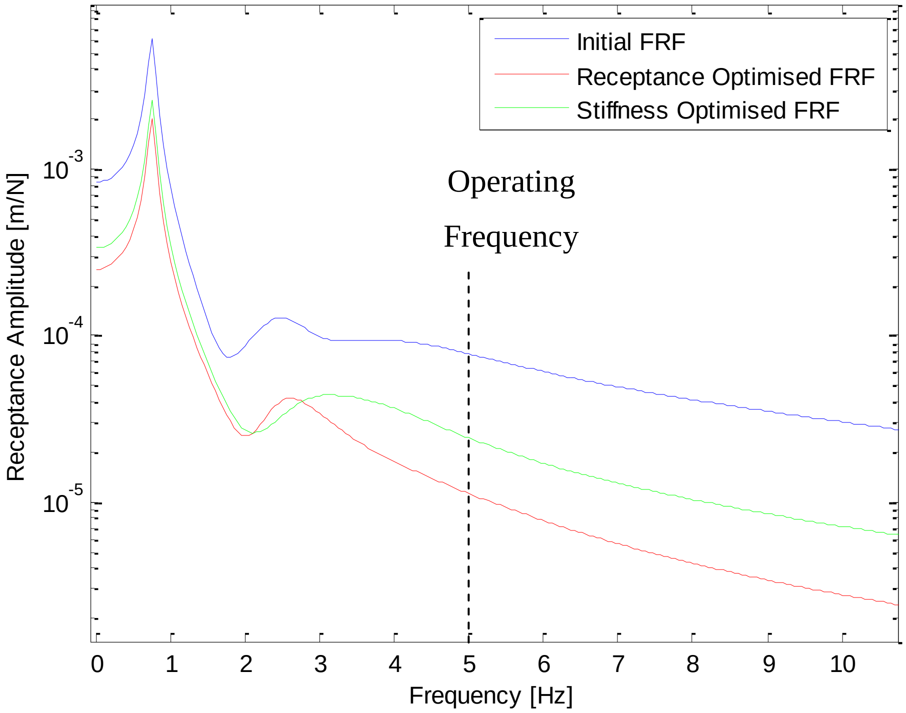

Figure 3.18: Simulated Manipulator End-Effector Drive Point Receptance at 5Hz and Rigid Body Stiffness Optimisation Results at Location (-2, 2)

The stiffness optimisation gave the same approximate configuration as the receptance optimisation in Figure 3.16 and thus the effects of frequency configuration can be more easily seen. Below 2Hz, the two optimisation algorithms give a similar FRF, however the stiffness optimisation does not account for the amplitude increase caused by natural frequencies in the 2-4Hz region. By adjusting the damping, resonant frequencies, and amplitude multipliers, the receptance optimisation is able to further reduce the amplitude sensitivity at the operating point. Although the DC response is not identical in this case, the advantage of a frequency dependent optimisation over stiffness optimisation can be seen from Figure 3.18 by looking at the greater improvement in receptance at 5Hz (a factor of 2.15) compared to the lesser improvement at 0Hz (a factor of 1.34).

The first resonant peak occurs slightly before 1Hz and is comparable for the two optimisations. Comparing the stiffness optimisation to the 1Hz receptance optimised configuration in Figure 3.19 shows how the receptance optimisation can place anti-resonances to reduce the sensitivity of the system.

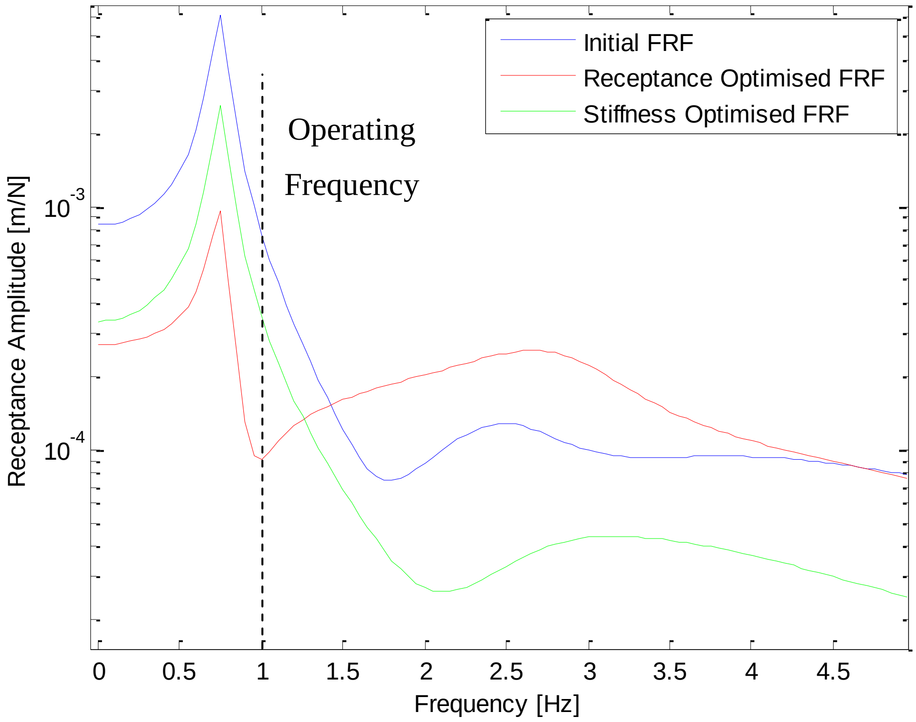

Figure 3.19: Simulated Manipulator End-Effector Drive Point Receptance at 1Hz and Rigid Body Stiffness Optimisation Results at Location (-2, 2)

The manipulator is moved to a configuration with less vertical alignment in this case. The benefit is far less intuitive since the anti-resonance cannot be inferred from the configuration. The alignment to a singularity previously identified as a desirable configuration in order to reduced the general amplitude of the curve has been ignored and instead a more obscure configuration was selected which places the anti-resonance at 1Hz. The benefit of the pole placement aspect of the receptance optimisation is now clear. Whereas the general resistance to vibrations is increased by the stiffness optimisation, the operating frequency considerations offer a vast improvement close to resonant frequencies. By changing the configuration, the system poles are being adjusted, which in turn affects the natural frequencies and damping ratios if the resonant peaks. Therefore the receptance optimisation indirectly affects the natural frequencies and damping ratios of the resonant peaks in order to reduce the receptance at the operating frequency. The configurations for the receptance optimisations at 1 and 5Hz, the stiffness optimisation, and the initial configuration are shown in Figure 3.20.

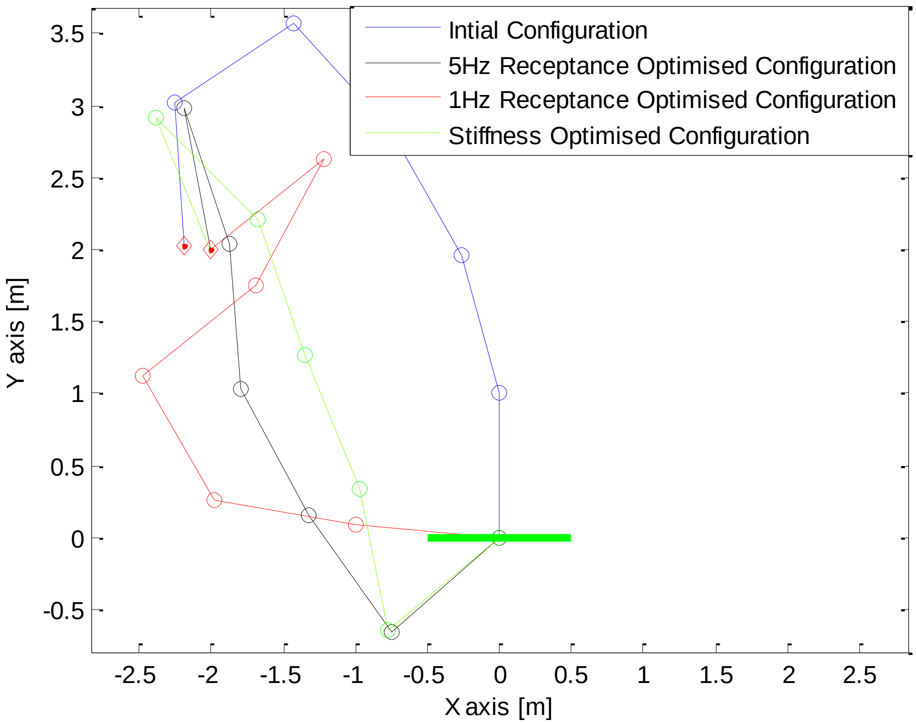

Figure 3.20: Simulated Manipulator Configurations for End-Effector Drive Point Receptance Optimisation at 1 and 5Hz and Rigid Body Stiffness Optimisation at Location (-2, 2)

As mentioned previously, the optimisation gains can cause the system to ‘hop’ over a local maximum from the vicinity of one local minimum to that of another. An example of this occurs during the 20Hz optimisation at (-3.5, 1). The direct gradient-descent solution yields a configuration similar to the expected alignment found in the 5Hz optimisation at (-2, 2) (see Figure 3.16), but when the optimisation gain is increased too far, the manipulator shifts to a configuration in the locality of another local minimum. The final configurations are shown in Figure 3.21.

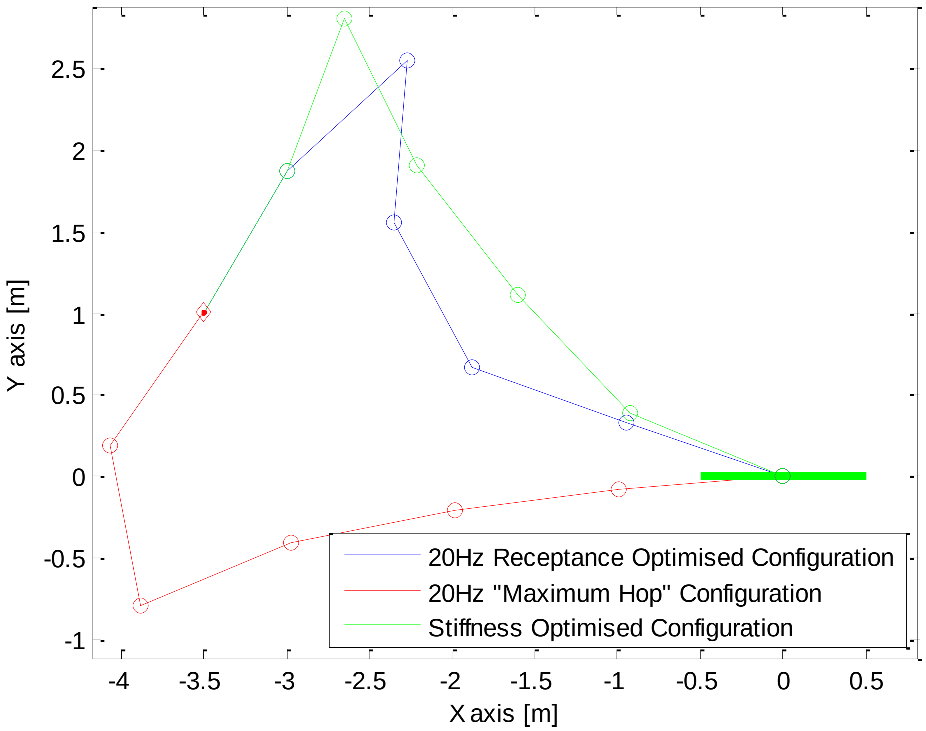

Figure 3.21: Simulated Manipulator Configurations for End-Effector Drive Point Receptance Optimisation and "Maximum Hopped" Configuration at 20Hz and Rigid Body Stiffness Optimisation at Location (-3.5, 1)

Surprisingly, the best configuration for receptance at 20Hz was given by the stiffness optimisation given by the velocity update scheme in (3.14) and the objective function (3.17). The final receptance value of 2.305×10^{-6} was less than 2.390×10^{-6} given by the receptance function optimisation. From Figure 3.21 it appears likely that the receptance optimisation would have eventually reached a configuration more similar to that of the stiffness optimisation, but was unable to in a reasonable amount of time due to the reduced optimisation gain. The 'maximum hop' configuration also settled to a configuration that improved the receptance at 20Hz, however this optimised configuration did not perform as well as either of the others and had a receptance value of 2.807×10^{-6}. When compared to the initial receptance value of 4.217×10^{-5}, all these configurations show a significant improvement and the variability between them is less significant.

Figure 3.22 shows the command values and the objective function value throughout the optimisation with the larger gain. It should be noted that the actual time value is small to match the large velocities allowed by the simulation. Recall that the optimisation gain is reduced to zero toward the end of the optimisation period and that the error gain is increased by a factor of ten to ensure that the final end-effector position is accurate. The sharp increase in the error command at 0.9 seconds is caused by this change in gain as is the disappearance of the objective function command at the same time. The scale of the objective function command has been adjusted to make the correlation to the objective function and the error command more visible, however it should be noted that the initial values of some joint velocity commands approach 1.5×10^7 for the first three steps. It can be seen that the initial improvement in the objective function is caused by an extremely large objective function command that cannot be contained in the null space of the manipulator thus causing the error command to grow and increase the objective function value through position correction. The error command eventually reduces allowing the cost function command to dominate and move to a new configuration with a lower objective function value. This is approximately the final configuration seen in Figure 3.21, and is adjusted very slightly at 0.9 seconds when the gains are adjusted. The transition from the region of one minimum to the other occurs at approximately 0.07 seconds when the error command increases in an attempt to recover from the high objective function command values at 0.05 seconds. This error correction causes the joints to begin moving under the end-effector as in Figure 3.23 and when the error command decreases, the optimisation now begins to traverse to a new local minimum.

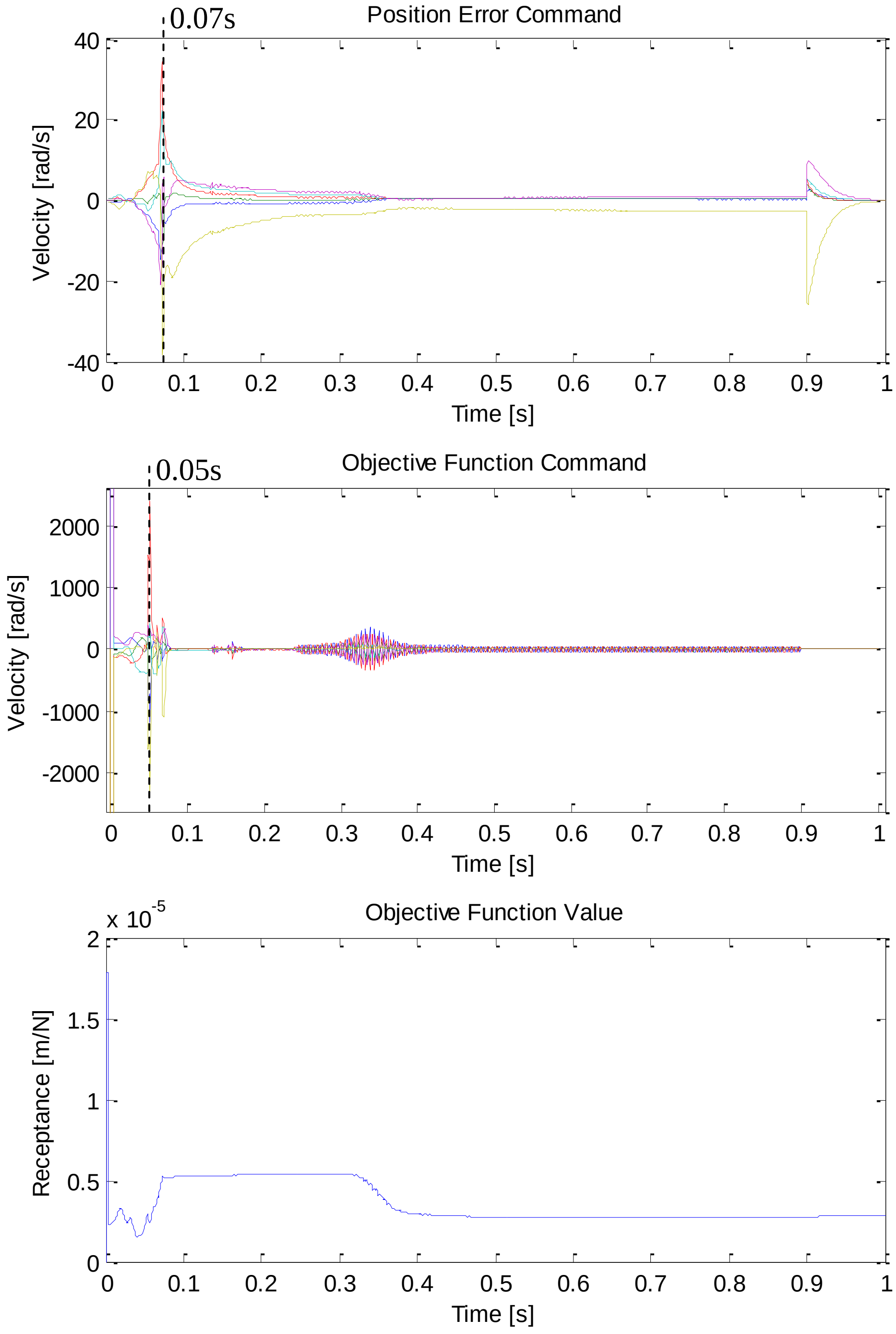

Figure 3.22: Command and Objective Function Values for 'Maximum Hopping' During End-Effector Drive Point Receptance Optimisation at 20Hz at Location (-3.5, 1)

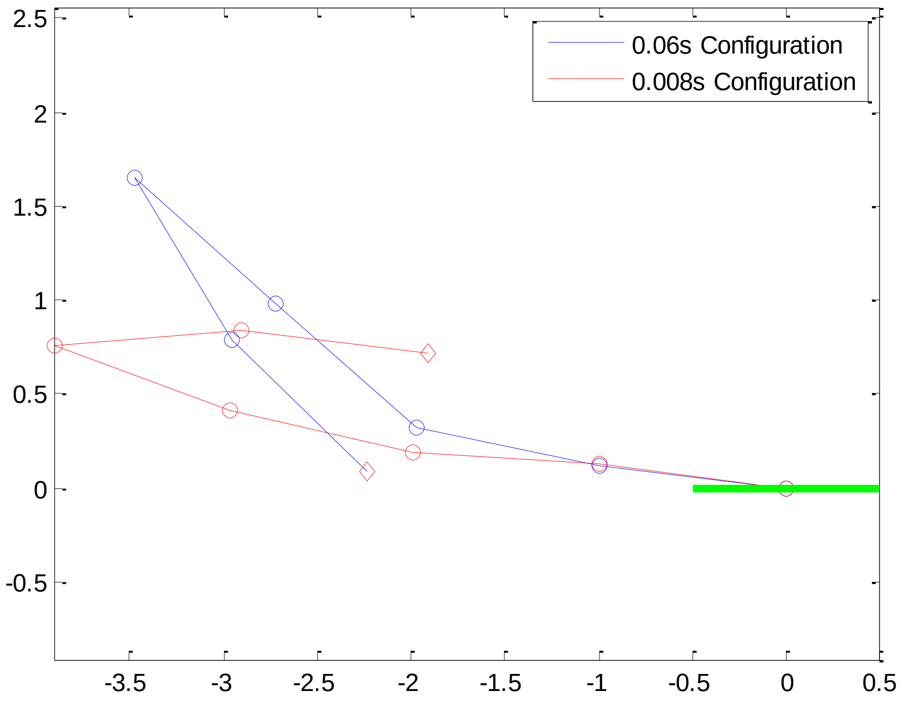

Figure 3.23: Intermediate Configurations for the ‘Minimum Hop’ at 20Hz at Location (-3.5, 1)

In order to find a globally optimal solution, several joint configurations are used as a starting point for the same end-effector location. The resultant configurations can then be compared to identify a globally optimal solution. In this case, the two local minima are essentially mirrored in the line that passes through the manipulator base and end-effector as shown in Figure 3.21. The other potential starting configurations are passed through by these two optimisations and therefore do not offer local minima. Thus, the global solution to the receptance optimisation is given by the configuration found using the lower optimisation gain and the overall optimal configuration is given by the stiffness optimisation, which was also performed at various starting configurations.

3.5 Summary

A comparison of model based receptance predictions to measured receptance shows that a lack of variability in the Fanuc S-360 machine dynamics in the restricted configurations is problematic. In particular, in the regions where the peaks are of similar amplitude throughout different configurations the volatility in the un-modelled dynamics makes the use of lower order models unfeasible. However, in the regions where the receptance is highly configuration dependent, the optimisation can accurately determine trends in the receptance with respect to configuration. Thus, for this particular manipulator, it is only productive to use a configuration optimisation in the 50-60Hz range where there are two neighbouring peaks whose relative amplitude is highly configuration dependent and the effects of higher order dynamics are negligible in comparison.

A frequency optimisation effectively avoided the resonant peaks, but was unable to find the true optimum configurations due to inaccurate placement of the anti-resonances. This shows the necessity of accurately identified mode shapes and suggests that while a heavily simplified model can be used to improve the performance, the model used needs to be fully identified before the true optimal configuration can be found. Furthermore, at frequencies above 300Hz, the modelled rigid body dynamics no longer dominated the response and thus the model is no longer relevant due to un-modelled high frequency dynamics. Beyond this frequency the response is fairly constant with low magnitude, although it is highly volatile. It was therefore determined that the optimum machining frequency would be above 300Hz and dependent on cutting parameters such as feed speed and chip thickness. Unlike the configuration optimisation, it is possible to identify a globally optimal operating frequency with absolute certainty below 300Hz with an accurate model since the location of all the local minima are known and thus it can be guaranteed that they will all be investigated.

A redundant manipulator with no joint restrictions was simulated in order to further investigate the results of posture optimisation and overcome the lack of variance in the Fanuc S-360 manipulator. The redundant manipulator tended toward a singularity that prevented motion in the measured axis. With this established, the optimisation was repeated with the optimisation restricted to the null space of the manipulator and the error from implementation was accounted for with an error correction term. This showed that while the manipulator still tended toward a low manipulability configuration, it also accounted for the shape of the FRF curve produced when reducing the receptance at a given frequency. The system was then optimised using a weighted mobility measure that considered the flexibility in each joint. The general trend of moving to a low manipulability configuration was retained, but the indirect placement of poles by the optimisation to further reduce the amplitude was absent. By comparing the two sets of results, the frequency consideration was found to be manifested in both the reduction of neighbouring peaks and the placement of anti-resonances at or around the operating point. Thus, the improvement in system receptance gained by compensating for operating frequency can be seen and quantified on a case by case basis. With the exception of a single case where the gains had to be reduced to prevent the solution from escaping to a neighbouring minimum, the frequency optimisation was seen to improve the performance of the simulated manipulator.

Chapter 4 Summary, Conclusions, and Future Work

4.1 Summary of Previous Chapters

4.1.1 Motivation

Industrial robotic manipulators are well established in many areas of life from entertainment to welding to materials handling. The current state of the art is predominantly in low force applications; however robots are becoming increasingly used for more demanding tasks such as material removal fabrication. To date, the applications in material removal have been predominantly limited to low precision tasks such as pre-machining stock material and finishing cast parts, and machining soft materials such as wax, plastic, or wood. The increasing capabilities of CNC machine tools often exceed the requirements to produce a given part and manufacturers are beginning to look to robots as a cheaper alternative where applicable in order to exploit several advantages such as lower capital cost and increased dexterous work volume. Research is currently being carried out to expand the capabilities of robotic machine tools in material removal applications, specifically metal cutting to increase the number of situations where this substitution is worthwhile.

As robotic machine tools are increasingly used for metal cutting, there is a need for more rigid robots to be constructed. However, several factors inherent in the design of industrial manipulators prevent rigidity that can compete with that of CNC machine tools. The most significant and widely investigated of these is the use of harmonic drives. Harmonic drives are an excellent choice for industrial robots as they allow very large reduction ratios and enable manipulators to handle very high payloads. When operating with machining forces, this is a desirable trait. The disadvantage associated with this is the flexibility inherent in their design. Several researchers have attempted to model the dynamics of these mechanisms with varying levels of detail and success and the problem is further amplified by the cantilever nature of serial manipulators.

In order to reduce the apparent flexibility of robotic machine tools, several researchers have investigated posture selection and control strategies that can compensate for the flexibility in the manipulator. In some cases, primarily in posture selection, the dynamic model needs to be known in advance, while in others an adaptive scheme can be used to correct for errors in the assumed dynamic parameters. The posture selection measures proposed to date are based on static loading dynamics even when applied to vibration problems. The motivation for this work is therefore to add to this body of knowledge by creating a posture measure that can include frequency effects and verify it experimentally. In order to do this, a manipulator needs to be parametrically identified to generate an accurate model and so it is desirable to both develop a method of parametrically identifying a dynamic model of the manipulator, while reducing the downtime of the machine in a factory setting, and to develop posture selection measure that will identify optimum configurations for carrying out tasks that include oscillating external loads.

4.1.2 Dynamic Modelling of Industrial Manipulators

Flexible manipulators can be modelled with flexibility in both the joints and links. It has been shown for industrial manipulators that the majority of flexibility can be modelled in the joints alone and so this model was selected. Additional pseudo-joints were added to compensate for any link flexibility.

The ideal dynamics of serial manipulators are nonlinear with configuration due to the gravitational and squared velocity terms. The gravity terms can be neglected from the model either by operating in a plane or by dismissing the force of gravity as a constant and therefore not part of the oscillatory response. Since the effects of gravity are constant with time for any given configuration and, when the deflections in the manipulator are small enough that the configuration can be considered constant, these terms are neglected by adjusting the equilibrium configuration of the manipulator. The squared velocity terms however are not necessarily negligible and so the experimental configurations were selected to minimise their effects.

The effect of the joint controllers as servo stiffness was found to be negligible when compared to the physical compliance and was therefore neglected. This was expected for an industrial manipulator since these machines generally offer very high repeatability and accurate positioning. For the Fanuc S-360 manipulator, the repeatability is listed at ±0.5mm [106], while the end-effector deflection that can be achieved by manually exciting the system near the first resonance is in excess of 1cm.

The rigidity of the links was also investigated and the model was updated to include pseudo-joints to compensate for the link flexibility. The first link was found to be rigid in that the motions of the measured points on the link joint did not match any fixed free beam modes and thus the parallel mechanism compensated for any significant link flexibility. The second link flexibility was found to have a significant effect on the end-effector and so the harmonic frequencies were also investigated. The harmonics were found to be negligible and thus only a single pseudo-joint was added to compensate for the link flexibility.

4.1.3 Modal Parameter Identification

Two separate modal analysis software packages were used with varying amounts of user input and model complexity to identify the modal parameters of the measured FRFs. Neither program was able to consistently identify accurate modal parameters despite the repeatable data used. In some experiments the mode shape vectors were accurate for certain FRFs, but the full set of FRFs corresponding to the system were never accurately obtained. The implication here is that once the more accurate mode shapes vectors had been identified, there was no solution for the remaining mode shape vectors that satisfied the restrictions placed by those already identified. It is expected that the failure of these programs is due to the nonlinear nature of the captured manipulators dynamics.

A more user intensive technique was then employed that allowed more operator input and thus could be adjusted for the peaks and locations where the data was significantly different from the modelled form of a linear system. A circle fit technique was used that identified natural frequency, damping ratio, and amplitude multipliers, but could have either the natural frequency, damping ratio, or both entered manually when the data quality was poor or the calculated results were considered too erroneous. The reduced restrictions on the modal parameters prevented the measured mode shape vectors from satisfying the orthogonality property that decouples the modal mass or equivalent matrix. This, in turn, prevented use of the high precision techniques used in model updating to identify the dynamic parameters since these techniques rely on the orthogonality condition. A more general approach was instead developed using a least squares optimisation.

4.1.4 Dynamic Parameter Identification

When identifying the dynamic parameters, the errors in the mode shape vectors were trivialised since the least squares optimisation was unable to correlate the dynamic parameters to the mode shapes. This prevented the use of the mode shape vectors when parameterising the dynamic model therefore led to inaccurate reconstructed eigenvectors. Surprisingly, these eigenvectors could still be used to generate the correct amplitude of the first peak with respect to the higher frequency response (after the effects of the remaining peaks had died out). However, as expected, the intermediate peaks were not accurately modelled when these eigenvectors were included. It was found that in the intermediate region, the eigenvectors could be completely ignored and the relative amplitude of the peaks could be adjusted using only the damping ratios and natural frequencies. The accuracy with this method was not a high as would be ideally desired since the anti-resonance information is contained in the amplitude multipliers, which depend on the system eigenvectors. To take advantage of the unexpected low frequency benefits of the eigenvectors given by the parameterised model, different models were used in different frequency ranges.

4.1.5 Industrial Manipulator Optimisation

The configuration optimisation with the parameterised model was unable to identify an optimum configuration at the first resonance due to the high sensitivity in the FRF around the peak and the small variances in the actual peak frequency between the configurations that become insignificant when compared to the signal noise. This trend was noticed in all regions where the dynamics of the system were relatively smooth. However, the configuration became relevant when comparing the 50-60Hz region of the different FRFs. Due to the increase in the configuration dependent dynamics in this range, the optimisation could be verified with the measured data and was found to accurately predict general trends with enough accuracy to be useful when machining. However, the optimisation still did not identify the trends exactly, particularly for the more extreme configurations.

Frequency optimisation with the industrial manipulator was limited by the anti-resonance errors as observed in the dynamic model parameterisation. Within this limitation however, the optimisation was found to be effective at identifying a desirable, if not optimum, frequency for operation. An additional beneficial characteristic of the frequency optimisation is that the worse case number of local minima is known and the approximate locations of each can be identified from the frequency locations of the resonance peaks. The region of accuracy for the model was also identified by comparing the modelled response at very high frequencies to the measured response at equivalent frequencies. It was established from the measured FRFs that the model reaches a frequency of constant returns after which point there is no benefit or penalty associated with increasing the frequency since the measured FRFs at these frequencies typically become extremely volatile and the benefits neither frequency nor configuration cannot be accurately measured. Conversely, the model continues to suggest reduced receptance with increasing frequency. This characteristic is common to all types of mechanism, although machines such as high precision CNC tools exhibit this characteristic at much higher frequencies and with lower receptance values due to the higher apparent stiffness of the mechanisms even after the introduction of control laws to increase the system bandwidth.

4.1.6 Redundant Manipulator Optimisation

The restricted configurations identified as problematic for the industrial manipulator were overcome in simulation by using a redundant six link planar manipulator. This ensured that the FRFs would vary significantly with configuration and also removed the experimental noise that was partially preventing verification of the optimisations for the industrial manipulator. Initially, unrestricted optimisation showed that the redundant manipulator generally converged to a vertical singularity. When the end-effector location was maintained and the optimisation was relegated to the manipulator null space, this trend continued with some notable exceptions corresponding to different mechanism in the optimisation and escaping local minima.

Two key results of the optimisation were identified this way. The first was the general improvement to the FRF by moving toward the singularity, and the second was the frequency specific pole placement effects. This first could be duplicated by using a weighted mobility measure using joint stiffness to weigh the DOF. This enabled the frequency specific results to be seen and by comparing the receptance optimised configuration to the stiffness optimised configuration. Although different for each machining point and operating frequency, the frequency optimisation generally performed better than the stiffness optimisation.

The exception to the trend above occurred when the optimisation gains were increased too far. In this case the manipulator moved to a sub-optimal local minimum by escaping the well of the initial local minimum, which offered a more beneficial solution. In order to keep the solution in the original locality, the optimisation gains had to be reduced, which prevented the optimisation from reaching the optimal configuration in the allotted time. The global solution was therefore the stiffness optimisation although the difference in the three optimised configurations was very small when compared to the improvement with respect to the initial configuration.

4.2 Conclusions

4.2.1 Dynamic Modelling and Parameterisation

In order to gain an accurate dynamic model through modal analysis, the complete set of modal data is required. When the mode shape vectors are not accurately identified, the parameterised model will not be able to accurately capture the frequency response of the system. This is particularly true of the anti-resonances, which were inaccurately placed by the reconstructed and predicted FRF curves. However, to create a useful model with reasonable accuracy, it is possible to use a subset of the data and rely on only the poles of the system for large sections of the model. This gives accurate FRF reconstructions in the range used to parameterise the model with the exception of the first peak, which was modelled with severely reduced amplitude. This can be corrected by using a two part model, but still generally fails outside the configuration range used for parameterisation due to the nonlinearities absorbed by the linear model.

4.2.2 Optimisation

Though the model was erroneous as mentioned above, it was beneficial in certain situations; particularly in the frequency regions where the manipulator dynamics were dominant. The model was better able to identify the resonances than the anti-resonances, however when used to minimise the receptance the optimisation successfully avoided the resonance peaks and improved performance. In other frequency regions the benefits of configuration were measured as negligible and thus there was no disadvantage to reconfiguring the manipulator. Thus it can be concluded that the optimisation is potentially beneficial and, when the model is not beneficial, will not produce configurations that degrade the performance of the manipulator significantly.

Frequency optimisation highlighted the errors with the dynamic model and suffered from the inaccurate anti-resonance placement in the model. The local minima were placed in the correct regions by the model; however the exact frequencies and thus the final receptance values were inaccurate. Where there was no disadvantage to the optimisation errors in the configuration optimisation, there was a clear and significant difference in the measured and predicted receptance for the frequency optimisation. A redeeming feature of the frequency optimisation is that the general locations of the local minima are all known at all times from the poles of the FRF at a given configuration and thus a global minimum can always be identified. From this it was concluded that for this model the frequency optimisation is only advantageous when trying to avoid resonance peaks. Identifying the true local minima is beyond the capability of the erroneous model.

Redundancy successfully overcame the limitations of the Fanuc S-360 manipulator when trying to get significant receptance variance with configuration. Two mechanisms were identified for the receptance optimisation allowing the frequency effects to be seen directly by comparing a receptance optimisation to a rigid body stiffness optimisation. The improvements varied for different operating frequencies; however the receptance optimisation consistently performed better than the rigid body stiffness optimisation. From this it was concluded that including frequency effects in the configuration selection is a superior method to reducing the vibration susceptibility of a manipulator. A further conclusion seen from the effects of increasing the optimisation gain too far is that the implementation of the optimisation must be considered to prevent the gradient from failing to reach the true local minimum or from escaping a local minimum and moving to a less optimal configuration.

4.3 Applications and Future Work

4.3.1 Applications of this Work

Robotic machining is moving toward harder materials in order to reduce the costs associated with CNC machining where possible and also to reduce the number of workers in hazardous environments. Previous work has been carried out for optimising the posture of industrial manipulators for machining operations such as grinding and pre-machining; however the effects of vibrations have been neglected when selecting postures to date. This work stands as an improvement on the current techniques to compensate for natural frequencies in the manipulators that could be unknowingly excited using existing posture measures.

The ideal application of posture optimisation with frequency consideration is when working with rotary tools and specifically when using a redundant kinematic system. The redundancy gives the manipulator a greater opportunity to reconfigure while performing a given task. Without this the manipulator will be unable to improve its dynamic characteristics without moving the end-effector to a different position in the workspace, which will significantly reduce the effective workspace and therefore the applications of the manipulator.

Additionally, this optimisation can be applied to any manipulator application where external or even self excitation is important since the excitation frequency can be set to 0Hz. The apparent compliance at a given frequency can be relevant to all workspace applications where force interactions are required at speed, or when self excited deflection needs to be controlled while travelling at speed.

4.3.2 Locally Weighted Models

The limited range of the linearised model is supported by the concept of Locally Weighted Learning (LWL) advocated by Schaal *et al.*[107] in machine learning for various complex tasks. The stated key concept is to use a series of linear models to approximate nonlinear functions over a large domain. This way, when the effects of a certain machine or task characteristic are absent for a given situation, a neural network learning algorithm is not required to forget useful information that is simply not relevant in the current circumstance. The set of models developed by the LWL process then gives a set of simplified models when only a subset of the system or task characteristics need to be considered.

A potential application of this concept is in the parameterisation of the Fanuc S-360 manipulator. It may be beneficial to include or ignore different peaks in different configurations. For example, the 51Hz peak, though still relevant in terms of amplitude, quickly becomes very narrow as the manipulator moves away from Configuration 1. While it cannot be neglected throughout the configuration space as the 33Hz peak was, it is none-the-less unimportant to the overall FRF in several configurations. In the configurations where this peak can be ignored, a second model could be introduced with fewer DOF and parameterised to match the remaining frequency data. The 38Hz peak shown in Figure 4.1 could also benefit from the use of multiple models.

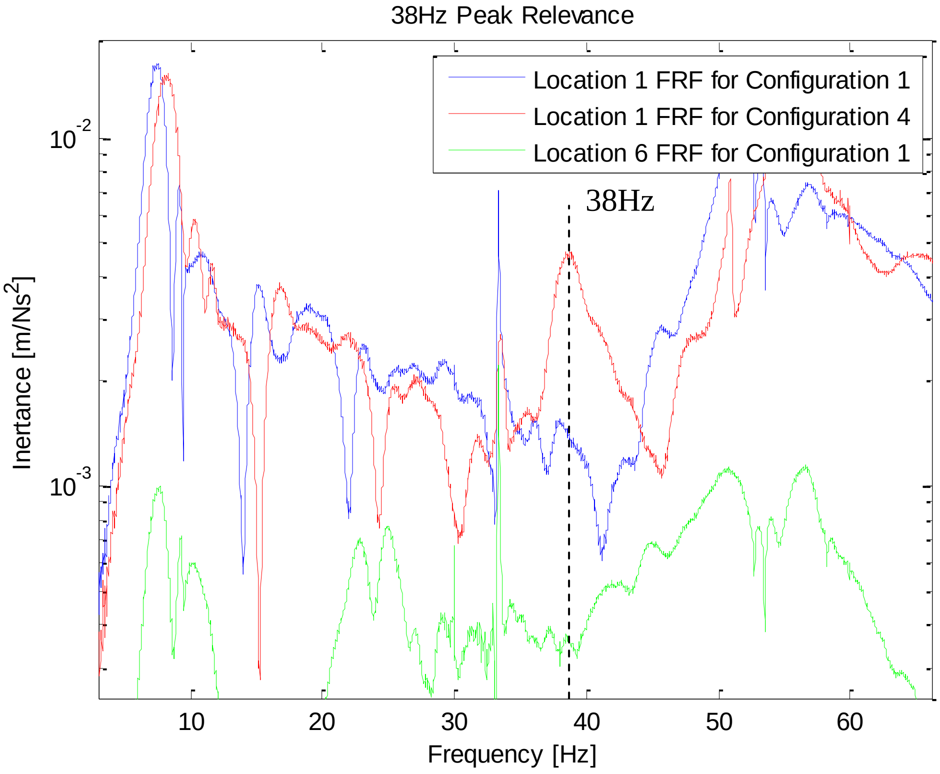

Figure 4.1: 38Hz Peak Variance with Configuration

There is a lack of relevance for the 38Hz peak for Configuration 1 when compared to Configuration 4 and in general it was not deemed important enough to be included in the model. This peak is within the amplitude range of the measurement noise in Configuration 1, whereas it is a crucial part of the inertance in Configuration 4. The declining relevance of the peak as the measurement point moves away from the end-effector is also clear. At the parameterisation configurations (Configurations 1, 2, 6, and 7), this peak was not well enough defined at each of the measurement locations for the mode shapes to be identified with any level of confidence as can be seen from Appendix C. Often the damping ratio and natural frequency had to be manually entered to get plausible results. An additional DOF could therefore not be parameterised since the mode shape vectors and poles were unidentified and so the peak was neglected. Conversely, in configuration 4 this peak is very relevant to the measured FRF. The implication here is that a single model for this range, while accurately identifying the peaks selected for the model parameterisation, was forced to neglect an important characteristic at Configuration 4. A multiple model approach would have been able to better identify this peak by adding another DOF for the region between Configurations 3 and 5, where the 38Hz peak is an important part of the manipulator FRF.

In addition to improving the order of the model in a particular range, multiple models would also improve the accuracy of the individual models in the reduced ranges. The un-modelled nonlinear dynamics such as the characteristics of harmonic drives cause errors in the model since they are absorbed into a model which does not contain the corresponding parameters. The effects are then falsely included in the model parameters used and. as the configurations considered move away from the identification configurations, these errors will be amplified and reduce the effectiveness of the model.

4.3.3 Extension to Multiple Axes

The stiffness measure used in chapter 3 was defined for an arbitrary projected axis, which in that instance was the vertical direction. The same was done with the receptance through the transformation Jacobian TR, which controlled the projection onto the measurement axes, which were also vertical. The same method can be used to transform the joint space model onto any arbitrary axis. The axes do not need to be decoupled to include, for example, the horizontal deflection. Defining an additional transformation Jacobian TS as

$$\dot{\boldsymbol{Z}}_H = [TS]\dot{\boldsymbol{q}}, \tag{4.1}$$

where $\dot{\boldsymbol{Z}}_H$ is the set of horizontal measurement axes, allows both axes to be considered. For a three dimensional model, a third transformation Jacobian can be added and similarly the angular deflections can also be included. This is useful for the parameterisation of the model as it allows more information to be included by simply concatenating the errors from the different FRFs in a least squares optimisation as was performed when identifying the dynamic parameters for multiple configurations simultaneously.

However, when using this process for prediction, the objective function must be expanded to include the additional axes and, more importantly, the coupling of these axes. The coupling relationship between the receptance of the two axes can be approximated assuming that the Jacobians are constant with deflection. Though not strictly accurate, the assumption is reasonable for very small deflections. The deflection on the measurement space axes can be approximated as

$$\boldsymbol{Z} = [TR]\boldsymbol{q} \tag{4.2a}$$

$$\boldsymbol{Z}_H = [TS]\boldsymbol{q} \tag{4.2b}$$

and recalling the force projections

$$\boldsymbol{\tau} = [TR]^T\boldsymbol{F}_z \tag{4.3a}$$

$$\boldsymbol{\tau} = [TS]^T\boldsymbol{F}_H \tag{4.3b}$$

where $\boldsymbol{F_z}$ and $\boldsymbol{F}_H$ are the applied force on the $\boldsymbol{Z}$ and $\boldsymbol{Z}_H$ axes respectively. The joint space receptance can be expressed as

$$\boldsymbol{\delta}_q = \boldsymbol{q}\boldsymbol{\tau}^{-1} \tag{4.4a}$$

and equivalently for the two measurement space axes

$$\boldsymbol{\delta}_z = \boldsymbol{Z}\boldsymbol{F}_z^{-1} \tag{4.4b}$$

$$\boldsymbol{\delta}_H = \boldsymbol{Z}_H\boldsymbol{F}_H^{-1} \tag{4.4c}$$

Substituting (4.3) and (4.4) into (4.5a) and solving for $\boldsymbol{\delta}_q$ yields

$$\boldsymbol{\delta}_q = [TR]^{-1}\boldsymbol{\delta}_z[TR]^{-T} \tag{4.5a}$$

$$\boldsymbol{\delta}_q = [TS]^{-1}\boldsymbol{\delta}_H[TS]^{-T} \tag{4.5b}$$

Equating (4.5a) and (4.5b) and solving for $\boldsymbol{\delta}_H$ yields

$$\boldsymbol{\delta}_H = [TS][TR]^{-1}\boldsymbol{\delta}_z[TR]^{-T}[TS]^T \tag{4.6}$$

An equivalent transformation can be used for any number of coupled axes. The total amplitude of a coupled axis also requires considering the coupling term from the other excitation axes. For these terms, the excitation axis a similar derivation is used. Solving (4.2a) for $\boldsymbol{q}$ and substituting into (4.2b) gives

$$\boldsymbol{Z}_H = [TS][TR]^{-1}\boldsymbol{Z} \tag{4.7}$$

and so

$$\boldsymbol{Z}_H\boldsymbol{F}_z = [TS][TR]^{-1}\boldsymbol{\delta}_z \tag{4.8}$$

gives the coupling term that relates the response along the horizontal axes for vertical excitation.

A new objective function needs to be identified for evaluating different postures with coupled axes. One application specific option is a weighted sum of receptance amplitudes. This requires that the model be accurate in amplitude rather than simply for the trends observed and would allow the variance in machining forces on different axes to be included. A simpler function may simply sum the deflections on reach axis and use a vector norm to generate a single value. Extension to multiple axes with axis coupling considered would create a valuable tool for predicting the deflection of a manipulator when exposed to oscillatory external vibrations.

References

[1] Munasinghe, S.R. Nakamura, M., Goto, S., and Kyura, N. "Optimum Contouring of Industrial Robot Arms, under Assigned Velocity and Torque Constraints," *IEEE Trans. Systems, Man, and Cybernetics-Part C: Applications and Reviews*, Vol. 31(2), pp. 159-167, 2001.

[2] Quaid, A.E. and Hollis, R.L. "Cooperative 2-DOF Robots for Precision Assembly," *Proc. IEEE Int. Conf. Robotics and Automation*, Minneapolis, 1996.

[3] Finley, D.S. and Nguyen, N.T. "Surgical Robotics," *Current Surgery*, Vol. 62(2), pp. 262-272, 2005.

[4] Yamane, S., Kaneko, Y., Kitahara, N., Oshima, K., Yamamoto, M. "Neural Network and Fuzzy Control of Weld Pool with Welding Robot," *Industry Application Society Annual Meeting*, Toronto, 1993.

[5] KUKA Roboter GmbH, "Robocoaster," http://www.kuka-robotics.com/en/products/systems/robocoaster/, referenced July 17th 2009.

[6] Groover, M.P. Automation, Production Systems, and Computer-Integrated Manufacturing, 2nd Ed., Prentice Hall Inc., Upper Saddle River, NJ, 2001.

[7] ABB robotics, "IRB 6000 for premachining," Accessed 5 August 2009. http://www.abb.com/product/seitp327/cb6581d257fb24ccc12573fe003d9436.aspx.

[8] Kazerooni, H. "Automated Robotic Deburring Using Impedance Control," *Control Systems Magazine*, Vol. 8(1), pp.21-25, 1988.

[9] Güvenç, L. and Srinivasan, K. "An Overview of Robot-Assisted Die and Mold Polishing with Emphasis on Process Modeling," *J. Manufacturing Systems*, Vol. 16(1), pp. 48-58, 1997.

[10] Wander, J. Hudgens, J., Aalund, M. and Tesar, D. "Precision Routing by an Industrial Robot using Deflection Compensation," *Proc. of Manufacturing International*, pp. 101-114, 1992.

[11] Tangelder, J.W.H. and Vergeest, J.S.M. "Robust NC Path Generation for Rapid Shape Prototyping," *J. Design and Manufacturing*, Vol. 4, pp. 281-292, 1994.

[12] Huang, H.K. and Lin, G.C.I. "Rapid and Flexible Prototyping through a Dual Robot Work Cell," *J. Robotics and Computer Integrated Manufacturing*, Vol. 15, pp. 263-272, 2003.

[13] Pan, X., Zhang, H., Zhu, Z., and Wang, J. "Chatter Analysis of Robotic Machining Process," *J. Materials Processing Technology*, Vol. 173(3), pp. 301-309, 2006.

[14] Altintas, Y. and Erkorkmaz, K. "Feedrate Optimisation for Spline Interpolation in High Speed Machine Tools," *CIRP Annals – Manufacturing Technology,* Vol. 52(1), pp. 297-302, 2003.

[15] Slotine, J-J, E. and Li, W. "On the Adaptive Control of Robot Manipulators," *Int. J. Robotics Research,* Vol. 6(3), pp.49-59, 1987.

[16] Delcam, "Delcam and KUKA Launch Machining by Robot", Press Release, 28 July 2005.

[17] ABB Robotics, "ABB Announces the Optimised Pre Machining Robot", Press Release, 6 March 2008.

[18] Ko, H., Kim, M-H, Park, H-G, and Kim, S-W. "Face Sculpturing Robot with Recognition Capability," *J. Computer Aided Design,* Vol. 26(11), pp. 814-821, 1994.

[19] Song, Y. and Chen, Y.H. "Feature Based Robot Machining Rapid Prototyping," *Proc. Institution of Mech. Eng. Part B: Journal of Engineering Manufacture,* Vol. 23 (5), pp. 451-459, 1999.

[20] Matsuoka, S-I, Shimizu, K., Yamazaki, N., and Oki, Y. "High Speed End Milling of an Articulated Robot and its Characteristics," *J. Materials Processing Technology,* Vol. 85, pp. 83-89, 1999.

[21] Coole, T.J., Cheshire, D.G., Mesquita, R.M.D., and Simões, J.F.C.P.A. "Analysis of Robot System Capabilities in Machining of Full Scale Prototypes for Sanitary Ware Industry," *British Ceramic Transactions*, Vol. 99(4), pp. 175-178, 2000.

[22] Simões, J.F.C.P.A., Coole, T.J., Cheshire, D.G., and Pires, A.R. "Analysis of Multi-axis Milling in an Anthropomorphic Robot Using the Design of Experiments Methodology," *J. Material Processing Technology*, Vol. 135, pp. 235-241, 2003.

[23] Zhang H., Wang, J., Zhang, G., Gan, Z., Pan, Z., Cui, H., Zhu, Z. "Machining with Flexible Manipulator: Toward Improving Robotic Machining Performance," *Proc. ASME/IEEE Int. Conf. Advanced Intelligent Mechatronics*. Monterey, USA. 24-28 July, 2005.

[24] Dimo, H.O., Jin, D., Zhang, J., and Gruver, W.A. "Vibration Control of a Redundant Robot for Grinding," *IEEE Int. Conf. System, Man, and Cybernetics,* Vol. 1, pp. 389-394, 2001.

[25] De Silva, C.W., Vibration Fundamentals and Practice, CRC Press, New York, 2000.

[26] Chen, Y.H. and Hu, Y.N. "Implementation of a Robot System for Sculptured Surface Cutting. Part1. Rough Machining," *J. Advanced Manufacturing Technology,* Vol. 15, pp. 624-629, 1999.

[27] Spong, M.W. "Modelling and Control of Elastic Joint Robots," *J. Dynamic Systems, Measurement, and Control*, Vol. 109(4), pp. 310-319, 1987.

[28] Alici, G. and Shirinzadeh, B. "Enhanced Stiffness Modeling, Identification, and Characterization for Robot Manipulators" *IEEE Trans. on Robotics*, Vol. 21(4), pp. 554-564, 2005.

[29] Abele, E., Weigold, M., and Rothenbücher, S. "Modelling and Identification of an Industrial Robot for Machining Applications," *Annals of the CIRP*, Vol. 56, pp. 387-390, 2007.

[30] Abele, E., Weigold, M., and Rothenbücher, S. "Cartesian Compliance Model for Industrial Robots using Virtual Joints," *J. Production Engineering, Research and Development*, Vol. 2, pp. 339-343, 2008.

[31] Chan, S.P. "An Efficient Algorithm for Identification of Robot Parameters Including Drive Characteristics," *J. Intelligent Robotic Systems*, Vol. 32, pp. 291-305, 2001.

[32] Hovtun, R. "Multiaxis Technology: Challenges to Overcome," *J. Manufacturing Engineering*, Vol. 123(2), pp. 104-116, 1999.

[33] Hung, J.Y. "Control of Industrial Robots that have Transmission Elasticity," *IEEE Trans. Industrial Electronics*, Vol. 38(6), pp. 421-427, 1991.

[34] Bridges, M.M. and Dawson, D.M. "Redesign of Robust Controllers for Rigid-Link Flexible-Joint Robotic Manipulators with Harmonic Drive Gearing," *IEE Proc. Control Theory and Applications*, Vol. 142 (5), pp. 508-514, 1995.

[35] Tjahjowidodo, T., Al-Bender, F., Van Brussel, H. "Nonlinear Modelling and Identification of Torsional Behaviour in Harmonic Drives," *Proc. of the ISMA Conference*, Leuven, Belgium, pp. 2785-2796, 2006.

[36] Tjahjowidodo T., Al-Bender, F., Van Brussel ,H., and Symens, W. "Positioning Controller for Mechanical Systems with a Mini Harmonic Drive Servo Actuator", *IEEE/ASME Int. Conf. Advanced Intelligent Mechatronics*, 4-7 Sept, pp. 1-6, 2007.

[37] Power Transmission Engineering, "The Basics of Harmonic Drive Gearing," Accessed 5 August 2009, http://www.powertransmission.com/issues/0706/harmonic.htm.

[38] Yoshikawa, T. "Manipulability of Robotic Mechanisms," *Int. J. Robotics Research*, Vol. 4, pp. 3-9, 1985.

[39] Chiu S.L. "Task Compatibility of Manipulator Postures," *Int. J. Robotics Research*, Vol. 7(13), pp. 13-21, 1988.

[40] Chiacchio, P., Chiaverini, S., Sciavicco, L., and Siciliano, B. "Global Task Space Manipulability Ellipsoids for Multiple-Arm Systems" *IEEE Trans. Robotics and Automation*, Vol. 7(5), pp. 678-682, 1991.

[41] Chiacchio, P., Boufard-Vercelli, Y., and Pierrot, F. "Force Polytope and Force Ellipsoid for Redundant Manipulators", *J. Robotic Systems*, Vol. 14(8), pp. 613-620, 1997.

[42] Walker, I.D. "Impact Configurations and Measures for Kinematically Redundant and Multiple Armed Robot Systems" *IEEE Trans. Robotics and Automation*, Vol. 10(5), pp. 670-683, 1994.

[43] Young, K.Y., Mao, C.C., and Shih, C.C. "Posture Measure for Control of Robot Compliance Tasks," *J. Robotic Systems*, Vol. 15(11), pp. 625-640, 1998.

[44] Owen, W.S., Croft, E.A., Benhabib, B. "A Multi-Arm Robotic System for Optimal Sculpting," *J. Robotics and Computer Integrated Manufacturing*, Vol. 24(1), pp. 92-104, 2008.

[45] Zhang, Y. and Ma, S. "Minimum-Energy Redundancy Resolution of Robot Manipulators Unified by Quadratic Programming and its Online Solution," *Proc. IEEE Int. Conf. Mechatronics and Automation*, 5-7 August, Harbin, China, 2007.

[46] Ding, H. and Chan, S.P. "A Real-Time Planning Algorithm for Obstacle Avoidance of Redundant Robots", *J. Intelligent Robotic Systems*, Vol. 16, pp. 229-243, 2006.

[47] Chan, T.F. and Dubey, R.V. "A Weighted Least Norm Solution Based Scheme for Avoiding Joint Limits for Redundant Joint Manipulators," *IEEE Trans. on Robotics and Automation*, Vol. 11(2), pp. 286-292, 1995.

[48] Chiaverini, S. "Singularity-Robust Task-Priority Redundancy Resolution for Real-Time Kinematic Control of Robot Manipulators," *IEEE Trans. on Robotics and Automation*, Vol. 13(3), pp. 398-410, 1997.

[49] Shim, I.C. and Yoon, Y.S. "Stabilized Minimum Infinity-Norm Torque Solution for Redundant Manipulators", *Robotica*, Vol. 16, pp. 193-205, 1998.

[50] Kazerounian, K. and Wang, Z. "Global Versus Local Optimisation in Redundancy Resolution of Robotic Manipulators," *Int. J. Robotics Research*, Vol. 7, pp. 3-12, 1988.

[51] Lim, S.Y., Hu, J., Dawson, D.M., deQueiroz, M. "A Partial State Feedback Controller for Trajectory Tracking of Rigid Link Flexible Joint Robots using an Observed Backstepping Approach," *Proc. of the American Control Conference*, Seattle, USA, June 1995.

[52] Ghorbel, F., Hung, J.Y., Spong, M.W. "Adaptive Control of Flexible Joint Manipulators," *IEEE Control Systems Magazine*, Vol. 9(7), pp. 9-13, 1989.

[53] Lozano, R. and Brogliato, B. "Adaptive control of Robot Manipulators with Flexible Joints," *IEEE Trans. Automatic Control*, Vol. 37(2), pp. 174-181, 1992.

[54] Brogliato, B., Ortega, O., and Lozano, R. "Global Tracking Controllers for Flexible Joint Manipulators: a Comparative Study," *Automatica*, Vol. 31(7), pp. 941-956, 1995.

[55] deQueiroz, M.S., Donepudi, S., Burg, T., Dawson, D.M. "Model-Based Control of Rigid-Link Flexible-Joint Robots: an Experimental Evaluation," *Robotica*, Vol. 16, pp. 11-21, 1998.

[56] Waibel, B.J., Kazerooni, H. "Theory and Experiments on the Stability or Robot Compliance Control," *IEEE Trans. Robotics and Automation*, Vol. 7(1), pp. 95-104, 1991.

[57] Salisbury, J.K. "Active Stiffness Control of a Manipulator in Cartesian Coordinates," *19th IEEE Conf. Decision and Control including the Symposium on Adaptive Processes*, Vol. 19, pp. 95-100, 1980.

[58] Kubica, E., and Wang, D. "A Fuzzy Control Strategy for a Flexible Single Link Robot", *Proc. of the IEEE Int. Conf. Robotics and Automation*, Atlanta USA, 2-6 May, 1993.

[59] Zuo, K. and Wang, D. "Closed Loop Shaped-Input Control of a Class of Manipulators with a Single Flexible Link", *Proc. IEEE Int. Conf. Robotics and Automation*, Nice, France, May, 1992.

[60] Wang, D. and Vidyasagar, M. "Passive Control of a Stiff Flexible Link: Communication," *Int. J. Robotics Research*, Vol. 11, pp. 572-578, 1992.

[61] Yue, S. "Redundant Robot Manipulators with Joint and Link Flexibility –I. Dynamic Motion Planning for Minimum End Effector Deformation," *J. Mechanism and Machine Theory*, Vol. 33(1), pp. 103-113, 1998.

[62] Yue, S. "Redundant Robot Manipulators with Joint and Link Flexibility –II. Residual Vibration Decreasing," *J. Mechanism and Machine Theory*, Vol. 33(1), pp. 115-122, 1998.

[63] Yue, S. "Weak Vibration Configurations for Flexible Kinematic Redundancy," *J. Mechanism and Machine Theory*, Vol. 35, pp. 165-178, 2000.

[64] Xu, W.L. and Yue, S. “Pre-Posed Configurations of Flexible Redundant Robot Manipulators for Impact Vibration Alleviating,” *IEEE Trans. Industrial Electronics*, Vol. 51(1), pp. 195-200, 2004.

[65] Luo, Z-H, Kitamura, N., and Guo, B-Z. “Shear Force Feedback Control of Flexible Robot Arms,” *IEEE Trans. Robotics and Automation*, Vol. 11(5), pp. 760-765, 1995.

[66] Konno, A., Uchiyama, M., and Murakami, Mahito, M. “Configuration Dependent Controllability of Flexible Link Manipulators,” *Int. J. Robotics Research*, Vol. 16, pp. 567-576, 1997.

[67] Konno, A. and Uchiyama, M. “Vibration Suppression Control of Spatial Flexible Manipulators,” *Control Engineering Practice*, Vol. 3(9), pp. 1315-1321, 1995.

[68] Wang, X. and Mills, J.K. “Modal Control Design of Configuration-Dependent Linkage Vibration in a Parallel Robot through Experimental Identification,” *Proc. IEEE/RSJ Int. Conf. Intelligent Robots and Systems*, Oct. 9-15, Beijing, China, 2006.

[69] Zhang, X. and Yu, Y.Q. “Motion Control of Flexible Manipulators via Optimizing Redundant Configurations,” *J. Mechanism and Machine Theory*, Vol. 36, pp. 883-892, 2001.

[70] Miller, R. Machinists Library: Basic Machine Shop vol. 1, Macmillan Publishing Company, New York, 1965.

[71] Wagner, R. CNC Technician, University of Waterloo, Personal Communication, August, 2009.

[72] Kalpakjian, S. and Schmid, S.R. Manufacturing Processes for Engineering Materials, 5th ed. Prentice Hall. Singapore. 2008.

[73] Radkhah, R., Kulic, D., and Croft, E. “Dynamic Parameter Identification for the CRS A640 Robot,” *Proc. of the IEEE/RSJ Int. Conf. Intelligent Robots and Systems*, San Diego, USA, Oct.29-Nov.2, pp. 3842-3847, 2007.

[74] Atkeson, C.G., and, C.H., and Hollerbach, J.M. “Estimation of Inertial Parameters of Manipulator Loads and Links,” *Int. J. Robotics Research*, Vol. 5, pp. 101-119, 1986.

[75] Khosla, P.K. “Estimation of Robot Dynamics Parameters,” *J. Robotics and Automation*, Vol. 3(1), pp. 35-41, 1988.

[76] Gautier, M. and Khalil, W. “Exciting trajectories for the Identification of Base Inertial Parameters of Robots,” *Int. J. Robotics Research*, Vol. 11, pp. 362-375, 1992.

[77] Presse, C. and Gautier, M. “New Criteria of Exciting Trajectories for Robot Identification,” *Int. Conf. Robotics and Automation*, Vol. 3, pp. 907-912, Atlanta, USA, May, 1993.

[78] Gautier, M. “Dynamic Identification of Robots with Power Model,” *Proc. IEEE Int. Conf. Robotics and Automation*, Alburquerque, New Mexico, April, 1997.

[79] Östring, M., Gunnarsson, S., Norrlöf, M. “Closed Loop Identification of an Industrial Robot Containing Flexibilities,” *J. Control Engineering Practice*, Vol. 11, pp. 291-300, 2003.

[80] Swevers, J., Ganseman, C., Tükel, D.B., and Schutter, J. “Optimal Robot Excitation and Identification,” *IEEE Trans. Robotics and Automation*, Vol. 13(5), pp. 730-740, 1997.

[81] deWit, C.C. and Aubin, A. “Robot Parameter Identification via Sequential Hybrid Estimation Algorithm,” *Proc. IEEE Int. Conf. Robotics and Automation*, Sacremento, U.S.A., April, 1991.

[82] Vandanjon, O., Gautier, M., and Desbats, P. “Identification of Robots Inertial Parameters by Means of Spectrum Analysis,” *Proc. IEEE Conf. Robotics and Automation*, Vol. 3, pp. 3033-3038, May, 1995.

[83] Khalil, W. and Dombre, E. Modeling, Identification, and Control of Robots, Hermes Penton Ltd., London, ON, 2002.

[84] Hsu, P., Bodson, M., Sastry, S., and Paden, B. “Adaptive Identification and Control for Manipulators without using Joint Accelerations,” *Proc. IEEE Int. Conf. Robotics and Automation*, Vol. 4, pp. 1210-1215, 1987.

[85] Reyes, F. and Kelly, R. “Experimental Evaluation of Identification Schemes on a Direct Drive Robot,” *Robotica*, Vol. 15, pp. 563-571, 1997.

[86] Berglund, E. and Hovland, G.E. “Automatic Elasticity Tuning of Industrial Manipulators,” *Proc. 39th IEEE Conf. Decision and Control*, Sydney, Australia, December 12-15, Vol. 5, pp. 5091-5096, 2000.

[87] Albu-Schäffer, A. and Hirzinger, G. “Parameter Identification and Passivity Based Joint Control for a 7DOF Torque Controlled Light Weight Robot,” *Proc. IEEE Conf. Robotics and Automation*, Seoul, Korea, May 21-26, 2001.

[88] Behi, F. and Tesar, D. “Parametric Identification for Industrial Manipulators Using Experimental Modal Analysis,” *IEEE Trans. Robotics and Automation*, Vol. 7(5), pp. 642-652, 1991.

[89] Jacubus, R.F., and Serna, A.M. “Modal Analysis of a Three Dimensional Flexible Robot,” *Proc. IEEE Int. Conf. Robotics and Automation*, pp. 2962-2967, San Diego, USA, 1994.

[90] Huston, R.L. Multibody Dynamics, Butterworth-Heinemann, Toronto, 1990.

[91] Al-Bedoor, B.O. and Almusalam, A.A. “Dynamics of Flexible-link and Flexible-joint Manipulator Carrying a Payload with Rotary Inertia,” *J. Mechanism and Machine Theory*, Vol. 35, pp. 785-820, 2000.

[92] Corke, P.I. “A Symbolic and Numerical Procedure for Manipulator Rigid-Body Dynamic Significance Analysis and Simplification,” *Robotica*, Vol. 16, pp. 589-594, 1998.

[93] Taghirad, H.D. and Bélanger P.R. “Modelling and Parameter Identification of Harmonic Drive Systems” *J. Dynamic Systems, Measurement, and Control*, Vol. 120(4), pp. 439-444, 1998.

[94] Tuttle, T.D. and Seering, W.P. “A Nonlinear Model of a Harmonic Drive Gear Transmission,” *IEEE Trans. Robotics and Automation*, Vol. 12(3), pp. 368-374, 1996.

[95] Wernholt, E. and Gunnarsson, S. “Estimation of Nonlinear effects in Frequency Domain Identification of Industrial Robots,” *IEEE Trans. Instrumentation and Measurement*, Vol. 57(4), pp. 856-863, 2008.

[96] Ewins, D.J. Modal Testing: Theory and Practice, Research Studies Press Ltd. Toronto, 1986.

[97] LMS International, LMS Theory and Background, Software Support Literature, 2000.

[98] Mathworks Inc. Support, http://www.mathworks.com/support, 2009.

[99] Mottershead, J.E., and Friswell, M.I. "Model Updating in Structural Dynamics: A Survey," *J. Sound and Vibration*, Vol. 167(2), pp. 347-375, 1993.

[100] Ewins, D.J. "Adjustment or Updating of Models," *Sadhana*, Vol .25(3), pp. 235-245, 2000.

[101] Pham, D.T. and Karaboga, D. Intelligent Optimisation Techniques: Genetic Algorithms, Tabu Search, Simulated Annealing, and Neural Networks, Springer, 2000.

[102] Owen, H. "Numerical Optimisation Methods: An Introduction," *Online PowerPoint Presentation*, Accelerator Science and Technology Centre, 2003.

[103] Gorniak, J. Masters Candidate, University of Waterloo, Personal Communication, 27 October 2009.

[104] Burdick, J.W. "1. The Moore Penrose Pseudo Inverse" *Course Material,* California Institute of Technology, Department of Mechanical Engineering, 2008.

[105] Ro, P.I., Lee, B.R., and Seelhammer, M.A. "Two-arm Kinematic Posture Optimization for Fixtureless Assembly," *J. of Robotic Systems*, Vol. 12(1), pp. 13-21, 1995.

[106] GMF Robotics Corporation, S-360/S-380 User's Reference Manual marors3681051.

[107] Schaal, S., Atkeson, C.G., and Vijaykumar, S. "Scalable Techniques for Real Time Robot Learning," *Applied Intelligence,* Vol. 17, pp. 49-60, 2002.

Appendices

Appendix A: Effects of Hammer Tips on Repeatability of FRF Measurements

The following figures show the results of experimental modal analysis on the Fanuc S-360 manipulator using soft and hard hammer tips at various locations throughout the structure in Configuration 7 as defined in Table 2.5. Each trial was excited at Location 2 and measured at the labelled locations defined in Figure 2.10. Three trials (trials 1-3) are shown for the softer hammer tip illustrating the repeatability of the soft tip results and single trial (trial 4) is shown for the harder tip for clarity. The repeatability of the hard tip results is equivalent to that of the soft tip results. The data was used to determine the qualitative characteristics of the manipulator vibrations and then the hard tip data was used to for the modal parameter identification using both the LS fit to (2.19) and the circle fit method.

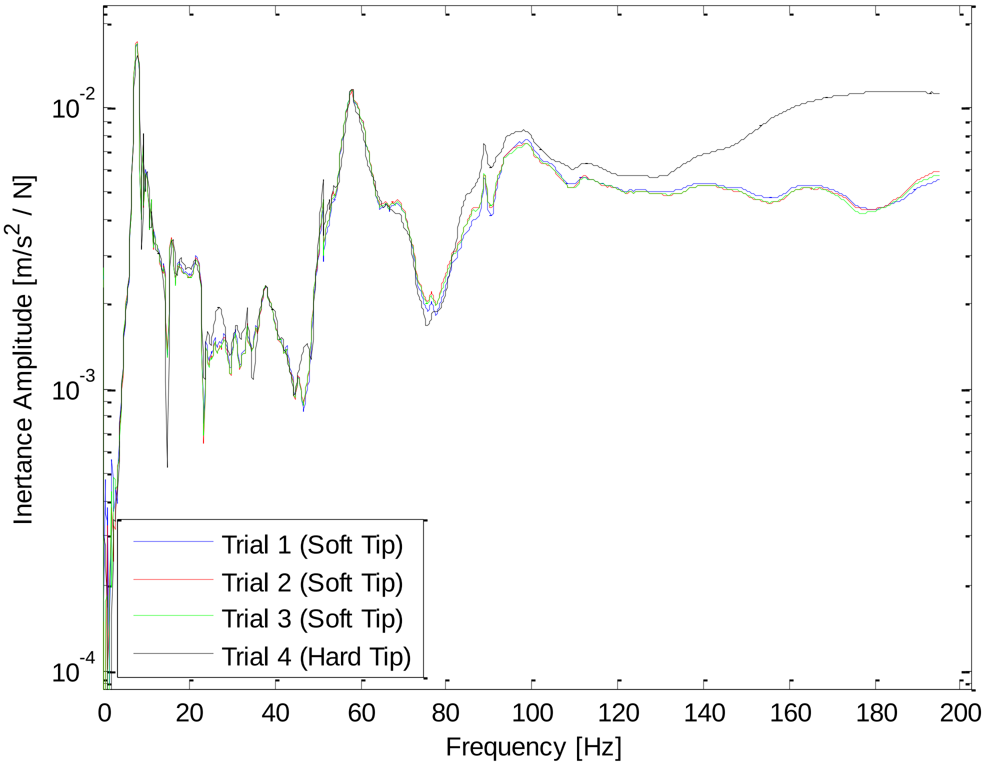

Figure A.1: Location 1 Inertance Response for Multiple Location 2 Excitation Trials with Different Hammer Tips

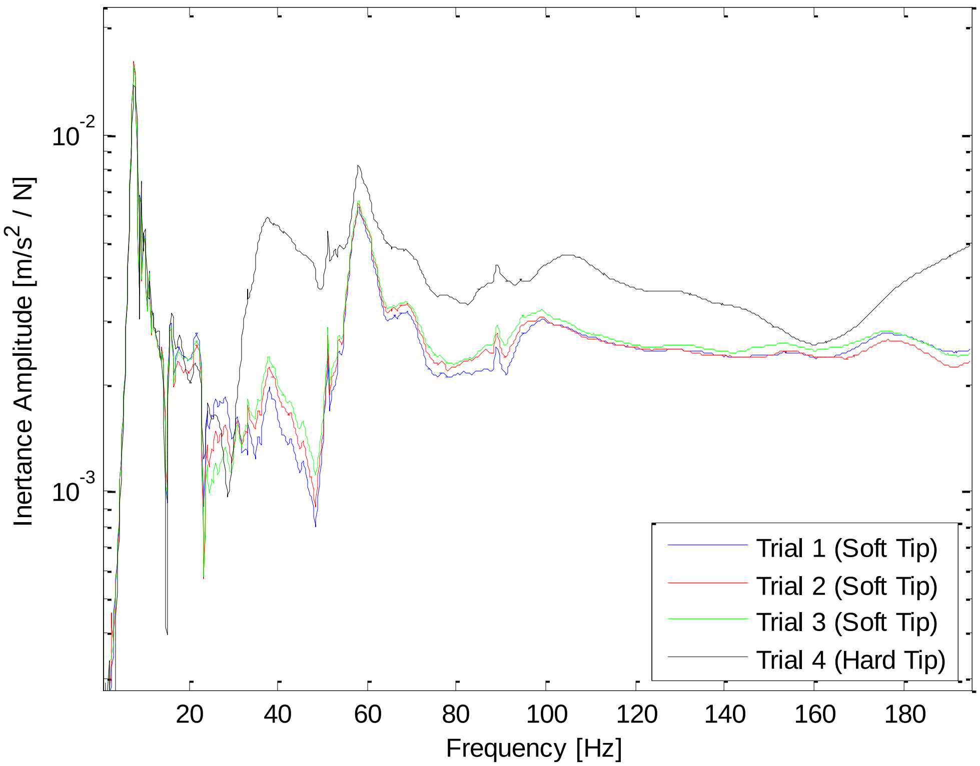

Figure A.2: Location 2 Inertance Response for Multiple Location 2 Excitation Trials with Different Hammer Tips

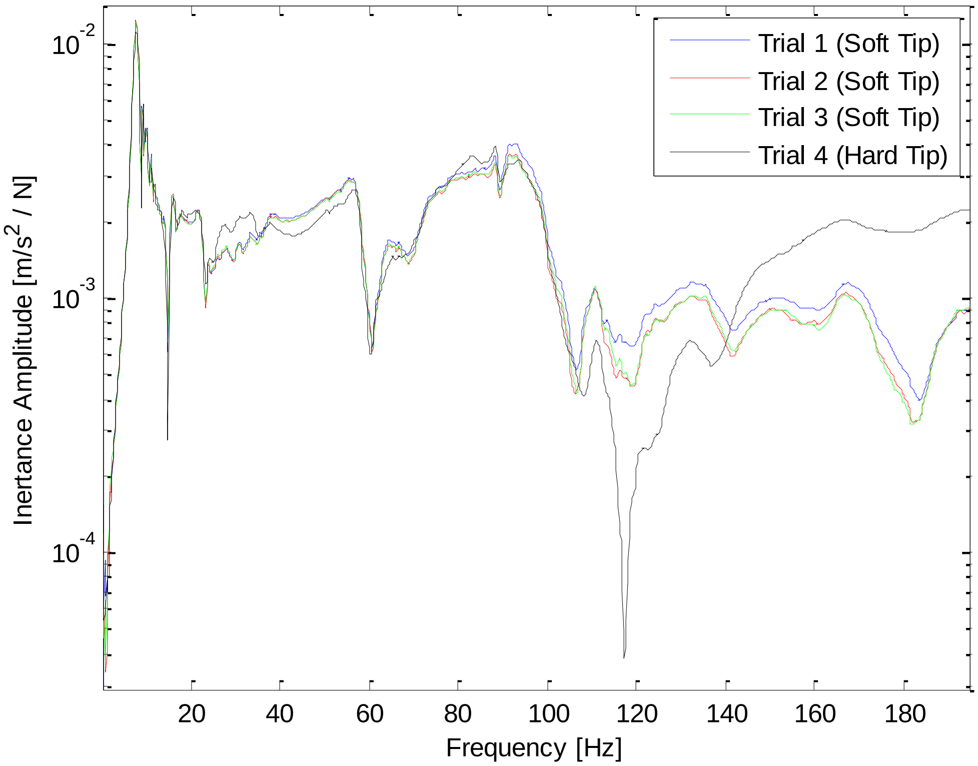

Figure A.3: Location 3 Inertance Response for Multiple Location 2 Excitation Trials with Different Hammer Tips

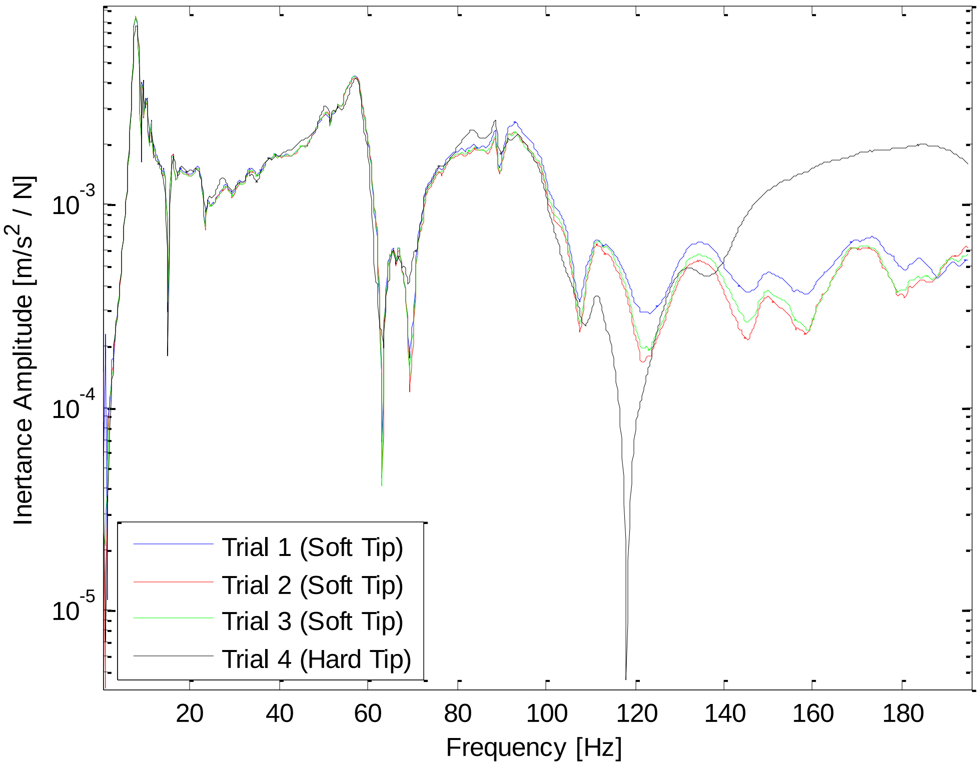

Figure A.4: Location 4 Inertance Response for Multiple Location 2 Excitation Trials with Different Hammer Tips

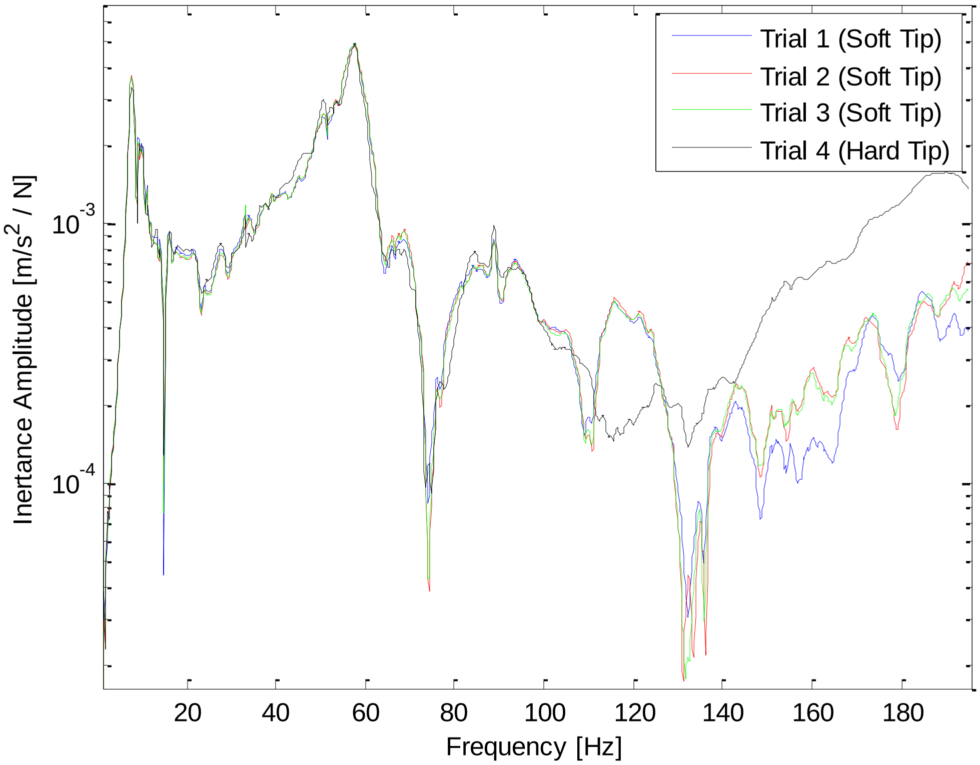

Figure A.5: Location 5 Inertance Response for Multiple Location 2 Excitation Trials with Different Hammer Tips

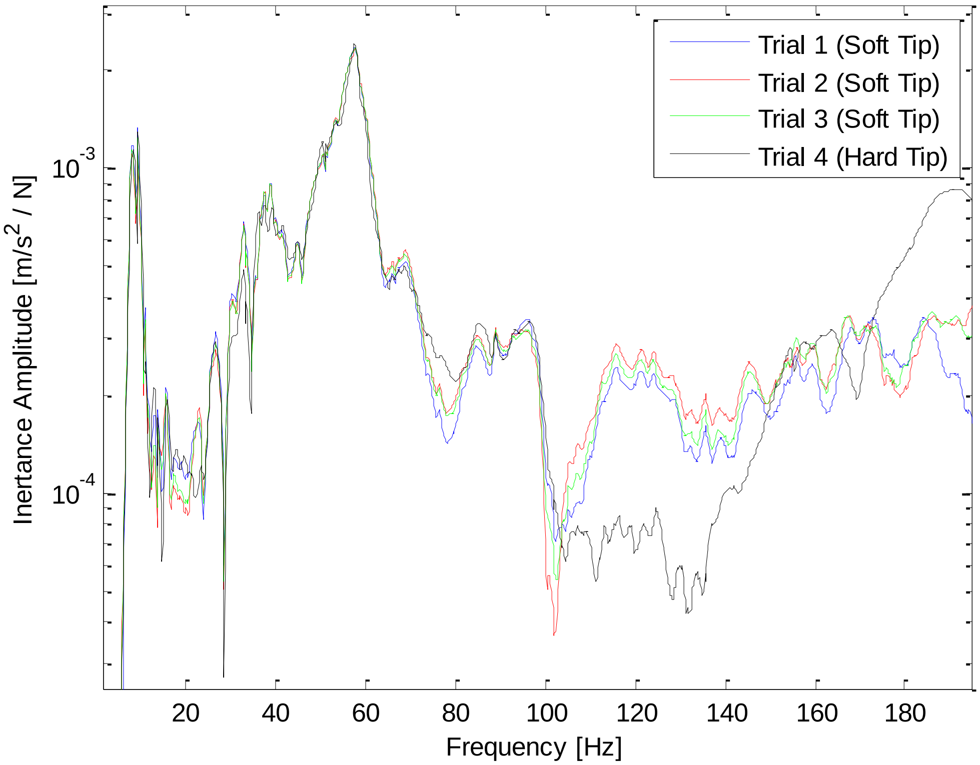

Figure A.6: Location 6 Inertance Response for Multiple Location 2 Excitation Trials with Different Hammer Tips

Appendix B: Repeatability of Flexible Link FRF Measurements

The following figures show the results of experimental modal analysis on the Fanuc S-360 manipulator at various locations throughout the structure in Configuration 7 as defined in Table 2.5. Each trial was excited at Location 2 and measured at the labelled locations defined in Figure 2.10. The three trials illustrate the repeatability of the results used in the identification of the flexible link dynamic characteristics.

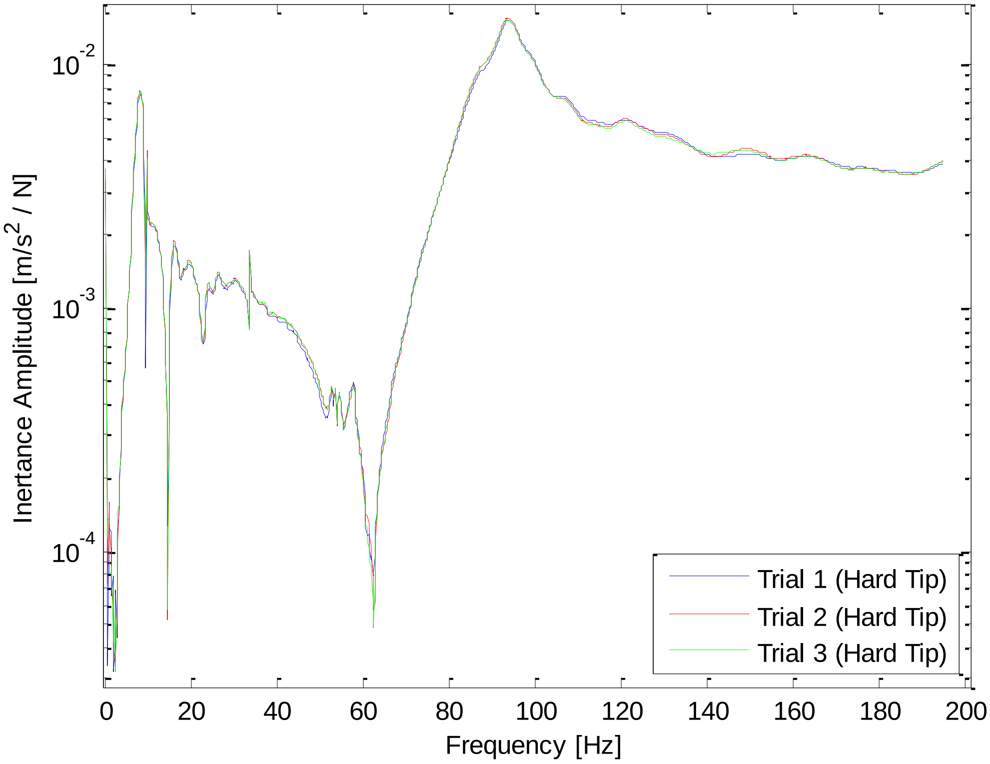

Figure B.1: Multiple Trials of Location 3 Drive Point Inertance Amplitude

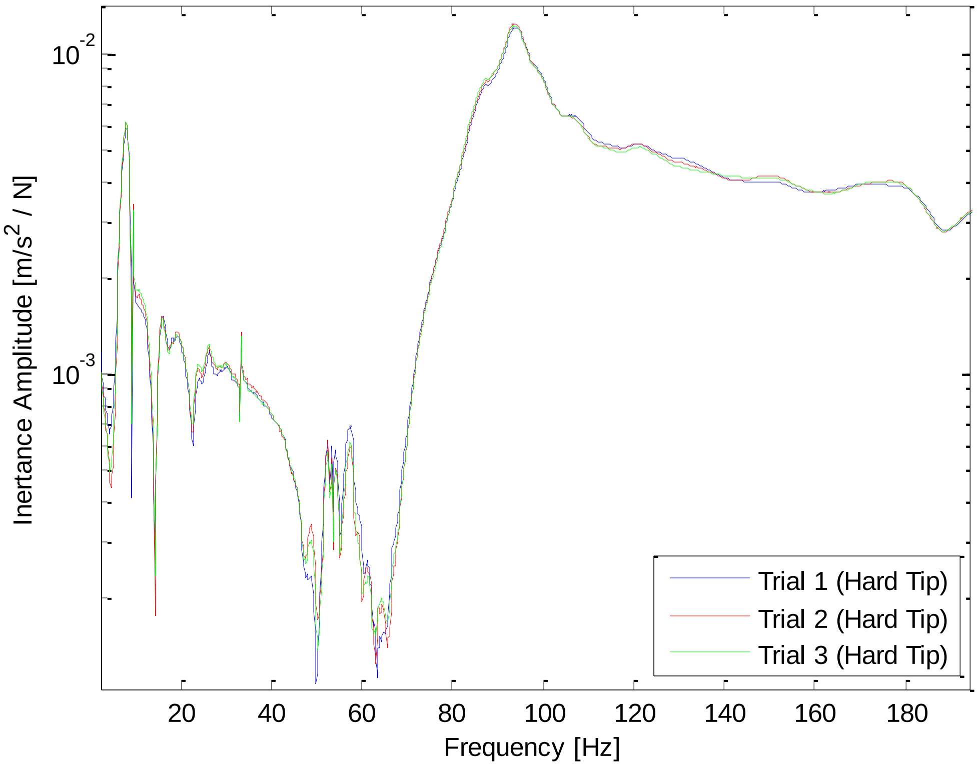

Figure B.2: Flexible Multiple Trials of Location 9 Inertance Amplitude Excited at Location 3

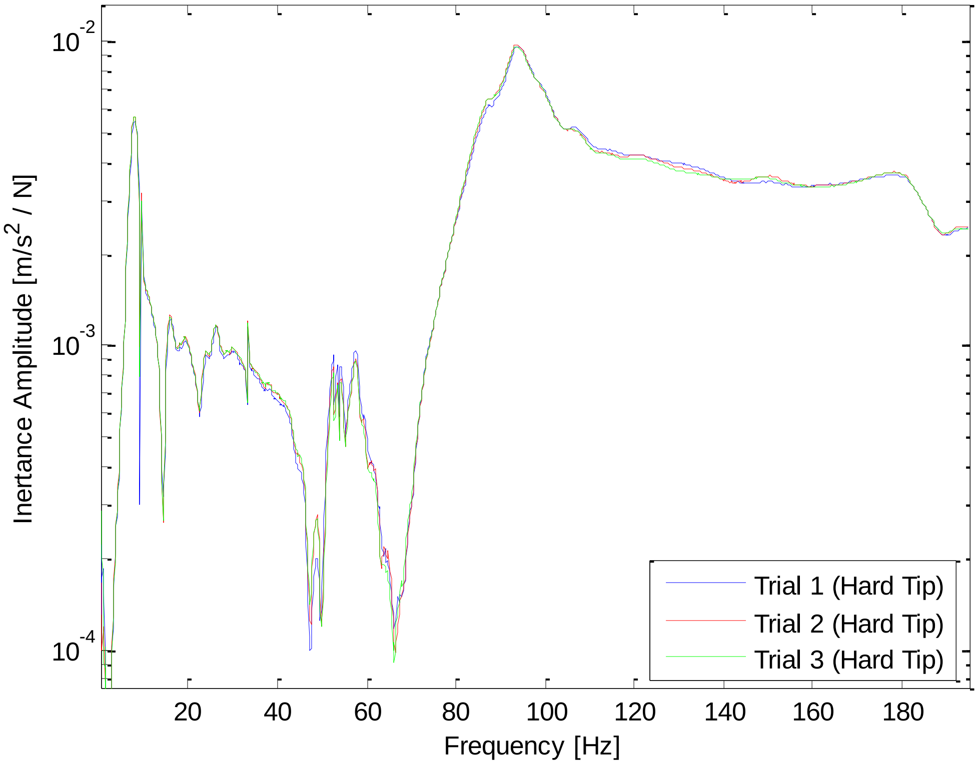

Figure B.3: Flexible Multiple Trials of Location 4 Inertance Amplitude Excited at Location 3

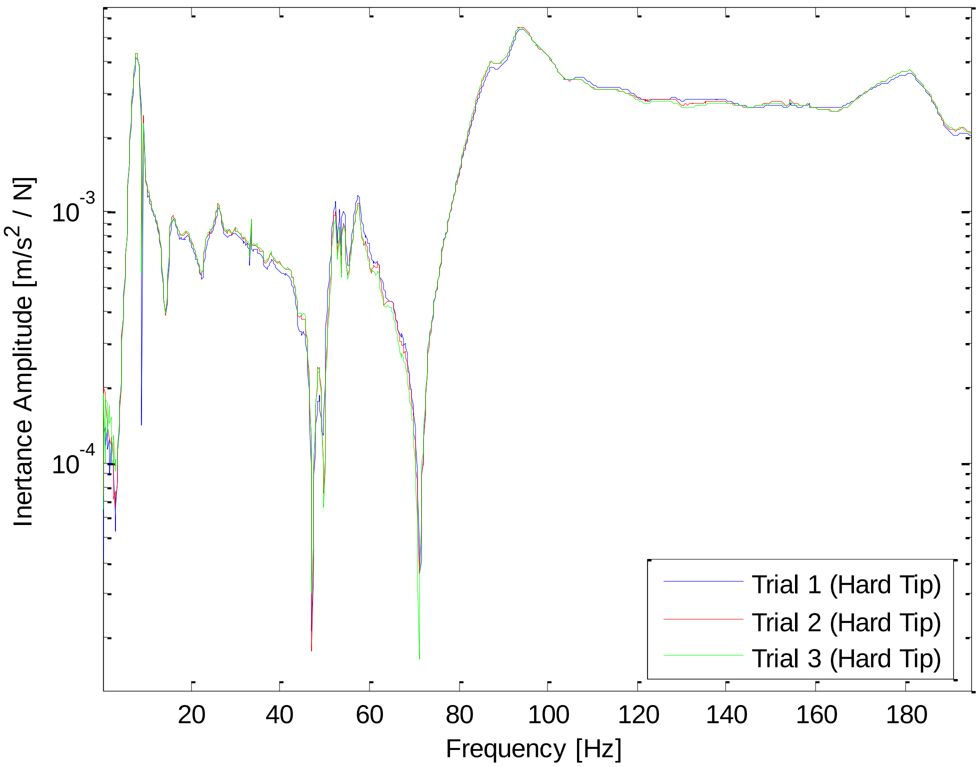

Figure B.4: Flexible Multiple Trials of Location 10 Inertance Amplitude Excited at Location 3

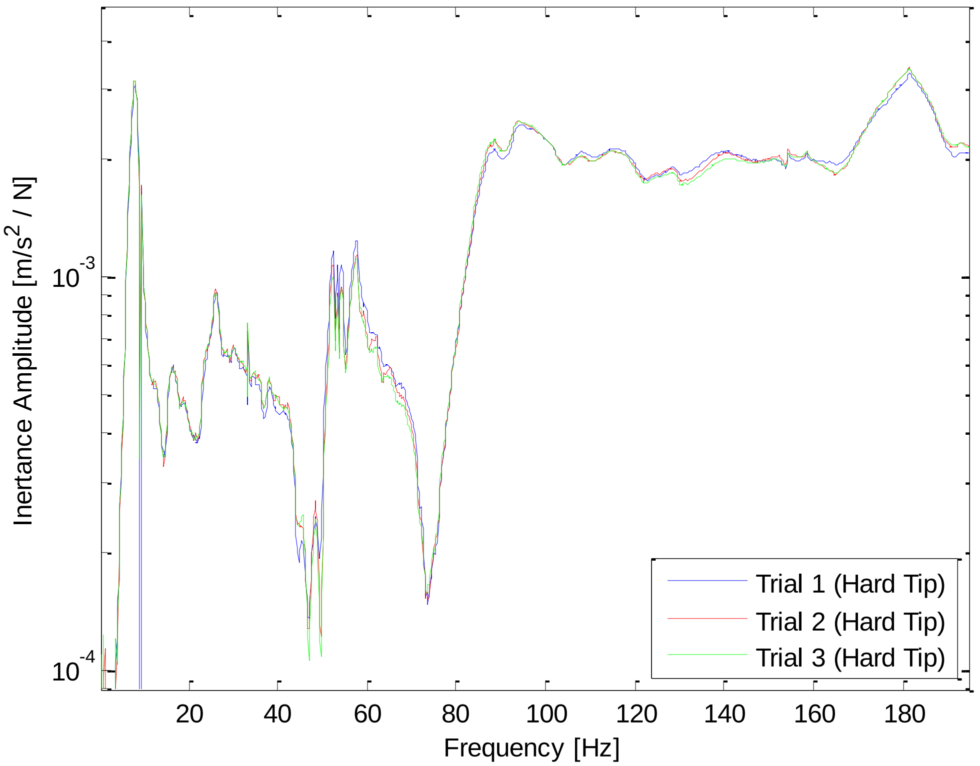

Figure B.5: Flexible Multiple Trials of Location 5 Inertance Amplitude Excited at Location 3

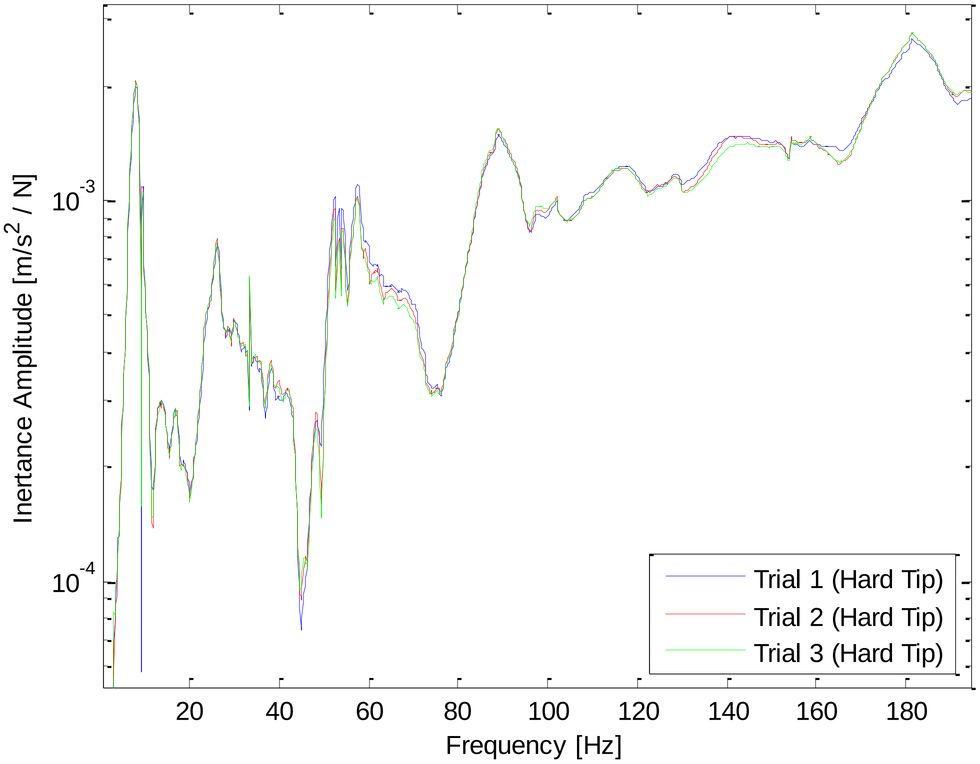

Figure B.6: Flexible Multiple Trials of Location 11 Inertance Amplitude Excited at Location 3

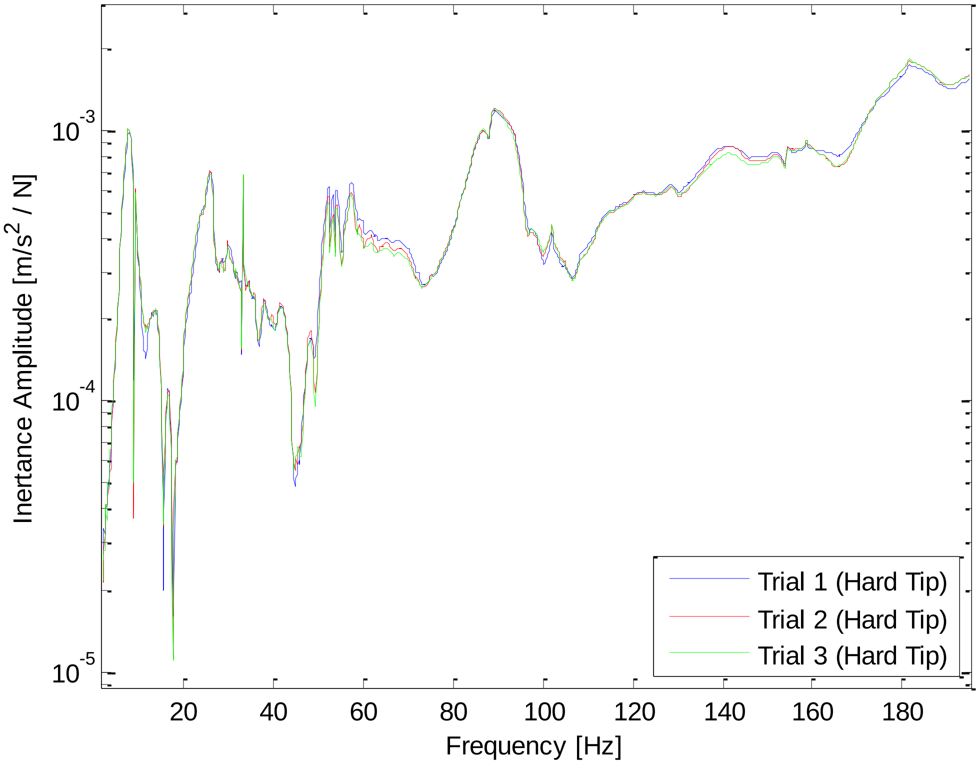

Figure B.7: Flexible Multiple Trials of Location 12 Inertance Amplitude Excited at Location 3

Appendix C: Circle Fit Modal Parameters

The following tables list the modal parameters identified through the circle fit method and, where indicated, the LS fit to (2.19). These values were used to identify the parameters in the dynamic model as outlined in Section 2.6.4. The parameters labelled as missing could not be identified with confidence and as such these values were rejected as unidentifiable.

Table C.1: Identified Modal Parameters for Configuration 1

Parameter	Peak	Location 1	Location 2	Location 3	Location 4	Location 5	Location 6
Natural Frequency [Hz]	8	7.4	7.5	7.4	7.5	7.4	7.5
Damping Ratio [-]		0.075	0.082	0.074	0.076	0.073	0.076
Amplitude Multiplier [-]		$4.4x10^{-4}$ - $1.7x10^{-4}$i	$3.7x10^{-5}$ - $2.2x10^{-4}$i	$2.6x10^{-4}$ - $1.3x10^{-4}$i	$2.3x10^{-4}$ -$1.7x10^{-4}$i	$9.3x10^{-4}$ - $5.3x10^{-4}$i	-$2.2x10^{-5}$ +$2.3x10^{-5}$i
Natural Frequency [Hz]	38	38.2	38.2	38.2	38.2	38.2	38.2
Damping Ratio [-]		0.12	0.12	0.12	0.12	0.12	0.12
Amplitude Multiplier [-]		MISSING	MISSING	MISSING	MISSING	MISSING	MISSING
Natural Frequency [Hz]	51	51.6	51.8	MISSING	50.5	51.0	51.0
Damping Ratio [-]		0.0415	0.0483	MISSING	0.0497	0.0452	0.0575
Amplitude Multiplier [-]		$8.7x10^{-5}$ -4.3 $x10^{-5}$i	$5.0x10^{-5}$ -4.0 $x10^{-5}$i	MISSING	-$3.3x10^{-5}$ -$2.5x10^{-5}$i	-$5.2x10^{-5}$ -$1.4x10^{-5}$i	-$5.2x10^{-6}$ +$1.5x10^{-5}$i
Natural Frequency [Hz]	58	56.9	57.0	MISSING	55.9	56.7	56.7
Damping Ratio [-]		0.06	0.075	MISSING	0.0253	0.0416	0.0373
Amplitude Multiplier [-]		$2.2x10^{-5}$ -4.4 $x10^{-5}$i	$1.4x10^{-5}$ -$2.9x10^{-5}$i	MISSING	-$7.2x10^{-6}$ -$3.4x10^{-6}$i	-$1.4x10^{-5}$ +$7.3x10^{-6}$i	$2.5x10^{-6}$ +$8.6x10^{-6}$i
Natural Frequency [Hz]	94	95.9	96.0	93.3	93.7	92.7	93.0
Damping Ratio [-]		0.1309	0.1268	0.0386*	0.0413	0.0640	0.0360
Amplitude Multiplier [-]		$7.5x10^{-5}$ - 2.2 $x10^{-4}$i	$6.3x10^{-5}$ -$4.6x10^{-4}$i	-$5.5x10^{-5}$ -$1.1x10^{-5}$i	-$2.6x10^{-5}$ +$2.7x10^{-5}$i	-$5.2x10^{-5}$ -$2.8x10^{-5}$i	$2.6x10^{-6}$ -$1.1x10^{-6}$i

*Excellent fit – Used for dynamic parameter identification

Table C.2: Identified Modal Parameters for Configuration 7

Parameter	Peak	Location 1	Location 2	Location 3	Location 4	Location 5	Location 6
Natural Frequency [Hz]	8	7.7	7.7	7.7	7.7	7.7	7.7^{*}
Damping Ratio [-]		0.0692	0.0692	0.0692	0.0694	0.0778	0.07^{*}
Amplitude Multiplier [-]		$4.5x10^{-4}$ $-9.5x10^{-5}i$	$3.7x10^{-4}$ $-8.4x10^{-5}i$	$3.0x10^{-4}$ $-6.9x10^{-5}i$	$2.1x10^{-4}$ $-4.9x10^{-5}i$	$9.1x10^{-5}$ $-1.7x10^{-5}i$	$-1.7x10^{-5}$ $-2.7x10^{-5}i$
Natural Frequency [Hz]	38	38.2	38.1	39.1	39.1	MISSING	39.0
Damping Ratio [-]		0.1123	0.1422	0.1300^{*}	0.1300^{*}	MISSING	0.0424
Amplitude Multiplier [-]		$1.2x10^{-5}$ $-2.3x10^{-5}i$	$5.6x10^{-5}$ $-4.3x10^{-5}i$	$-1.4x10^{-7}$ $-1.2x10^{-5}i$	$5.5x10^{-6}$ $-2.2x10^{-6}i$	MISSING	$-4.4x10^{-7}$ $+4.2x10^{-6}i$
Natural Frequency [Hz]	51	51.1	51.2	MISSING	50.8	50.7	50.8
Damping Ratio [-]		0.0224	0.0120	MISSING	0.0855	0.0627	0.0541
Amplitude Multiplier [-]		$1.0x10^{-5}$ $+6.6x10^{-6}i$	$3.4x10^{-6}$ $+7.8x10^{-7}i$	MISSING	$-1.3x10^{-5}$ $-2.5x10^{-5}i$	$-1.7x10^{-5}$ $-2.1x10^{-5}i$	$-6.0x10^{-6}$ $+1.9x10^{-6}i$
Natural Frequency [Hz]	58	58.1	58.1	MISSING	57.5	57.7	57.9
Damping Ratio [-]		0.0473	0.0512	MISSING	0.0379	0.0336	0.0297
Amplitude Multiplier [-]		$5.9x10^{-5}$ $-7.1x10^{-5}i$	$2.9x10^{-5}$ $-4.2x10^{-5}i$	MISSING	$-4.8x10^{-5}$ $-1.2x10^{-5}i$	$-3.8x10^{-5}$ $+9.7x10^{-6}i$	$1.6x10^{-5}$ $-6.0x10^{-6}i$
Natural Frequency [Hz]	94	93.9	95.8	92.36	92.7	93.3	94.5
Damping Ratio [-]		0.0729	0.0729^{*}	0.0505	0.0447	0.0276	0.0638
Amplitude Multiplier [-]		$2.9x10^{-5}$ $+8.1x10^{-5}i$	$6.4x10^{-6}$ $-1.8x10^{-5}i$	$1.4x10^{-5}$ $-4.0x10^{-5}i$	$-1.7x10^{-5}$ $+1.6x10^{-5}i$	$1.7x10^{-6}$ $+1.6x10^{-6}i$	$4.1x10^{-6}$ $-3.6x10^{-6}i$

*Not measured – Taken from existing values

Table C.3: Identified Modal Parameters for Configuration 2

Parameter	Peak	Location 1	Location 2	Location 3	Location 4	Location 5	Location 6
Natural Frequency [Hz]	8	7.7	7.7	7.5	7.5	7.5	8
Damping Ratio [-]		0.0994	0.0999	0.0927	0.1153	0.1021	0.0741
Amplitude Multiplier [-]		$3.8x10^{-4}$ $-1.8x10^{-4}i$	$3.2x10^{-4}$ $-1.6x10^{-4}i$	$2.7x10^{-4}$ $-1.4x10^{-4}i$	$2.7x10^{-4}$ $-9.8x10^{-5}i$	$1.0x10^{-4}$ $-5.5x10^{-5}i$	$-1.9x10^{-6}$ $+1.4x10^{-5}i$
Natural Frequency [Hz]	38	MISSING	MISSING	MISSING	MISSING	MISSING	MISSING
Damping Ratio [-]		MISSING	MISSING	MISSING	MISSING	MISSING	MISSING
Amplitude Multiplier [-]		MISSING	MISSING	MISSING	MISSING	MISSING	MISSING
Natural Frequency [Hz]	51	51.1	51.1	52.3	52.4	52.3	49.9
Damping Ratio [-]		0.0155	0.0123	0.2606	0.0143^{+}	0.0265	0.07
Amplitude Multiplier [-]		$8.5x10^{-6}$ $-4.0x10^{-6}i$	$2.8x10^{-6}$ $-3.2x10^{-6}i$	$1.8x10^{-5}$ $-1.6x10^{-5}i$	$-4.2x10^{-6}$ $-1.6x10^{-6}i$	$7.8x10^{-6}$ $-3.3x10^{-6}i$	$-2.7x10^{-6}$ $+3.6x10^{-6}i$
Natural Frequency [Hz]	58	56.1	56.1	MISSING	54.6	55.3	55.4
Damping Ratio [-]		0.0507	0.0635	MISSING	0.0461	0.0337	0.0357
Amplitude Multiplier [-]		$4.6x10^{-5}$ $-8.5x10^{-5}i$	$3.4x10^{-5}$ $+1.1x10^{-5}i$	MISSING	$-2.6x10^{-5}$ $-9.7x10^{-6}i$	$-2.0x10^{-5}$ $+2.0x10^{-5}i$	$3.6x10^{-6}$ $+1.1x10^{-5}i$
Natural Frequency [Hz]	94	92.3	95	91.4	91.5	91.6	91.8
Damping Ratio [-]		0.0886	0.3251	0.0728	0.0636	0.0590	0.0432
Amplitude Multiplier [-]		$9.8x10^{-5}$ $+8.5x10^{-5}i$	$2.6x10^{-5}$ $-3.6x10^{-5}i$	$1.9x10^{-6}$ $-6.6x10^{-5}i$	$-2.5x10^{-5}$ $-3.1x10^{-5}i$	$-7.8x10^{-6}$ $-2.6x10^{-6}i$	$3.1x10^{-6}$ $-6.9x10^{-7}i$

$^{+}$Identified from (2.19)

Table C.4: Identified Modal Parameters for Configuration 6

Parameter	Peak	Location 1	Location 2	Location 3	Location 4	Location 5	Location 6
Natural Frequency [Hz]	8	7.7	7.6	7.7	7.7	7.6	8.3
Damping Ratio [-]		0.0871	0.0898	0.0819	0.0830	0.1241	0.0589
Amplitude Multiplier [-]		$4.0x10^{-4}$ $+1.5x10^{-4}$i	$3.2x10^{-4}$ $-1.2x10^{-4}$i	$2.5x10^{-4}$ $-1.0x10^{-4}$i	$1.7x10^{-4}$ $-6.9x10^{-5}$i	$8.5x10^{-5}$ $-1.6x10^{-5}$i	$-3.3x10^{-5}$ $+2.7x10^{-5}$i
Natural Frequency [Hz]	38	36.7	36.4	37.5	37.9	38.3	36.3
Damping Ratio [-]		0.0645	0.0898	0.1350	0.0800*	0.1089	0.0363
Amplitude Multiplier [-]		$3.6x10^{-5}$ $-3.1x10^{-5}$i	$8.5x10^{-5}$ $-1.2x10^{-5}$i	$7.1x10^{-6}$ $-3.6x10^{-5}$i	$7.0x10^{-7}$ $-1.9x10^{-5}$i	$-2.5x10^{-6}$ $-1.0x10^{-5}$i	$-1.3x10^{-5}$ $+2.3x10^{-6}$i
Natural Frequency [Hz]	51	51.0	51.1	MISSING	48.9	49.3	50.4
Damping Ratio [-]		0.0066	0.0072	MISSING	0.1374	0.0812	0.0771
Amplitude Multiplier [-]		$4.1x10^{-6}$ $+4.7x10^{-8}$i	$2.9x10^{-6}$ $+3.4x10^{-7}$i	MISSING	$-8.5x10^{-6}$ $+3.5x10^{-5}$i	$-1.9x10^{-5}$ $-2.7x10^{-5}$i	$4.4x10^{-6}$ $+7.0x10^{-6}$i
Natural Frequency [Hz]	58	56.9	57.1	54.0	56.4	56.5	56.5
Damping Ratio [-]		0.0366	0.0275	0.1951	0.0371	0.0343	0.0305
Amplitude Multiplier [-]		$6.8x10^{-5}$ $-5.9x10^{-5}$i	$1.2x10^{-5}$ $-3.1x10^{-5}$i	$1.5x10^{-5}$ $-5.7x10^{-5}$i	$-4.2x10^{-5}$ $-7.9x10^{-6}$i	$-3.9x10^{-5}$ $-2.5x10^{-6}$i	$1.5x10^{-5}$ $-2.6x10^{-6}$i
Natural Frequency [Hz]	94	96.4	97.0	92.3	92.5	92.6	93.6
Damping Ratio [-]		0.100*	0.100*	0.0300*	0.0581	0.1052	0.0474
Amplitude Multiplier [-]		$9.3x10^{-5}$ $+1.9x10^{-5}$i	$2.1x10^{-5}$ $+6.7x10^{-6}$i	$-6.1x10^{-6}$ $+4.7x10^{-6}$i	$-6.1x10^{-6}$ $+8.0x10^{-6}$i	$-3.6x10^{-6}$ $+7.4x10^{-7}$i	$1.9x10^{-6}$ $-2.2x10^{-6}$i

*Not measured – Taken from existing values

Appendix D: Initial and Boundary Conditions for Dynamic Parameter Optimisation

The table shows the initial and boundary conditions for the LS parameterisation of the dynamic parameters. The initial values are based on experimental static stiffness values and natural frequency approximations and were adjusted to improve identification results. The lower bounds are to prevent the parameters from becoming negative since they are intended to represent physical dynamic parameters. The upper bounds were found to be necessary to improve the results when fitting to the eigenvalues as outlined in Section 2.6.4. When attempting to fit to the eigenvectors as well as the eigenvalues, the bounds and intial conditions were varied unsuccessfully.

Table D.1: Initial and Boundary Conditions for Dynamic Parameter Optimisation

Condition	Link	Mass [kg]	Inertia [kgm^2]	Stiffness [Nm/rad]	Damping [Nms/rad]
Minimum	1	1.00	1.00	1.00	1.00
Minimum	2	1.00	1.00	1.00	1.00
Minimum	3	1.00	1.00	1.00	1.00
Minimum	4	1.00	1.00	1.00	1.00
Initial	1	50.0	50.00	5.00×10^5	100.00
Initial	2	50.00	50.00	5.00×10^5	100.00
Initial	3	5.00	50.00	5.00×10^5	10.00
Initial	4	50.00	50.00	5.00×10^5	100.00
Maximum	1	50.00	50.00	1.00×10^6	200.00
Maximum	2	50.00	50.00	1.00×10^6	200.00
Maximum	3	10.00	50.00	1.00×10^6	200.00
Maximum	4	50.00	50.00	1.00×10^6	200.00

Appendix E: Six Link Planar Manipulator Receptance Optimisation Results

The following tables list the initial and final joint values, natural frequencies, and receptance amplitude values for the redundant manipulator receptance optimisation simulations. The results were determined using a gradient descent optimisation defined by the objective function derivative (3.2), the objective function (3.3) and an update algorithm. The results in Section E.1 are for the unrestricted case whereby the end-effector is free to move in the workspace and uses the update algorithm defined by (3.4) and (3.15). The results in Section E.2 are for the restricted optimisations whereby the end-effector is held in position through a Cartesian error term and the links are configured in the simulated manipulator null space using the redundancy of the robot. This uses the update algorithm define by (3.4) and (3.13).

E.1 Unrestricted Optimisations at 0Hz and 100Hz

Table E.1: Initial and Final Natural Frequencies and Receptance Values for End-Effector Drive Point Optimisation at 0Hz Starting at Location (-3.5, 1)

Initial Joint Values [rad]	Initial Natural Frequencies[7] [Hz]	Final Joint Values [rad]	Final Natural Frequencies [Hz]
1: 1.57	10.63	1: 1.12	11.01
2: 0.52	4.55	2: 0.65	4.48
3: 0.52	3.90	3: 2.22	5.27
4: 0.52	3.29	4: 1.10	3.55
5: 0.52	2.57	5: -0.21	2.98
6: 0.52	1.28	6: -0.25	1.98
	0.52		0.58
Initial Receptance Amplitude [m/N]	2.62×10^{-3}	Final Receptance Amplitude [m/N]	2.64×10^{-5}

---

[7] Repeated Frequency Values are Omitted

Table E.2: Initial and Final Natural Frequencies and Receptance Values for End-Effector Drive Point Optimisation at 0Hz Starting at Location (-2, 2)

Initial Joint Values [rad]	Initial Natural Frequencies [Hz]	Final Joint Values [rad]	Final Natural Frequencies [Hz]
1: 1.57	9.86	1: 1.58	33.12
2: 0.26	4.75	2: 0.07	6.67
3: 0.26	5.79	3: -0.07	7.64
4: 0.21	4.64	4: -0.07	6.88
5: 1.43	3.05	5: 2.74	5.06
6: 1.05	1.45	6: 0.97	2.51
	0.81		1.21
Initial Receptance Amplitude [m/N]	8.38×10^{-4}	Final Receptance Amplitude [m/N]	2.60×10^{-5}

Table E.3: Initial and Final Natural Frequencies and Receptance Values for End-Effector Drive Point Optimisation at 0Hz Starting at Location (0, 1.5)

Initial Joint Values [rad]	Initial Natural Frequencies [Hz]	Final Joint Values [rad]	Final Natural Frequencies [Hz]
1: 0.79	10.95	1: 1.75	39.76
2: -0.63	9.36	2: -0.27	11.05
3: 1.05	5.16	3: 0.05	7.56
4: 0.78	4.50	4: 0.15	6.44
5: 1.65	3.31	5: 3.07	5.59
6: 0.39	1.70	6: 0.01	4.45
	1.19		2.44
			1.25
Initial Receptance Amplitude [m/N]	6.85×10^{-4}	Final Receptance Amplitude [m/N]	1.30×10^{-6}

Table E.4: Initial and Final Natural Frequencies and Receptance Values for End-Effector Drive Point Optimisation at 100Hz Starting at Location (-3.5, 1)

Initial Joint Values [rad]	Initial Natural Frequencies [Hz]	Final Joint Values [rad]	Final Natural Frequencies [Hz]
1: 1.57	10.63	1: 1.12	11.14
2: 0.52	4.55	2: -0.06	10.96
3: 0.52	3.90	3: 0.53	6.91
4: 0.52	3.29	4: 2.45	4.49
5: 0.52	2.57	5: 0.27	3.81
6: 0.52	1.28	6: 0.29	0.85
	0.52		2.67
Initial Receptance Amplitude [m/N]	8.45×10^{-7}	Final Receptance Amplitude [m/N]	2.87×10^{-8}

Table E.5: Initial and Final Natural Frequencies and Receptance Values for End-Effector Drive Point Optimisation at 100Hz Starting at Location (-2, 2)

Initial Joint Values [rad]	Initial Natural Frequencies [Hz]	Final Joint Values [rad]	Final Natural Frequencies [Hz]
1: 1.57	9.86	1: 1.21	31.54
2: 0.26	4.75	2: -0.06	9.33
3: 0.26	5.79	3: 0.02	6.70
4: 0.21	4.64	4: 0.38	6.11
5: 1.43	3.05	5: 2.37	5.85
6: 1.05	1.45	6: 0.98	4.99
	0.81		2.53
			1.23
Initial Receptance Amplitude [m/N]	8.64×10^{-8}	Final Receptance Amplitude [m/N]	6.63×10^{-5}

Table E.6: Initial and Final Natural Frequencies and Receptance Values for End-Effector Drive Point Optimisation at 100Hz Starting at Location (0, 1.5)

Initial Joint Values [rad]	Initial Natural Frequencies [Hz]	Final Joint Values [rad]	Final Natural Frequencies [Hz]
1: 0.79	10.95	1: 1.47	40.24
2: -0.63	9.36	2: 0.05	11.07
3: 1.05	5.16	3: 0.02	7.81
4: 0.78	4.50	4: 0.03	6.49
5: 1.65	3.31	5: 3.11	5.59
6: 0.39	1.70	6: 0.03	4.45
	1.19		2.44
			1.25
Initial Receptance Amplitude [m/N]	1.29×10^{-7}	Final Receptance Amplitude [m/N]	2.93×10^{-10}

E.2 Position Controlled Optimisations at 1Hz, 5Hz, and 20Hz

Table E.7: Initial and Final Natural Frequencies and Receptance Values for End-Effector Drive Point Receptance Optimisation at 1Hz at Location (-3.5, 1)

Initial Joint Values [rad]	Initial Natural Frequencies [Hz]	Final Joint Values [rad]	Final Natural Frequencies [Hz]
1: 1.57	10.63	1: 3.09	14.38
2: 0.52	4.55	2: -0.06	7.10
3: 0.52	3.90	3: -0.63	5.09
4: 0.52	3.29	4: -1.03	4.76
5: 0.52	2.57	5: 1.62	2.90
6: 0.52	1.28	6: 1.74	2.64
	0.52		0.71
Initial Receptance Amplitude [m/N]	6.20×10^{-4}	Final Receptance Amplitude [m/N]	9.01×10^{-4}

Table E.8: Initial and Final Natural Frequencies and Receptance Values for End-Effector Drive Point Receptance Optimisation at 1Hz at Location (-2,2)

Initial Joint Values [rad]	Initial Natural Frequencies [Hz]	Final Joint Values [rad]	Final Natural Frequencies [Hz]
1: 1.57	9.86	1: 3.05	25.47
2: 0.26	4.75	2: -0.08	6.57
3: 0.26	5.79	3: -0.88	5.76
4: 0.21	4.64	4: -1.43	3.66
5: 1.43	3.05	5: 0.041	2.09
6: 1.05	1.45	6: 2.74	0.90
	0.81		
Initial Receptance Amplitude [m/N]	1.20×10^{-3}	Final Receptance Amplitude [m/N]	4.10×10^{-4}

Table E.9: Initial and Final Natural Frequencies and Receptance Values for End-Effector Drive Point Receptance Optimisation at 1Hz at Location (0, 1.5)

Initial Joint Values [rad]	Initial Natural Frequencies [Hz]	Final Joint Values [rad]	Final Natural Frequencies [Hz]
1: 0.79	10.95	1: 1.93	11.26
2: -0.63	9.36	2: -1.59	8.60
3: 1.05	5.16	3: 0.88	8.36
4: 0.78	4.50	4: 0.39	4.56
5: 1.65	3.31	5: 2.88	2.54
6: 0.39	1.70	6: -0.54	1.46
	1.19		3.97
Initial Receptance Amplitude [m/N]	1.78×10^{-3}	Final Receptance Amplitude [m/N]	3.24×10^{-4}

Table E.10: Initial and Final Natural Frequencies and Receptance Values for End-Effector Drive Point Receptance Optimisation at 5Hz at Location (-3.5, 1)

Initial Joint Values [rad]	Initial Natural Frequencies [Hz]	Final Joint Values [rad]	Final Natural Frequencies [Hz]
1: 1.57	10.63	1: 2.41	10.14
2: 0.52	4.55	2: -0.01	5.64
3: 0.52	3.90	3: -0.05	4.64
4: 0.52	3.29	4: -0.05	4.25
5: 0.52	2.57	5: 2.36	2.92
6: 0.52	1.28	6: -0.58	1.46
	0.52		0.68
Initial Receptance Amplitude [m/N]	9.34×10^{-5}	Final Receptance Amplitude [m/N]	2.65×10^{-5}

Table E.11: Initial and Final Natural Frequencies and Receptance Values for End-Effector Drive Point Receptance Optimisation at 5Hz at Location (-2, 2)

Initial Joint Values [rad]	Initial Natural Frequencies [Hz]	Final Joint Values [rad]	Final Natural Frequencies [Hz]
1: 1.57	9.86	1: 3.87	48.05
2: 0.26	4.75	2: -1.69	7.00
3: 0.26	5.79	3: -0.12	5.75
4: 0.21	4.64	4: -0.41	4.21
5: 1.43	3.05	5: 0.24	3.43
6: 1.05	1.45	6: 3.01	2.55
	0.81		0.75
Initial Receptance Amplitude [m/N]	2.95×10^{-5}	Final Receptance Amplitude [m/N]	1.13×10^{-5}

Table E.12: Initial and Final Natural Frequencies and Receptance Values for End-Effector Drive Point Receptance Optimisation at 5Hz at Location (0, 1.5)

Initial Joint Values [rad]	Initial Natural Frequencies [Hz]	Final Joint Values [rad]	Final Natural Frequencies [Hz]
1: 0.79	10.95	1: 0.44	11.27
2: -0.63	9.36	2: 0.15	9.13
3: 1.05	5.16	3: 1.09	8.52
4: 0.78	4.50	4: 1.19	4.56
5: 1.65	3.31	5: 0.06	3.72
6: 0.39	1.70	6: 2.11	2.55
	1.19		1.43
Initial Receptance Amplitude [m/N]	4.22×10^{-5}	Final Receptance Amplitude [m/N]	3.245×10^{-5}

Table E.13: Initial and Final Natural Frequencies and Receptance Values for End-Effector Drive Point Receptance Optimisation at 20Hz at Location (-3.5, 1)

Initial Joint Values [rad]	Initial Natural Frequencies [Hz]	Final Joint Values [rad]	Final Natural Frequencies [Hz]
1: 1.57	10.63	1: 2.81	11.01
2: 0.52	4.55	2: -0.02	6.63
3: 0.52	3.90	3: -0.7	4.49
4: 0.52	3.29	4: -0.57	4.83
5: 0.52	2.57	5: 2.41	3.17
6: 0.52	1.28	6: 0.29	1.66
	0.52		0.71
Initial Receptance Amplitude [m/N]	1.78×10^{-5}	Final Receptance Amplitude [m/N]	2.39×10^{-6}

Table E.14: Initial and Final Natural Frequencies and Receptance Values for End-Effector Drive Point Receptance Optimisation at 20Hz at Location (-2, 2)

Initial Joint Values [rad]	Initial Natural Frequencies [Hz]	Final Joint Values [rad]	Final Natural Frequencies [Hz]
1: 1.57	9.86	1: 1.57	10.27
2: 0.26	4.75	2: 0.24	8.60
3: 0.26	5.79	3: 0.26	5.98
4: 0.21	4.64	4: 0.25	4.78
5: 1.43	3.05	5: 1.42	3.97
6: 1.05	1.45	6: 1.01	1.75
	0.81		0.98
Initial Receptance Amplitude [m/N]	2.07×10^{-6}	Final Receptance Amplitude [m/N]	1.92×10^{-6}

Table E.15: Initial and Final Natural Frequencies and Receptance Values for End-Effector Drive Point Receptance Optimisation at 20Hz at Location (0, 1.5)

Initial Joint Values [rad]	Initial Natural Frequencies [Hz]	Final Joint Values [rad]	Final Natural Frequencies [Hz]
1: 0.79	10.95	1: 0.47	30.81
2: -0.63	9.36	2: 0.19	10.96
3: 1.05	5.16	3: 0.79	6.57
4: 0.78	4.50	4: 1.35	5.17
5: 1.65	3.31	5: 0.26	5.75
6: 0.39	1.70	6: 1.79	4.47
	1.19		2.48
			1.42
Initial Receptance Amplitude [m/N]	3.03×10^{-6}	Final Receptance Amplitude [m/N]	2.90×10^{-6}

Appendix F: Six Link Planar Manipulator Stiffness Optimisation Results

The following tables list the initial and final joint values, natural frequencies, and receptance amplitude values for the redundant manipulator stiffness optimisation simulations. The results were determined using a gradient descent optimisation defined by the objective function derivative (3.17) and an update algorithm defined by (3.13) and (3.5).

Table F.1: Initial and Final Natural Frequencies and Projected Stiffness Values for Stiffness Optimisation at (-3.5, 1)

Initial Joint Values [rad]	Initial Natural Frequencies [Hz]	Final Joint Values [rad]	Final Natural Frequencies [Hz]
1: 1.57	10.63	1: 2.75	10.95
2: 0.52	4.55	2: -0.43	5.98
3: 0.52	3.90	3: -0.09	4.49
4: 0.52	3.29	4: -0.20	4.36
5: 0.52	2.57	5: 2.33	3.01
6: 0.52	1.28	6: -0.17	1.49
	0.52		0.70
Initial Stiffness [m/N]	2.50×10^3	Final Stiffness [m/N]	1.31×10^4

Table F.2: Initial and Final Natural Frequencies and Projected Stiffness Values for Stiffness Optimisation at (-2, 2)

Initial Joint Values [rad]	Initial Natural Frequencies [Hz]	Final Joint Values [rad]	Final Natural Frequencies [Hz]
1: 1.57	9.86	1: 2.24	10.36
2: 0.26	4.75	2: -0.33	8.45
3: 0.26	5.79	3: -0.07	5.66
4: 0.21	4.64	4: -0.23	4.68
5: 1.43	3.05	5: 2.31	4.00
6: 1.05	1.45	6: 0.76	1.66
	0.81		0.99
Initial Stiffness [m/N]	8.52×10^3	Final Stiffness [m/N]	2.07×10^4

Table F.3: Initial and Final Natural Frequencies and Projected Stiffness Values for Stiffness Optimisation at (0, 1.5)

Initial Joint Values [rad]	Initial Natural Frequencies [Hz]	Final Joint Values [rad]	Final Natural Frequencies [Hz]
1: 0.79	10.95	1: 2.00	10.95
2: -0.63	9.36	2: -1.57	9.36
3: 1.05	5.16	3: 1.11	5.16
4: 0.78	4.50	4: -0.42	4.50
5: 1.65	3.31	5: 3.26	3.30
6: 0.39	1.70	6: -0.35	1.70
	1.19		1.19
Initial Stiffness [m/N]	7.88×10^3	Final Stiffness [m/N]	5.25×10^4

Appendix G: Optimised Configuration Plots

The following figures show the final configuration for the redundant manipulator optimisation simulations. The configurations were determined using a gradient descent optimisation defined by the objective function derivative (3.2), the objective function (3.3) and an update algorithm. The results in Section G.1 are for the unrestricted case whereby the end-effector is free to move in the workspace and uses the update algorithm defined by (3.4) and (3.15). The results in Section G.2 are for the restricted optimisations whereby the end-effector is held in position through a Cartesian error term and the links are configured in the simulated manipulator null space using the redundancy of the robot. This uses the update algorithm define by (3.4) and (3.13). These figures also include the results of the stiffness optimisation, which uses the objective function defined by (3.17).

G.1 Unrestricted Optimisations at 0Hz and 100Hz

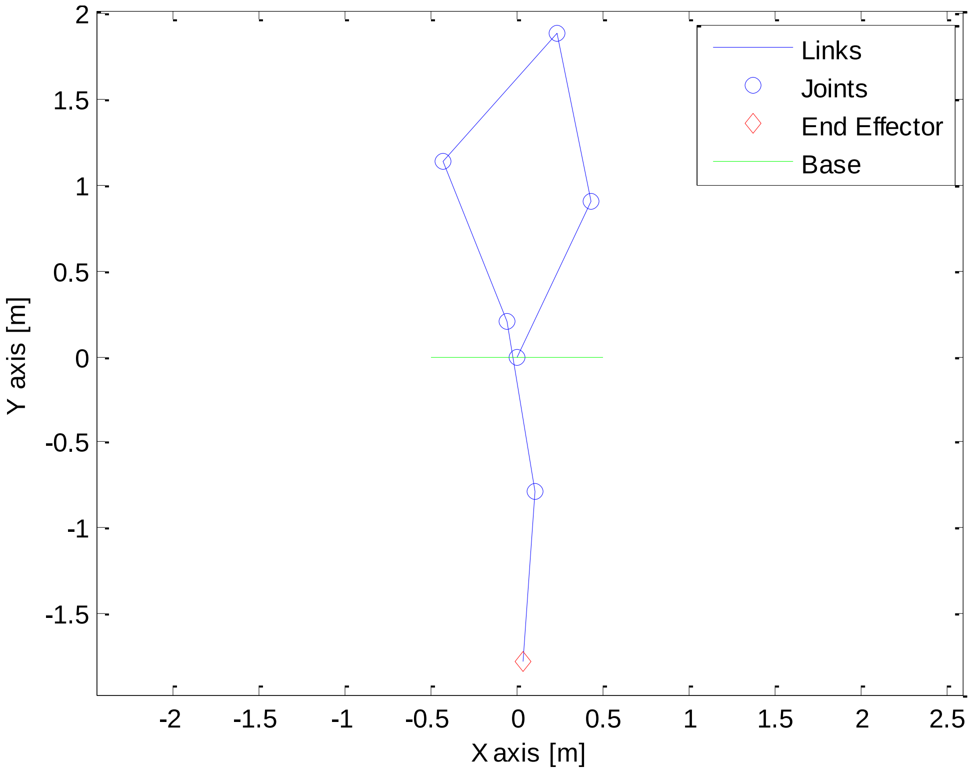

Figure G.1: End-Effector Drive Point Receptance Optimised Configuration of the Simulated Manipulator at 0Hz Initially Positioned at Location (-3.5, 1)

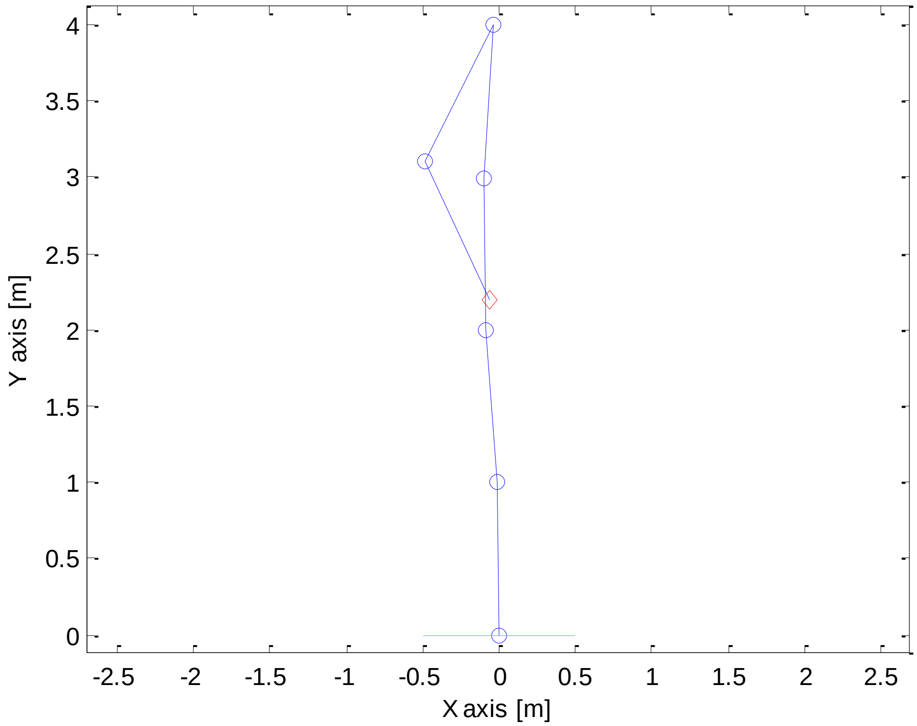

Figure G.2: End-Effector Drive Point Receptance Optimised Configuration of the Simulated Manipulator at 0Hz Initially Positioned at Location (-2, 2)

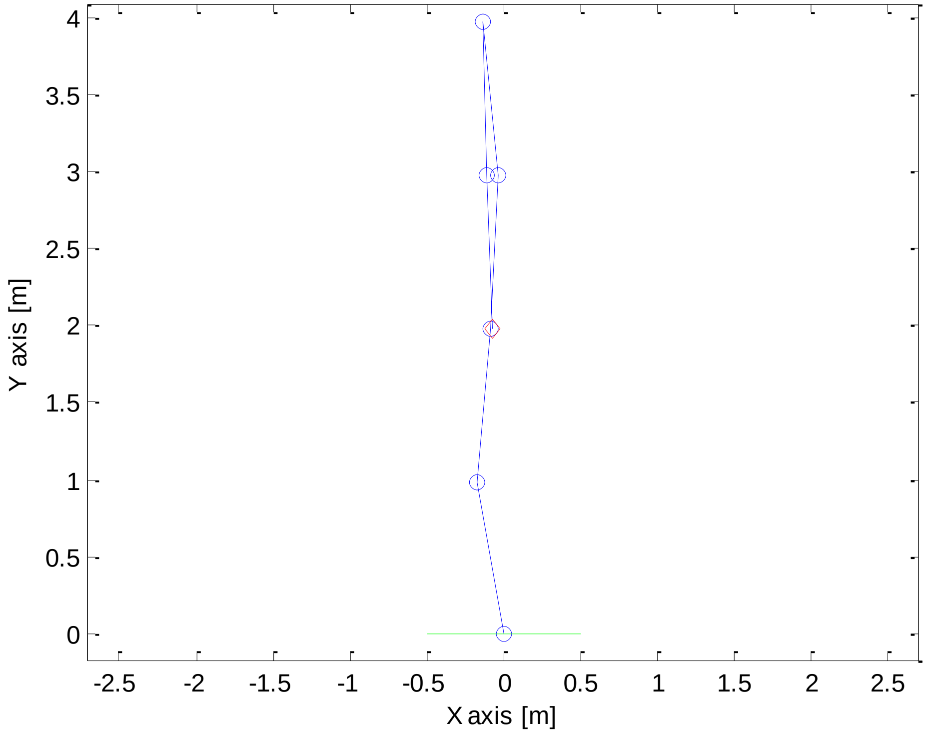

Figure G.3: End-Effector Drive Point Receptance Optimised Configuration of the Simulated Manipulator at 0Hz Initially Positioned at Location (0, 1.5)

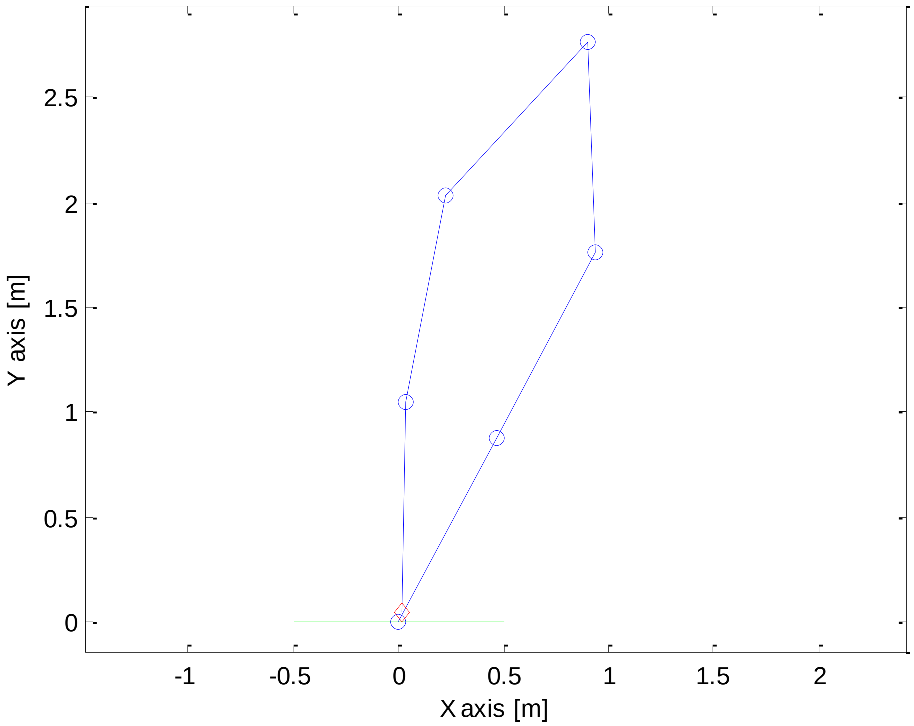

Figure G.4: End-Effector Drive Point Receptance Optimised Configuration of the Simulated Manipulator at 100Hz Initially Positioned at Location (-3.5, 1)

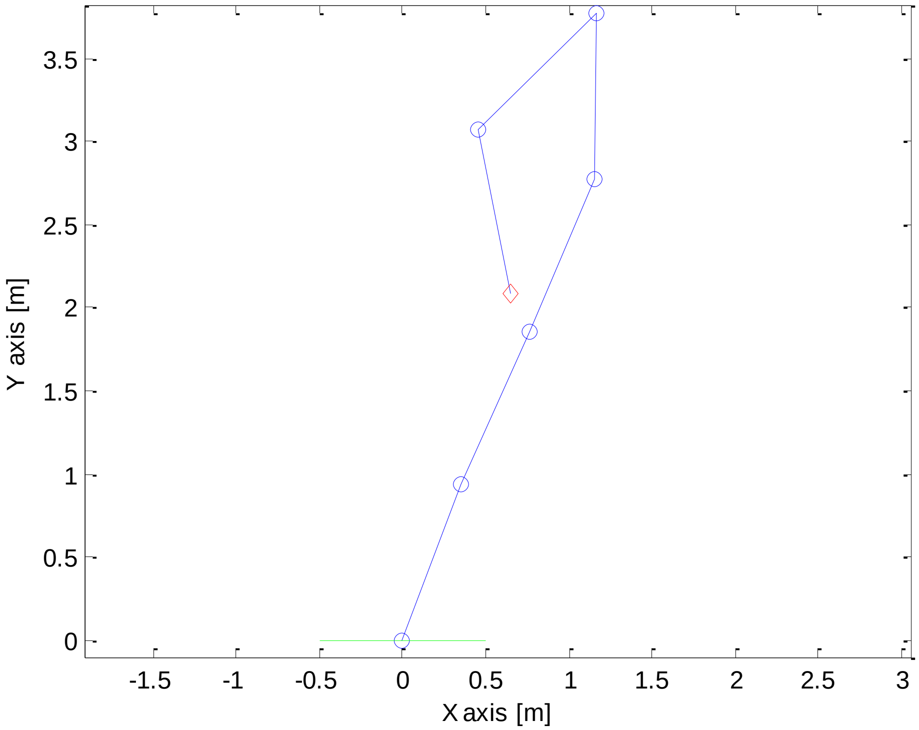

Figure G.5: End-Effector Drive Point Receptance Optimised Configuration of the Simulated Manipulator at 100Hz Initially Positioned at Location (-2, 2)

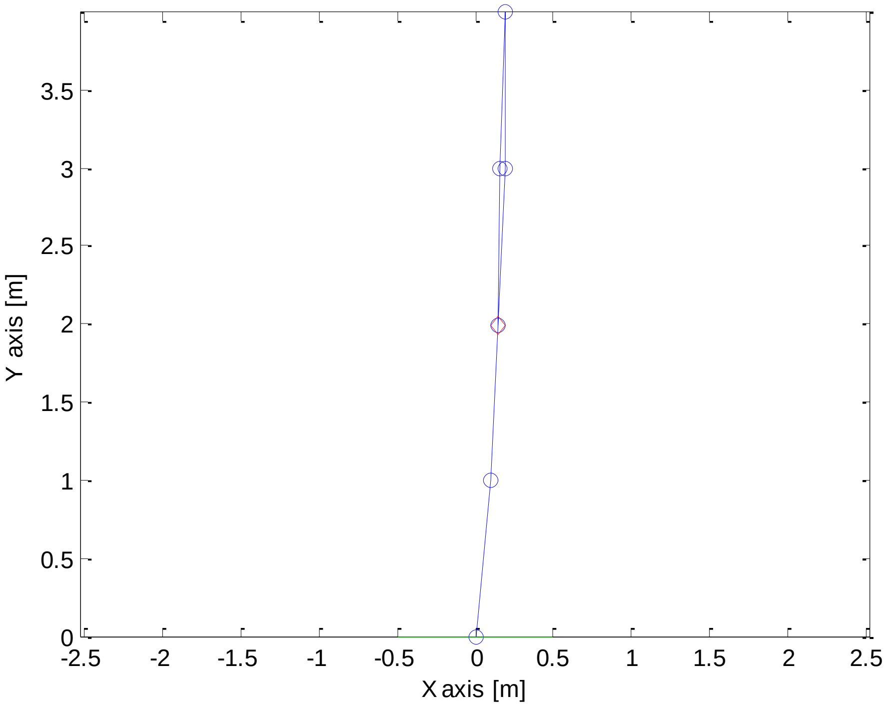

Figure G.6: End-Effector Drive Point Receptance Optimised Configuration of the Simulated Manipulator at 100Hz Initially Positioned at Location (0, 1.5)

G.2 Position Controlled Optimisations at 1Hz, 5Hz, and 20Hz

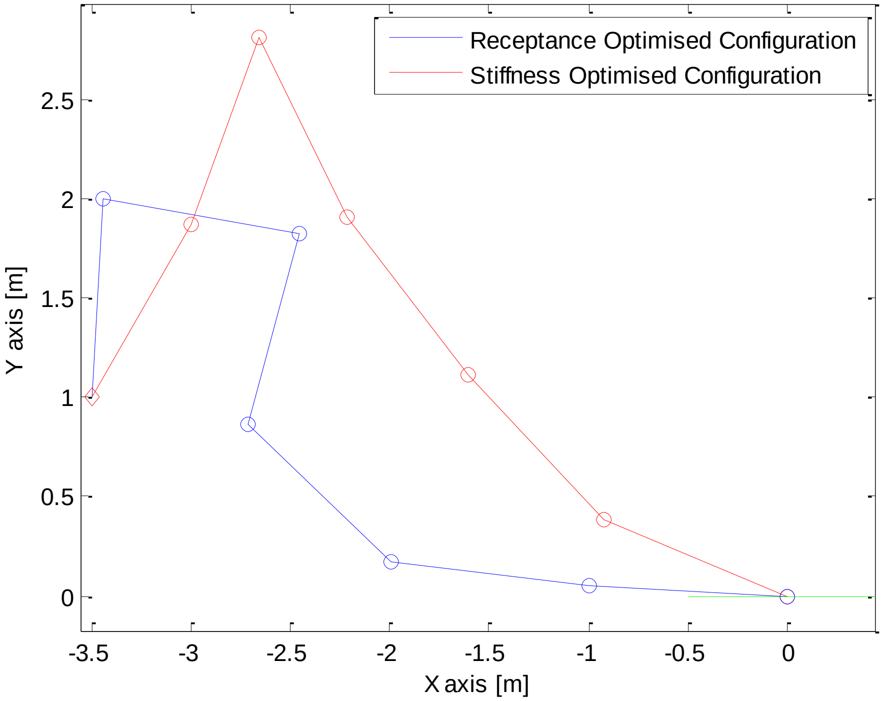

Figure G.7: Simulated Manipulator End-Effector Drive Point Receptance at 1Hz and Rigid Body Stiffness Optimisation Results at Location (-3.5, 1)

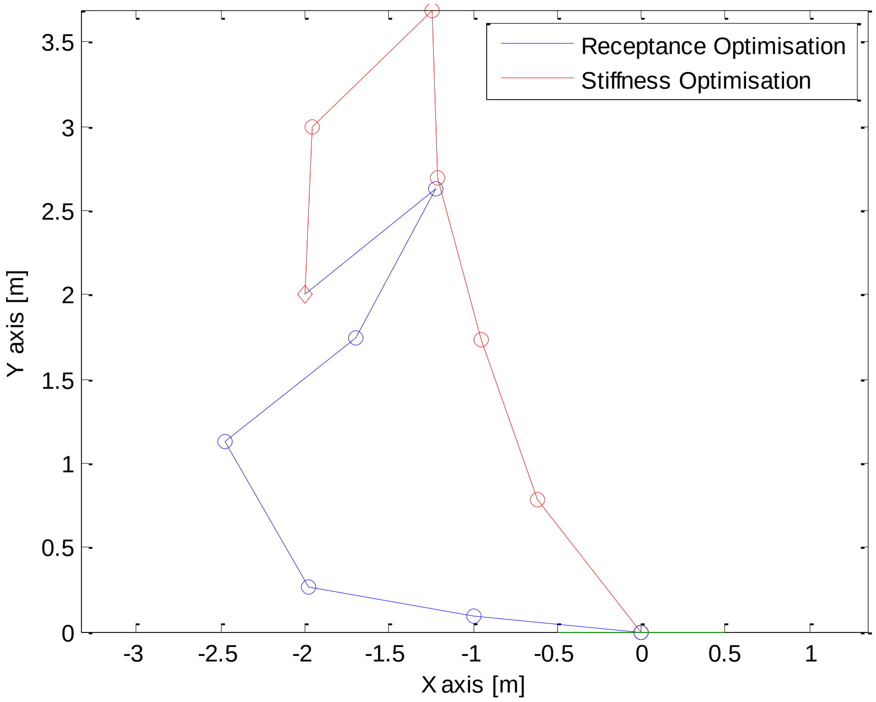

Figure G.8: Simulated Manipulator End-Effector Drive Point Receptance at 1Hz and Rigid Body Stiffness Optimisation Results at Location (-2, 2)

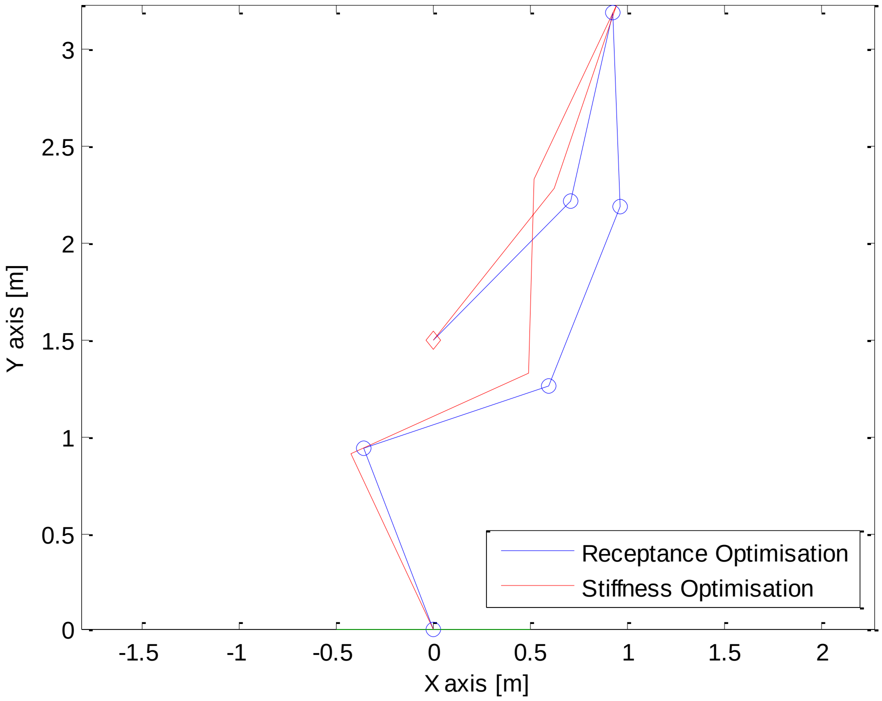

Figure G.9: Simulated Manipulator End-Effector Drive Point Receptance at 1Hz and Rigid Body Stiffness Optimisation Results at Location (0, 1.5)

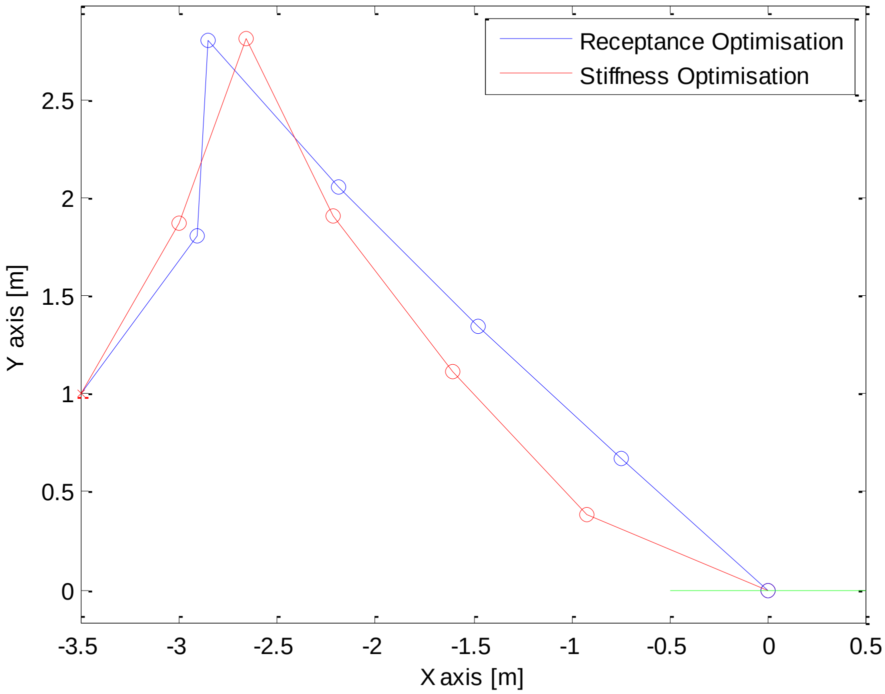

Figure G.10: Simulated Manipulator End-Effector Drive Point Receptance at 5Hz and Rigid Body Stiffness Optimisation Results at Location (-3.5, 1)

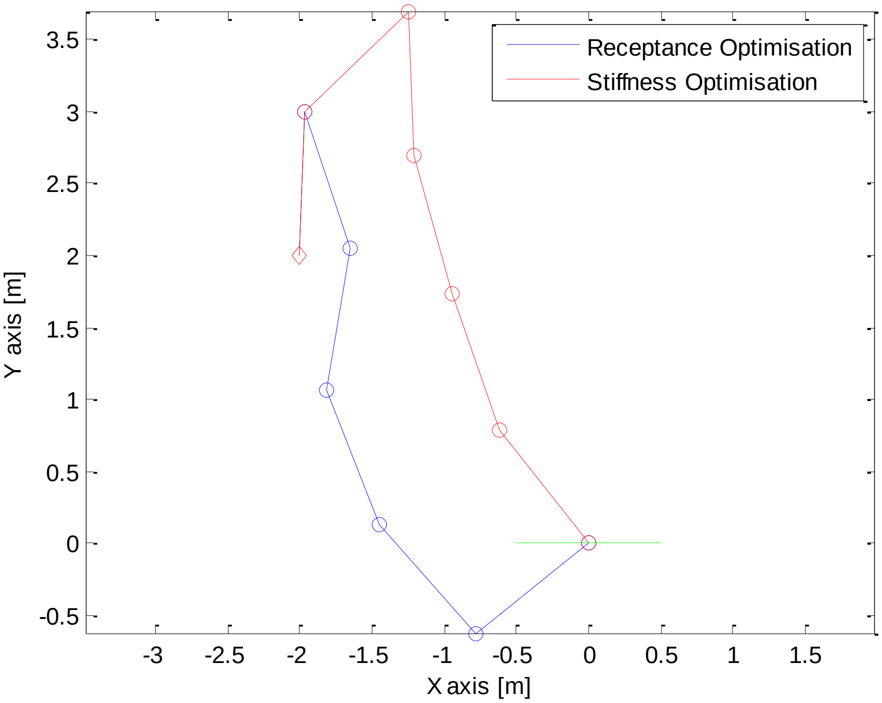

Figure G.11: Simulated Manipulator End-Effector Drive Point Receptance at 5Hz and Rigid Body Stiffness Optimisation Results at Location (-2, 2)

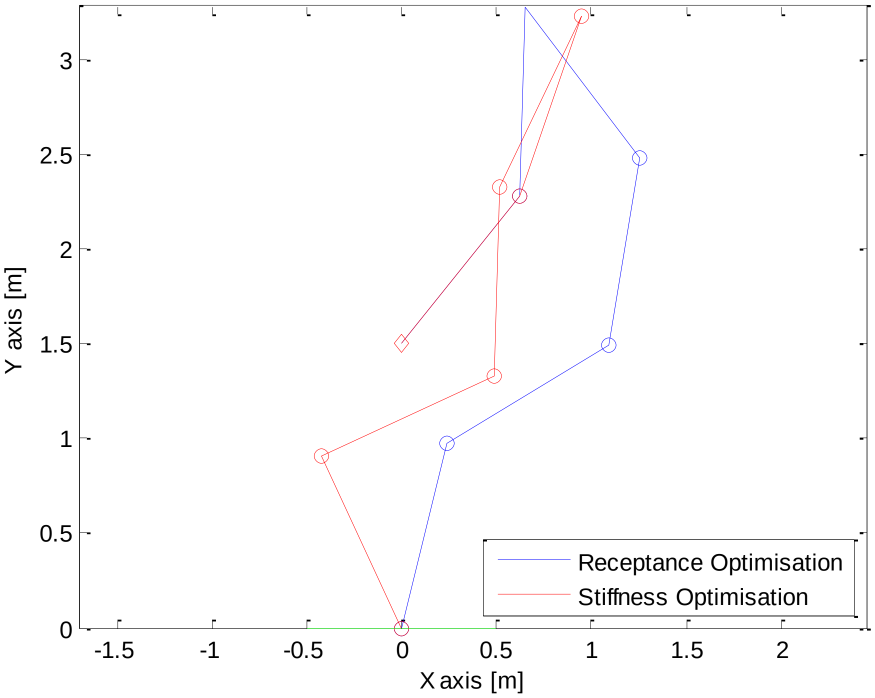

Figure G.12: Simulated Manipulator End-Effector Drive Point Receptance at 5Hz and Rigid Body Stiffness Optimisation Results at Location (0, 1.5)

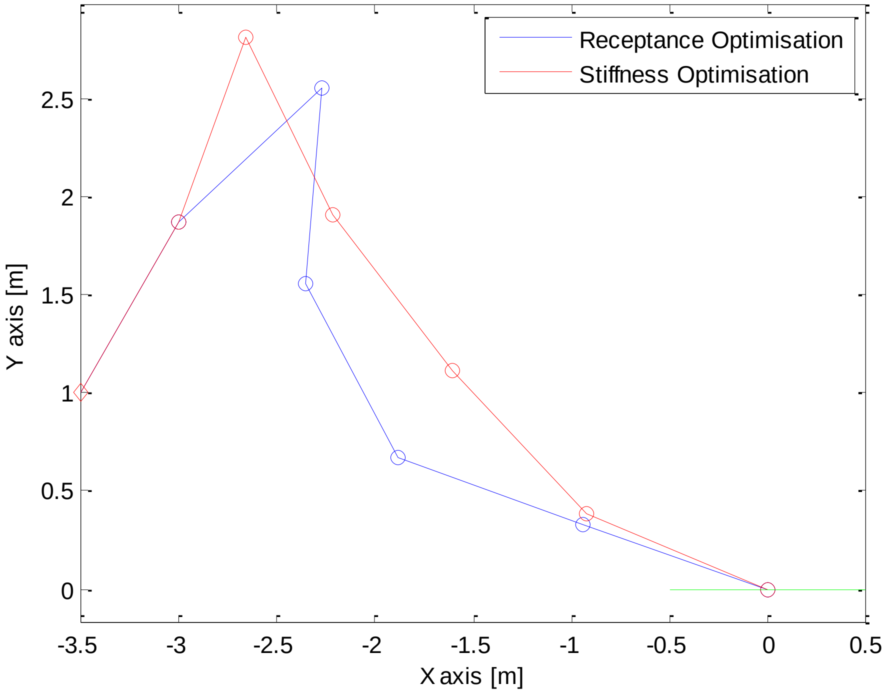

Figure G.13: Simulated Manipulator End-Effector Drive Point Receptance at 20Hz and Rigid Body Stiffness Optimisation Results at Location (-3.5, 1)

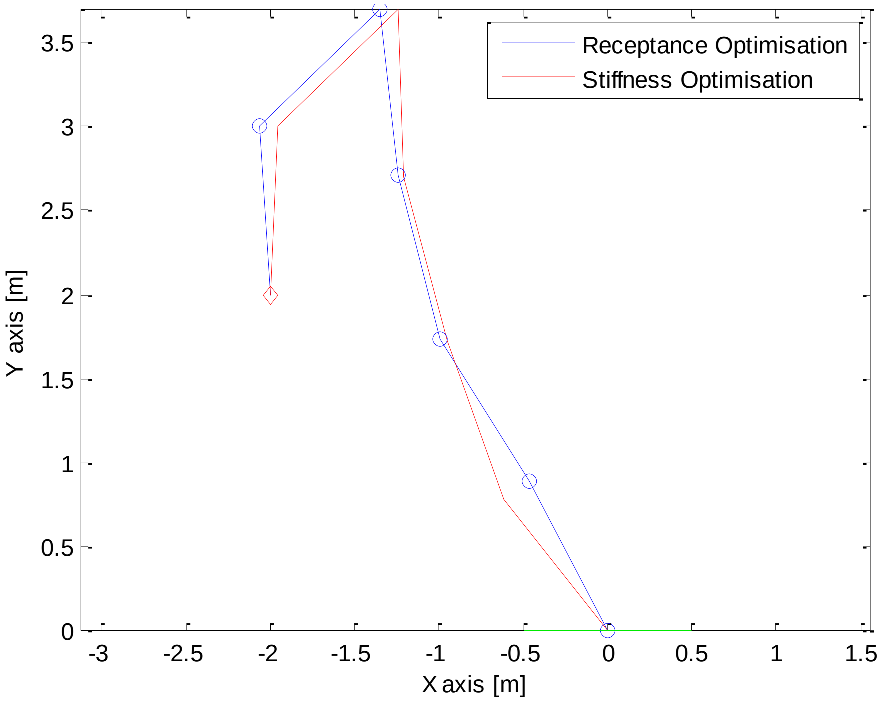

Figure G.14: Simulated Manipulator End-Effector Drive Point Receptance at 20Hz and Rigid Body Stiffness Optimisation Results at Location (-2, 2)

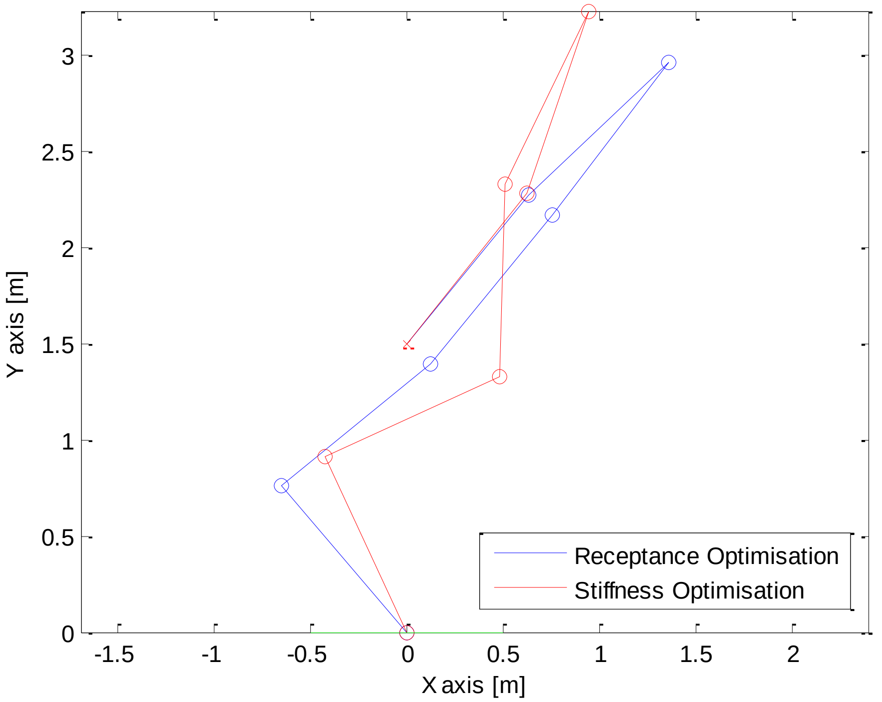

Figure G.15: Simulated Manipulator End-Effector Drive Point Receptance at 20Hz and Rigid Body Stiffness Optimisation Results at Location (0, 1.5)

Appendix H: Receptance Manipulation throughout Optimisations

The following figures show the end-effector drive point receptance throughout the receptance optimisations. The optimisations follow a gradient-descent method defined by the objective function derivative (3.2), the objective function (3.3) and an update algorithm. The results in Section H.1 are for the unrestricted case whereby the end-effector is free to move in the workspace and uses the update algorithm defined by (3.4) and (3.15). The results in Section H.2 are for the restricted optimisations whereby the end-effector is held in position through a Cartesian error term and the links are configured in the simulated manipulator null space using the redundancy of the robot. This uses the update algorithm define by (3.4) and (3.13).

H.1 Unrestricted Optimisations at 0Hz and 100Hz

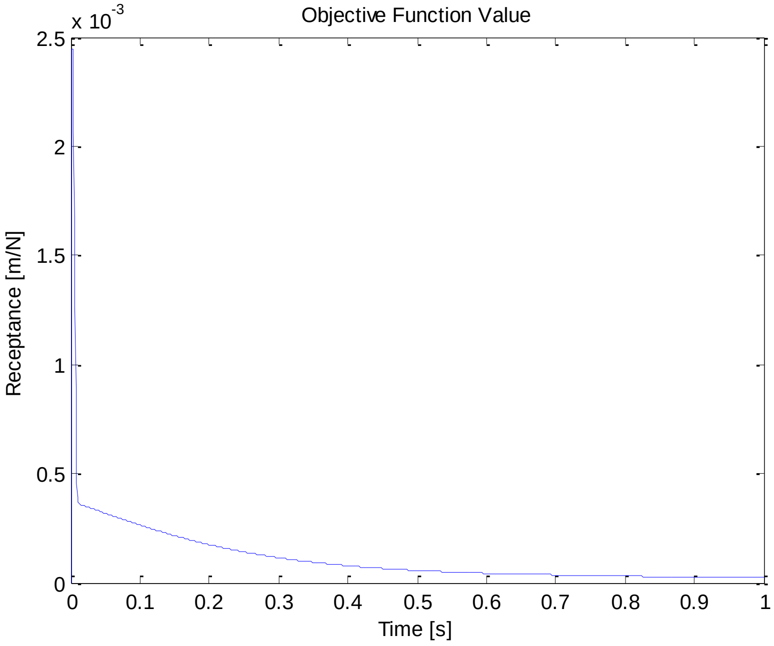

Figure H.1: Objective Function Manipulation for End-Effector Drive Point Receptance Optimisation at 0Hz Starting at Location (-3.5, 1)

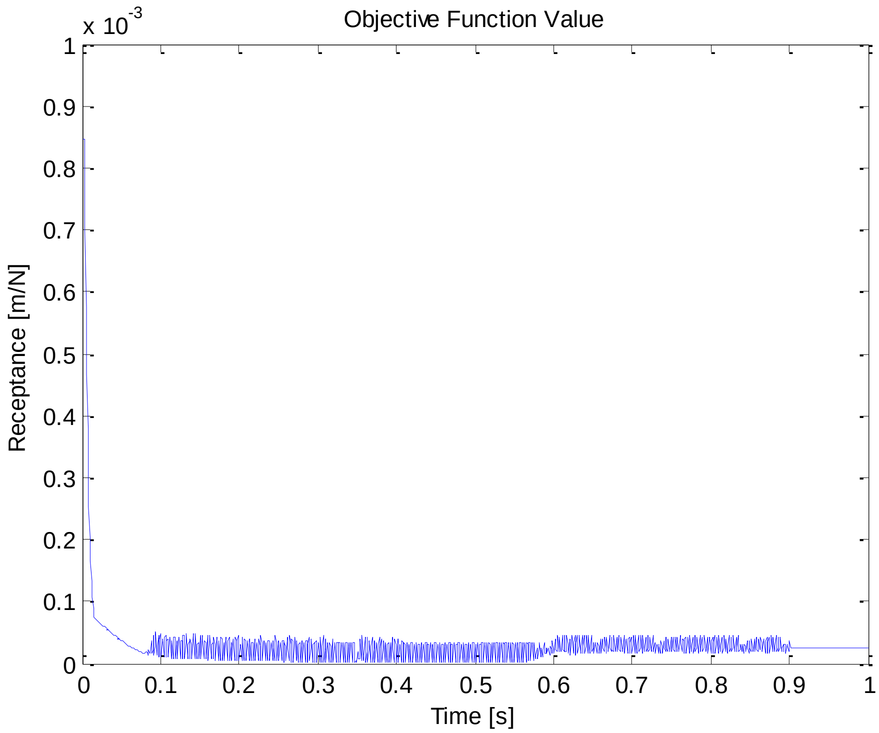

Figure H.2: Objective Function Manipulation for End-Effector Drive Point Receptance Optimisation at 0Hz Starting at Location (-2, 2)

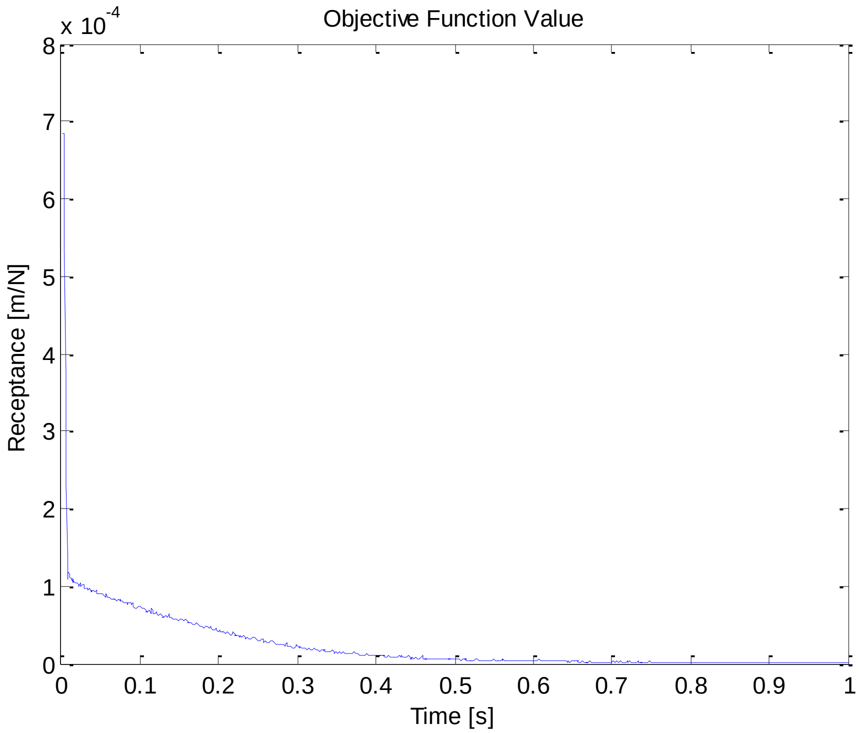

Figure H.3: Objective Function Manipulation for End-Effector Drive Point Receptance Optimisation at 0Hz Starting at Location (0, 1.5)

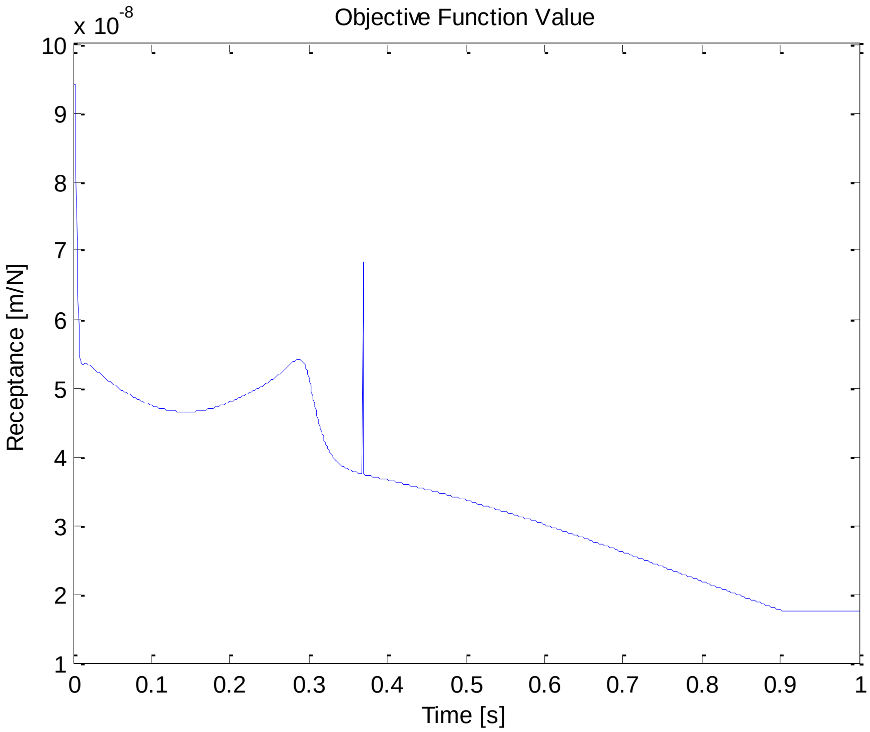

Figure H.4: Objective Function Manipulation for End-Effector Drive Point Receptance Optimisation at 100Hz Starting at Location (-3.5, 1)

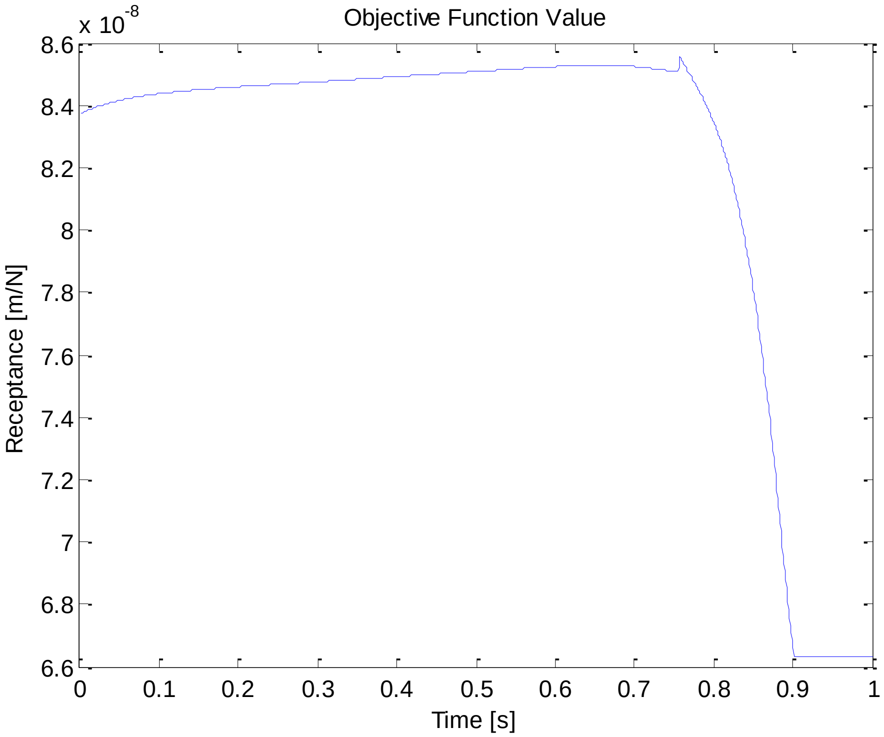

Figure H.5: Objective Function Manipulation for End-Effector Drive Point Receptance Optimisation at 100Hz Starting at Location (-2, 2)

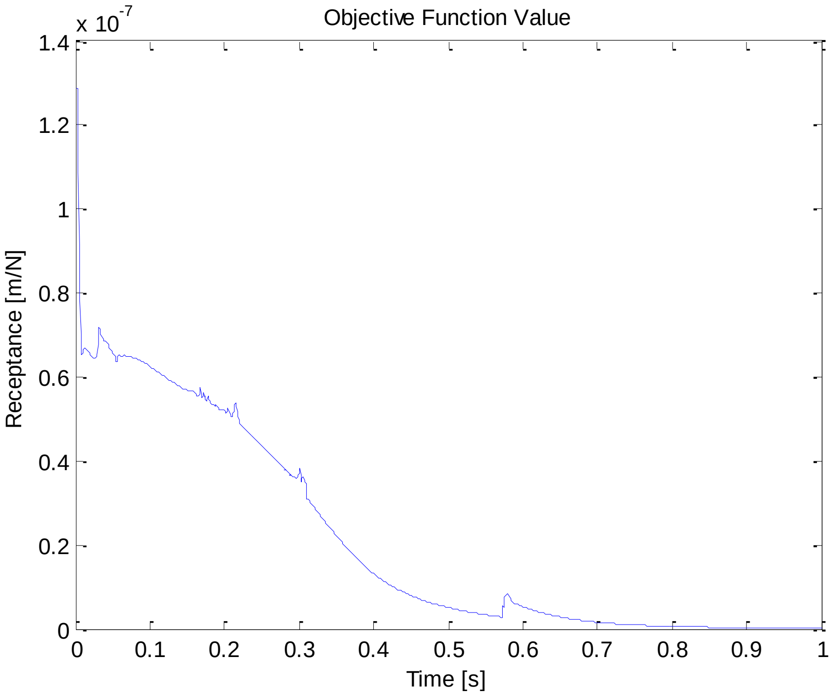

Figure H.6: Objective Function Manipulation for End-Effector Drive Point Receptance Optimisation at 100Hz Starting at Location (0, 1.5)

H.2 Position Controlled Optimisations at 1Hz, 5Hz, and 20Hz

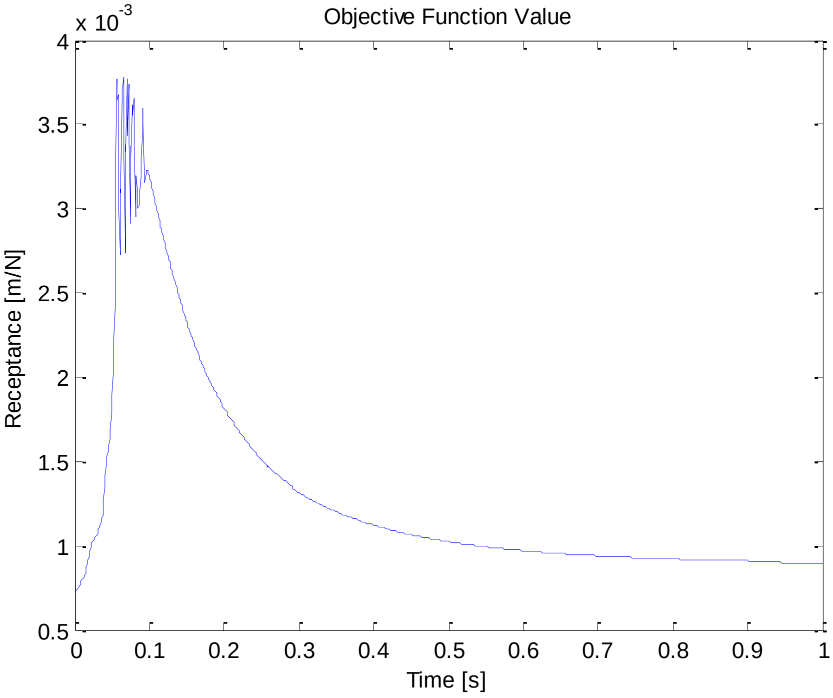

Figure H.7: Objective Function Manipulation for End-Effector Drive Point Receptance Optimisation at 1Hz at Location (-3.5, 1)

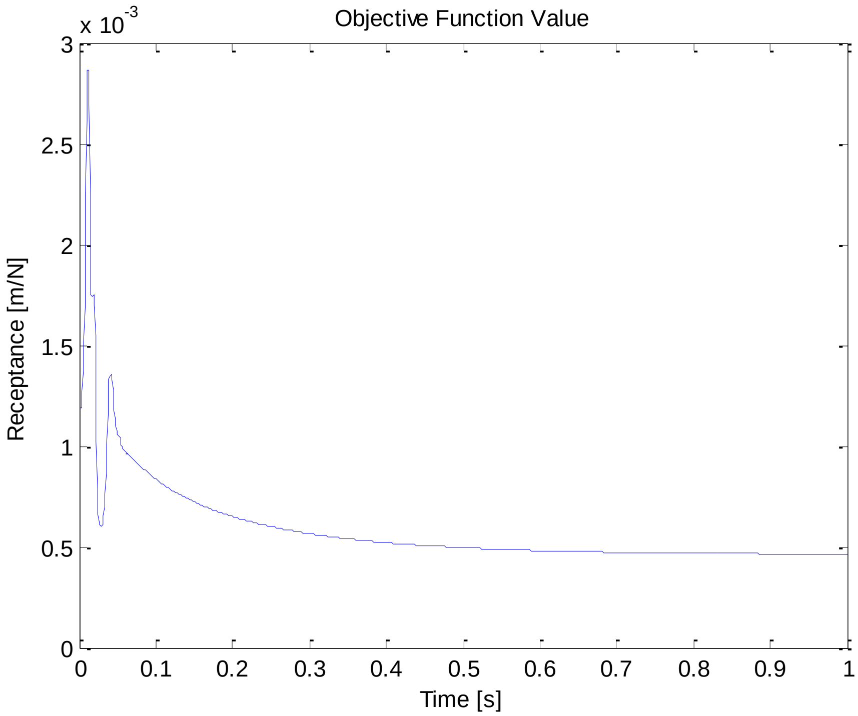

Figure H.8: Objective Function Manipulation for End-Effector Drive Point Receptance Optimisation at 1Hz at Location (-2, 2)

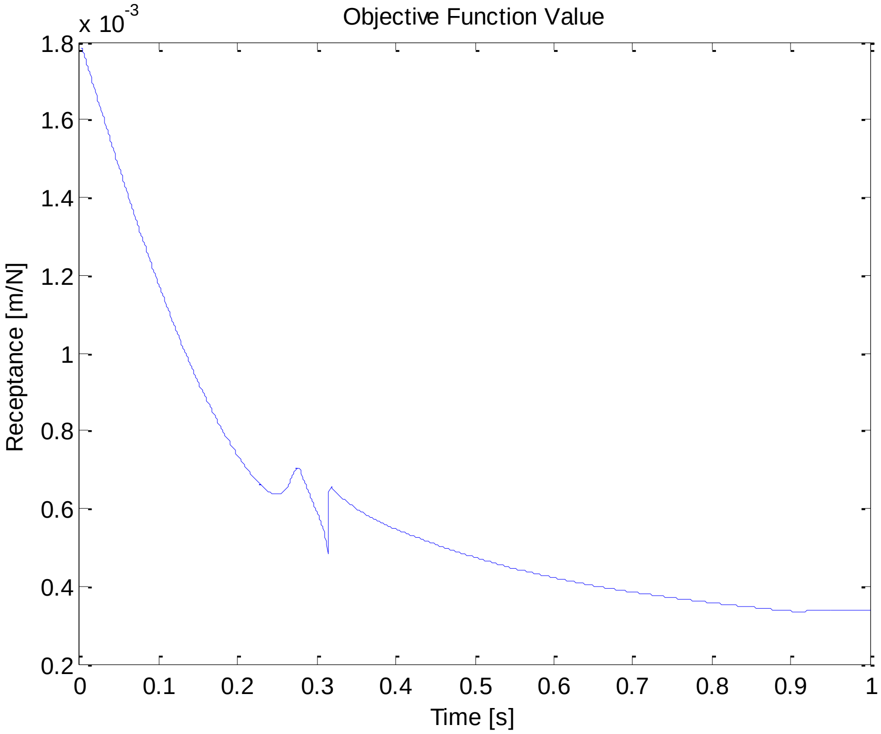

Figure H.9: Objective Function Manipulation for End-Effector Drive Point Receptance Optimisation at 1Hz at Location (0, 1.5)

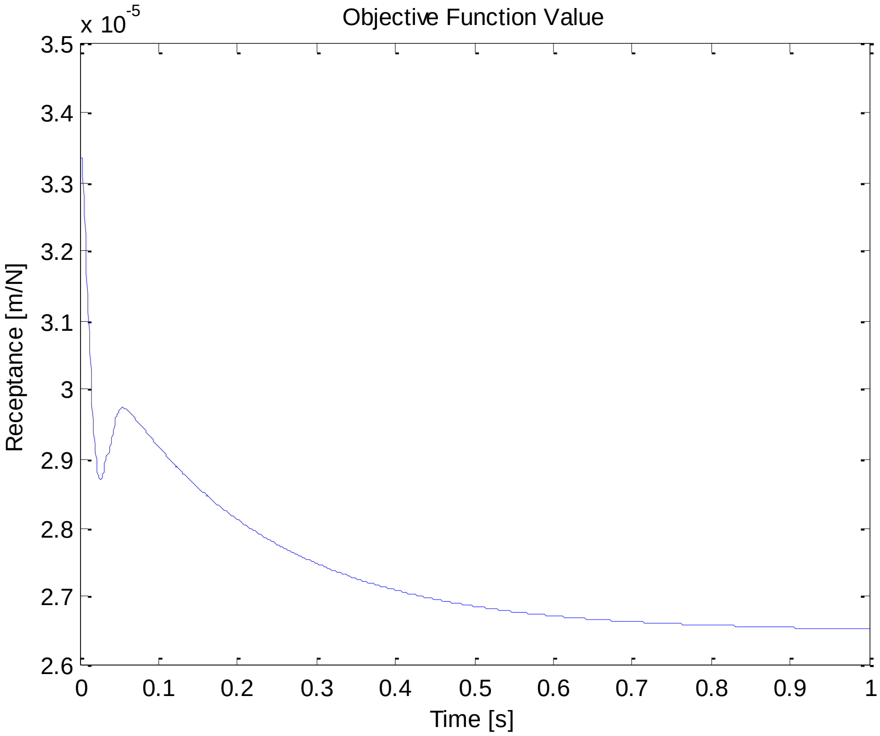

Figure H.10: Objective Function Manipulation for End-Effector Drive Point Receptance Optimisation at 5Hz at Location (-3.5, 1)

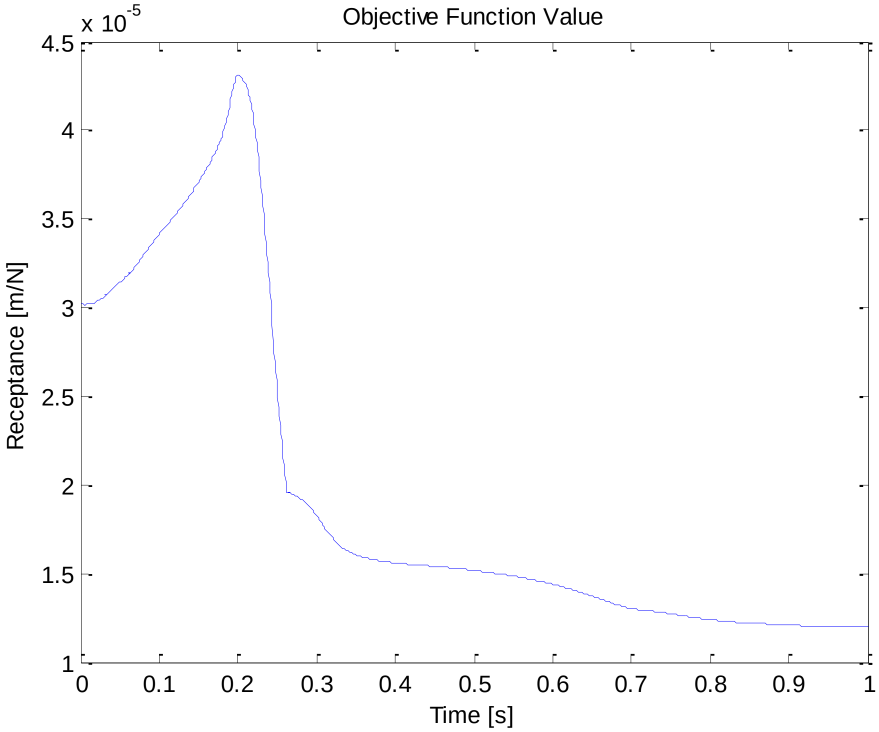

Figure H.11: Objective Function Manipulation for End-Effector Drive Point Receptance Optimisation at 5Hz at Location (-2, 2)

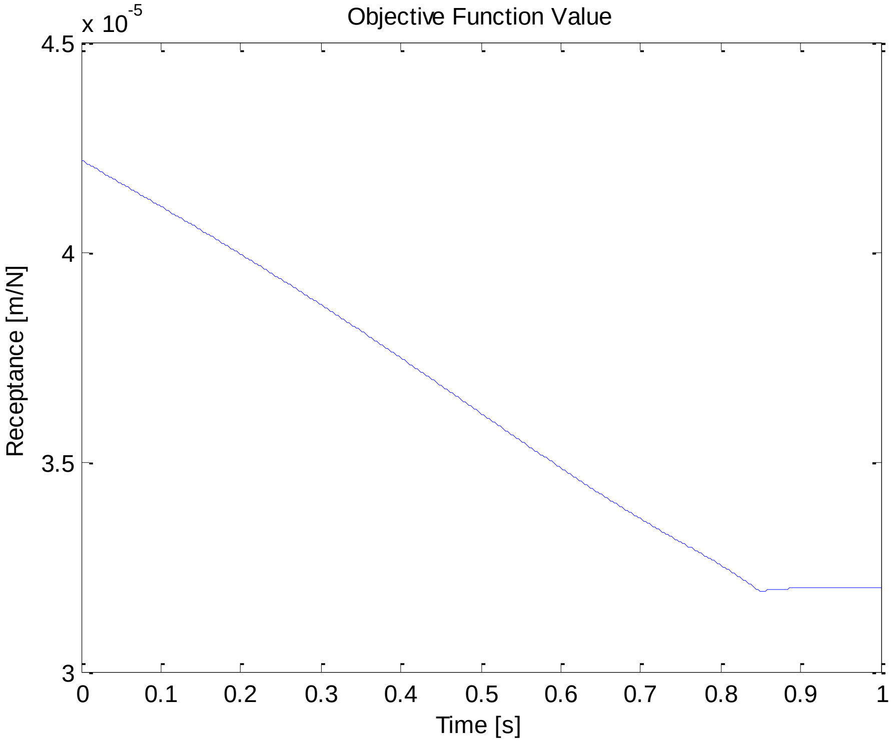

Figure H.12: Objective Function Manipulation for End-Effector Drive Point Receptance Optimisation at 5Hz at Location (0, 1.5)

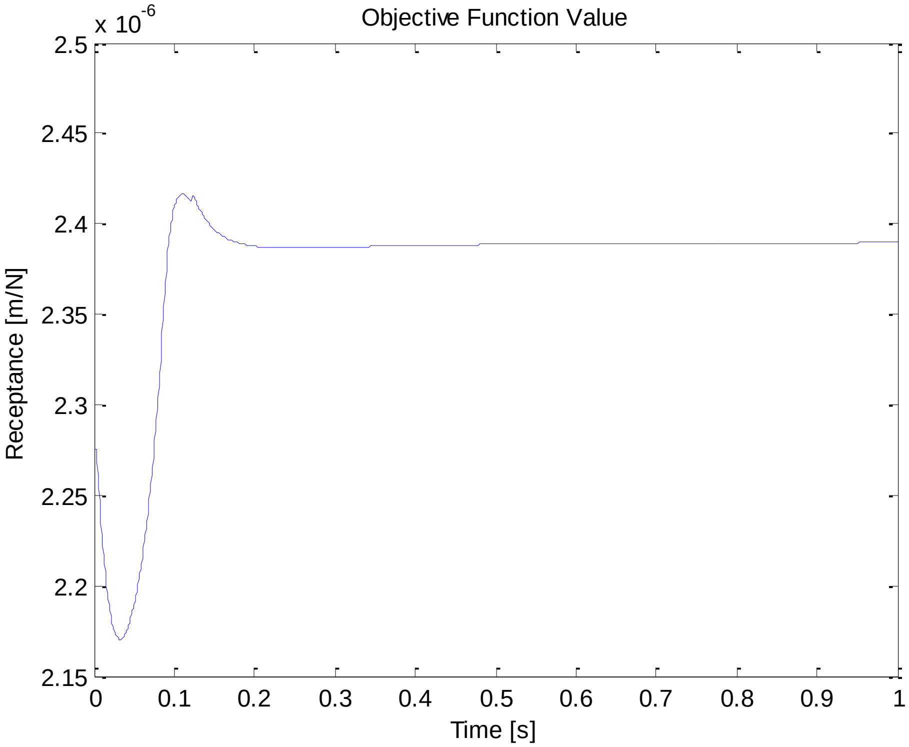

Figure H.13: Objective Function Manipulation for End-Effector Drive Point Receptance Optimisation at 20Hz at Location (-3.5, 1)

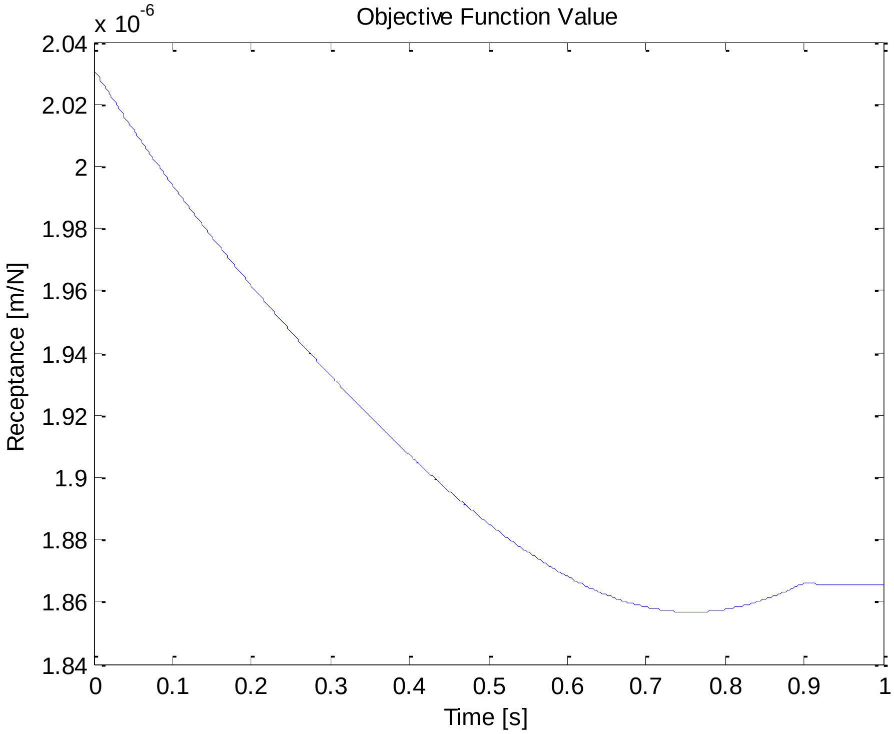

Figure H.14: Objective Function Manipulation for End-Effector Drive Point Receptance Optimisation at 20Hz at Location (-2, 2)

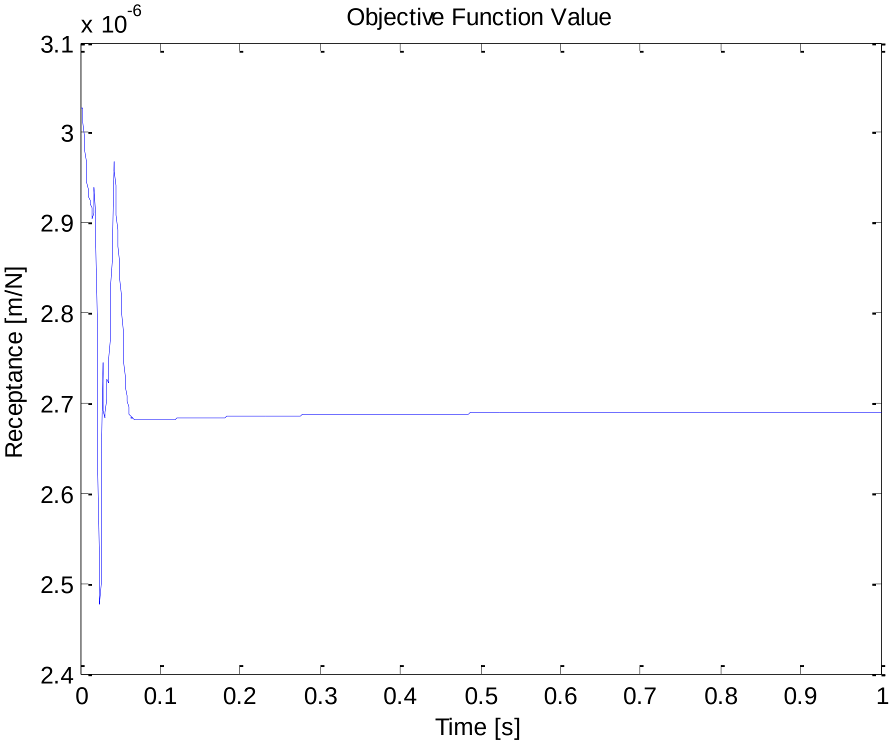

Figure H.15: Objective Function Manipulation for End-Effector Drive Point Receptance Optimisation at 20Hz at Location (0, 1.5)